High Resolution Characterisation of H on Stress Corrosion Cracking in Nuclear Materials



Edward Roberts

Lincoln College

University of Oxford

A thesis submitted for the degree of

Doctor of Philosophy

Trinity 2021

To my family, friends, and all those who supported me.

Acknowledgements

This thesis would not be possible without the help and support of others. I would like to take this opportunity to thank them:

First and foremost, I would like to thank my supervisor Prof. Sergio Lozano-Perez, for giving me this opportunity, and being engaged in my work over the years. I would also like to thank my co-supervisor Prof. Edmund Tarleton. Throughout my project you have both made time to help me experimentally, or computationally, and as a result I have learnt so much. I have been fortunate to be your student.

I would like to show my gratitude to Électricité de France for financial support throughout this project under the Materials Ageing Institute - Scientific Network (MAI-SN) grant. and I would like to thank both my industrial supervisors Florence Carrette and Thierry Couvant for providing samples and taking interest in my work.

I would like to thank the Materials Performance Center at the University of Manchester for their continued discussion on the joint EPSRC project, and helping with the autoclave experiments.

I would like to thank the members of the Nano-analysis group, who have been my "nuclear-family". A big thanks to Dr Phani Karamched, who has taught me everything experimentally and theoretically I know about EBSD/TKD and crystallography. There has never been an issue you can not fix, and I am lucky to have had such a skilled post-doc to support me through my studies. I would also like to thank Dr Guanze He for helping with TEM-EDX observations, and Dr Junliang Liu for completing NanoSIMS experiments at Oxford.

I would like to thank the David Cockayne Centre for Electron Microscopy staff, particularly Dr Gareth Hughes, Dr Ian Griffiths, Ms Jennifer Holter and Mr Graham Wyatt for their help and friendship over the years. Without you my time in the microscopy suite would of been much less enjoyable...albeit maybe more productive.

Thank you to Dr Yevhen Zayachuk, for your help and support using the thermal desorption spectroscopy at the Culham Center for Fusion Energy.

Thanks to Dr Katie Moore, Dr Kexue Li, and the Henry Royce Institute, for providing experimental NanoSIMS assistance at the University of Manchester.

I would like to thank my parents, Susan Roberts and Clive Roberts, my brother, Frank Roberts, my partner, Laura Wheatley, and my friends, of which there are too many to name. I am certain that without your love and support I would not be in the position I am today. Thank you.

Preface

This thesis is the result of my own work completed at the University of Oxford between 2017-2021, under the supervision of Prof. Sergio Lozano-Perez and Prof. Edmund Tarleton. No part of this work has been submitted for a degree at this, or any other, university. Parts of this work have been submitted for publication or presented at conferences, details are provided below:

Publications:

Shen, Z. **Roberts, E.** Saravanan, N, Karamched, P. Terachi, T. Yamada, T. Wu, S. Tarleton, E. Armstrong, D. Withers, P. Arioka, K. Lozano-Perez, S. "On the role of intergranular nanocavities in long-term stress corrosion cracking of Alloy 690". Acta Materialia. (submitted 2021).

Roberts, E. Shen, Z. Carrette, F. Tarleton, E. Armstrong, D. Withers, P. Arioka, K. Lozano-Perez, S. "The effects of intergranular carbides and cavitation on the bonding strength of grain boundaries in alloy 690". Applied Surface Science. (submitted 2021).

Roberts, E. Tarleton, E. Carrette, F. Lozano-Perez, S. "Investigating the Role of Hydrogen on Stress Corrosion Cracking by Micromechanical Testing". The 19th International Conference on Environmental Degradation of Materials in Nuclear Power Systems - Water Reactors, Boston, MA, US. (2019).

Conferences:

Roberts, E. Tarleton, E. Carrette, F. Lozano-Perez, S. "Investigating the Role of Hydrogen on Stress Corrosion Cracking by Micromechanical Testing". The 19th International Conference on Environmental Degradation of Materials in Nuclear Power Systems - Water Reactors, Boston, MA, US. (2019).

Roberts, E. Tarleton, E. Carrette, F. Lozano-Perez, S. "Understanding the Effect of Hydrogen on Stress Corrosion Cracking in Austenitic Alloys by Micromechanical Testing and Modelling". Microscience Microscopy Congress. Manchester, UK. (2018).

Roberts, E. Tarleton, E. Carrette, F. Lozano-Perez, S. "Experimental and Computational Approach to Characterising Hydrogen in Austenitic Alloys". Hydrogen in Metal, Oxford, UK (2018).

Abstract

Austenitic alloys are commonly used in the nuclear industry due to their high corrosion resistance and excellent mechanical properties. Despite boasting an impressive service history, it is possible for critical structural components made from these alloys to undergo stress corrosion cracking (SCC) under pressurised water reactors (PWR) conditions. As the primary method of material degradation, SCC has been studied extensively for several decades, and many factors have been shown to affect SCC susceptibility, these include cold-work, temperature and water chemistry. To develop a better mechanistic understand of SCC further research is required. This body of research evaluates the effect of hydrogen on mechanical deformation in SCC. Localised and high-resolution testing has been employed successfully to characterise key processes in SCC crack propagation. For this reason, nanoindentation, transmission Kikuchi diffraction (TKD), NanoSIMS and Thermal desorption spectrscopy (TDS) have been used to characterise material deformation on a length-scale relevant for SCC.

The main objective of this thesis was to correlate the SCC crack growth rate's (CGR) dependency on nickel content, first observed by Coriou, with both the localised mechanical deformation and hydrogen up-take at PWR temperatures. To satisfy this objective three alloys have been systematically tested in every chapter, these include SS316L (12%-Ni), A800 (32%-Ni) and A600 (72%-Ni) as they represent commercially available alloys with low, intermediate and high nickel contents.

Room temperature micromechanical testing has been used to compare the mechanical properties of austenitic alloys on a length-scale that is relevant to SCC. The mechanical properties of all austenitic alloys are

highly comparable at room temperature, and show no deviation with changing nickel content. High-magnification cross-sectional analysis shows that the deformation mechanisms in A800 differ from SS316L and A600 at room temperature. A800 does not undergo $\Sigma 3$ deformation twinning, but instead deforms by dislocation glide. This is unexpected as the stacking fault energy of A800 is an intermediate of the other alloys. Deformation is a main SCC mechanism, and the observed alloy deformation correlates with Arioka's reported SCC CGR in PWRs, i.e the slowest CGR undergoes no twinning. As the mechanical properties of alloys with a 25-40% nickel content do not differ significantly from other austenitic alloys, it is thought that their corrosion resistance is weighted towards diffusion-based SCC mechanisms. Such an explanation is consistent with findings at hotter temperatures, where diffusion-based mechanisms are more active. High temperature micromechanical testing supports these observations, and can be used to better understand the individual mechanism weights depending on alloy composition and temperature.

NanoSIMS and TDS were used to quantitatively and qualitatively explore the hydrogen trapping in austenitic alloys exposed to pure heavy water at PWR temperatures. Hydrogen is found trapped by various microstructural features, such as carbides, grain boundaries and oxides by NanoSIMS. The total hydrogen content of SS316L and A800 is five-times greater than that of A600, which correlates with the enthalpy of diffusion in the alloys. These results show an inverse trend with the SCC failure reported by Coriou, and a weaker inverse correlation to Arioka's results. The weaker correlation with Arioka's results is due to a change in the corrosive medium from pure water, used in this study and by Coriou, to simulated primary PWR water. It is suggested that the inverse relationship could be due to the elastic shielding provided by the hydrogen enhancing dislocation motion, and preventing the stress intensity factor reaching a critical values that will initiate crack propagation.

Contents

1 Introduction **1**

1.1 The Issue of Hydrogen 1

1.2 Pressurised Water Reactors and Material Degradation 2

1.3 Coriou's Observations 3

1.4 Research Objectives 5

2 Literature Review **7**

2.1 Stress Corrosion Cracking 7

2.1.1 Crack initiation 7

2.1.2 Influencing factors 10

2.1.2.1 Alloy Composition 10

2.1.2.2 Cold-Working 11

2.1.2.3 Grain Boundary 12

2.1.2.4 Carbon Content and Carbide Precipitates 13

2.1.2.5 Temperature 14

2.1.3 SCC Mechanisms in Austenitic Alloys 15

2.1.3.1 Film-Rupture Model 16

2.1.3.2 Internal Oxidation Model 16

2.1.3.3 Hydrogen Mechanisms 18

2.1.4 Summary 20

2.2 Hydrogen 21

2.2.1 Entry of Hydrogen into Materials 22

2.2.1.1 Gaseous 22

2.2.1.2 Electro-chemical Charging 23

2.2.1.3 PWR conditions 24

2.2.2 Hydrogen Diffusion . . . 26
2.2.2.1 Macroscopic . . . 26
2.2.2.2 Microscopic . . . 27
2.2.3 Hydrogen Trapping . . . 29
2.2.3.1 Models and Simulations . . . 29
2.2.3.2 Point Defects . . . 32
2.2.3.3 Dislocations . . . 32
2.2.3.4 Slip Planes . . . 33
2.2.3.5 Grain Boundaries . . . 33
2.2.4 Summary . . . 35
2.3 Experimental Characterisation of Hydrogen . . . 36
2.3.1 Atom Probe Tomography . . . 36
2.3.2 Transmission Electron Microscopy . . . 39
2.3.3 Secondary Ion Mass Spectroscopy . . . 39
2.3.4 Scanning Kelvin Probe Force Microscopy . . . 40
2.3.5 Neutron Tomography . . . 41
2.3.6 Thermal Desorption Spectroscopy . . . 41
2.3.7 Summary . . . 43

3 Experimental Methodology **45**
3.1 Materials . . . 45
3.2 Sample Preparation . . . 46
3.2.1 Micromechanical Testing Samples . . . 46
3.2.2 Autoclave Samples . . . 47
3.3 Nanoindentation . . . 47
3.3.1 Mechanics . . . 47
3.3.1.1 Berkovich Tip . . . 47
3.3.1.2 Spherical Tip . . . 48
3.3.2 Continuous Stiffness Measurements (CSM) method . . . 50
3.3.3 Instrumentation . . . 50
3.3.3.1 Nanoindenter XP . . . 51
3.3.3.2 In-situ Electrochemical Hydrogen Charged Nanoindentation . . . 52

3.3.3.3 Xtreme High Temperature Nanoindenter 53
3.3.3.4 Nanoindenter Tips 54
3.3.4 Nanoindentation Phenomena 55
3.3.4.1 Surface Roughness 55
3.3.4.2 Indentation Size Effect 56
3.3.4.3 Pile-ups and Sink-ins 56
3.3.4.4 Pop-ins 57
3.4 Scanning Electron Microscopes 58
3.4.1 Electron Backscattered Diffraction 60
3.4.2 Transmission Kikuchi Diffraction 61
3.5 Focused Ion Beam 63
3.5.1 TEM/TKD Sample Preparation 63
3.6 Transmission Electron Microscopes 64
3.7 Autoclave 65
3.8 NanoSIMS 66
3.9 Thermal Desorption Spectroscopy 67

4 Coupled Diffusion-Mechanical Hydrogen Transport Sub-routine (UMATHT) 69
4.1 Hydrogen Diffusion 69
4.2 Oriani's Assumption 71
4.3 Analogous Implementation of the UMATHT Subroutine 73
4.4 3D - UMATHT 76
4.5 Summary 80

5 Preliminary Characterisation 81
5.1 Materials Microstructure 81
5.1.1 Chemical Composition 81
5.1.2 Grain Statistics 81
5.1.3 CSL Boundary Types 83
5.1.4 Inclusions 85
5.1.5 Phase Transformations 88
5.1.6 Carbides Analysis 88

5.1.7 Background Dislocation Density 91
5.1.8 Summary 93
5.2 Oxidation Characterisation 93
5.2.1 Surface Morphology 94
5.2.2 Oxidation Chemistry and Development 94
5.2.2.1 Post-Autoclave SS316L 94
5.2.2.2 Post-Autoclave A800 98
5.2.2.3 Post-Autoclave A690 99
5.2.2.4 Post-Autoclave A600 CW 101
5.2.3 Quantification of Oxide Nano-Porosity 104
5.2.3.1 Post-Autoclave SS316L 104
5.2.3.2 Post-Autoclave A800 105
5.2.3.3 Post-Autoclave A690 105
5.2.3.4 Post-Autoclave A600 CW 107
5.2.4 Summary 110

6 Room-Temperature Micromechanical Testing of Nuclear Alloys 111
6.1 Introduction 111
6.2 Converting Load-displacement data to Stress-strain 112
6.3 Results 117
6.3.1 Room-Temperature Mechanical Testing 117
6.3.1.1 SS316L 117
6.3.1.2 A800 120
6.3.1.3 A600 122
6.3.2 High-Magnification Analysis 126
6.3.2.1 Localised Deformation Zones 126
6.3.2.2 Deformation Mechanisms and Dislocation Analysis 126
6.4 Discussion 132
6.4.1 Mechanical Properties in Austenitic Alloys 132
6.4.1.1 Young's Modulus 132
6.4.1.2 Yield Stress 134
6.4.1.3 Experimental Reliability 135
6.4.2 Lattice Rotations 137

6.4.3 Deformations and Dislocations . . . 137
6.4.4 Quantifying a Mechanical Deformation Mechanism in SCC . 141
6.5 Summary . . . 142

7 Room-Temperature In-situ Hydrogen-Charged Micromechanical Testing of Nuclear Alloys 143
7.1 Introduction . . . 143
7.2 Experimental . . . 144
7.2.1 Results . . . 144
7.2.1.1 Electrochemical Potentiodynamic Polarisation . . . 144
7.2.1.2 Effects of Charging Conditions on the Sample Surface 146
7.2.1.3 Nanoindentation in a Liquid Environment . . . 149
7.2.1.4 In-situ Electro-chemical Hydrogen Charged Nanoindentation . . . 150
7.2.2 Discussion . . . 153
7.2.2.1 Limitations of In-situ Nanoindentation . . . 153
7.2.2.2 Tip Condition . . . 154
7.3 Computational Analysis of In-situ Hydrogen Experiments . . . 155
7.3.1 Results . . . 155
7.3.2 Discussion . . . 160
7.4 Summary . . . 162

8 PWR-Temperature Micromechanical Testing of Nuclear Alloys 163
8.1 Introduction . . . 163
8.2 Results . . . 164
8.2.1 Room Temperature . . . 164
8.2.2 Cool Operating Temperature - 280°C . . . 166
8.2.3 Hot Operating Temperature - 360°C . . . 167
8.3 Discussion . . . 171
8.3.1 Temperature Dependence of Mechanical Properties . . . 171
8.3.2 Oxidation . . . 175
8.3.3 Comparison to Crack Growth Rate . . . 175
8.4 Summary . . . 178

9 Hydrogen Uptake and Trapping Under PWR Conditions 179
9.1 Introduction . . . 179
9.2 Thermal Desorption Spectroscopy . . . 179
9.2.1 Preliminary Findings and Calibration Tests . . . 180
9.2.2 Impact of oxide on hydrogen desorption . . . 181
9.2.3 Cold-worked Samples . . . 184
9.2.4 Effect of Cr-content . . . 187
9.2.5 Effect of Nickel Content . . . 189
9.3 NanoSIMS . . . 193
9.3.1 Normalisation Process . . . 193
9.3.2 Cross-section Analysis . . . 193
9.3.2.1 Matrix Concentration . . . 193
9.3.2.2 Grain Boundaries and Oxidised Grain Boundaries . 197
9.3.2.3 Carbides . . . 200
9.3.3 Top-down Analysis . . . 202
9.3.3.1 Depth Profiling - Hydrogen Diffusion . . . 202
9.3.3.2 3D Reconstruction . . . 204
9.3.3.3 Depth Profiling - Hydrogen Concentrations . . . 208
9.4 Summary and Discussion . . . 209

10 Conclusions and Future Work 213
10.1 Conclusions . . . 213
10.2 Future Work . . . 215

A Testing the Effect of Intergranular Carbides and Cavities on Grain Boundary Cohesion in A690 by Microcantilever Fracture 217
A.1 Introduction . . . 217
A.2 Experimental Micromechanical Cantilevers . . . 218
A.2.1 Autoclave Testing . . . 218
A.2.2 Methodology . . . 219
A.2.3 Results . . . 222
A.2.3.1 *A690* with intergranular carbide coverage and no cavities . . . 222

A.2.3.2 *A690* with intergranular carbide coverage and cavities . . . 224
A.2.3.3 Nanoindentation . . . 227
A.2.4 Discussion . . . 227
A.3 Modelling Micromechanical Cantilevers . . . 230
A.3.1 Finite Element Methods . . . 230
A.3.1.1 Crystal Plasticity . . . 231
A.3.1.2 Boundary Traction Law . . . 233
A.3.2 Material Definition, Model Specifications and Parameter Studies . . . 235
A.3.2.1 Crystal plasticity Parameter Fitting . . . 236
A.3.2.2 Cohesive Boundary . . . 239
A.3.2.3 Carbides and Cavities . . . 243
A.3.2.4 *Case Study:* Carbides . . . 246
A.3.2.5 *Case Study:* Cavities . . . 248
A.3.3 Results . . . 249
A.3.3.1 *A690* with intergranular carbide coverage and no cavities . . . 249
A.3.3.2 *A690* with intergranular carbide and cavity coverage 250
A.3.4 Discussion . . . 251
A.4 Summary . . . 253

References **255**

Chapter 1

Introduction

1.1 The Issue of Hydrogen

Hydrogen is detrimental to material properties, causing hydrogen embrittlement (HE) or hydrogen induced cracking. Since Johnson's first report in 1872, thousands of peer-reviewed papers have investigated and explored the effects of hydrogen in materials [1]. Intense research is indicative of a complex and detrimental problem that is of interest to the scientific community and industry alike.

The majority of countries have committed to net-zero goals by 2050, keeping global warming under 2°C as agreed in the Paris agreement [2]. The transition away from fossil fuels is crucial in order to minimise the emission of CO_2 and other greenhouse gases. However, the emerging sustainable energy sector, which is replacing the 65% of global electricity [3] generated by fossil fuels, is effected by hydrogen in numerous ways. Firstly, hydrogen as a renewable energy source is limited by the degradation of the materials used to store and transport hydrogen [4]. Secondly, the bearing materials used in wind turbines are affected by hydrogen accelerated contact rolling fatigue from the hydrogen present in lubricants [5]. Finally, hydrogen is thought to be a potential precursor to stress corrosion cracking (SCC), the dominant degradation mechanism in pressurised water reactors (PWR) [6]. The hydrogen is added to the water in the primary circuit to prevent oxidation, by combining with oxygen ions to form water.

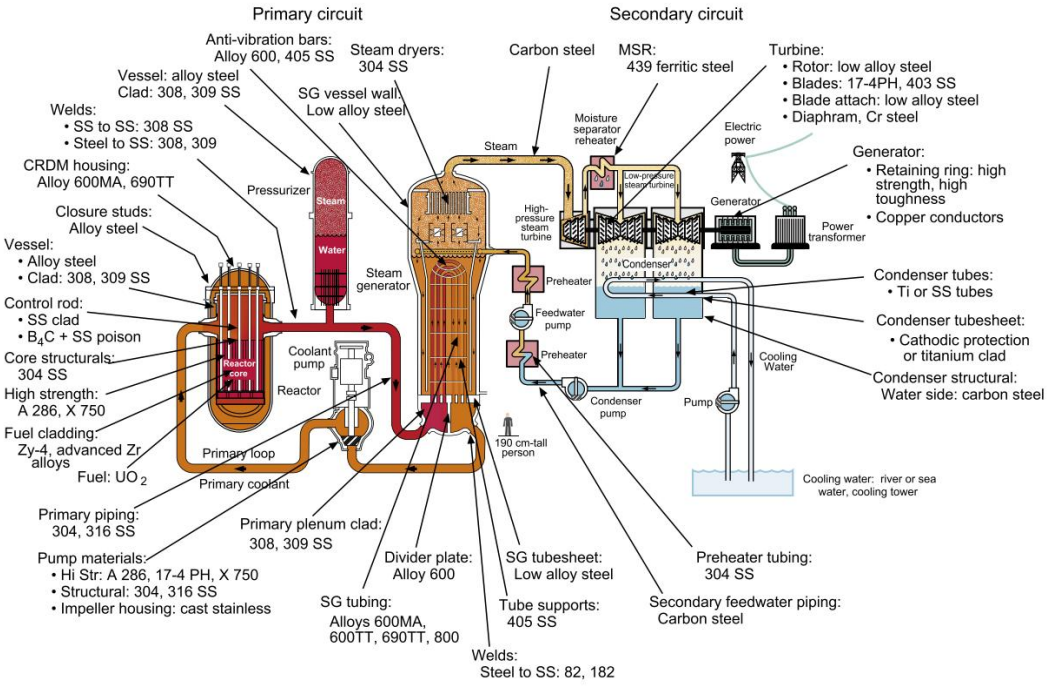


Figure 1.1: Overview of the components and materials used in a pressurised water reactor, from [8]. Reprinted from Stress Corrosion Cracking of Nickel Based Alloys in Water-cooled Nuclear Reactors, R.W. Staehle, pp 3-131., Copyright (2016), with permission from Elsevier.

1.2 Pressurised Water Reactors and Material Degradation

Pressurised water reactors were first built to power US navy submarines, aircraft carriers and icebreakers, any vessel that needed to operate independently for long periods of time. This technology eventually found civilian use, and was commercialised to produce electricity. As of 2019, the international atomic energy authority (IAEA) reported that there are currently 304 operational PWRs producing a combined 1927 TWh of low-carbon electricity [7].

A PWR contains many materials and components, seen in Figure 1.1. These can be broadly split in to two groups, nuclear materials and structural materials. Nuclear materials are critical for the safe operation of the reactor and include the control rods and fuel cladding. Structural materials make up the infrastructure

necessary to turn the pressurised water into electricity, this includes the piping, turbines and heat exchanger. This thesis is concerned with the materials used to make structural components in the primary side of the reactor. The safe and economic running of a PWR reactor is dependent on each component fulfilling its role over its entire service life.

Nuclear facilities originally had a nominal design operating lifetime of 25 to 40 years; but of the 304 PWRs in service, 200 have already surpassed 30–39 years of operation and a further 92 have surpassed 40 years of operation [7]. In western Europe and the United States, where these older reactors are located, building new reactors is not favourable, instead opting for increased capacity and extended operating times, subject to regular engineering assessment.

However, long operating times can lead to the environment degradation of critical structural components needed for PWR operation, threatening economic impact, safety concerns, and power losses. The primary material degradation in these systems is SCC. In order to ensure the integrity of a PWR, and to prevent loosing the low-carbon electricity, a through understanding of SCC is required to better predict component life-times and performance.

1.3 Coriou's Observations

Stress corrosion cracking in PWRs is not a new problem. The earliest alloy development for the nuclear industry started back in the 1950s, as companies sought-out a replacement for the stainless steel (18Cr-10Ni) used in the first wave of PWRs. This steel was highly susceptible to SCC from the chlorine and oxygen contaminants that existed in early primary circuits. In an attempt to prevent SCC in PWRs, metallurgists developed the high Ni-alloy Alloy 600 (Inconel 600). Alloy 600 possessed similar structural properties to steels and had a high resistance to SCC under chlorine-attacks.

It was thought that A600 was immune to the issues that plagued steels, until Coriou et. al [9] first identified SCC behaviour at the CEA laboratories in 1959. This work was immediately challenged by US-based alloy manufacturers INCO and Westinghouse, who under the lead of Copson, had no success in cracking A600 [10] and later dismissed Coriou's results as anomalous. In spite of the slander

from INCO and Westinghouse, Coriou was able to repeatedly demonstrate the cracking of A600 over the course of the following decade. The rhetoric between the two researchers finally came to an end in the early 1970s, when the first case of primary-side SCC in A600 was observed in steam tubing at Obrigheim (Germany), as predicted by Coriou.

While Coriou successfully highlighted SCC in A600, he inadvertently demonstrated a far more interesting observation. As illustrated in Figure 1.2, any Fe-Cr-Ni alloy that possesses a intermediate nickel content will have a higher SCC resistance. This effect has been further investigated by Arioka et. al [11, 12, 13, 14] and Lozano-Perez [15, 16, 17, 18, 19, 20], who demonstrated that alloys with a 30–40 % nickel-content will have an increased corrosion resistance at higher temperatures (340°C) compared to cooler temperatures (320°C) (Figure 1.3). The mechanisms driving this temperature-dependent corrosion resistance are currently under inves-

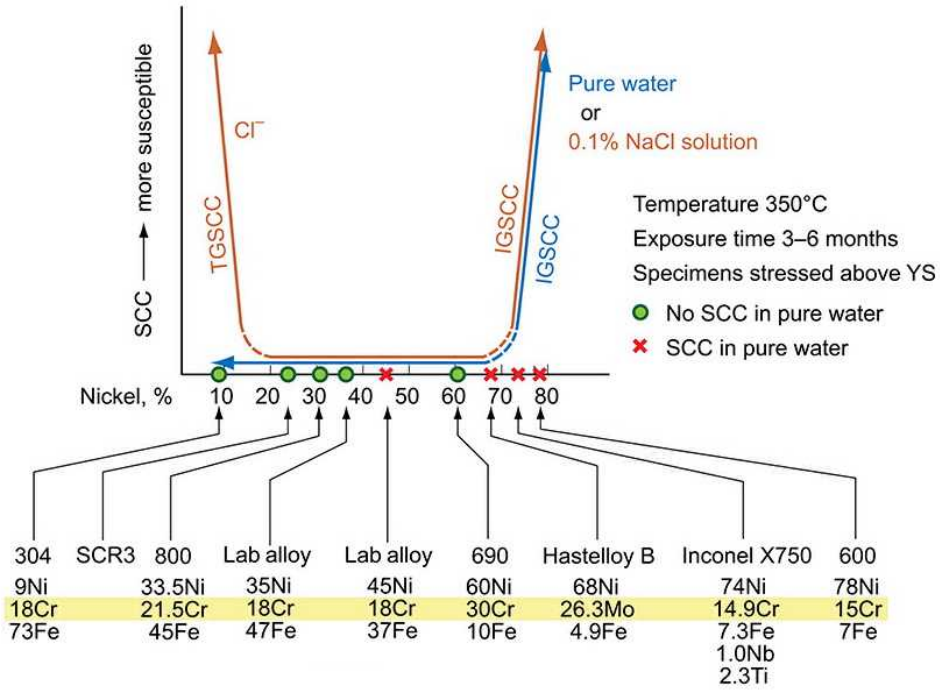


Figure 1.2: How nickel concentration in Fe-Cr-Ni alloys affects the alloys resistance to SCC in pure deoxygenated water [8]. Reprinted from Corrosion, Vol. 22, Coriou et al. Sensitivity to Stress Corrosion and Intergranular Attack of High-Nickel Austenitic Alloys. Copyright (1996), with permission from NACE International.

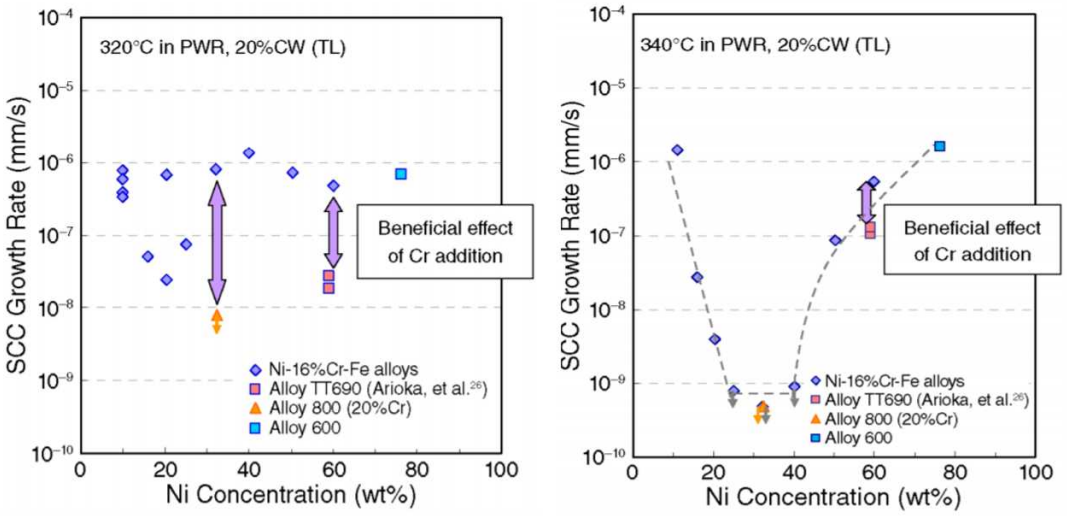


Figure 1.3: The temperature-dependent resistance of nickel alloys [12]. Reprinted from CORROSION SCIENCE, vol 70 (7), Intergranular Stress Corrosion Cracking Growth Behavior of Ni-Cr-Fe Alloys in Pressurized Water Reactor Primary Water, Koji Arioka, Takuyo Yamada, Tomoki Miyamoto, Masanori Aoki, pp 702, Copyright (2014), with permission from National Association of Corrosion Engineers., NACE International.

tigation. Understanding the material properties that give these alloys enhanced corrosion resistance is crucial to designing more resistant alloys in the future, and better evaluating the likely cause of failure in current reactors.

1.4 Research Objectives

This aim of this thesis is to evaluate the effect of hydrogen on the mechanical properties in austenitic alloys, and correlate these findings with Coriou's observations to determine if hydrogen plays a dominant role in this effect. Localised and high-resolution testing techniques have been previously employed to successfully characterise other key processes in SCC crack propagation [16, 17, 18, 19]. So, a similar multi-technique approached is used for the effects of hydrogen throughout in this thesis. This research project is broken into manageable sections that form the chapters of this thesis. They are outlined below:

1. Identify the mechanical properties and deformation mechanisms of commercial austenitic alloys with no external influences (Chapter 6).

2. Evaluating the effects of hydrogen on the mechanical properties of austenitic alloys by comparing hydrogen charged results to reference experiments with no external influences previously completed (Chapter 7).

3. Evaluating the effects of PWR temperatures on the mechanical properties of austenitic alloys (Chapter 8).

4. Quantitatively and qualitatively evaluating the hydrogen-uptake, and identify different trapping behaviours in austenitic alloys (Chapter 9).

5. Use the skills and techniques developed over the thesis to explore the effects of interganular cavitation on the grain boundary strength in alloy 690 (Appendix A).

Chapter 2

Literature Review

2.1 Stress Corrosion Cracking

Stress corrosion cracking (SCC) is generally accepted as the sub-critical cracking of materials under a synergistic combination of material susceptibility, an applied and/or residual stress, and a liquid or gaseous environment, as presented in Figure 2.1. If one of these elements (environment, material, or stress) is absent then SCC will not usually occur. SCC is a single mode of corrosion made up of multiple sub-modes, with intergranular (IGSCC) and transgranular (TGSCC) being the most distinctive. The characteristic behaviour of IGSCC is that the cracks follow the grain boundaries of a polycrystalline material, while TGSCC cracks ignore the granular structure of a polycrystalline material, producing two highly unique crack paths. In primary water environments, primary water stress corrosion cracking (PWSCC), a sub-mode of IGSCC, is of interest. This is characterised by the low corroding potential, resulting from the negligible ion content of primary water, and intergranular cracking traits.

2.1.1 Crack initiation

Stress corrosion cracking is a process that occurs in distinct phases: the initiation- (precursors, incubation, and slow growth) and the propagation- phase, as seen in Figure 2.2. The precursor is the period in which local environmental changes occur to facilitate crack initiation, and can often last from hundreds to thousands of hours. A crucial environmental change to the SCC process is the accumulation

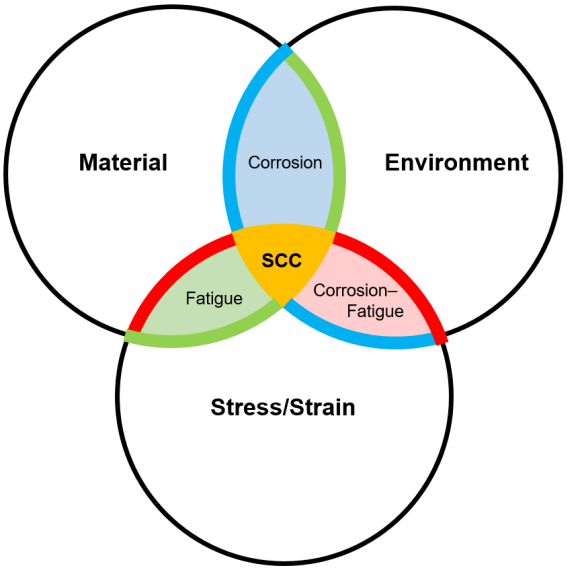


Figure 2.1: Factors affecting stress corrosion cracking and some of their synergistic effects.

and transport of ions between the negative cathode and the positive anode where corrosion occurs. However, other frequently observed changes include depletion and the accumulation of alloying species. The precursor stage is strictly limited to the environmental changes that lead up to SCC, so throughout this stage the materials protective oxide film is not breached.

After an environment favourable to SCC has been created, nano-cracks can initiate on the surface of the specimen and penetrate the materials oxide film. During the incubation stage, the nano-cracks are below the threshold for instrumental detection, so the specimen will undergo no observable transformation. While SCC cracks can not be observed at this stage, small detectable cracks can be found within pre-existing crack-like initiation sites. These are distinctly different from SCC and undergo an alternative evolutionary time-line. Such initiation sites include: pits, coating defects, welds, intergranular corrosion (at grain boundary sites with favourable chemistry), and through slip-dissolution (in a material with a low stacking fault energy)[21]

Upon crossing the detection threshold, the cracks enter the slow-growth regime. In this regime small cracks will often coalesce to form larger cracks reaching upwards of 500 μm in length. To further aid in relieving the building stresses, new

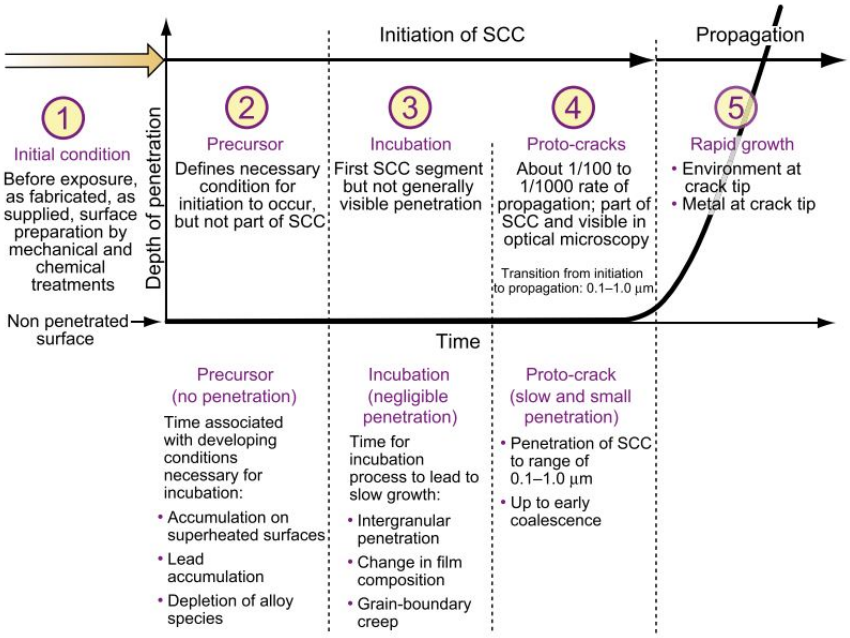


Figure 2.2: The development of a crack resulting from SCC, from [8]. Reprinted from Stress Corrosion Cracking of Nickel Based Alloys in Water-cooled Nuclear Reactors, R.W. Staehle, pp 3-131, Copyright (2016), with permission from Elsevier.

cracks are also simultaneously being formed at the surface, which fuels a continuous cycle of coalescence and growth. Throughout cycles a dominate crack begins to emerge. This stage can continue for hundreds to thousands of hours, until the velocity of the dominate primary crack increases, by an order of magnitude, and the velocity of secondary cracks stall.

Arioka et al [13] has dedicated considerable experimental time investigating the phenomena of crack initiation. In SS316L, it has been reported that for a 50 μm pre-crack, slight deformation caused a considerable stress development. When local stress reached a threshold, SCC growth begins. It was reported that initiation could be accelerated by cold-work or elevated temperatures. Similar observation for the effect of CW and temperature have been noted for A600 in simulated primary PWR water [22].

This emergence of the primary crack signifies a change from the initiation period, to the crack propagation period; a change that is formally defined as an

increase in the stress intensity factor K_I beyond the threshold value K_{ISCC}. The introduction of the stress intensity factor, and its critical value, indicates that SCC can only from from a corrosion-generated flaw characterised by a radius, r. This is not necessarily true, and it requires the simultaneous application of applied stress and environmental exposure to achieve sub-critical crack propagation.

The propagation phase of SCC is still not fully understood [23], but it is commonly separated into three distinct stages. The first stage has already been observed, it is the rapid propagation that occurs then the stress intensity factor K_I surpasses the threshold value K_{ISCC}. The crack will continue to propagate until it hits the second stage, the plateau stage. During this period K_I continues to grow, but yields little crack growth in return. The crack will then re-enter a phase of rapid propagation, similar to that in the first stage, where it is able to grow very quickly. For a sufficiently high crack density, rapid coalescence can occur throughout all three stages to further increase the crack density, and dramatically shorten the time to failure of the component [24, 25].

This assessment of crack growth highlights the complexity of detecting SCC over the time-scales mentioned, and how to best prevent it provides grounds for debate within this area of research. To deepen the communities understanding of SCC, recognising the effects of influencing factors on different alloys, and the mechanism by which SCC propagates is crucial. Summarising these factors, and mechanisms, will be the focus of the remaining section.

2.1.2 Influencing factors

Stress corrosion cracking is a complex and multi-faceted phenomenon that relies on numerous material properties and environmental conditions. There are several factors that are known to influence the initiation and propagation of SCC in nickel alloys. Over the next section these will be discussed.

2.1.2.1 Alloy Composition

The SCC characteristics of any given material is greatly influenced by its elemental composition. In 1989, Yonezawa et al [26] conducted a study during which the influence of Ni- (73 - 87 wt.%) and Cr-concentration (1 - 20 wt.%) on IGSCC

in PWR conditions was investigated. The study concluded that the Ni content, with the Cr concentration being held at 5 wt.%, had an inconsequential effect on the corrosion resistance, while increasing the Cr content from 5 wt.% to 20 wt.% greatly increased the time to failure, as seen in Figure 2.3. Increasing Cr is the most impactful compositional change. This is illustrated by comparisons between A600 (15 % Cr, 73% Ni), an alloy known to exhibit IGSCC in PWR conditions, and A690 (30% Cr, 67% Ni), which has a greater SCC resistance under the same environmental conditions [27]. Cr helps the formation of carbides, and influences oxide formation.

As reported by Angeliu and Was [28], increasing the Cr level from 5 - 17 wt.% induces a change in the surface oxide from $Ni(OH)_2$ to a more compact Cr-rich oxide Cr_2O_3. It was also noted that a sufficiently high Cr content can reduce the creep and the deformation rate in nickel-based alloys [29], a resulting feature from the chromium-hardening of the underlying Nickel matrix [30, 31]. Similar reports have been made by Lozano-Perez et al [32] for 304 stainless steel. The increased resistance of SUS304 is due to the reduced penetration of the oxide layer ahead of the crack tip. The concentrated Cr-oxide minimises the volume of brittle material ahead of the crack and slows down the CGR by a significant amount.

Recent reports by Arioka [11, 33] and Bruemmer [34] have found that the growth of intergranular cavities, which form at carbide-matrix interfaces, can lead to failure of heavily cold-worked A690 in laboratory tests. While Cr is known to enhance corrosion resistance, and aside from the aforementioned cavity growth, it has not been found to alter material properties [35, 29, 36].

2.1.2.2 Cold-Working

As a material is cold-worked (CW) it is plastically deformed, and becomes increasingly saturated with dislocations, stacking faults, localized slip planes or deformation bands [37]. The saturated lattice prevents new dislocations from nucleating, and existing dislocations from propagating. This leads to a higher yield stress.

The introduction of cold-work in PWR components is almost unavoidable through component manufacturing or installation, so the effect of cold work should be taken into account when testing susceptible materials. It has been established by Bruemmer and Moshier that cold working non-sensitised materials is always

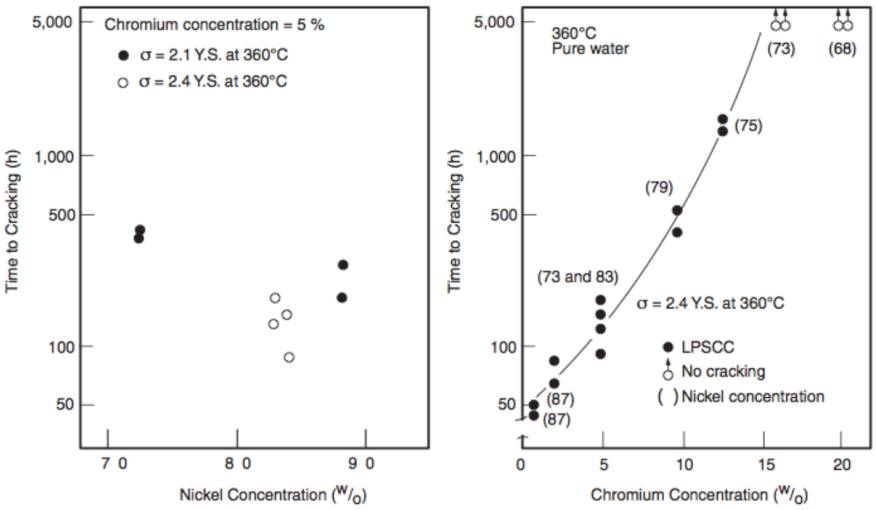


Figure 2.3: The impact of Cr and Ni concentrations on the time to crack initiation in nickel alloys, from [26].

detrimental to Ni-alloys, in cases, drastically increasing the crack growth rate (CGR) when compared to as-received conditions [38, 39]. Whereas, West et al [40] showed that sensitized and cold worked 304 stainless steel has a higher propensity for high temperature SCC retardation behavior than non-sensitized and cold worked material in deaerated pure water. Terachi established an equivalent observation in both SS304 and SS316 [41]. Quantifying the effects of cold-working on a material is difficult, and the change in yield strength is often used as a measure of cold-work [41]. In SCC experiments, the high defect density surrounding boundaries interferes with the deformation ahead of the crack tip [32, 37], and dissipates the stress [39] and can lead to the development of inferior protective oxide layers [42, 43] when compared to their as-received counter-parts.

2.1.2.3 Grain Boundary

The microstructure of the alloy is very important to understanding the SCC susceptibility. Since 1984, the idea of selecting material properties though grain boundary control has been extensively investigated [44]. There are numerous ways to classify grain boundaries. One such way is to group boundaries based on their misorientation angle, low angle boundaries (LAB, misorientation $< 15°$) and high angle

boundaries (HAB, misorientation $> 15°$). However, this is a crude simplification of what is a complex 3-dimensional material interface.

The coincident site lattice (CSL) model, established by Kronberg and Wilson in 1949 [45], is a much more robust way of classifying grain boundary alignment. A boundaries CSL value, Σ, is defined as the fraction of the number of coincident sites between two-neighbouring grains separated by a boundary [46]. For example, $\Sigma 3$ indicates that one out of three sites is coincident, i.e. the same in both individual grain crystal structure. It follows that grain boundaries with more coincident sites have a low grain boundary energy. These low energy configurations are called special grain boundaries, or coincident site boundaries.

As defined by Wasnik et al, any grain boundary with a CSL value up to 29 is considered a coincident site boundary, any value above this threshold is called a random boundary [47]. It has been demonstrated that random boundaries will always crack before CSL boundaries regardless of the microstructure or testing conditions, and that $\Sigma 3$ boundaries will always systematically increase the resistance to SCC [44, 48].

2.1.2.4 Carbon Content and Carbide Precipitates

Carbon is typically an impurity element in both nickel alloys and nuclear grade steels, making up to 0.015% of the material by weight. In the austenitic alloys examined, carbon mainly interacts with the underlying microstructure of the material forming both intergranular and intragranular Cr-based carbide precipitates. The dominant carbide precipitates types are mainly $Cr_{23}C_6$ and Cr_7C_3, depending on the locally available chromium content [49]. Grain boundaries with higher Σ values, or random grain boundaries, are most susceptible to carbide precipitation [50]; while, coherent $\Sigma 3$ and $\Sigma 9$ grain boundaries are thought to be resistant to carbide formation [51, 52].

It is widely acknowledged that in Ni-alloys a continuous network of intergranular carbides can result in improved SCC resistance [39, 53], and that intragranular carbides have a deleterious effect [54]. The mechanism responsible for increasing SCC resistance is still under investigation. Numerous explanations have been offered, Bruemmer et al [39] proposed that carbides could act as dislocation sources that blunt the crack tip. Airoka et al [55] suggested that intergranular carbides

prevent grain boundary sliding. Was et al [56] considered that the chromium-rich nature of carbides could see them preferentially oxidise as "oxygen-sinks", trapping diffusive oxygen and resisting further intergranular oxidation.

More recently, Dugdale demonstrated, using microcantilevers, that a stress corrosion crack propagates around the metal-oxide interface around a carbide and terminated at the oxide-metal interface [57]. This lead the authors to suggest that oxidation is a precursor for SCC. Shen et al [58] undertook high-resolution analysis on the deformed cantilever cross-section, and demonstrated that the carbides were rarely oxidised and that the Cr was not able to diffuse to the surrounding matrix. In light of this, a new mechanism was proposed: crack path diversion. In a further publication, Shen et al demonstrated that oxide-metal interfaces diverted the crack from straight path to curved path. This mechanism is thought to provide two SCC mitigating effects, by increasing the total crack path length and decreasing the effective applied stress locally [19].

Material sensitization is the term given to the formation of chromium depleted areas surrounding a carbide. The effect on SCC can vary in austenitic alloys depending on the environmental conditions applied [39, 59]. Kai et al [59] reported after conducting a modified Huey test performed in boiling 40% HNO_3 that the amount of chromium depletion plays a role in SCC, but the shape and width of the depletion is irrelevant. Under a more relevant medium, Bruemmer et al [39] stated that chromium-depletion is not necessary for the onset of IGSCC in A600. It is commonly accepted that carbides are always beneficial in reducing environments.

2.1.2.5 Temperature

SCC occurs in the hot leg of steam generator tubes in a PWR, where the temperature is a high as 345°C In contrast, it has never been found in regions where the temperature is regularly lower than 250 °C. This observation naturally indicates a temperature sensitivity to SCC. Given that temperature effects the properties of the materials, the oxidation process, the stability of oxides, and the diffusion rate of metallic elements and oxygen. It is hard to imagine a situation in which temperature would not be an important factor in SCC.

For nickle rich alloys, such as A600, Casagne et al [60] reported that the crack initiation time and CGR increase with temperature, which is consistent with Arrhenius law. Similar observations have been reported by other researchers. Cowan et al reported that for A600 exposed to high temperature de-arated water the crack initiation time underwent a five-fold decrease, while the temperature increased from 290 - 340°C.

In a study of austenitic steels conducted by Arioka and Shen [61, 62, 17, 18] found that the CGR increased with temperature between 250 - 330°C in both hydrogenated and oxygenated waters. The diffusion of vacancies was considered to be a important factor in this process. However, the CGR declined at higher temperatures above 330°C, and the greatest CGR occurred between 320 - 340 °C. A peak in the CGR was not only found in SS316L and SS304, but also in A690. The author could not locate a paper that suggested that A600 exhibited a peak CGR, similar to those other alloys investigated. As temperature is clearly influential on SCC, further studies should be undertaken to understand the effect of temperature on SCC.

2.1.3 SCC Mechanisms in Austenitic Alloys

There are essentially four atomistic processes by which a crack can grow. These processes are: the removal of atoms at the crack tip, the shear movement by the emission of dislocations, the tensile separation of atoms, and the receding surface diffusion of atoms [46]. However, due to the complexity of the SCC, and factors that contribute to it, it has been difficult to integrate these atomistic models into a single complete theory for every material at every environment [63]. The next section comprises an overview of three commonly reported models, film-rupture, internal oxidation, and hydrogen assisted, that will undoubtedly form the groundwork for future unified models. Other import models (such as: induced micro-cleavage [64], film-induced cleavage [65] and surface mobility [66]), are not discussed here, but can be found via the relevant citations.

2.1.3.1 Film-Rupture Model

The film-rapture model (FRM), sometimes referred to as the slip-dissolution model, was first conceptualised by Mears et al [67] and later refined and popularised by a series of publications starting with Logan in 1952 [68, 69, 70, 71]. In the FRM (Figure 2.4), a build up of plastic strain at the passivated SCC crack tip tears apart the protective oxide (1), and exposes the unprotected metal interface to the corrosive environment (2). The tip of the exposed metal interface undergoes localized anodic dissolution i.e corrosion (3), before the protective oxide layer can be fully repaired. The combination of strain and corrosion advance the crack (4). The FRM is a highly plausible mechanism for situations where there is an applied strain, or loading, but static loads are more complex. Vermilyea et al [72] postulated that under static conditions, creep is responsible for causing the deformation that causes the oxide layer to tear apart.

This model may be conceptually the simplest way to describe crack growth. There are numerous instances where the crack growth rate and strain rate have been well described, but there have been many instances where this is not the case. As a result, the FRM has been the subject of much discussion in the SCC community. The FRM put forward by Anderson & Ford and Rebak Szklarska-Smialowska has been statistically verified for SS304, SS316, A182 and A600 in high temperature water and PWR environmental conditions [70, 29]. Gaining praise for reflecting the inverse relation between the threshold stress intensity value K_{ISCC} and environmental effects. However, these achievements were overshadowed when it was suggested by Jones [74] that the predicted rates of dissolution in stainless steels are considerably lower than that required to mirror observed results [71].

2.1.3.2 Internal Oxidation Model

The selective internal oxidation (SIO) model was first suggested by Scott and Le Calvar for Ni-alloys in 1993 [75]. The development of this model started after two fundamental observations. Grain boundaries in Ni-alloys preferentially oxidise internally after exposure to PWR environments, and this leads to an intergranular mode of failure. In the SIO, surface oxidation facilitates the diffusion of oxygen along the grain boundaries. As SCC evolves around the Ni/NiO phase transition,

less noble alloying elements (such as Cr and Fe) are preferentially oxidised. The segregated elements will often from a brittle chromium-rich oxide *i.e.* Cr_2O_3, which are believed to fail under stress. These opening crack fronts facilitate further penetration of the oxide along the grain boundary [75, 76]

Internal oxidation has found favour with the community, as it is the only SCC model that describes both the initiation and propagation of cracks. It is however, not without its limitations. As stated by Lozano-Perez et al [77] and Dugdale et al [57], internal oxidation requires the Cr-rich oxide growth to outpace the crack propagation, and despite numerous studies reporting intergranular cracking [78, 79, 37], evidence for this is sparse. Rebak and Szklarska-Smialowska [80] criticised the predicted quick crack growth rates, and implemented a stress independent

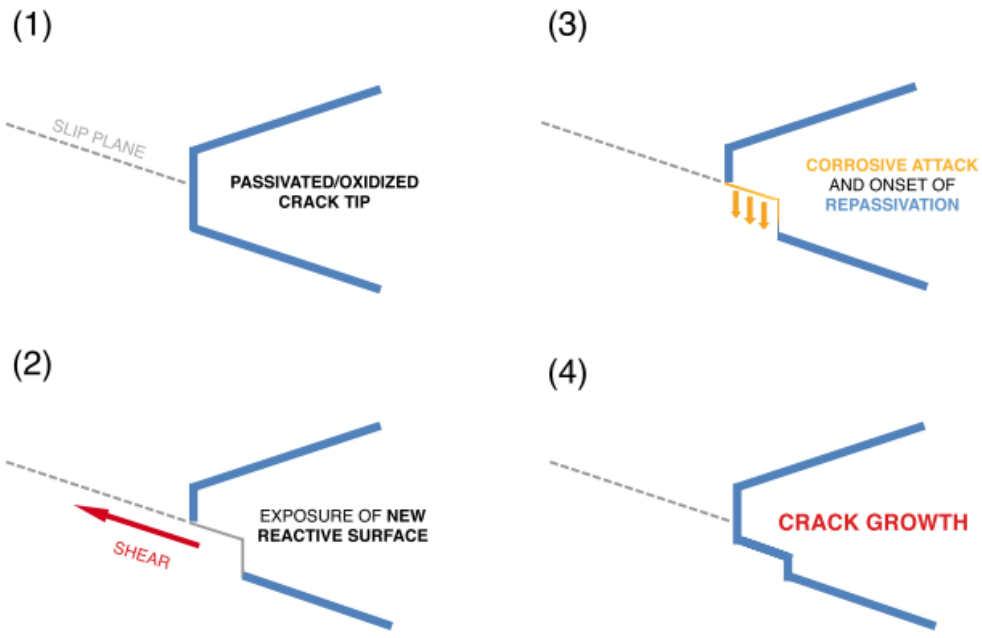


Figure 2.4: Illustration of crack propagation in the film rapture model. (1) Passivated crack tip with intersecting slip plane. (2) strain causes shearing, which exposes metal to the environment. (3) Corrosion attacks the bare surface before a protective oxide can form. (4) Material passivates, but crack progresses incrementally [73].

diffusion coefficient. Even after the revision, a study by Capell and Was [76] showed that the values of oxygen diffusion along grain boundaries are still several magnitudes lower than those required to account for the observed crack rates.

To facilitate the observed crack growth, Greer proposed that stress-induced dislocations and vacancies could assist the diffusion of chromium and oxygen along grain boundaries [81]. This was subsequently experimentally confirmed by Lozano-Perez et al in SS304 [82]. It was also subsequently suggested that diffusion induced grain boundary migration (DIGM) can also increase diffusivity [83]. Researchers investigating Ni-alloys are confident that internal oxidation is an occurring mechanism, as Cr-rich oxides and intergranular cracking has been reported for various austenitic alloys [84, 85].

2.1.3.3 Hydrogen Mechanisms

Hydrogen embrittlement (HE) is broadly defined as the mechanical degradation, in particularly the reduction of ductility and fracture stress, of a material containing hydrogen (H) [86]. HE seen in most metallic materials, but it is particularly notable in steels. SCC and HE can be differentiated by the potential regimes they occur under, SCC is anodic and HE is cathodic. Despite this, SCC and HE are fundamentally intertwined [87], as they may occur through a common mechanism [88, 89]. Due to the detrimental effects of hydrogen, intensive research has been invested to understand the mechanisms behind HE. But, since the first report of HE by Johnson in 1874 [1], our confidence in the underlying mechanism has stagnated, despite the continuous advancements of experimental techniques.

Under our current framework, HE operates on two classes of material: hydride forming and non-hydride forming. For hydride forming materials (group IV elements, titanium, and zirconium alloys), the hydride fracture and cleavage mechanisms are widely accepted to be responsible for HE. A good review on these theories is provided by Lynch [90]. In contrast, for non-hydride forming materials (austenitic steels and nickel alloys) there are three dominant mechanisms: hydrogen enhanced de-cohesion (HEDE), adsorption-induced dislocation emission (AIDE), and hydrogen enhanced localized plasticity (HELP). Each of these mechanisms have received widespread praise and each has its issues and inconsistencies, this will be the topic of this section.

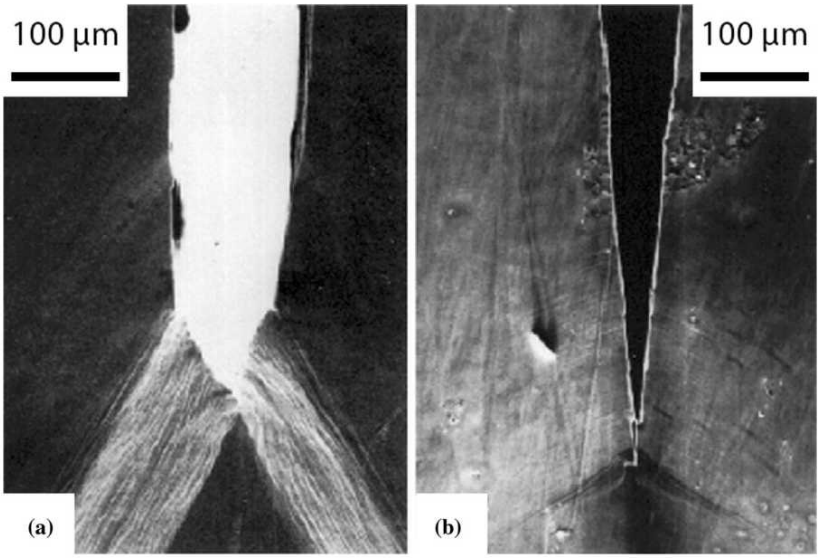


Figure 2.5: The crack-tip angle reduction of Fe-Si (3wt%) after strain test in (a) a vacuum and (b) in a hydrogen environment. [94]. Reprinted originally from Perspectives in Hydrogen in Metals, H. VEHOFF, W. ROTHE, Gaseous hydrogen embrittlement in FeSi-and Ni-single crystals, 647-659, Copyright (1986), with permission from Elsevier.

The HEDE theory - also called hydrogen induced decohesion (HID) - hypothesises that hydrogen reduces the bonding energy of atoms, and increases the risk of decohesion [91, 92]. Hydrogen migrates to regions of high tensile stress ahead of the crack tip. In sufficient concentrations H can weaken the interatomic bonds, and give rise to an increased crack growth rate. Once cracking has occurred, the stress field can drag the solute hydrogen and the process repeats. As HEDE can not be directly observed [93], and the majority of supporting evidence has focused on characterising the reduced crack-tip opening angle. This is the dominant indication of HEDE, and can be seen in Figure 2.5.

The HELP mechanism was first suggested by Beachem et al [95] in 1972, and has subsequently been developed by Birnhaum and Robertson et al for nickel alloys [96], stainless steels [97, 98], and titanium alloys [99]. In the HELP model it is postulated that H participates in a four step process (hydrogen diffusion, surface dissociation, migration and enhanced deformation) that results in an increase in dislocation mobility. To explain why dislocation mobility is increased, a few factors

need to be established. Hydrogen is charged, and has its own electrostatic field. This field shields part of the elastic stress field of dislocations [100]. As the repulsive forces between dislocations are lowered, less stress is required to induce a given plastic strain [101]. The HELP mechanism has gained supported by experimental studies on macroscopic flow stress measurements [102, 103], in-situ TEM studies [100, 104], and measurements of dislocation motion [105, 106]. However, the HELP model is limited by the diffusion rate of hydrogen with respect to the CGR in the material, and for the systems where the CGR is above the hydrogen diffusion rate, alternative models based on adsorption processes can best describe the cracking process.

The AIDE mechanism, as summarised by Lynch [90, 107], allows the hydrogen environment to activate dislocation sources ahead of the crack tip in austenitic alloys. Once activated they create blunt-cracks and blunt-voids that upon coalescing contribute to crack growth. The sources themselves egress behind the crack tip and contribute to the crack opening and the strain-field ahead of the crack tip, as illustrated in Figure 2.6. The adsorption of H atoms near the crack tip requires the dissolution of H molecules, H-sulphide, or water molecules; or the production of H during an electrochemical reaction in an external environment [37]. For materials with low H diffusivity, only adsorbed H should be present at the crack tip, if the crack has a high velocity there should not be enough time for H to diffuse ahead of the crack tip. On this basis, only materials that have a ratio of H diffusivity to CGR greater than $\approx 10^{-8}$ cm are applicable to the AIDE model. However, it is possible to transport H at rates above the diffusivity using dislocations [108], but this would not lead to a consistent hydrogen environment ahead of the crack tip, because of the steeply inclined slip-planes [88].

2.1.4 Summary

SCC is a time-dependent and highly localised phenomenon, in which a susceptible material fails prematurely due to a synergistic combination of a sustained tensile stress and a corrosive environment. This subject has been extensively studied. Many influential factors have been identified, including, but not limited to cold-work, alloy composition and temperature; and several mechanisms have

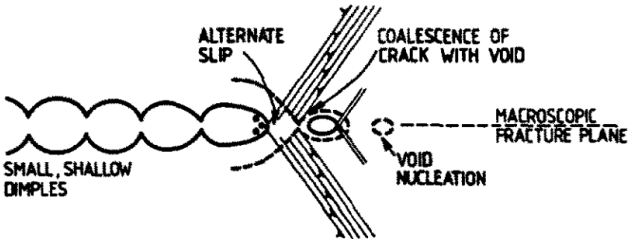


Figure 2.6: Schematic drawings illustrating the AIDE mechanism [88]. Reprinted from Acta Metallurgica, Vol 36, S.P. Lynch, Environmentally assisted cracking: Overview of evidence for an adsorption-induced localised-slip process, pp 2639-2661, Copyright (1988), with permission from Elsevier.

been suggested. Despite this, the exact failure mechanisms occurring during PWR operation are still unclear. Different mechanisms have been proposed for different austenitic alloys, illustrating how situational SCC theories can be. SCC remains a difficult topic because the influential factors are not independent from each other. However, to predict the life-time of structural components, it is crucial to better understand the effects of different factors on SCC.

2.2 Hydrogen

It is established that hydrogen (H) adsorbed during corrosion processes can drastically alter a component's ability to fulfill its designated role [1]. This material degradation typically manifests as a transition from ductile to brittle failure, as seen in Hydrogen Embrittlement (HE). While Section (2.1.3.3) outlined the possible mechanisms for hydrogen-related failure, there are numerous features of hydrogen still to be discussed. The aim of this chapter is to examine the sorption process, understand the inter-play between traps and interstitial diffusion, and to discuss the effects on the bulk mechanical properties. Understanding these factors will be important in establishing a fundamental and robust analysis of hydrogen's role within stress corrosion cracking (SCC).

2.2.1 Entry of Hydrogen into Materials

In order for hydrogen to have influence over a material's properties, it must first infiltrate and accumulate in sufficient concentrations. The mechanisms by which hydrogen enters a material can be complicated, and strongly depend on the environment which provides the hydrogen. There are two main methods for introducing hydrogen in an experiment: (i) gaseous charging at elevated temperatures [109], and (ii) electrochemical charging [110]. These two commonly employed entry routes are outlined. Then the method of hydrogen adsorption under PWR conditions is discussed in the remaining part of the chapter.

2.2.1.1 Gaseous

The gas-solid interaction can be summarised by a process of adsorption and absorption. Adsorption is the process of binding to a surface, this can be characterised by two distinct stages: physical adsorption (physisorption) and chemical adsorption (chemisorption).

Physiosoprtion arises from the inter-molecular Van der Waals force between the surface and the adsorbent H_2 molecule. During this stage, the long range Van der Waals force binds multiple layers of physisorbed hydrogen molecules to the surface. These layers of molecular hydrogen can be characterised as a kind of liquid. Therefore, the binding energy is equivalent to the heat of condensation of the gaseous adsorbent (<20 kJ mol^{-1}) [111]. The low binding energy suggests that phyiosorption is reversible. In chemisorption a chemical reaction occurs between the surface and adsorbent. The chemical bonds extend a short range, which limits the effects of chemisorption to a mono-layer of hydrogen molecules on the surface. This is the rate limiting step of hydrogen uptake. In order for adsorption H_{ads} to take place, a covalent bond must be formed between the transitional metal, M, and a hydrogen atom from dissociated H_2 gas

$$2M + H_2 \rightleftharpoons 2MH_{ads}. \tag{2.1}$$

Absorption is the incorporation of the products of chemisorption into the bulk lattice of the metal. In the case of hydrogen it will be in either a H^-_{abs} or H^+_{abs}

charge state depending on whether or not the hydrogen ion is an electron donor or receiver.

$$MH_{ads} \rightleftharpoons H_{abs} + M. \tag{2.2}$$

2.2.1.2 Electro-chemical Charging

Hydrogen absorption in liquids is associated with the reduction of hydrogen on the surface of a metallic sample. In electrochemistry the process of reduction and oxidation is described by the Tafel equation, which relates the observed over-potential, $\eta = V_{applied} - V_{OCP}$, and current density ,$i_c$

$$\eta = a + b\, log(\, i_c\,), \tag{2.3}$$

where a and b are constants that are unique to each combination of material and electrolyte.

To reduce hydrogen on the metallic surface, the metal, M, must donate an electron to a molecular structure containing hydrogen, either H_3O^+ or H_2O. In the case presented, hydrogen comes from the discharge of hydrated protons (acids), or the dissociation of water molecules (alkaline). This typically occurs at low applied over-potentials, when there is a low coverage of adsorbed hydrogen on the surface.

$$H_3O^+ + M + e^- \longrightarrow MH_{ads} + H_2O, \tag{2.4}$$

$$H_2O + M + e^- \longrightarrow MH_{ads} + OH^-, \tag{2.5}$$

Once adsorbed, hydrogen is free to migrate over the surface, and it will remain adsorbed until it either becomes absorbed or is liberated from the surface. As established in gaseous charging, there is an equilibrium between adsorbed and absorbed hydrogen. The migrating hydrogen will be used to maintain the equilibrium following the equation

$$MH_{ads} \rightleftharpoons H_{abs} + M. \tag{2.6}$$

An alternative route to leaving the adsorbed state is the process of desorption. Two atoms of adsorbed hydrogen can recombine to form a molecule that can escape the surface. The desorption process follows the reaction

$$2MH_{ads} \longrightarrow H_2 + 2M. \tag{2.7}$$

So long as a potential is applied, the amount of adsorbed hydrogen will increase (i.e. hydrogen fugacity increases). There is a critical surface concentration, above which the desorption of hydrogen can occur through an additional electrochemical process. Applying a high overpotential has a similar effect. Electrochemical desorption is the process of an adsorbed hydrogen atom bonding directly with a dissociated hydrogen atom from the environment (see Eq 2.4 or Eq 2.5), to escape the surface. This process can be described as

$$MH_{ads} + H_3O^+ + e^- \longrightarrow H_2 + H_2O + M \tag{2.8}$$

$$MH_{ads} + H_2O + e^- \longrightarrow H_2 + OH^- + M \tag{2.9}$$

This implies that at high hydrogen fugacities there are two chemical routes for hydrogen to escape the surface, and results in rolling bubbles of H_2 from the surface.

2.2.1.3 PWR conditions

The absorption of hydrogen can occur in austenitic alloys from the water in the primary-side of the reactor. However, the mechanisms required to explain absorption stray away from the idealised cases previously presented. Some of the factors that complicate hydrogen absorption include: (i) the mixed mode of gaseous and electrochemical hydrogen adsorption, (ii) the protective oxides that form on austenitic alloys [112], (iii) the hydrogen mobility throughout the lattice, and (iv) the temperature dependence of hydrogen diffusivity and permeability in different Ni alloys. A successful approach to investigating the uptake of hydrogen in PWR conditions would need to isolate, and differentiate, the aforementioned complications. One such strategy, which has seen success in literature, is to utilise isotopic tracers of hydrogen ^{2}H and oxygen ^{18}O to probe the connection between corrosion and oxidation on hydrogen absorption. These complex factors will be discussed through experimental results obtained using isotropic tracers.

In PWR conditions, hydrogen can originate from either the cooling liquid, or dissolved hydrogen. To determine which is responsible for supplying hydrogen to material components, autoclave experiments were completed by Jambon et al [113, 114] on two identical samples of A600. During these tests, the samples were

exposed to either a H_2O/D_2 or a D_2O/H_2 mixture of water/dissolved hydrogen. The samples were analysed using secondary ion mass spectroscopy (SIMS) to determine the ratio of $^2H/H$. The results overwhelmingly indicated that hydrogen originates from the cooling liquid, and that it is generated by the dissociation of water during oxide formation. Similar results have been observed by Dumerval et al [115] in SS316L, and by Chen [116] in ferritic steels. As a result of these studies, it has become widely accepted that the adsorbed hydrogen originates from the dissociation of water, and in the tests performed in this work this is the assumed case.

Oxide films are a barrier to hydrogen absorption in metals, especially in the 20 - 300°C temperature range [117, 118]. The barrier effect has been investigated by Rios et al [117] using ex-situ electrolytic charging experiments. Two samples of A600 were charged with hydrogen in an autoclave, one sample was pre-deformed (reverse U-bend test) and the other was deformed in-situ (slow strain rate test). The sample that was deformed in-situ had a significantly higher hydrogen concentration. This indicates that the oxide layer established prior to autoclave exposure inhibited hydrogen uptake under PWR conditions. The barrier effects is thought to slow hydrogen absorption in two ways, first by reducing the kinetics of hydrogen dissociation at the oxide, and secondly by slowing hydrogen diffusion once absorbed.

Transport across the oxide barrier still occurs. Two mechanisms have been proposed for hydrogen absorption in Ni-alloys and stainless steels by Jambon et al [113] and Dumerval et al [115]. Jambon et al [113] proposed a transport link between ^{18}O and ^2H in the form of a hydroxide ion, OH^-. The hydroxide ion would traverse the oxide and separate to form a deep oxide and an interstitial hydrogen. Dumerval et al [115] proposed a hydrogen absorption mechanism based on proton H^+ transport in 316L stainless steel after reporting a deuterium peak in the inner-oxide layer. Dumerval assumes that the oxide will possess different diffusive properties to the bulk matrix. If the rate of diffusion is slower in the oxide, then this could account for the observed peak. On the other hand, if diffusion is enhanced in the oxide, then there must be an active trapping mechanism in the oxide. If traps are present in the oxide, it is likely that they are vacancies that were created during the oxide growth by cationic diffusion process through the inner

Cr-oxide. In both cases presented, once hydrogen has crossed the oxide layer it may be absorbed by the metal. In the lattice the hydrogen will assume interstitial sites and diffuse around the structure. In the next section, the means of diffusion are discussed and the models used to characterise diffusion explored.

2.2.2 Hydrogen Diffusion

2.2.2.1 Macroscopic

The diffusion of hydrogen between interstitial lattice sites is the primary mechanism for hydrogen movement in a matrix. Diffusion is driven by a concentration gradient in the material, with the hydrogen flux moving from regions of high to low concentration. In the bulk samples examined, diffusion is described by a one dimensional Fick's law

$$J = -D\frac{\partial C}{\partial x} \tag{2.10}$$

where J is the flux of diffusion, D is the diffusivity or the speed of transport of the hydrogen in the lattice and $\partial C/\partial x$ is the concentration gradient. The change of the concentration gradient, the driving force of diffusion, is determined by Fick's second law

$$\frac{\partial C}{\partial t} = D\frac{\partial^2 C}{\partial x^2}, \tag{2.11}$$

where $\partial C/\partial t$ is the change in concentration over time. Depending on the boundary conditions imposed, there are two possible solutions, the infinite source solution and the finite source solution. The concentration in a thick material can be modelled by an infinitely thick plate solution. As noted by Olden et al [119], this solution is in the form of the error function.

$$\frac{C(x,t) - C_0}{C_s - C_0} = 1 - erf\left(\frac{x}{\sqrt{4Dt}}\right) \tag{2.12}$$

$$erf(u) = \frac{2}{\sqrt{\pi}}\int_0^u exp(-u^2)du, \text{ where } u = \frac{x}{\sqrt{4Dt}}, \tag{2.13}$$

where C(x,t) is the hydrogen concentration at position x after a charging period of t, C_0 is the uniform initial bulk hydrogen concentration, and C_s is the constant surface hydrogen.

D is the diffusion constant. It is given as $D = D_0 \exp(-E/RT)$, where D_0 is an experimentally determined scaling factor. For stainless steel 316L, Brass et al [120] determined this factor to be 6.2x10^{-19} $m^2 \cdot s^{-1}$. R is the gas constant (8.314 J/mol·K), and T is the temperature in Kelvin. It is assumed that the hydrogen concentration at the surface is constant, i.e. $C(0,t) = C_i$, the concentration in the material at a sufficient depth L is negligible and assumed zero, i.e. $C(L,t) = 0$, and that the initial bulk hydrogen concentration is negligible compared to surface concentration, i.e. $C_i >> C_0$. This allows Fick's law in equations (2.12-2.13) to be simplified to

$$\frac{C(x,t)}{C_s} = 1 - erf\left(\frac{x}{\sqrt{4Dt}}\right). \tag{2.14}$$

Just as Fick's law can be used to model hydrogen adsorption, Fick's law can be used to model hydrogen desorption from a non-uniform initial concentration. The non-uniformity of the initial conditions breaks the steady state assumptions made previously, so the new solution is non-trivial. During desorption it is now assumed that as the electrolyte or the overpotential is removed, so that the surface concentration becomes zero, i.e. $C_s = 0$, and the concentration at a large distance still remains negligible, i.e. $C(L,t) = 0$. The desorption concentration can be expressed as a series of sums, and is presented by Wang et al [121] as

$$\begin{aligned} C(x,t) = C_s &+ (C(L,t) - C_s)\frac{x}{L} \\ &+ \frac{2}{\pi}\sum_{1}^{\infty} \frac{C(L,t)cos(n\pi) - C_s}{n} sin\frac{n\pi x}{L} exp\left(\frac{Dn^2\pi^2 t}{L^2}\right) \\ &+ \frac{2}{L}\sum_{1}^{\infty} sin\frac{n\pi x}{L} exp\left(\frac{Dn^2\pi^2 t}{L^2}\right) \int_0^L f(r) sin\frac{n\pi r}{L} dr, \\ =&\frac{2}{L}\sum_{1}^{\infty} sin\frac{n\pi x}{L} exp\left(\frac{Dn^2\pi^2 t}{L^2}\right) \int_0^L f(r) sin\frac{n\pi r}{L} dr, \\ &\text{where } f(r) = 1 - erf\left(\frac{r}{\sqrt{4Dt}}\right). \end{aligned} \tag{2.15}$$

2.2.2.2 Microscopic

Observations in polycrystalline materials suggest that diffusion on the microscopic level is not the same as the macroscopic level. The assumptions made above, do

not necessarily hold true for all length-scales [122]. A more appropriate definition of the diffusion process is,"*the hydrogen flux is driven to minimise the chemical potential energy of the solute hydrogen in the material*". Chemical potential energy has replaced concentration gradient. The chemical potential energy can be affected by numerous factors. These can include the induced stresses caused by the solute hydrogen, the injection of vacancies, and the Burgers vector [123, 124].

The impact of crystallographic orientation on diffusion rates has been evaluated by Li et al [125]. They performed a series of electrochemical permeation experiments on nickel single crystals with orientations of <100>, <110>, <219> and <111>. A significant variation in the diffusion coefficient was recorded, depending on crystallographic orientation tested. The results are displayed in Figure 2.7. This anisotropy is due to the crystals elastic response to the applied stresses of the diffusing hydrogen, and leads to a significant variation in the chemical potential, and therefore the diffusion coefficient [125, 126]. This demonstrates that enhanced preferential diffusion is possible in Ni-alloys, which would allow for a deeper intragranular penetration of hydrogen into the material along {111} planes. Trapping will also significantly affect a material's response to hydrogen. This will be examined in the next section.

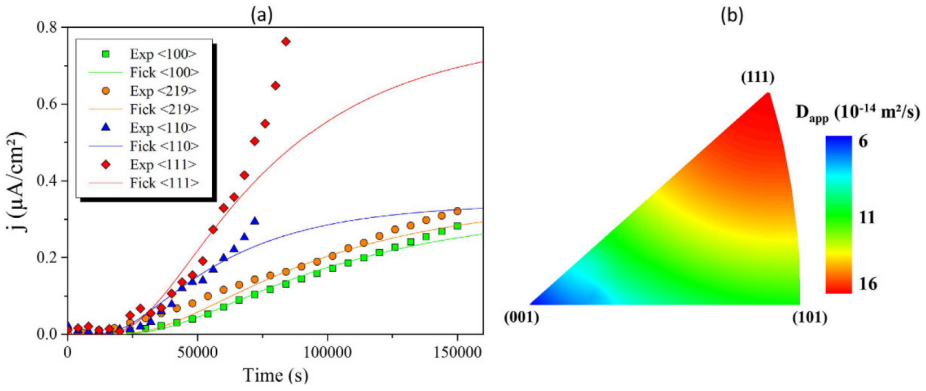


Figure 2.7: Anisotropic diffusion of hydrogen in nickel single crystals as (a) a function of charging time at a constant cathodic current density and calculated <hkl> diffusion using Fick's law, and (b) the apparent diffusion as a function of crystallographic orientations. Image taken from [125]. Open access article (https://creativecommons.org/licenses/by/4.0/).

2.2.3 Hydrogen Trapping

In a perfect crystal, hydrogen will diffuse to minimise the chemical potential of the matrix. However, the matrix is not a perfect crystalline structure, and the interactions between hydrogen and the crystal defects often dominate diffusion behaviour. Defects - such as dislocations, vacancies, and grain boundaries - are commonly referred to as trapping sites; they offer a low-energy site in the lattice for hydrogen atoms to occupy, see Figure 2.8. Trapping sites are able to inflate the hydrogen content above a solubility limit [127], and decrease the observed diffusivity. Once trapped, hydrogen is rendered immobile at temperatures at which it would be expected to diffuse rapidly [128]. Therefore, for this investigation into the role of H within SCC, particular care should be taken to examine the nature of trapping sites on the concentration of hydrogen stored in different austenitic alloys.

2.2.3.1 Models and Simulations

There are several methods available for analysing trapping behaviour. Most models are, in some way, variations and improvements over Kissinger's original [130]. This model is based upon a reaction rate theory that is commonly used for assigning

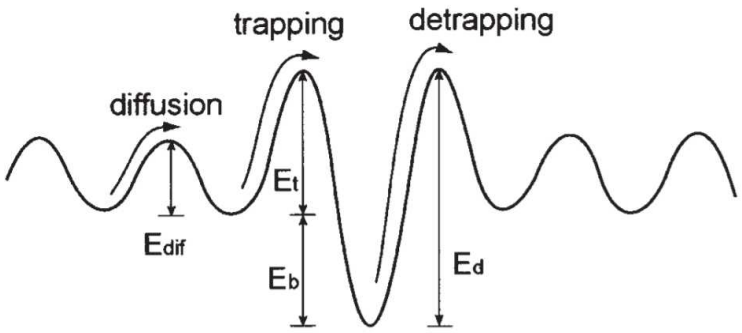


Figure 2.8: Schematic diagram illustrating the energy boundaries for trapping and detrapping processes [129]. Reprinted by permission from Springer Nature: Springer Nature, Metallurgical and Materials Transactions B, Precise determination of the activation energy for desorption of hydrogen in two Ti-added steels by a single thermal-desorption spectrum, F. G. Wei et al, [COPYRIGHT] (2004).

activation energies, E_p, to hydrogen desorption from samples. This method is summarised by the following equation

$$\frac{E_p}{R} = \frac{\partial ln(\phi/T_m^2)}{\partial(1/T_m^2)}, \tag{2.16}$$

where ϕ is the imposed temperature ramp, T_m is the temperature at the maximum rate of desorption, and R is the ideal gas constant. This model is limited, and it fails to consider the trapping density [131, 132]. Four iterations are reported from McNabb and Foster, Orani's, Kircheim and Yagodzinskyy. Binding energies for different traps are listed in Table 2.1, and the desorption temperature peaks are shown in Figure 2.9.

The McNabb and Foster model [154] is derived from the fundamental laws of activation energy and conservation of mass. It also incorporates the kinetics of trapping and de-trapping. This model has been employed by Enmoto et al [155] in modelling binding energies, but requires numerous fitting parameters, which has seen it neglected by many experimentalists [156, 157]. Orani's model [158], is

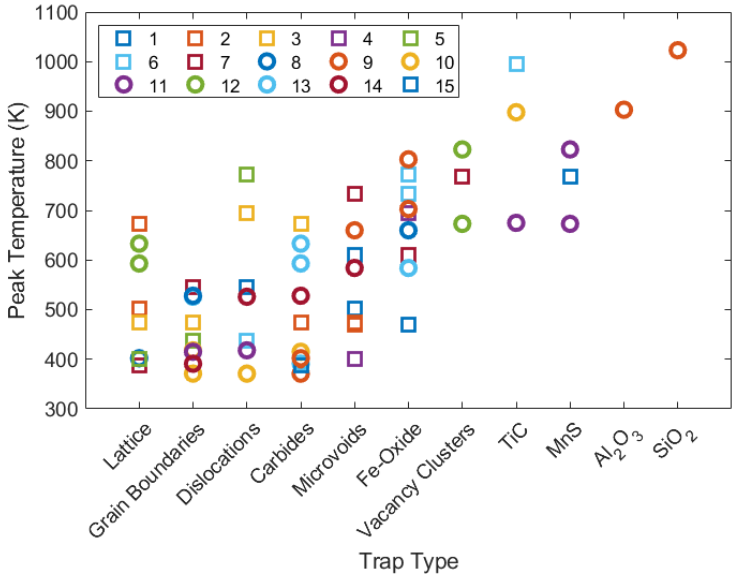


Figure 2.9: Showing the experimental peak temperature found in a range of Fe-Ni-Cr alloys in Table 2.1. References are as follows: 1=[145], 2=[146], 4=[147], 5=[148], 6=[149], 7=[138], 8=[136], 9=[129], 10=[150], 11=[151], 12=[142], 13=[152], 14=[141], 15=[153].

Table 2.1: Trap binding energies for austenitic alloys in literature. Bold values indicate the activation energy required to escape the trap collected from Choo-Lee plots.

Trapping sites	Binding Energies/kJmol^{-1}	Reference
Stainless Steels or (pure-Fe)		
Lattice Site	**7**	[133]
Grain boundary (Average)	**26**, 22, (49)	[134, 129, 135]
Grain boundary (Random)	53-58	[134]
Dislocation	**27**, 22, 36, (45)	[136, 129, 137, 135]
Micro-void	**29**, 48	[136, 138]
Interface of Fe oxide	**47**, **69**	[139]
Interface of MnS	**72**	[138]
Interface of TiC	**85**,86, 94	[140, 129]
Interface of TiC (incoherent)	**77-85**	[140]
Interface of Al_2O_3	**86.2**	[139]
Interface of SiO_2	**112.1**	[139]
A600 or (pure-Ni)		
Grain boundary	18, **20**, (13)	[141, 142]
Dislocation	18.3, **24.1** $\pm$ 2.9	[138]
Vacancy	(23)	[143]
Vacancy Cluster	(70.4, 85.9)	[144]
As-Received Interface of Cr_7C_3	**26**	[142]
10%CW Interface of Cr_7C_3	**28**	[142]
30%CW Interface of Cr_7C_3	**36**	[142]
A690 or (Mixed Ni/Fe ratios)		
Interface of $Cr_{26}C_6$	**37**	[142]
10%CW Interface of $Cr_{26}C_6$	**41**	[142]

similar to that of McNabb and Foster, but it differentiates itself by establishing a local equilibrium between the hydrogen concentrations in the traps and in the lattice. The assumption of a local equilibrium drastically simplifies the McNabb and Foster model, and has seen wider application. However, the assumption made restricts analysis to only a single type of trap, which limits accuracy. Kircheim

proposed an "energy-box" approach using Oriani's model. This in essence allows for multiple traps to be considered [159] at once. This is a interesting development, but, in its current state, is over-simplified and allows for an over-generous assignment for energy values.

The final approach mentioned is a complete numerical-based analysis that has been proposed by Yagodzinskyy et al [160] and Todoshchenko et al [161]. This approach has been favoured, as it accounts for the short falls of the Kissinger model (diffusion and the density of traps occupied), while considering initial hydrogen concentration profiles. This numerical approach requires fewer factors than the available alternatives, improving comparability between materials. Nonetheless, accurately reproducing experimental results has been difficult by Yagodzinskyy's own admission [160]. This is thought to stem from the series of assumptions made to reduce the number of fitting factors.

2.2.3.2 Point Defects

Vacancies are the simplest point defects possible in a crystal lattice. They are very small, and cannot realistically be observed outside of atomic resolution microscopes, therefore, most investigations have been theoretical or simulation-based experiments. The results from these studies suggest that hydrogen is strongly attracted to these imperfections. It has been hypothesised that a single vacancy can accommodate up to six hydrogen atoms, which is a thermodynamic limit [144, 162]. This is imposed because as hydrogen increases beyond six atoms per vacancy, a negative defect formation energy would be produced [144, 162]. The reduced formation energy has lead to the suggestion that superabundant vacancies can be formed in the presence of interstitial hydrogen in Ni [163, 164] and Fe [165]. Experimentation by Fukai et al concluded that, once hydrogen can promote the formation of vacancies to such an extent, the vacancy concentrations in Ni systems can reach $10 - 30$ at% [144].

2.2.3.3 Dislocations

Dislocations are always present in a material in high concentrations. Dislocations comprise the dislocation core and a surrounding elastic strain field. It is

known that hydrogen causes dislocations to undergo behavioural changes. Based on current literature, these changes can be summarised to four main observations. Firstly, dislocations become more mobile in Ni-Fe-Cr alloys. This has been directly observed in nickel alloys by in-situ environmental TEM [166, 167], and indirectly by stress relaxation tests [168, 169]. The dislocation velocities recorded have been up to 10-times those reported in uncharged samples [170]. Secondly, the packing density of dislocations is increased, particularly at pile-ups [171]. This is due to the hydrogen at the core altering the stress field of the dislocation, and reducing the repulsion between dislocations and other microstructural features. Thirdly, edge dislocations are stabilised and cross-slip minimised [172]. Finally, it is claimed that the stacking fault energy is also reduced [100, 173], but this is highly disputed as it is highly challenging to isolate. Such factors should be considered when discussing SCC in steels and nickel alloys, as dislocations will directly aid crack propagation [174, 175].

2.2.3.4 Slip Planes

Yagodzinskyy et al [176] illustrated through atomic force microscopy (AFM), that hydrogen alters the height and separation of slip-related surface relief in austenitic 316 stainless steel. It was found that incorporating interstitial hydrogen to a concentration of 0.64 at%, increases the separation and height of surface relief by a factor of three. The increase in the spacing between slip planes is consistent with the elastic shielding of edge dislocations due to hydrogen. Slip planes do not act as trapping sites, but the dislocations that travel along the slip planes can trap and drag solute hydrogen throughout the lattice [177, 178, 179].

2.2.3.5 Grain Boundaries

The available literature on hydrogen diffusion and solubility is incoherent and often contradictory. This can be attributed to the absence of micro-structural characterisation in many of the reviewed articles, making it impossible to accurately measure and compare hydrogen diffusion coefficients [182]. Grain boundaries can be thought of as very dense regions of dislocations, that appear to take on conflicting roles. It is reported that boundaries act as fast diffusion paths

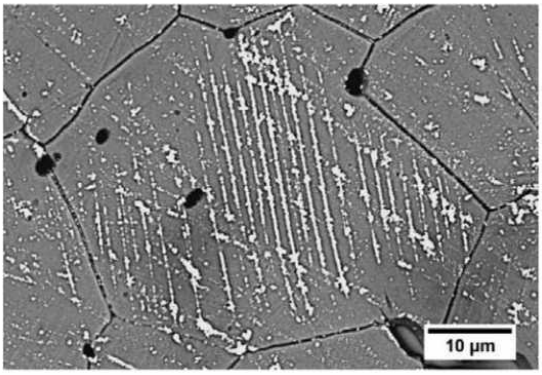


Figure 2.10: Micro-printed Ag on austenitic stainless steel. Hydrogen reduces Ag^+ ions, and deposits Ag on the surface of the sample wherever there is a high concentration of trapped hydrogen. The samples were plastically deformed by compression after hydrogen charging. This method of demonstrating is susceptible to interstitial hydrogen leaving the sample as no reference of time between charging and micro-printing is mentioned [178]. Reprinted from Materials Science and Engineering: A, Vol 761, S.D. Pu, S.W. Ooi, Hydrogen transport by dislocation movement in austenitic steel, pp 138059, Copyright (2019), with permission from Elsevier.

[183, 184, 185, 186, 187], as there is an amorphous structure [188]; while, simultaneously trapping hydrogen in the dislocations that make up boundaries, slowing down diffusion [189]. In an attempt to understand this duality, Oudriss et al suggested that there is a correlation between the grain boundary type and diffusivity along the boundary [180, 181]. It was reported that accelerated hydrogen diffusion along GBs is due to random (high-angle) grain boundaries (Figure 2.11c), and special grain boundaries Σ <29 are preferential trapping sites. This is due to their high symmetry and order. Figure 2.11d shows that as the fraction of random boundaries increase the effective diffusion coefficient increases, explaining the differing views in literature. In the nuclear grade materials studies, the grain boundaries are engineered to have a high concentration of special-CSL boundaries as they are highly resistive to SCC. This means that the trapping phenomenon will be the dominant role of the GBs.

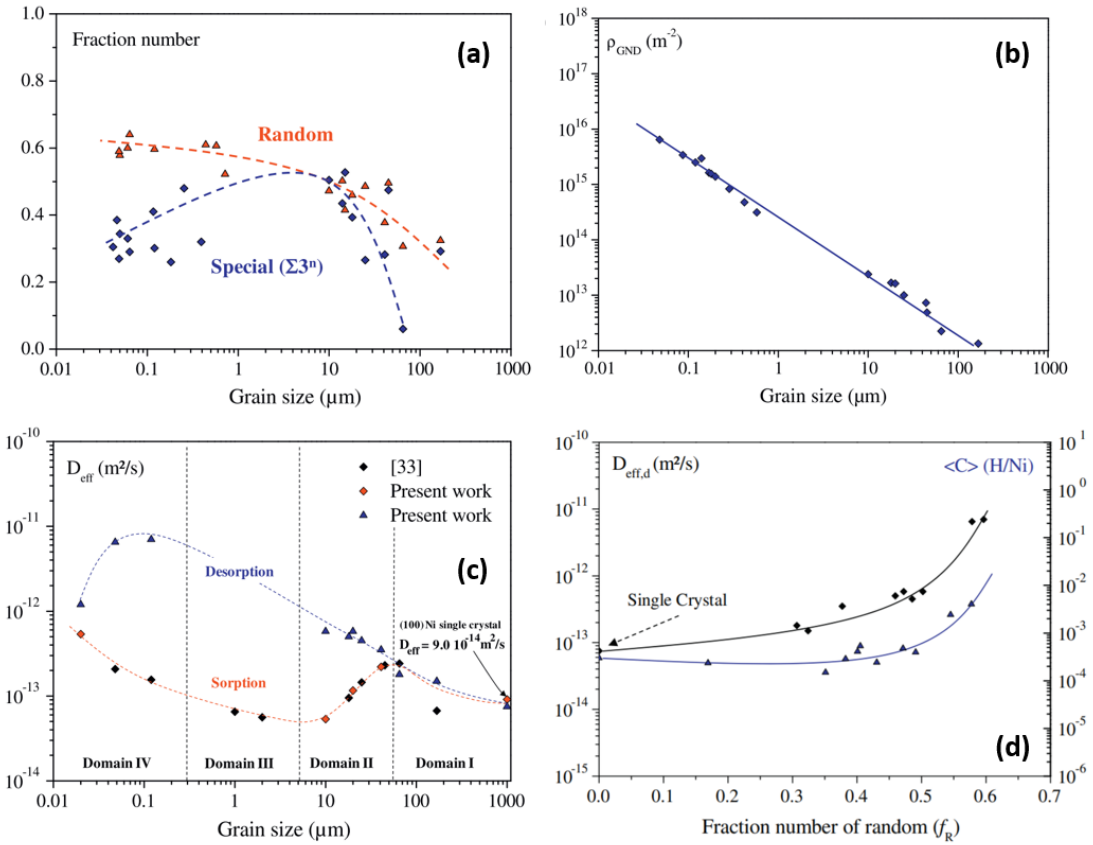


Figure 2.11: Characterisation of the nickel samples presented in the study (a) shows the number of random and CSL boundaries as a function of grain size, remaining fraction is low angle Σ1 boundary. (b) is the number of GNDs calculated from misorientations from EBSD measurements, using a method outline in [180]. (c) shows the desorption and adsorption of the various different grain sizes. (d) shows both the evolution of the desorption diffusion coefficient, as it is void of trapping effects, and the mean interstitial hydrogen concentration as a function of random grain boundaries [181]. Reprinted from Acta Materialia, Vol 60, A. Oudriss, J. Creus, J. Bouhattate, E. Conforto, C. Berziou, C. Savall, X. Feaugas, Grain size and grain-boundary effects on diffusion and trapping of hydrogen in pure nickel, 6814-6828, Copyright (2012), with permission from Elsevier.

2.2.4 Summary

Hydrogen is, in itself, a complex topic. There is little meaningful experimental evidence gathered on hydrogen embrittlement, and little development on the

mechanisms driving HE has recently been made. A serious concern for PWR applications is the implication of hydrogen on SCC mechanisms, for this no comparative experimental studies have been attempted. The materials that have been tested show many influential factors, and speculate on the implications to HE. This review hopefully points out some of the short-comings of the previous research in this area, partly due to experimental limitations and poor characterisation. In the next chapter, I will review the methods of characterising hydrogen.

2.3 Experimental Characterisation of Hydrogen

Characterising the effects of hydrogen on austenitic alloys is crucial to developing a deeper mechanistic understanding of SCC. The techniques used to characterise SCC have changed dramatically due to the developments in sample preparation, and the introduction of focused ion beams (FIB) microscopes [15]. Accordingly, the methods used to characterise hydrogen have also evolved, but at a laboured pace. Figure 2.12 presents an overview of the commonly used techniques. Over the next chapter, multiple methods of examining hydrogen, using both traditional techniques and modern microscopy methods, will be examined.

2.3.1 Atom Probe Tomography

Atom probe tomography (APT) is able to reconstruct, and provide chemical information about, a small 3-dimensional volume of a needle-shaped sample. Ions are removed individually, using a voltage (voltage mode) or thermal pulse (laser mode), from the apex of the needle. The atoms are chemically identified by a time-of-flight spectrometer. The spatial position of the atoms in the sample can be calculated by a position-sensitive detector with nm resolution [190]. APT has become popular as it is able to analyse microstructural features, such as grain boundaries, internal oxides or crack tips. A detailed review of APT is presented by Gault and Moody [191].

APT has enabled the first direct observation of hydrogen atoms at the carbide-matrix interface [192], dislocations [193], and grain boundaries [193] in steels.While this is not a new methodology [194], the diffusion of hydrogen has previously limited results [195]. To overcome this, Chen et al developed a cryogenic cooling stage

and transfer system to slow hydrogen diffusion [196, 197, 198]. There are several limitations to APT. Each needle has a limited size of approximately 100-200 nm in depth, therefore features of interest need to be small enough to be visible on this length scale. Furthermore, the small sample volume limits how representative each tip is of the whole sample. Correlative techniques on the micron-scale are required to provide context for APT. The background deuterium content of the system and sample is calibrated using uncharged samples. To determine an accurate deuterium count, the atom probe must be run in a voltage mode, as the laser mode favours the formation of complex ions, preventing a true count of deuterium to be established as deuterium in complex ions is almost impossible to accurately quantify.

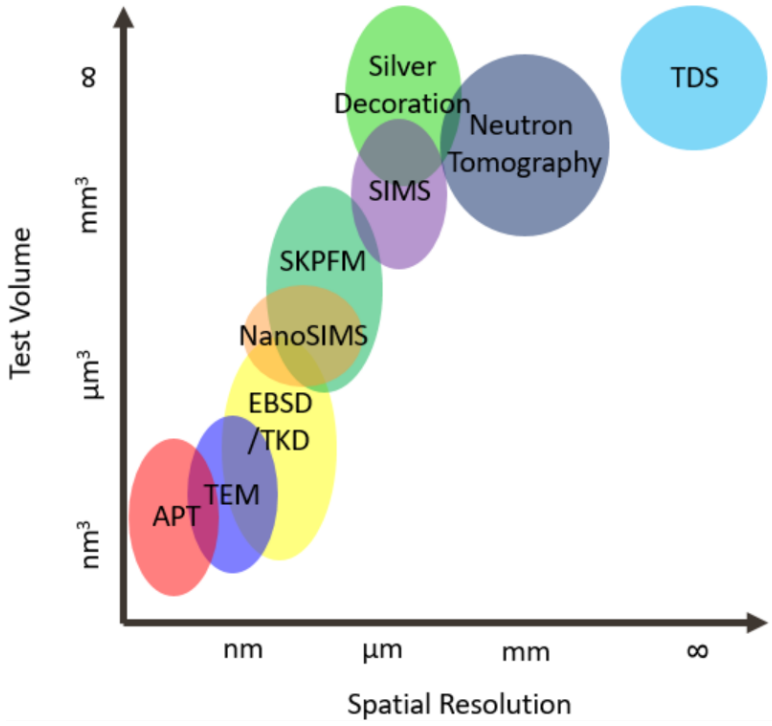


Figure 2.12: Overview of different methods of mapping hydrogen. The diagram illustrates the volume of the characterised material and the spatial resolution achieved. The method of hydrogen entry into the material can vary.

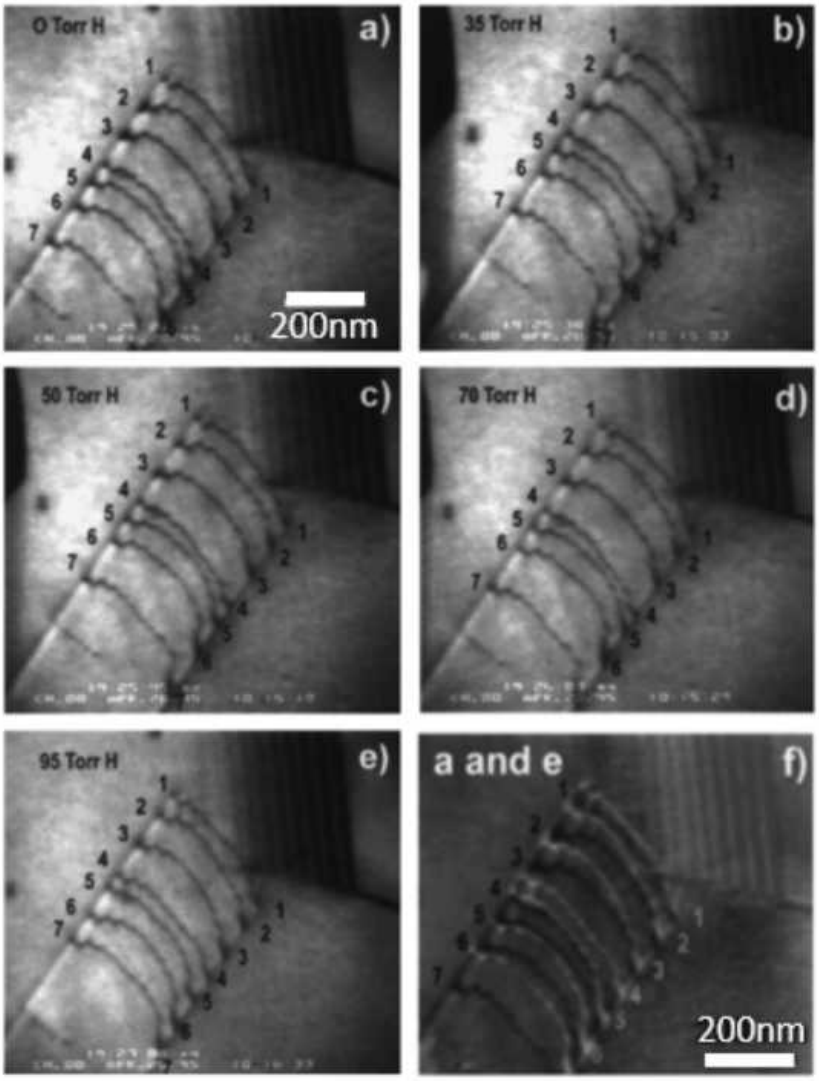


Figure 2.13: (A-E) show bright field images captured from a video tape showing the change in the dislocation arrangement as a function of hydrogen content in 310 stainless steel. It can be seen that the average spacing between the dislocations decreases as the hydrogen pressure increases. (F) shows a composite image created by subtracting the images (A) and (E) from each other. The black dislocation lines represent their original position, while the white lines represent the final position [171]. Reprinted from Acta Materialia, Vol 46/5, P.J. Ferreira, I.M. Robertson, H.K. Birnbaum, Hydrogen effects on the interaction between dislocations, 1749-1757, Copyright (1998), with permission from Elsevier.

2.3.2 Transmission Electron Microscopy

Transmission electron microscopy (TEM) is a characterisation tool which has a resolution on the nm scale. When partnered with suitable detectors, it can produce highly localised chemical analysis through energy dispersive X-ray spectroscopy (EDX) and electron energy loss spectroscopy (EELS). These techniques have been employed extensively, and with great success, in the study of SCC [58, 19, 79, 41, 199, 18, 16, 17, 200, 20]. Hydrogen is too light to be chemically identified using these techniques, so in-situ environmental TEM is used to analyse the hydrogen-induced changes, i.e. the elastic-shielding of hydrogen resulting in enhanced dislocation motion [171, 166, 201, 202, 203, 204]. The TEM operates on certain assumptions, the most challenging in this context being that thin-film observations must be related to behaviour of the bulk.

2.3.3 Secondary Ion Mass Spectroscopy

Secondary ion mass spectroscopy (SIMS) is a surface analysis technique, that sputters material to provide a 3-dimensional topographical and chemical reconstruction. Both SIMS and NanoSIMS use this operating principle, but the spatial resolution of the NanoSIMS is greatly improved over its conventional counter-part [206]. SIMS is able to resolve every element and differentiate between their isotopes [207], making it an ideal candidate for micron-scale deuterium visualisation [113, 114, 208, 209, 210, 211]. During sputtering the lattice is destroyed, this means that SIMS can only reliably detect trapped hydrogen, as interstitial hydrogen is mobile and can appear to originate from false sources. The counts and relative intensity of mass signals are recorded in SIMS techniques. This means that, to achieve a quantitative analysis, a complementary calibrated technique, such as thermal desorption spectroscopy, must be undertaken. This technique has recently been applied to investigate deuterium at a crack tip in 304SS with interesting results [205], capturing numerous hydrogen-rich regions surrounding the crack tip, as seen in Figure 2.14. Further reading about the nanoSIMS is provided by Moore et al [212].

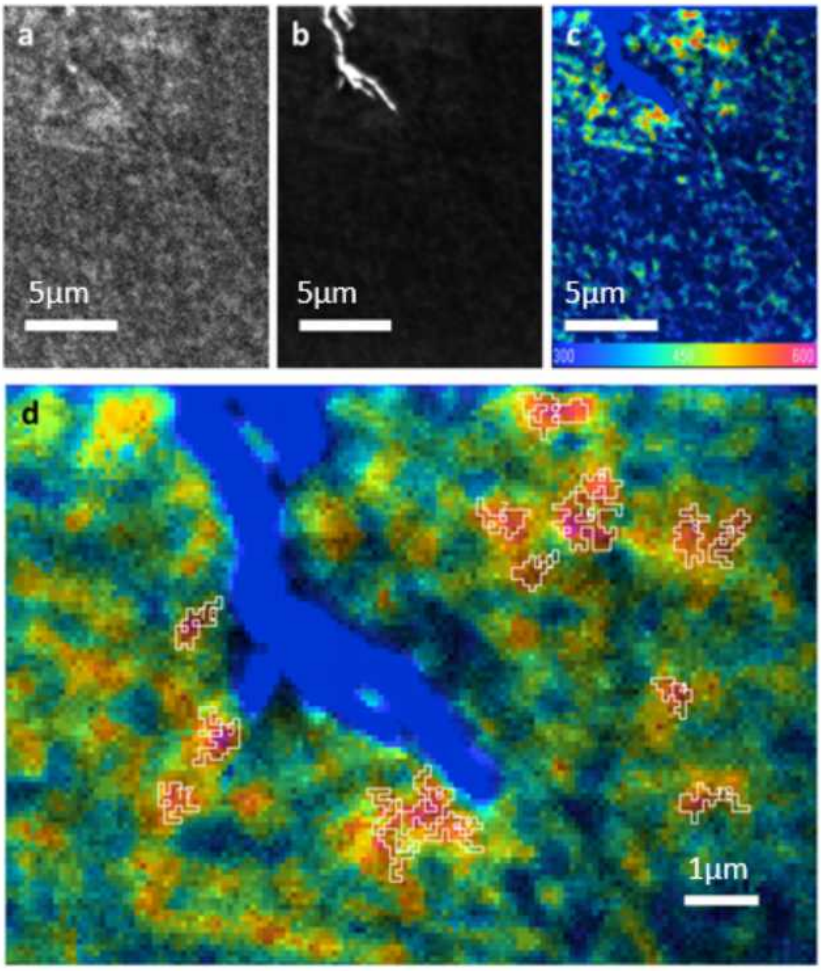


Figure 2.14: NanoSIMS isotopic images and derived ratio images at crack tip of 304SS. (A) 2H image, (B) 16O image and (C) 2H/16O ratio displayed as HSI image. (D) shows the 2H/16O ratio at regions of interest that were generated by a segmentation algorithm indicating a mean ratio at least 50% higher than the background taken from an area away from the crack tip [205]. Open access article (https://creativecommons.org/licenses/by/4.0/).

2.3.4 Scanning Kelvin Probe Force Microscopy

Scanning Kelvin probe force microscopy (SKPFM) is a non-contact, non-destructive technique, which is a descendant from atomic force microscopy (AFM). SPKFM measures the local potential difference between a tip and sample with a high spatial resolution. The variation of hydrogen within a sample will cause a detectable

difference in the measured potential, and surface work function. The non-intrusive nature of the SPKFM means that multiple rasters can be completed on a single sample to investigate the outgassing of hydrogen. Figure 2.15 shows a recent SKPFM study, in which trapped [213, 214] and diffusing hydrogen [215, 216] were investigated. This method is sensitive enough to determine the effects of crystallographic orientation on hydrogen adsorption and trapping [217]. The biggest drawback of this method is calibrating a measured potential to a known hydrogen fugacity. To the authors knowledge, no standardised method has been reported, meaning comparing results from different groups is unreliable.

2.3.5 Neutron Tomography

Neutron Tomography (NT) is a non-destructive three-dimensional method of imaging the bulk of a material [218]. It is an appealing method to use, as hydrogen undergoes strong scattering due to its large neutron cross-section, when compared to Ni-Fe-Cr elements in steels and Ni-alloys [219]. In recent years, the development of fast detectors and large neutron fluxes has enabled the quantitative characterisation of dynamic adsorption processes[220]. Figure 2.16 shows current capabilities of NT in pure-Fe. The high scattering from trapped hydrogen shows the presence of surface blisters after electrochemical charging. The size, density and frequency of the blisters can be determined. The maximum resolution achieved was 20 μm and the tomographic reconstruction comprises 600 images taken over 14 hours [221]. The temporal and spatial resolution limits the applications of this technique, currently small mobile microstructural features, e.g. dislocations, are inaccessible. To further optimise this technique, better detectors and neutron sources will be needed to improve the spatial and temporal resolution of NT.

2.3.6 Thermal Desorption Spectroscopy

Thermal desorption spectroscopy (TDS) is a technique that provides quantitative information about the hydrogen stored in a material, and to a lesser extent the type of microstructural trap. TDS involves heating a sample at a fixed ramp rate, and measuring the desorbed hydrogen using a mass spectrometer. The results can be analysed using numerous methods depending on the situation and the material

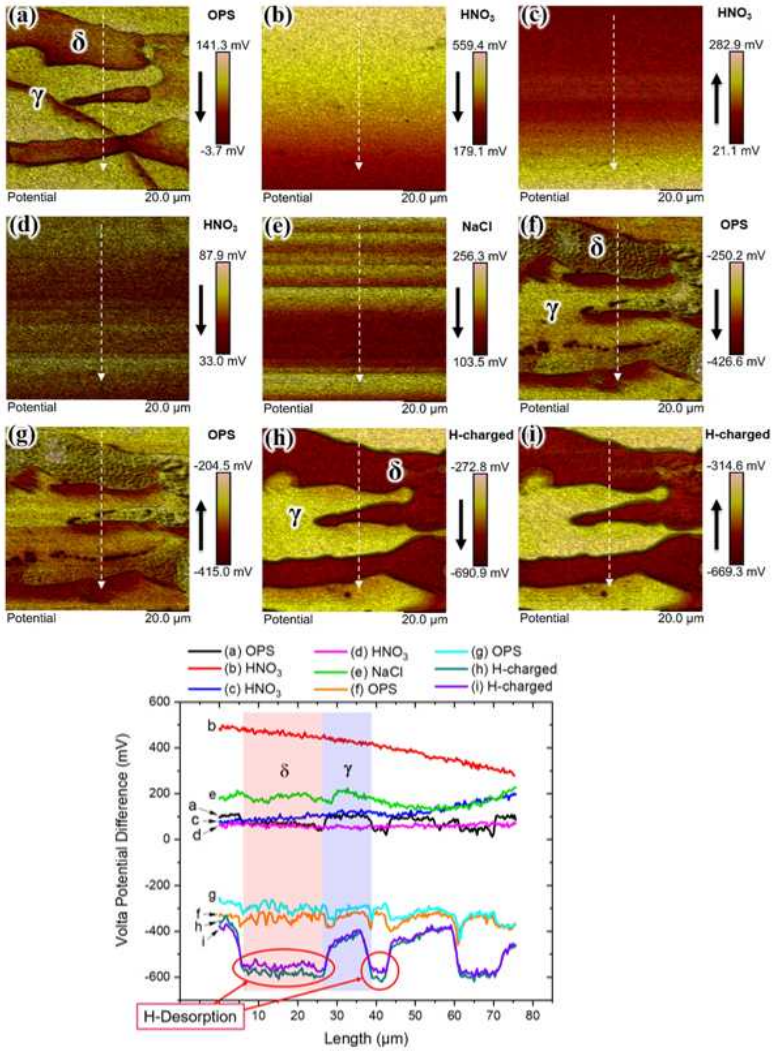


Figure 2.15: Potential measurements taken from duplex stainless steel. (a,f,g) have a colloidal silica finish. (b,c,d) have been passivated in nitric acid. (e) was passivated in 1M NaOH. (h,i) cathodically charged sample in a 0.1M NaOH solution. Passivated samples show that the oxide layer effects the work function and makes collecting results impossible. Below is a graph that shows the potential maps extracted from (a-i) [214]. Open access article (https://creativecommons.org/licenses/by/4.0/).

[222, 223, 224, 225]. The mass resolution for TDS is very high, but there is no spatial resolution typically associated with the technique. TDS has been used extensively to determine the hydrogen content of A600 [226, 227, 126, 142, 228,

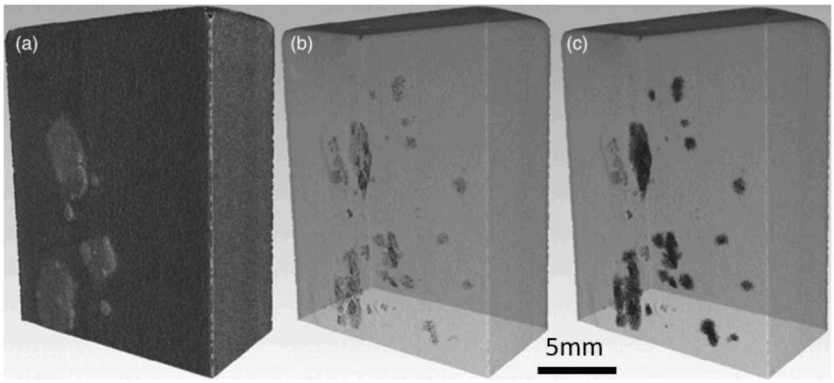


Figure 2.16: Inclined view of the 3-D reconstruction of a hydrogen-charged pure Fe sample. The surface blisters are shown in (a). The crack distribution in the interior is presented in (b), and the additional hydrogen distribution in (c). Most of the cracks are filled with hydrogen, except some of the cracks underneath blisters [221]. Reprinted from Acta Materialia, Vol 78, Axel Griesche, Eitan Dabah, Thomas Kannengiesser, Nikolay Kardjilov, André Hilger, Ingo Manke, Three-dimensional imaging of hydrogen blister in iron with neutron tomography, 14-22, Copyright (2014), with permission from Elsevier.

229], A690 [230] and stainless steel [160, 176, 161, 231, 232, 148, 233]. This method is compatible with both electrochemcial, and autoclave studies [234]. However, oxide layers can act as a diffusion barrier and influence the results [235, 113]. The peaks indicate a release of hydrogen from trapping features, multiple peaks implicate that multiple traps are releasing hydrogen. Peaks at higher temperatures can indicate higher binding energies. Mobile hydrogen starts to be desorbed at a cryogenic temperatures, to investigate this cryogenic TDS (C-TDS) was created to determine weak trap energies [236].

2.3.7 Summary

In this project we hope to investigate hydrogen entry into austenitic alloys, and link this to SCC. To complete this investigation, the selected techniques need to fulfill the following three criteria. (1) The results should be easily comparable across multiple samples. (2) The chosen techniques should overall provide qualitative and quantitative information about the samples. (3) The chosen techniques should be sensitive enough to either detect low deuterium concentrations, or the effects low

deuterium levels produce.

To estimate the total hydrogen concentration in the samples, TDS with a deuterium proxy is the strongest candidate; it is routinely used to compare samples, and can detect low levels of trapped deuterium. To investigate the type of traps storing hydrogen, TDS will be complemented by the NanoSIMS, which offers good spatial and chemical resolution over a modest testing volume. Its semi-regular use within literature makes it a favourable choice when compared to NT and SKPFM.

To summarise, the various methods for detecting hydrogen have been reviewed, and the advantages of each technique discussed. A list of desirable experimental criteria has been presented, and the techniques that best fulfill this criteria selected. The multi-technique approach selected will also help overcome reliability issues typically associated with investigating hydrogen.

Chapter 3

Experimental Methodology

3.1 Materials

Over the course of this thesis, a maximum of six materials were tested. These materials include: SS316L, A800, A690, A600, A600CW and A182. These alloys were chosen as they have different Ni/Fe ratios and should capture the temperature dependent corrosion resistance observed by Coriou. The chemical composition of the tested alloys can be viewed in Table 3.1. The thermal treatment and history of these alloys are known to be different and mentioned where known. A600 is from a forged control-rod drive mechanism nozzle. A690 and SS316L were from a warm rolled plates, and had subsequent heat treatments at 1050°C. A182 is from a V-shaped weld.

Cold-working Ni-alloys is detrimental to their stress corrosion cracking (SCC) resistance. Given some degree of cold-working is inevitable during installation, experiments will also be conducted on cold-worked variants of the Ni-alloys, to better simulate likely reactor conditions. The cold-work amounts vary through the alloys. Cold-work was introduced to the alloys through uni-directional rolling at room temperature, except A600 where cold-work was introduced by tensile straining at room temperature. The percentage reduction in thickness, or equivalent, is listed in Table 3.1.

Table 3.1: Chemical composition of the alloys tested, information supplied by manufacturer.

Source	Material	Ni	Fe	Cr	C	Mn	Al+Ti	Nb+Ta	Mo	Si	S	P	Cold-Work(%)
EDF	SS316L	12.0	65.4	17.3	0.03	1.81	-	-	-	0.004	0.004	0.033	20
EDF	A800	32.7	45.4	20.0	0.07	0.76	0.29	-	-	0.270	0.001	0.012	20
EDF	A690	61.7	8.6	28.6	0.02	0.20	<1.00	-	-	0.300	0.002	<0.015	20
EDF	A182	66.8	6.9	15.0	0.03	6.20	<0.13	2.0	2.57	0.350	0.003	<0.020	N/A
EDF	A600	73.2	8.8	16.0	0.06	0.81	0.29	-	-	0.450	<0.001	0.007	0, 15

3.2 Sample Preparation

3.2.1 Micromechanical Testing Samples

All samples were cut using a fast saw with an abrasive blade. The samples measured approximately (10 x 10 x 2) mm^2. The cutting direction of the samples are along the S-L plane of cold-working, see Figure 3.1. SiC paper with the following grits 400, 600, 800, 1200 were used to level and grind away damage layers from cutting. Diamond suspensions of diameter 9, 3 and 1 μm were used to polish the material. A final polishing stage of 0.04 μm colloidal silica suspension lasted from 30 - 120 minutes. The samples achieved an EBSD quality finish. Electropolishing was experimented with, however Col-Si was able to give a good and more reproducible surface finish to a larger fraction of the sample. As seen by Pathak and Kalidindi, Col-Si polishing and electrochemical polishing provide the same surface

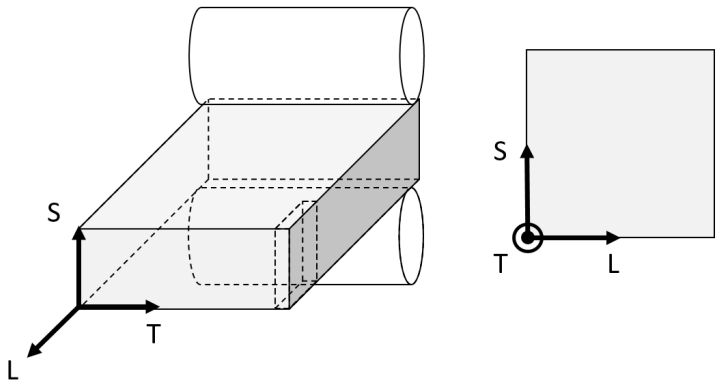


Figure 3.1: Schematic diagram showing the rolling direction and orientation of samples. T = Transverse, L = Long, S = Normal.

finish for micromechanical testing [237].

3.2.2 Autoclave Samples

The autoclave samples were cut using a fast saw with an abrasive blade. Two samples were cut from every alloy, the samples measured approximately (10 x 10 x 1) mm^2 and (5 x 8 x 1) mm^2 for TDS and nanoSIMS experiments respectively. The alloy designation was engraved on the back of each test piece to avoid mixing up the identical test pieces. The samples were ground and polished using the same method outlined in micromechanical sample preparation.

3.3 Nanoindentation

The nanoindentation test has become a commonly used technique for characterising the mechanical properties of a material with a small volume [238, 239, 240, 241]. A number of systems have emerged to measure the displacement and load simultaneously during the indentation procedure. This section will describe the basic mechanics behind nanoindentation, the continuous stiffness measurement (CSM) method, the instrumentation used, and some observed experimental phenomena.

3.3.1 Mechanics

3.3.1.1 Berkovich Tip

Indentation hardness can be calculated using load divided by the contact area. For a sharp Berkovich tip geometry, the projected contact area can be expressed as a function of the contact depth, h_c

$$A_c(h_c) = C_0 \cdot h_c^2 + C_1 \cdot h_c^1 + C_2 \cdot h_c^{1/2} + C_3 \cdot h_c^{1/4} + C_4 \cdot h_c^{1/8} + ..., \tag{3.1}$$

where for a perfect indenter tip, $C_0 = \pi \cdot tan^2\theta = 24.5$ and θ=70.32^o is the effective semi-angle of the equivalent conical indenter (Figure 3.2 & Table 3.2). The constants C_1 to C_n are fitted experimentally using a material of known modulus, usually fused silica [241].

Measurement of the modulus requires the material contact stiffness, S, and area, A. The contact stiffness is the gradient of the unloading curve, typically taken at the maximum load

$$S = \frac{dP}{dh}. \tag{3.2}$$

For a cylindrical column, the reduced modulus, that is the measured modulus of the combined tip and sample system, and contact area can be equated to the contact stiffness [242], and re-arranged for the reduced modulus

$$\frac{dP}{dh} = 2 \cdot E_r \frac{\sqrt{A_c(h_c)}}{\sqrt{\pi}}, \tag{3.3}$$

$$E_r = \frac{1}{2} \cdot \frac{dP}{dh} \cdot \frac{\sqrt{\pi}}{\sqrt{A_c(h_c)}}. \tag{3.4}$$

For a non-rigid indenter, the material modulus can be calculated from the reduced modulus

$$\frac{1}{E_r} = \frac{1 - \nu_s^2}{E_s} + \frac{1 - \nu_i^2}{E_i}, \tag{3.5}$$

where ν_x denotes the Poission's ratio and E_x represents the Young's modulus of the tip, $_i$, and sample, $_s$, respectively.

3.3.1.2 Spherical Tip

Spherical indentation is very similar to Berkovich. The indentation stress can be calculated from indentation, P, load divided by contact area, A_c, [243]

$$\sigma_{ind} = \frac{P}{A_c}. \tag{3.6}$$

The contact area is described by the geometric function [244, 242]

$$A_c(h_c) = B_0 \cdot h_c^{B_1} - B_2 \cdot h_c^2, \tag{3.7}$$

which describes a perfect sphere of radius, R, if $B_0 = 2 \cdot R \cdot \pi$, $B_1 = 1$ and $B_2 = \pi$. This function is back calculated using the stiffness measurement, load and displacement from a material with a known modulus, like fused silica [241].

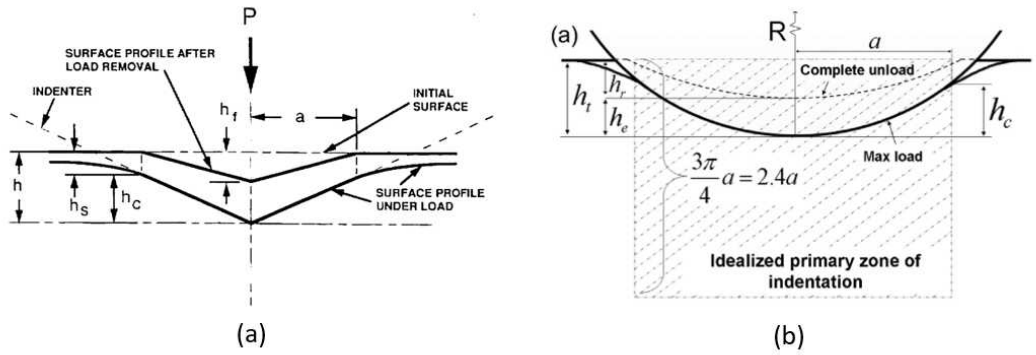


Figure 3.2: (a) Schematic diagram illustrating the area under the Berkovich indentation tip, from [241] Reprinted by permission from Springer Nature: Springer Nature, Journal of Materials Research, An improved technique for determining hardness and elastic modulus using load and displacement sensing indentation experiments, W. C. Oliver et al, [COPYRIGHT] (2011). (b) Schematic diagram illustrating the area under the spherical indentation tip, from [237]. Reprinted from Materials Science and Engineering: R: Reports, Vol 91, Siddhartha Pathak, Surya R. Kalidindi, Siddhartha Pathak,Surya R. Kalidindi, 1-36, Copyright (2015), with permission from Elsevier.

The indentation strain is defined as the ratio between the compression of the material, h, and the contact radius of the material a_c, as defined by Pathak and Kalidindi [245, 237, 246] and illustrated in Figure 3.2,

$$\epsilon_{ind} = \frac{4}{3\pi}\frac{h}{a_c}. \tag{3.8}$$

The radius of contact area is related to the contact area by the area of a circle $A_c = \pi a_c^2$. The modulus is defined as the gradient of the elastic portion of the indentation stress-strain curves, but the equation of Sneddon [242] can also be used

$$E_r = \frac{\sigma_{ind}}{\epsilon_{ind}}, \quad \text{and} \quad E_r = \frac{\sqrt{\pi}}{2} \cdot \frac{S}{\sqrt{A_c}} \tag{3.9}$$

the material modulus can be determined from the reduced modulus using Equation (3.5).

3.3.2 Continuous Stiffness Measurements (CSM) method

The development of the continuous stiffness measurement method is explained for spherical indentation. The concept of indentation stress and strain was first developed by Tabor [243], as a natural extension to hardness measurements made by Brinell and Vickers. The first definition of stress was the mean contact pressure, or applied load divided by contact area. This is also called the Meyer's hardness. Tabor's implementation of stress-strain yielded a single data point on the stress strain curve from each indent. This was due to the manual extraction of the contact area from directly observing the residual indent left after testing. Several attempts were made to improve efficiency by extracting multiple data points from a single indent.

Field and Swain were able to successfully extract multiple data points from a single indent. Their method used partial load-and-unloads, in conjunction with Hertzian theory, to estimate the surface area between the indenter and surface after each loading cycle [247, 248]. This method strayed significantly from Tabor's original attempt by forgoing direct observations of the contact area, and instead calculating it using estimations from Hertzian theory. While this has greatly increased the quantity of extracted data from each indent, substantial error has been inadvertently introduced in estimating the contact area.

The CSM method is the natural progression of this methodology, instead of undertaking multiple complete loading and unloading cycles, a sinusoidal force is superimposed over the applied force. This creates a continuous cycle of partial loading and unloading as the tip penetrates the sample, and allows one data point to be extracted every period of the sine wave. This method was first introduced by Pethica and Oliver [249] and extended by Oliver and Pharr [241]. It is now the standard method for measuring modulus and hardness of materials as a function of depth.

3.3.3 Instrumentation

A number of systems have emerged to measure the displacement and load simultaneously during the indentation procedure. A commercially available MTS XP

nanoindenter model is used to complete room temperature and in-situ electrochemical testing, and a prototype Xtreme high temperature nanoindenter from MicroMaterials is used for the high temperature testing. In the following section the means of force generation and measurement is documented and the possible tip geometries are explored.

3.3.3.1 Nanoindenter XP

A schematic diagram of the MTS XP nanoindenter used can be viewed in Figure 3.3a. This machine, like many commercial products, operates on a load-controlled basis. The force is generated by an inductive system (I), in which a coil is suspended in a permanent magnetic field B by a series of springs. When current I flows through the coil it becomes an electromagnet, generating an electromagnetic force on the indenter shaft (II)

$$F_e = BlI, \tag{3.10}$$

where l is the length of the coil. The force is measured by a series of springs (III & VI) that support the indenter shaft and hold the coil in the magnetic field. The model of this spring system is illustrated in 3.3b. Taking into account the additional forces of the indenter system, the applied force of the sample F_{app} is given by

$$F_{app} = F_e - K_s \times h, \tag{3.11}$$

where K_s is the spring stiffness of the spring in the vertical direction and h is the displacement of the indenter. This method of generating a load is commonly used and allows the user to apply a wide range of loads - up to 50 mN. However, the accuracy is limited by the uniformity of the applied magnetic field and the stiffness of the springs at a given displacement.

The tip displacement is determined by measuring the changing capacitance (V in Figure 3.3) between a series of plates either side of the indenter shaft. This method allows for high precision, with a displacement error of < 1Å[251]. To achieve such accuracy, the maximum displacement is limited by the distance between the parallel capacitor plates, typical a few microns.

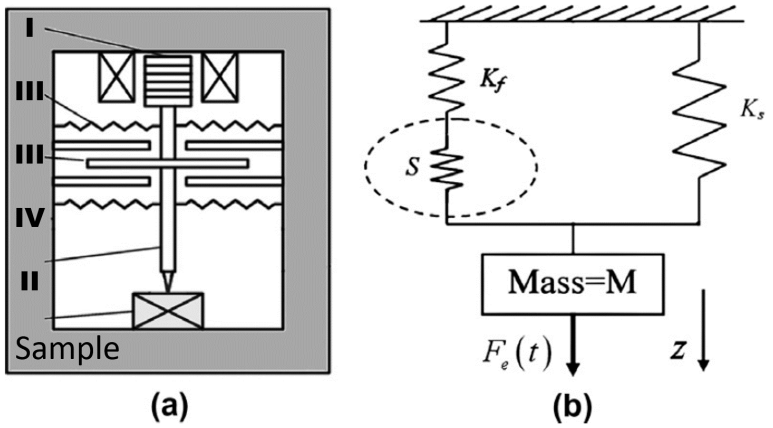


Figure 3.3: MTS Nanoindenter XP: (a) schematic diagram (b) mechanics model [250]. Reprinted from Measurement, Vol 43, Yong Huan, Dongxu Liu, Rong Yang,Taihua Zhang, Analysis of the practical force accuracy of electromagnet-based nanoindenters, 1090-1093, Copyright (2010), with permission from Elsevier.

In this work, nanoindentation was undertaken at a constant strain rate. To implement displacement-controlled operation on a load-controlled machine, a proportional integral derivative (PID) is used to automatically change the applied load to keep the strain rate constant.

3.3.3.2 In-situ Electrochemical Hydrogen Charged Nanoindentation

In-situ electrochemical hydrogen charged nanoindentation was conducted in the MTS XP nanoindenter. A McGill potentiostat was used to control the electrochemical conditions. The in-situ testing cell is based around a conventional three-electrode system that is compatible with the current XP stage, with a stainless steel counter-electrode, a saturated calomel reference electrode (SCE) and the sample forming the active electrode [252, 111]. The cell was filled with the electrolyte, electronically connecting the sample to the counter-electrode and reference electrode. Nanoindentation was then conducted on the samples situated in the electrochemical cell after a period of charging prior to the start of the test, see Figure 3.4.

One constant issue that interferes with the electrochemical process is the presence of dissolved oxygen in the electrolyte. In conventional electrochemical ex-

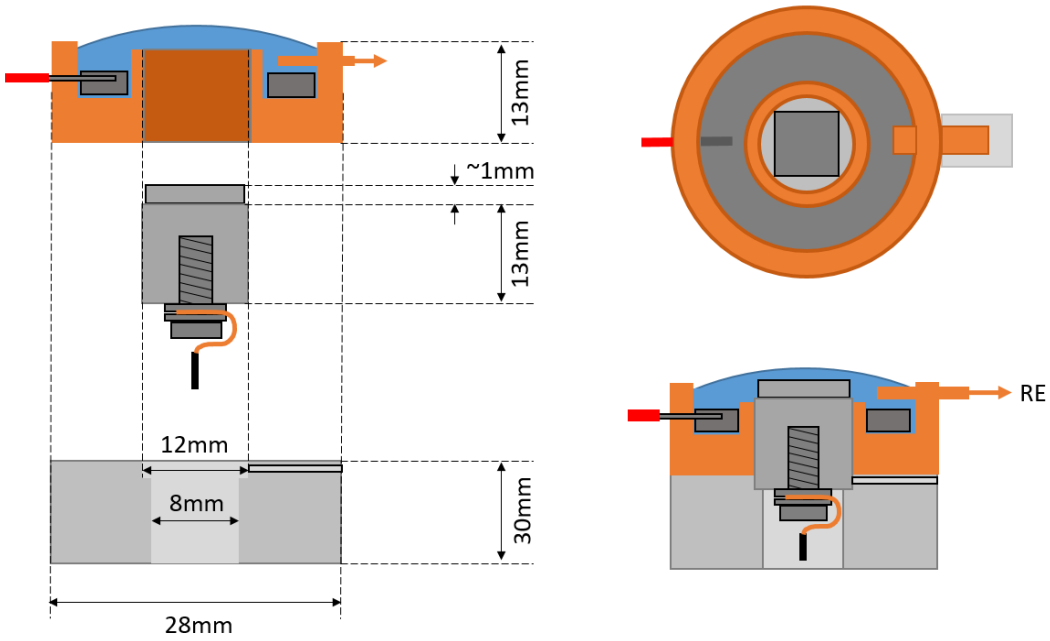


Figure 3.4: Schematic Diagram show the dimensions of the electrochemical charging cell using in the NI.

periments it is common practice to constantly bubble an inert gas to remove the oxygen, e.g nitrogen [253]. During the in-situ experiments no such bubbling was possible due to available space inside the nanoindenter, and the complications that a turbulent medium would have on the stability of the testing platform.

The equipment was cleaned prior to each experiment with isopropanol and distilled water, and the electrolytes were made from analytic grade reagents and distilled water. The cleanliness of the equipment is highly important to achieve the accuracy desired, and to prevented the deposition of corrosion products onto the surface or tip. Artifacts from surface deposition are very clear in the load-displacement data, as they prematurely trigger the surface find function and are much softer than the bulk. To achieve the best results, these parameters should be optimised for each nanoindenter system.

3.3.3.3 Xtreme High Temperature Nanoindenter

The fundamentals of nanoindentation in the Xtreme system are the same as the MTS XP system. There are several additional components to facilitate the high

temperature testing. A schematic of the Xtreme nanoindenter used is shown in Figure 3.5. Firstly, the indenter is placed in a vacuum chamber, with low-vibration pumps, to prevent oxidation. Secondly, the system in mounted sideways on a pendulum assembly, this better allows for the removal, or flow, of heat around the system. Finally, there is a heat shield, and cooling system in place to protect the measuring equipment.

3.3.3.4 Nanoindenter Tips

An appropriate and defined probe is crucial for determining reliable and accurate results. In nanoindentation, the geometry and the material from which the tip is made from can dramatically influence the observations. The most common tip geometries used are listed in Table 3.2. In this project spherical geometry is used for room temperature tests. The strain field imposed by a spherical tip varies as a function of indentation depth, which allows for an examination of the materials full stress-strain response [255, 256]. A Berkovich tip is used for high temperature testing, as the behaviour of spherical indenters at high temperatures are not well

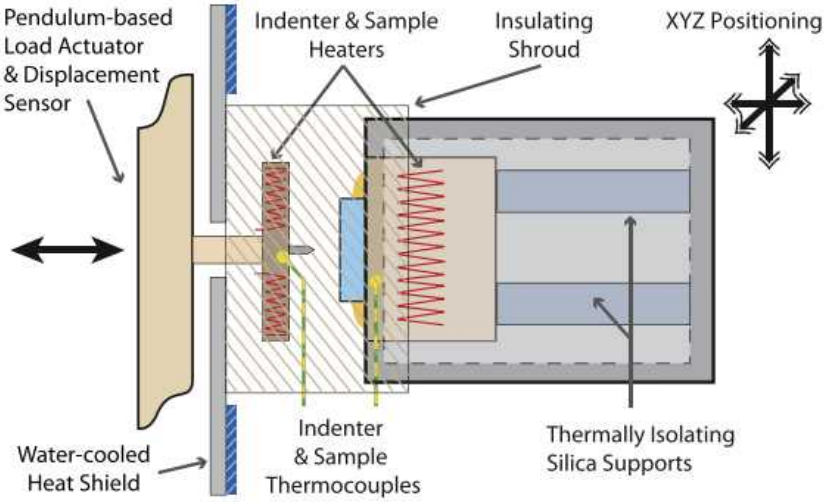


Figure 3.5: Micro Materials xtreme nanoindenter schematic diagram [254]. Reprinted from Current Opinion in Solid State Materials Science, 19 /6, J.M. Wheeler, D.E.J. Armstrong,W. Heinz, R. Schwaiger, High temperature nanoindentation: The state of the art and future challenges, 354-366, Copyright (2015), with permission from Elsevier.

Table 3.2: Nanoindenter tip parameters [251]

Indenter Tip Geometry	Projected Area	Semi-angle (θ)	Effective Cone Angle (α)	Intercept Factor	Geometry correction factor (β)
Sphere	$A = \pi 2Rh_p$	N/A	N/A	0.75	1
Berkovich	$A = 3h_p^2\tan^2(\theta)$	65.3°	70.2996°	0.75	1.034
Vickers	$A = 4h_p^2\tan^2(\theta)$	68°	70.32°	0.75	1.012
Knoop	$A = 2h_p^2\tan(\theta_1)\tan(\theta_2)$	$\theta_1 = 86.25°$, $\theta_2 = 65°$	77.64°	0.75	1.012
Cube Corner	$A = 3h_p^2\tan^2(\theta)$	35.26°	43.38°	0.75	1.034
Cone	$A = \pi h_p^2\tan^2(\alpha)$	α	α	0.72	1

understood and introduce more uncertainty into the results.

3.3.4 Nanoindentation Phenomena

The methods of evaluating material properties by nanoindentation are idealised into elastic and plastic deformations components, shackling the analysis to restrictive branches of classical theory. A plethora of phenomena regularly occur underneath and surrounding the indenter tip that are incompatible with this rigid framework. Relevant phenomena are presented, some of which we may want to investigate, or similarly impede us from obtaining relevant data.

3.3.4.1 Surface Roughness

All indentation data analysis uses the assumption that the surfaces are flat, or of a large curvature. This is, however, not true. During macroscopic indentation the surface roughness plays little to no effect on the indentation result. This is because the length-scales used to describe the tip and surface roughness are separated by several orders of magnitude. In nanoindentation these length-scales overlap. This means the contact area is usually an overestimated [257] and results in erroneous values of stress and hardness. These errors are more pronounced in shallow indentation [258]. It is for this reason that great care must be taken when preparing samples for micromechanical testing to ensure that an appropriate average surface roughness is achieved. There are now several models and methods to account for undesirable surface roughness [259]. The issue with these models is that they are only able to account for lateral roughness. The best way to overcome

surface roughness is to produce a high quality surface throughout the grinding and polishing stages [260].

3.3.4.2 Indentation Size Effect

The indentation size effect (ISE) refers to the"smaller is stronger" principle, hardness increases with smaller indenter tip radius. Nix and Gao [261] have created a successful model explaining the origins of the ISE, by evaluating the way that geometrically necessary dislocations (GNDs) are created around the indenter tip to accommodate a materials plastic deformation. The relation of measured hardness H to indentation depth h is described by

$$H^2 = H_0^2\left(1 + \frac{h_0}{h}\right), \tag{3.12}$$

where h_0 is a length-scale relating to the statistically stored dislocations and H_0 is the hardness due to statistically stored dislocations in the absence of any GNDs. A linear relation exists for $\mathrm{H}^2\,\mathrm{vs}\,\mathrm{h}^{-1}$, as shown experimentally [262, 263, 261] in Figure 3.6. This increase in hardness is due to the way GNDs are confined to a hemispherical plastic deformation zone. For shallow indents the GNDs will extend beyond the plastic zone due to strong repulsive forces. This results in an increased hardness due to an increase in the effective plastic zone.

3.3.4.3 Pile-ups and Sink-ins

The contact area between the tip and the surface does not only depend on the tip shape, but also on the elastic properties of the material. Depending on the elastic properties of the material, either pile-ups or sink-ins can be experienced. If the material has a limited elastic response then the material accommodates the indenter volume by plastic deformation. This results in pile-ups surrounding the tip, and typically underestimates the contact area between the tip and sample. However, if the material is very elastic then the volume of the indenter can be accommodated by long range elastic deformation. This results in sink-ins that overestimate the contact area between the tip and sample. An illustration of both pile-ups and sink-ins are shown in Figure 3.7.

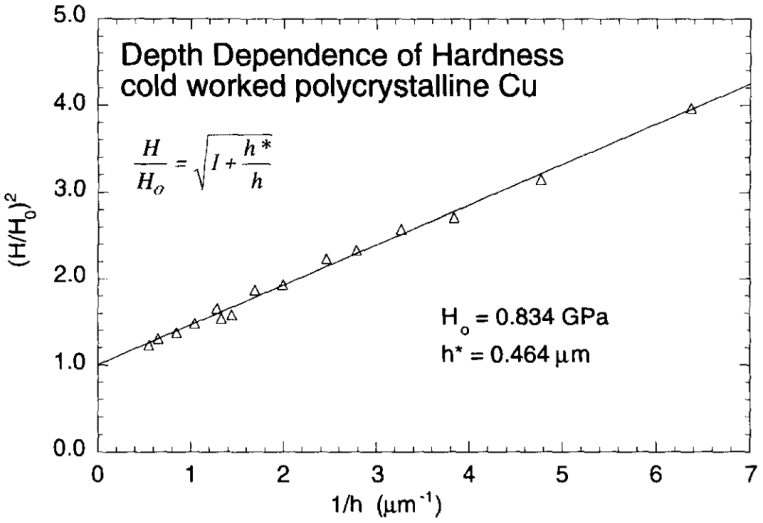


Figure 3.6: Indentation size effect as reported by Nix and Gao [261]. An increase in hardness is reported for decreasing indentation depth in poly-crystalline copper due to GND nucleation. Reprinted from Journal of the Mechanics and Physics of Solids, 44/3, William D. Nix, Huajian Gao, Indentation size effects in crystalline materials: A law for strain gradient plasticity, 411-425, Copyright (1998), with permission from Elsevier.

3.3.4.4 Pop-ins

A pop-in is the discrete transition from elastic to plastic deformation in a crystalline material. In the moments immediately before the pop-in occurs the material can exhibit near theoretical strengths, much higher than those normally seen in an engineering context. The value of shear strength is described by Shim et al [264] and used Hertzian contact theory

$$\tau_{max} = 0.31 \times \left(\frac{6PE_{Eff}^2}{\pi^3 R_{Eff}^2} \right)^{\frac{1}{3}}. \tag{3.13}$$

In the context of this work, pop-ins are caused by the sudden nucleation of dislocations. This is typically because the spacing between dislocations/dislocation sources is greater than the tested volume. Pop-in events are a function of many parameters such as indenter shape and size, temperature and strain rate [265, 266].

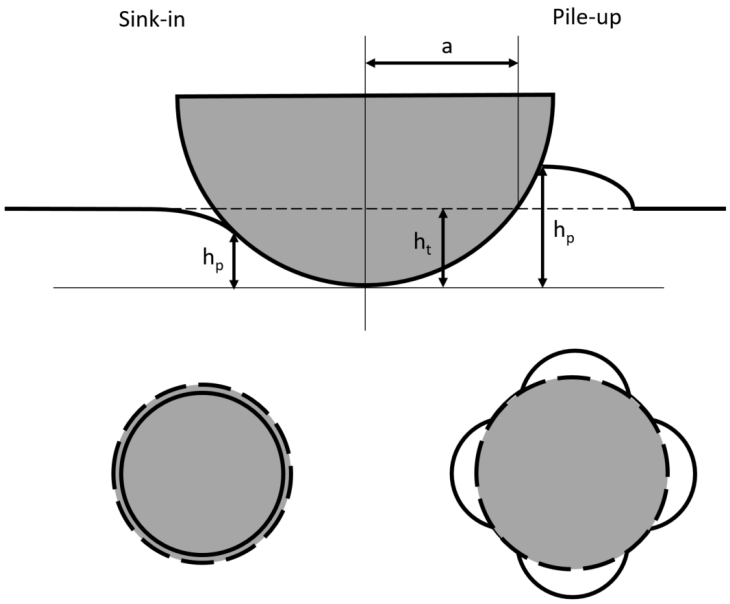


Figure 3.7: The shape of pile-ups and sink-ins in austenitic alloys before and after spherical NI.

3.4 Scanning Electron Microscopes

A scanning electron microscope (SEM) uses a series of electromagnetic lenses to focus an electron beam to a probe point on the sample surface. This probe point can then be rastered across the surface by varying the current in the scanning coils. The electrons interact with a volume of the sample. Depending on the location on the detector, and nature of the interaction, different information can be retrieved (Figure 3.8). Secondary electrons -1 (SE1) are generated on the surface, or very close to it, by the electron beam. The electrons undergo a single interaction or collision with the material. They carry the highest resolution, and can contain information relating directly to the surface topology.

Secondary electrons -2 (SE2) are generated when an electron penetrates further into the sample, and undergoes multiple scattering events due to colliding with the lattice. SE2s have several uses, ranging from imaging to identifying phases. Due to the scattering events, SE2s can leave the surface some distance away from the probe point. The exiting SE2s can be pulled towards a E-T detector by applying

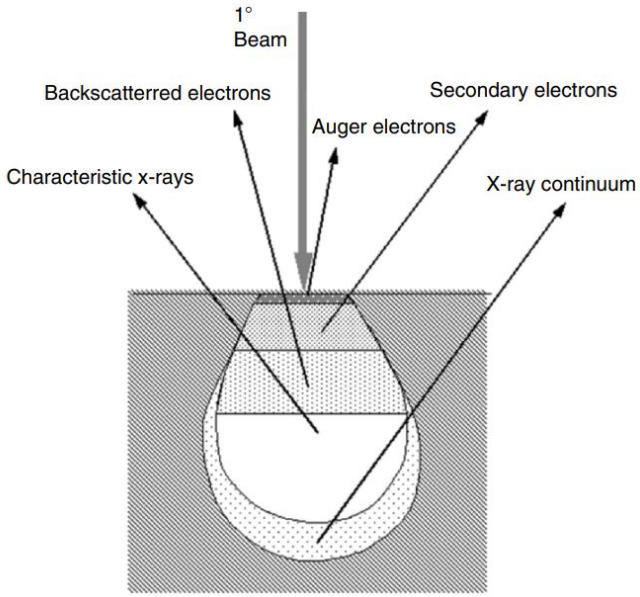


Figure 3.8: The interaction volume between an electron beam and a sample surface, detailing the different information achievable, from [267]. Reprinted/adapted by permission from Springer Nature: Springer, Fundamentals of Scanning Electron Microscopy (SEM) by Weilie Zhou, Robert Apkarian, Zhong Lin Wang et al [COPYRIGHT] (2006).

a potential bias. This reduces the resolution of imaging. Back scattered electrons (BSE) are the same as SE2s, except they are higher energy, and after escaping the material they return to the pole piece.

Electrons that penetrate deep into the bulk lose so much energy, they can no long escape the sample. Energy is lost to the matrix via collisions, during which electrons transfer part of their energy to promote electrons of the atoms in the matrix. As the electrons fall back down energy levels, they emit X-rays that can be used to provide chemical information. The spatial resolution the x-rays are the worst as the interaction volume of the electron beam is the largest.

Throughout this project, several SEMs have been utilised. The majority of this work has been completed on a Evo (Zeiss) W filament, Zeiss Auriga (Zeiss) FEG-SEM and Merlin(Zeiss) FEG-SEM. The quality and resolution of the electron columns increase throughout this list.

3.4.1 Electron Backscattered Diffraction

Electron backscattered diffraction (EBSD) is a technique that is widely used to identify microstructural properties, such as measuring relative intragranular strain, grain boundary characteristics, and determining crystallographic orientation and texture. In practice, EBSD is conducted within a scanning electron microscope. A rastering electron beam interacts with a sample tilted to 70^o, with respect to the horizontal axis. The tilt is selected as it increases the yield of backscattered electrons, without losing too much spatial resolution. The emitted electrons are detected by a phosphor screen and a low light CCD camera behind the screen, which is later transferred to a PC. A schematic diagram illustrates the experimental set-up in Figure 3.9a.

The emitted back-scattered electrons are diffracted by a set of parallel atomic planes on the surface of the sample. The diffracted electrons from a single pair of atomic planes that satisfy the Bragg's criteria ($n\lambda=2d\ \sin(\theta)$), create a band across the phosphorus screen, this is called a Kikuchi band. Every set of parallel atomic planes that satisfies Bragg's criteria produces a distinct Kikuchi band (i.e. yellow or red). Multiple diffracting (Kikuchi) bands form a Kikuchi pattern, which is recorded by the detector (Figure 3.9b).

The point at which two or more Kikuchi bands intersect is called a zone-axis. The Kikuchi pattern and zone-axes are then compared to a catalogue of patterns,

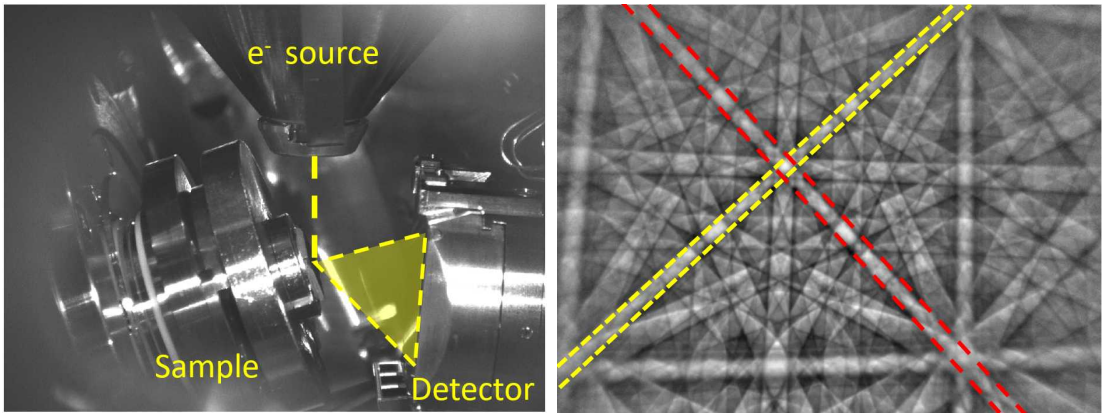


Figure 3.9: (a) The chamber view of a SEM configured for EBSD measurements (b) Kikuchi bands as detected.

and indexed as a certain gnomonic projection of the Kikuchi sphere by commercial software. The angles between a list of zone axes are compared to a table to identify the crystal structure, and orientation of a particular pattern resulting from a point on the sample. The resulting orientation that produced this Kikuchi pattern projection can then be calculated by the geometry of the setup and the orientation of that point (or grain) can be calculated with respect to the sample co-ordinate system. Similarly, small rotations and shifts of the Kikuchi patterns between neighbouring pixels (within the same grain), can be used to calculate misorientations, elastic strain and the density and Burgers vector of geometrically necessary dislocations (GND). For more information and examples, the reader can view the following sources [268, 269, 270, 271].

In this thesis, the EBSD experiments were completed on a Zeiss Evo and Zeiss Merlin, fitted with a Bruker EBSD detector system. The working distance of the sample was approximately 18 mm, and the detector distance was also 18 mm from the sample surface. The operating conditions of the SEMs were a 20kV accelerating voltage and a beam current of 5nA. For each material the inverse pole figure, pole figure, pattern quality and Kernel misorientatioin (KMO) map were recorded.

3.4.2 Transmission Kikuchi Diffraction

EBSD is routinely used to explore the microstructural properties of crystalline samples. The technique probes the bulk of the sample, and the interaction volume artificially limits the resolution of EBSD to approximately 50nm [271]. To overcome this, transmission electron back-scattered diffraction (t-EBSD), or transmission Kikuchi diffraction (TKD) has been developed [272, 273, 58, 271]. This technique uses a thinned sample, which greatly reduces the interaction volume of the probe, and increases the spatial resolution to approximately <5 nm. The incident electron beam diffracts similarly to conventional EBSD, from parallel planes in the crystal lattice, but it is instead the transmitted electrons that are collected and produce the Kikuchi pattern. The detector distance, or detector tilt, can be changed to either increase or decrease the number of projected zone axes in the Kikuchi pattern. There are two types of TKD, off-axis TKD, and the newly developed on-axis TKD. The difference being the position of the detector, relative

to the optical axis of the microscope.

The work completed in this study uses on-axis TKD on a Zeiss Merlin, using a Bruker e-flash high-resolution EBSD detector with an OPTIMUS^{TM} head. In on-axis TKD, the sample is positioned perpendicular to the electron beam, at a working distance of 5mm. The detector is inserted immediately underneath the sample at a distance of 16mm, allowing the transmitted beam to be collected. A diagram of the arrangement is shown in Figure 3.10. This orientation has three distinct benefits over the off-axis arrangement. Firstly, the acquisition time is greatly reduced due to the increased signal strength. Secondly, the on-axis configuration eliminates sample tilt, increasing the spatial resolution. Finally, the OPTIMUS^{TM} detector head is fitted with three forescattered electron detectors (FSD) [272], which can be used to image thinned samples. The central FSD captures low-angle deflections, as it is aligned with the optical axis, resulting in a bright-field images, and the outer FSDs capture high-angle deflections which results in a dark-field image.

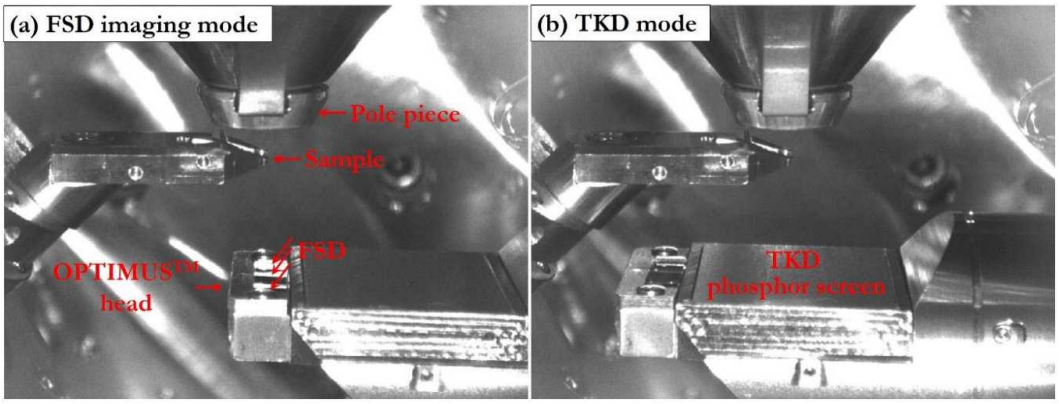


Figure 3.10: Schematic diagram of the OPTIMUS ^{TM} detector head used during TKD in both (a) forescattered electron imaging mode and (b) TKD mode. Image from [272]. Reprinted from Materials Characterization, 155, Junliang Liu, Sergio Lozano-Perez, Phani Karamched, Jennifer Holter, Angus J. Wilkinson,Chris R.M. Grovenor, Forescattered electron imaging of nanoparticles in scanning electron microscopy, 109814, Copyright (2019), with permission from Elsevier.

3.5 Focused Ion Beam

The focused ion beam (FIB) is a very similar instrument to that of the SEM, but instead of using electrons, it uses Gallium (Ga^+) ions. The focused ion beam can modify the sample surface via a sputtering process, that is referred to as milling. It is also possible to deposit material by injecting gas directly on to the region that it being milled. This milling/deposition can be controlled to a high degree of precision, typically to the tens of nanometers. The versatility of the FIB is realised when paired with an SEM to become a dual-beam (FIB/SEM) system. This allows site-specific fabrication of micro-scale features and samples.bIn this study a Zeiss Auriga FIB/SEM was used to make TEM/TKD lamellas.

3.5.1 TEM/TKD Sample Preparation

This preparation method is well detailed by several sources [274, 275, 16, 272]. Details of the lift-out process are illustrated in Figure 3.11. (a) A layer of Pt is first deposited on the area of interest to protect it from FIB damage (volume of 20 x 3 x 3 μm^3 using 240 pA, 30 kV), if the surface is sensitive the e^- beam can be used to deposit Pt. (b) Trenches are sequentially milled either side of the Pt (volume of 20 x 20 x 20 μm^3 using 4 nA, 30 kV). (c) Tilt the stage to -5°. The lift-out can be undercut and a supporting side removed using 2 nA, 30 kV. (d) The stage is tilted to 10°. A micro manipulator is inserted and welded to the corner of the lamella using Pt (2 x 2 x 1 μm^3 using 120 pA, 30 kV). (e&f) The remaining support can be cut, and the sample should be free from the bulk.

(g) A copper grid is inserted. Mill a notch in the base of the 'M' using 16 nA. This will minimise shadowing from the copper grid during TKD [272]. (h) Raster the FIB over the area the sample will be attached, this is to remove any copper oxide which will result in a stronger weld. Manoeuvre the lamella using the micro-manipulator to the prepared site and weld using Pt (8 x 5 μm^2 for 300s using 120 pA, 30 Kv). (i) Cut away the manipulator. (k) Progressively thin both sides of the sample with milling currents of 2000 - 240 pA at 30kV. (L) Stop when the sample is uniformly transparent at 7kV. Perform a low energy polish to remove FIB damage (200 pA, 5 kV). Continue until the sample becomes transparent at 5kV.

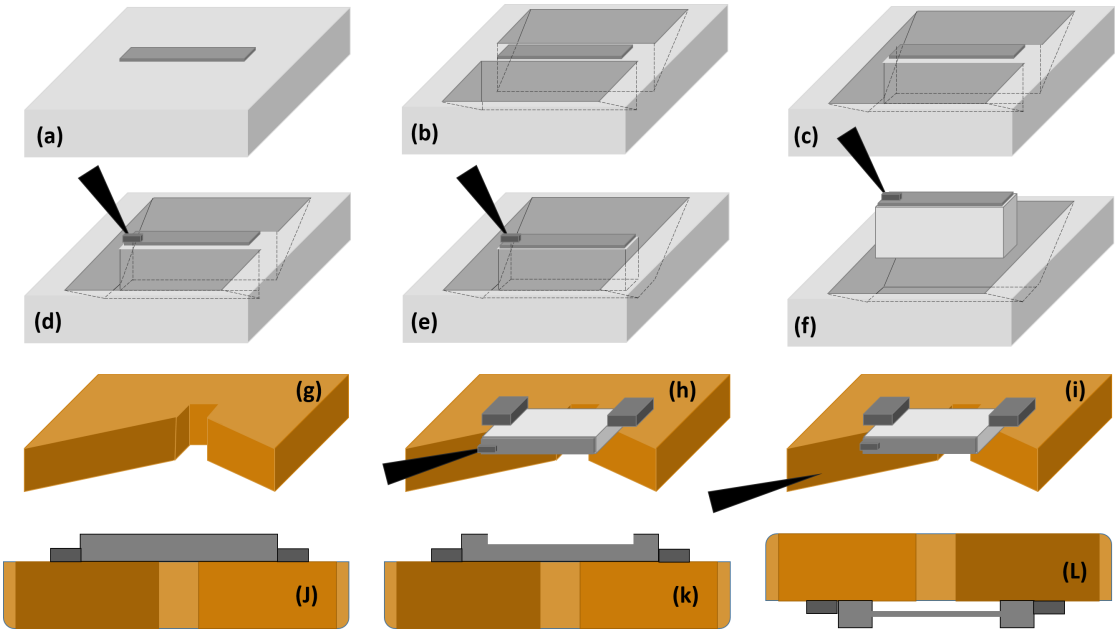


Figure 3.11: An illustration of the steps required to prepare TEM/TKD samples.

In the authors experience, this produced the best results and should correspond to a sample thickness of 50-100 nm.

3.6 Transmission Electron Microscopes

Transmission electron microscopy (TEM) represents the forefront of characterisation and analytical abilities in the field of electron microscopy. A text outlining the principles of the TEM is provided by Williams and Carter [276].

At the top of the column, a beam of electrons is rapidly accelerated to high energies and emitted from the gun along the microscope's optical axis. The beam is focused through the condenser lens to one of two illumination modes, either convergent or parallel. A convergent beam allows for a small point probe to focus on a specific feature on the sample. This is used for analytical microscopy. A parallel beam provides an even low-density illumination over the entire sample. This mode is highly coherent and is used for bright and dark field imaging. The beam, in whichever imaging condition, interacts with the sample, and enters into the objective lens and apertures. The beam finally passes through a magnifying

lens to give the projected image.

The majority of the microscopy work in this thesis was performed on a JEOL 2100 microscope with a LaB6 electron source and 200kV accelerating voltage. TEM is used to characterise the surface oxides on autoclaved materials. Fresnel imaging and Energy Dispersive X-Ray (EDX) spectroscopy are selected to determined porosity and chemical information. TEM work was completed by Dr Guanze He. Fresnel imaging is explained well by Hutchinson et al. [277], this method highlights large defects in the lattice by changing the Bragg condition. EDX characterises composition by identifying the energy of detected X-rays. X-rays are generated when promoted electrons in the material, fall back down to a lower energy state. More information can be found [278].

3.7 Autoclave

The University of Oxford does not own any autoclave systems, so autoclave tests were completed at the University of Manchester. The autoclave is the selected method for introducing deuterium into the alloys under PWR conditions for mapping in the nanoSIMS and thermal desorption spectrometer. Prior to testing, the heavy water was purged with nitrogen to dearate the water. It was then hydrogenated with an overpressure of 0.85 bar to produce a dissolved hydrogen concentration of 3 ppm H_2 at STP.

This system has an internal volume of 600ml and comprises a main vessel and glass feed tank. During operation the autoclave was operating at a flow rate of 2 L/hr. The heavy water enters the bottoms of the vessel, flowing to the samples and to the exit at the top. The recirculated water passed through a heat exchanger to maintain a constant 340 °C temperature. Throughout the entire test length of 1572 hours, the conductivity and dissolved oxygen content was continuously measured by an ABB AC221 conductivity sensor and a luminescent Hach Orbisphere respectively. The dissolved oxygen content was kept below 5 ppb. Contaminants from the autoclave vessel and samples were removed by circulating the water through a mixed bed ion exchange resin prior to return to the feed tank.

3.8 NanoSIMS

Secondary ion mass spectrometry (SIMS) is a popular technique because of its high mass resolution, surface and chemical sensitivity, and lateral and depth resolution. The distinct advantage of SIMS over other chemical analysis tools, is that it can detect every element and mass isotope. This includes hydrogen and deuterium with parts per billion sensitivity. During time-of-flight SIMS, the primary beam consists of high energy ions, either O^-/O^{2-} or Cs^+, that are condensed and deflected by a series of lenses and apertures towards the surface of the sample. The incident primary ion beam on the sample surface causes sputtering. These spluttered ions are then collected and form the secondary ion beam, which is directed towards a time-of-flight mass spectrometer. Once in the time-of-flight spectrometer the elements are separated by m/z ratios and collected by the detectors.

A CAMECA NanoSIMS 50 and a CAMECA NanoSIMS 50L has been used in this thesis.The NanoSIMS differs from the conventional TOF-SIMS outlined is several significant ways. Firstly, the NanoSIMS 50 employs co-axial optics to direct the primary and secondary ions [212]. The advantage of this system is that the working distance to the sample can be reduced; enhancing the focus and spatial control of the primary beam onto the surface, while also increasing the collection of sputtered ions. Secondly, the mass analyser is in a Mauttach-Herzog configuration, with 5 individual magnetic sector mass spectrometers [279]. This allows simultaneous high ion transmission and mass resolution (i.e. $^{12}C^{15}N^-$ 26.9996 amu, and $^{13}C^{14}N^-$ 27.0059 amu can be separated). The CAMECA NanoSIMS 50 can provide high spatial resolution (i.e. sub-micron) on up to 5 m/z ratios, while the CAMECA NanoSIMS 50L can detect up to 7 m/z ratios.

In this thesis two main analysis geometries were used, top-down and cross-sectional. Cross-sectional NanoSIMS analysis (Figure 3.12a) simultaneously analyses the oxide and matrix by conducting conventional NanoSIMS analysis on a pre-polished cross-section of a sample. Pre-polishing to EBSD standard is required to reveal the position of carbides, grain boundaries, and oxide layers. A top-down analysis (Figure 3.12b) does not require polishing and the surface oxide is sputtered first followed by the underlying matrix. A main benefit of the cross-sectional analysis is that objects deep in the bulk can be analysed, as the top-down

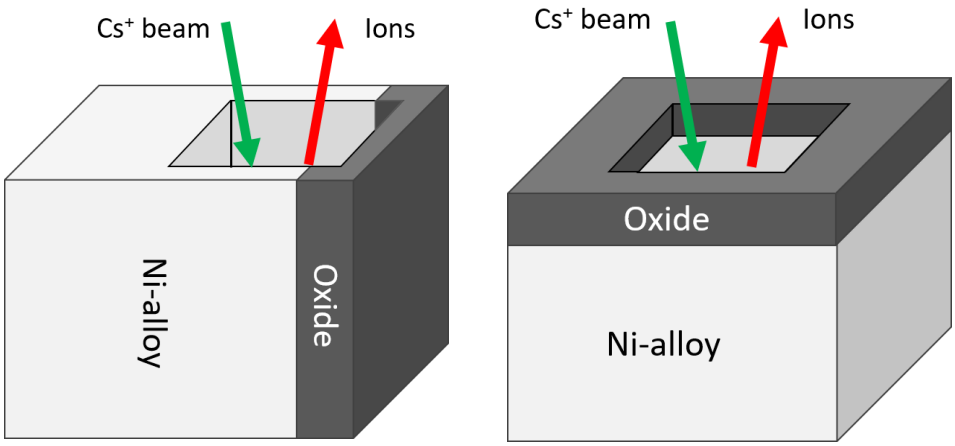


Figure 3.12: Schematic diagrams of the (a) cross-sectional sample geometry in comparison to (b) the top-down methods.

approach only tests the top ten microns. In this project the cross-sectional method is used to examine grain boundaries, carbides, and regions ahead of intergranular oxidation.

3.9 Thermal Desorption Spectroscopy

Thermal desorption spectroscopy (TDS) is a bulk technique capable of providing quantitative information about desorbed gaseous species. This technique is favoured for complementing qualitative information provided by the NanoSIMS. The system has been tuned to allow mass separation of the He and D_2 peaks at approximately 4 atomic mass units (amu), making it ideal for examining desorbed heavy water samples and hydrogen studies. The TDS system used in this study is manufactured by Hiden, and is located at materials research facility (MRF) as part of the Culham centre for fusion energy (CCFE), UK.

The system comprises a main analytical stainless steel vacuum chamber, that is maintained at ultra-high vacuum ($\sim 10^{-9}$ mbar) at all times, and a load/lock chamber that is used to exchange samples. The analytical chamber is fitted with a quadrapole mass spectrometer and a sample heating stage. The sample sits on the heating stage, which is made of molybdenum.

The heating process is achieved by resistive heating elements fitted within the stage. The walls of the chamber do not heat-up during testing. The temperature is measured by two thermocouples, one of which is embedded in the stage and in contact with the sample. The sample is heated using a bottom-up approach, meaning that regions of interest are not in direct contact with the heat source.

The quadrapole mass spectrometer is located directly over the sample for direct line-of-slight detection. This is beneficial as the detector is much closer to the sample, allowing for increased detection efficiency. This combination of the line-of-sight detector and UHV conditions minimises the interference of hydrogen from external sources. The TDS is a calibrated machine, meaning that a single count can be directly compared to a minimum number of hydrogen molecules. The calibrated hydrogen count-to-atoms data is presented by Baron-Wiechec et al [280].

Chapter 4

Coupled Diffusion-Mechanical Hydrogen Transport Sub-routine (UMATHT)

Mechanical properties can be challenging to extract from micromechanical experiments, often requiring finite element modelling to determine the yield stress or modulus. A range of subroutines exist for accurately determining the properties from in-air experiments, i.e. crystal plasticity [281], but no such tool is readily available for use on hydrogen-charged specimens. In this chapter, a three-dimensional fully coupled hydrogen transport subroutine is presented that can be used to determine changing hydrogen concentrations and material properties. This subroutine is a User MATerial Hydrogen Transport (UMATHT) subroutine, and is based on the initial two-dimensional version first published by Barerra et al [282]. The formulation and method of calculating hydrogen concentration is outlined over the next chapter. This chapter covers published theories in subsections 4.1-4.3, and my own contributions are outlined in subsection 4.4.

4.1 Hydrogen Diffusion

Hydrogen diffuses readily through the lattice by occupying interstitial lattice sites (NILS). The majority of hydrogen atoms occupy NILS [253], but a fraction can temporarily reside at trapping sites, such as dislocations, grain boundaries, carbide/matrix interface, voids and other defects. It is defined at the outset that

the hydrogen concentration in the lattice is denoted by C_L, and the concentration of hydrogen in the traps is denoted by C_X, and barred variables, such as $\bar{C}_L$ denote molar quantities (C_L/N_A), where N_A is Avogadro's number. The total concentration of hydrogen in the samples is given by $C_T = C_L + C_X$.

To achieve an expression for the diffusion of mobile hydrogen, let us start by considering fundamental diffusion principles: the conservation of mass and chemical potential. The conservation of mass defines the total movement of hydrogen around the material. It equates the total rate of change of hydrogen in a volume Ω to the hydrogen flux $\bar{\mathbf{J}}$ through the surface $\partial\Omega$

$$\frac{\partial}{\partial t}\int_{\Omega}(\bar{C}_L + \bar{C}_X)d\Omega + \int_{\partial\Omega}\bar{\mathbf{J}}\cdot\mathbf{n}dS = 0, \tag{4.1}$$

where $\mathbf{n}$ is the outward normal of $\partial\Omega$. Diffusion is driven by the gradient of the chemical potential $\nabla\mu$, when minimised this represents the lowest energy solution of the system. The chemical potential at any point in the volume Ω can be expressed as a sum of three factors

$$\mu = \mu_0 + RTln\bar{C}_L + \mu_\sigma. \tag{4.2}$$

The first term μ_0 represents the chemical potential under standard conditions. The second term $RTln\bar{C}_L$ is part of the general solution of the diffusion equation, $\bar{C}_L$ is in the logarithm as it drives the change in chemical potential. Finally, $\mu_\sigma = -\sigma_H V_H$ is the chemical potential change due to the presence of hydrogen, where V_H is the partial molar volume of hydrogen. With this definition of the chemical potential, we can find an expression for the chemical potential gradient

$$\nabla\mu = RT\frac{\nabla\bar{C}_L}{\bar{C}_L} - V_H\nabla\sigma_H. \tag{4.3}$$

As the chemical potential gradient drives the movement of hydrogen, it can be used to express the flux through the surface $\partial\Omega$

$$\bar{\mathbf{J}} = -\frac{D_L\bar{C}_L}{RT}\nabla\mu = \frac{D_L\bar{C}_L V_H}{RT}\nabla\sigma_H - D_L\nabla\bar{C}_L. \tag{4.4}$$

The hydrogen flux (Eq.4.4) can be substituted into the conservation of mass equation (Eq.4.1), which gives

$$\frac{\partial}{\partial t}\int_{\Omega}(\bar{C}_L + \bar{C}_X)d\Omega + \int_{\partial\Omega}\left(\frac{D_L V_H\bar{C}_L}{RT}\nabla\sigma_H - D_L\nabla\bar{C}_L\right)\cdot\mathbf{n}dS = 0. \tag{4.5}$$

The integrals can be avoided by applying the divergence theorem, which results in a simplified form,

$$\frac{\partial \bar{C}_L}{\partial t} + \frac{\partial \bar{C}_X}{\partial t} + \nabla \cdot \left(\frac{D_L V_H \bar{C}_L}{RT} \nabla \sigma_H \right) - \nabla \cdot \left(D_L \nabla \bar{C}_L \right) = 0. \tag{4.6}$$

Currently, the diffusion equation can not be solved as it consists of two unrelated variables $\bar{C}_L$ and $\bar{C}_X$. To solve this equation $\bar{C}_X$ will need to be written as a function of $\bar{C}_L$, or vice-versa. The assumptions made in Oriani's model of diffusion allows this substitution to be made, over the next section will outline how to combine these terms.

4.2 Oriani's Assumption

The concentration of hydrogen in lattice sites, C_L, can be expressed in terms of the number of atoms of solvent hydrogen per unit volume (atoms/m^3) N_L

$$C_L = \beta \theta_L N_L, \quad N_L = \frac{\rho N_A}{A_r} = Const., \tag{4.7}$$

where β is the number of NILS sites per solvent hydrogen atom, θ_L is the occupancy of the NILS sites ($0 \leq \theta_L \leq 1$), ρ is the density of the solvent atoms ($\rho_H = 1$) and A_r is the relative atomic mass ($A_r = 1$). Similarly the hydrogen concentration trapped at dislocations can be expressed in terms of the number of atomic trapping sites along the total dislocation line (L/m^3)

$$C_X = \alpha \theta_X N_X, \quad N_X(\epsilon^p) = \frac{\sqrt{2}}{a} \rho^d(\epsilon^p), \tag{4.8}$$

where $\alpha = 1$ denotes the number of trapping sites per solvent hydrogen atom, θ_X is the fraction of trapping sites occupied by H atoms ($0 \leq \theta_X \leq 1$). Here it is possible to see the implications of the dependence on the plastic strain as stated by Krom et al [283], as the number of atomic trapping sites along a dislocation line is a function of the plastic strain.

In the diffusion equation (Eq.4.6) there exist two unknown variables to solve $\bar{C}_L$ and $\bar{C}_X$. However, Oriani's theory on diffusion suggests that the concentration

between the traps and the lattice is at equilibrium; meaning once the lattice concentration is known, then the concentration in the traps is known. Oriani's theory [284] states that

$$\frac{\theta_X}{1-\theta_X} = K\theta_L, \tag{4.9}$$

given that the number of occupied lattice sites occupied is small $\theta_L << 1$, it is appropriate to define K as a probability distribution describing the chance of a lattice site with a binding energy of W_B being occupied

$$K = exp\left(\frac{-W_B}{RT}\right) = const. \tag{4.10}$$

The fraction of trapping sites occupied by hydrogen atoms, θ_X, can be rearranged into a form suitable for the substitution of Oriani's assumption (Eq. 4.9)

$$\theta_X = \frac{\theta_X}{1+(\theta_X-\theta_X)} = \frac{1}{1+(1-\theta_X)/\theta_X} = \frac{K\theta_L}{1+K\theta_L}. \tag{4.11}$$

This links the fraction of trapping sites occupied by H atoms, θ_X, to the fraction of lattice sites occupied by H atoms, θ_L. Therefore, the concentration of hydrogen in the traps, $\bar{C}_X$, can be expressed in terms of the concentration of hydrogen in the lattice sites knowing that $\bar{C}_L = \beta\theta_L\bar{N}_L$. This is expressed as

$$\bar{C}_X(\bar{C}_L, \bar{N}_X(\epsilon)) = \theta_X\bar{N}_X = \frac{k\theta_L}{1+k\theta_L}\cdot\bar{N}_X(\epsilon) = \frac{k\bar{C}_L}{\beta\bar{N}_L+k\bar{C}_L}\cdot\bar{N}_X(\epsilon), \tag{4.12}$$

However, to use this definition in the diffusion equation, the time derivative is needed. It is known that both the lattice concentration of hydrogen and the plastic strain will change with time. The changing trap concentration of hydrogen is expressed as the sum of partial derivatives

$$\frac{\partial\bar{C}_X}{\partial t} = \frac{\partial\bar{C}_X}{\partial\bar{C}_L}\frac{\partial\bar{C}_L}{\partial t} + \frac{\partial\bar{C}_X}{\partial\bar{N}_X}\frac{\partial\bar{N}_X}{\partial\epsilon}\frac{d\epsilon}{dt}, \tag{4.13}$$

the exact derivatives can be calculated using the new definition of $\bar{C}_X$

$$\frac{\partial\bar{C}_X}{\partial\bar{C}_L} = \frac{\partial}{\partial\bar{C}_L}\left(\frac{k\bar{C}_L}{\beta\bar{N}_L+k\bar{C}_L}\cdot\bar{N}_X\right) = \frac{\beta\bar{N}_Lk\bar{N}_X}{(\beta\bar{N}_L+k\bar{C}_L)^2}, \tag{4.14}$$

$$\frac{\partial\bar{C}_X}{\partial\bar{N}_X} = \left(\frac{k\bar{C}_L}{\beta\bar{N}_L+k\bar{C}_L}\right), \tag{4.15}$$

and re-substituted into the conservation of mass equation (Eq. 4.6)

$$\begin{aligned}\frac{\partial \bar{C}_L}{\partial t}\left(1+\frac{\beta \bar{N}_L k \bar{N}_X}{(\beta \bar{N}_L + k\bar{C}_L)^2}\right) - \nabla\cdot(D_L \nabla \bar{C}_L) \\ +\nabla\cdot\left(\frac{D_L V_H \bar{C}_L}{RT}\nabla\sigma_H\right) + \frac{k\bar{C}_L}{\beta\bar{N}_L + k\bar{C}_L}\frac{d\bar{N}_X}{d\epsilon}\frac{d\epsilon}{dt} = 0.\end{aligned} \tag{4.16}$$

This process has reduced the diffusion equation to a solvable state, with dependence on a single variable $\bar{C}_L$. It is worth noting that if the temperature is non-uniform then the temperature gradient in the material would also contribute to the diffusion of hydrogen, however this is normally ignored [285]. For many engineering applications this is a valid assumption and has a major practical advantage, it allows commercial finite element software (e.g. ABAQUS) to solve thermal-mechanical problems. In the context of our work, reactors operate at a carefully maintained temperature, and the experiments conducted reflect this stability. The way in which the following diffusion problem is implemented into software will be explored in the following section.

4.3 Analogous Implementation of the UMATHT Subroutine

Finite element software, such as ABAQUS, is able to solve coupled thermal-mechanical problems, but not diffusion-mechanical problems. Given the similarities between the forms of the governing second order partial differential equations of mass and thermal diffusion, it should possible to trick ABAQUS into solving coupled diffusion-mechanical problems. This is completed through careful substitution of analogous parameters [286]. The analogy between the thermal and mass diffusion parameters in ABAQUS is summarised in Table 4.1.

Thermal transfer in the ABAQUS sub-routine UMATHT can be defined by the variations of the internal energy U_q and thermal flux $\bar{\mathbf{J}}_T$ with temperature $(\partial U_q/\partial T, \partial \bar{\mathbf{J}}_T/\partial T)$ and spatial temperature gradient $(\partial U_q/\partial(\nabla T), \partial \bar{\mathbf{J}}_T/\partial(\nabla T))$. The analogy suggests that under our implementation of the UMATHT sub-routine, the mass diffusion can be defined by changing multiple terms. These include the total hydrogen concentration ($\bar{C}_T = \bar{C}_L + \bar{C}_X$), the hydrogen flux $\bar{\mathbf{J}}_H$ with respect

to the lattice concentration of hydrogen ($\partial\bar{C}_T/\partial\bar{C}_L, \partial\bar{\mathbf{J}}_H/\partial\bar{C}_L$), and the density of hydrogen traps $\partial\bar{C}_T/\partial\bar{N}_X(\epsilon)$ as a function of plastic strain and the hydrogen concentration gradient $\partial\bar{\mathbf{J}}_T/\partial(\nabla\bar{C}_L)$. These necessary parameters are defined in the following way:

$$\frac{\partial\bar{C}_T}{\partial\bar{C}_L} = 1 + \frac{\partial\bar{C}_X}{\partial\bar{C}_L} = 1 + \frac{\beta\bar{N}_L k\bar{N}_X}{(\beta\bar{N}_L + k\bar{C}_L)^2}, \tag{4.17}$$

$$\frac{\partial\bar{C}_T}{\partial\bar{N}_X} = \frac{k\bar{C}_L}{\beta\bar{N}_L + k\bar{C}_L}, \tag{4.18}$$

$$\frac{\partial\bar{\mathbf{J}}_H}{\partial\bar{C}_L} = \frac{DV_H}{RT}\nabla\sigma_H, \tag{4.19}$$

$$\frac{\partial\bar{\mathbf{J}}_H}{\partial(\nabla\bar{C}_L)} = -D\mathbf{I}, \tag{4.20}$$

Table 4.1: The equivalence between mass and thermal diffusion in the UMATHT application, from [285].

Thermal Diffusion	Mass Diffusion
Energy Conservation, $\rho_m c_m \frac{\partial T}{\partial t} + \nabla\cdot\boldsymbol{f} + r_m = 0$	Mass Conservation, $\rho s\frac{\partial\theta}{\partial t} + \nabla\cdot\boldsymbol{j} + r = 0$
Thermal Energy per unit mass (J kg^{-1}), U	H atoms per H lattice site, C
Mass density (kg m^{-3}), ρ_m	H lattice site density (m^{-3}), ρ
Temperature (K), T	Lattice Occupancy, θ $(0< \theta <1)$
Specific heat capacity (J kg^{-1} K^{-1}), $c_m = \frac{\partial U}{\partial T}$	Solubility per H lattice site, $s = \frac{\partial C}{\partial\theta}$
Heat Flux (J s^{-1} m^{-2}), $\boldsymbol{f}$ = -$\rho_m\alpha\ c_m\boldsymbol{g}$	Hydrogen Flux (s^{-1} m^{-2}), $\boldsymbol{j}$=-$\kappa_\theta(\boldsymbol{g}$-$\frac{\Omega\theta}{k_B T}\nabla\sigma_H)$
Temperature Gradient (K m^{-1}), $\boldsymbol{g}$=∇T	Lattice occupancy gradient (m^{-1}), $\boldsymbol{g}$=$\nabla\theta$
Thermal conductivity (J s^{-1} m^{-1} K^{-1}), κ	Lattice conductivity (s^{-1} m^{-1}), κ_θ=ρD
Thermal diffusivity (m^2 s^{-1}), $\alpha = \frac{\kappa}{\rho_m c_m}$	Effective diffusivity (m^2 s^{-1}), $D_{eff} = \frac{\kappa_\theta}{\rho s}$

where $\mathbf{I}$ is the identity matrix. Having formally defined the analogous terms, it is now possible to formalism the diffusion equation (Eq.4.16) in a way appropriate to the ABAQUS sub-routine

$$\begin{aligned}
\bar{C_T}(t+\delta t) &= \bar{C_T}(t) + \frac{\partial \bar{C_T}}{\partial t}\delta t, \\
&= \bar{C_T}(t) + \frac{\partial}{\partial t}(\bar{C_L} + \bar{C_X})\partial t, \\
&= \bar{C_T}(t) + \left(\frac{\partial \bar{C_X}}{\partial \bar{C_L}}\frac{\partial \bar{C_L}}{\partial t} + \frac{\partial \bar{C_L}}{\partial t} + \frac{\partial \bar{C_X}}{\partial \bar{N_X}}\frac{\partial \bar{N_X}}{\partial \epsilon}\frac{d\epsilon}{dt}\right)\partial t, \\
&= \bar{C_T}(t) + \frac{\partial \bar{C_T}}{\partial \bar{C_L}}d\bar{C_L} + \frac{\partial \bar{C_X}}{\partial \bar{N_X}}\frac{\partial \bar{N_X}}{\partial \epsilon}d\epsilon.
\end{aligned} \tag{4.21}$$

To calculate the variation of the hydrogen flux (Eq 4.19) we need to know the gradient of the hydrostatic stress (or the gradient of the trace of the stress tensor). This presents a problem. In finite element analysis the stress states are calculated separately and systematically in each element at each interval. In other words, the stress states surrounding an element are not known. This implies that it is not possible to calculate a gradient of the hydrostatic stress in the most recent time interval. To overcome this problem the hydrostatic stress is calculated from the previous interval's stress state, which is stored and read in from an external file. To implement this work-around a commonblock is used within the USDFLD subroutine. The USDFLD is explained in the next section. The hydrostatic stress is then interpolated, in an identical manner to the strain field, from the nodal points to the Gaussian points in each element. The full calculation of the hydrostatic stress in a three-dimensional mass diffusion is found in the next section.

In modelling the micromechanical experiments, quadratic elements must be used. This is because ABAQUS imposes a constant pressure at the Gaussian points in a coupled thermal-mechanical problem, meaning that if linear elements are used, then the calculated hydrostatic gradient would be zero. In the presented simulations a (C3D20RT) 20-noded thermally coupled brick with tri-quadratic elements and a reduced number of integration points was used.

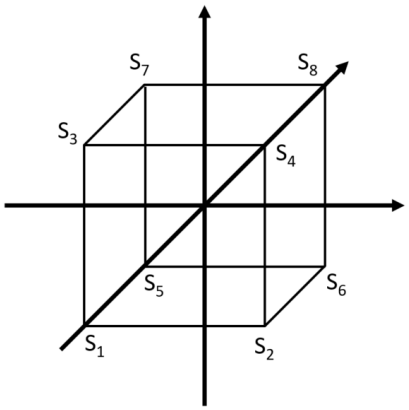


Figure 4.1: The node numbering order for the C3D20RT element used in ABAQUS.

4.4 3D - UMATHT

In this sub-section, I outline the contributions I have made to developing this software. The UMATHT sub-routine used to simulate the mechanical effects of hydrogen comprises numerous other sub-routines to capture diffusive and mechanical effects. The USDFLD subroutine is responsible for calculating the movement of the elemental nodes during deflection. It is therefore understandable that this sub-routine has undergone the most radical transformation while increasing the level of dimensions from two to three from the case presented by Barrera [282]. Outlined below are the major changes implemented.

First it is important to state that all the assumptions made in the inherited 2D case are still valid for the 3D extension. For example, we are assuming that the Gaussian integration points employed coincide with the nodal positions of the parent element. In the 3D case the new coordinates of these integration points are as follows, see Figure 4.1,

$$\begin{aligned} N_1(s_1,s_2,s_3) &= (-1,-1,-1), \quad N_2(s_1,s_2,s_3) = (+1,-1,-1), \\ N_3(s_1,s_2,s_3) &= (-1,+1,-1), \quad N_4(s_1,s_2,s_3) = (+1,+1,-1), \\ N_5(s_1,s_2,s_3) &= (-1,-1,+1), \quad N_6(s_1,s_2,s_3) = (+1,-1,+1), \\ N_7(s_1,s_2,s_3) &= (-1,+1,+1), \quad N_8(s_1,s_2,s_3) = (+1,+1,+1). \end{aligned} \tag{4.22}$$

We are applying a reduced integration elemental mesh, meaning that we only have 8 points of integration instead of the full 27 typically used. This is permissible as the element type used (C3D20RT) is a good all around choice and avoids hourglassing despite the reduced number of integration points. For each integration point we must determine the shape functions used to extrapolate information between nodes, illustrated in Figure 4.2. In this analysis we are using a tri-linear shape functions,

$$\begin{aligned}
N_1(s_1,s_2,s_3) &= 1/8(1-s_1)(1-s_2)(1-s_3),\\
N_2(s_1,s_2,s_3) &= 1/8(1+s_1)(1-s_2)(1-s_3),\\
N_3(s_1,s_2,s_3) &= 1/8(1-s_1)(1+s_2)(1-s_3),\\
N_4(s_1,s_2,s_3) &= 1/8(1+s_1)(1+s_2)(1-s_3),\\
N_5(s_1,s_2,s_3) &= 1/8(1-s_1)(1-s_2)(1+s_3),\\
N_6(s_1,s_2,s_3) &= 1/8(1+s_1)(1-s_2)(1+s_3),\\
N_7(s_1,s_2,s_3) &= 1/8(1-s_1)(1+s_2)(1+s_3),\\
N_8(s_1,s_2,s_3) &= 1/8(1+s_1)(1+s_2)(1+s_3).
\end{aligned} \tag{4.23}$$

The partial derivatives of those shape functions are needed for calculations, the full differential rapid grows in complexity for the additional dimension

$$\begin{aligned}
\frac{\partial N_1(s_1,s_2,s_3)}{\partial s_1} &= -1/8(1-s_2)(1-s_3), \quad \frac{\partial N_2(s_1,s_2,s_3)}{\partial s_1} = +1/8(1-s_2)(1-s_3),\\
\frac{\partial N_3(s_1,s_2,s_3)}{\partial s_1} &= -1/8(1+s_2)(1-s_3), \quad \frac{\partial N_4(s_1,s_2,s_3)}{\partial s_1} = +1/8(1+s_2)(1-s_3),\\
\frac{\partial N_5(s_1,s_2,s_3)}{\partial s_1} &= -1/8(1-s_2)(1+s_3), \quad \frac{\partial N_6(s_1,s_2,s_3)}{\partial s_1} = +1/8(1-s_2)(1+s_3),\\
\frac{\partial N_7(s_1,s_2,s_3)}{\partial s_1} &= -1/8(1+s_2)(1+s_3), \quad \frac{\partial N_8(s_1,s_2,s_3)}{\partial s_1} = +1/8(1+s_2)(1+s_3),
\end{aligned} \tag{4.24}$$

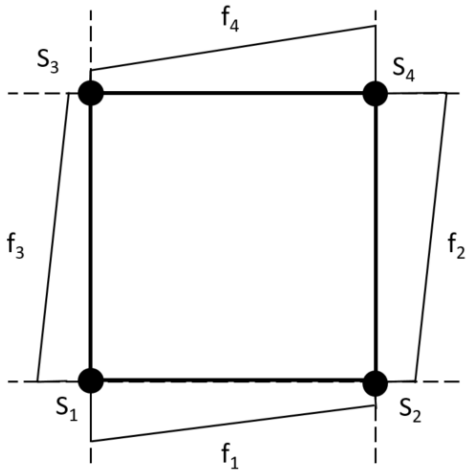


Figure 4.2: Tri-linear shape functions are used during the analysis. A simplified two dimension examples is presented. This shows that a linear line with function f is used to describe every point between adjacent nodes. The tri- referrers to every node having three linear equations, one for each dimension.

$$\begin{aligned}
\frac{\partial N_1(s_1,s_2,s_3)}{\partial s_2} &= -1/8(1-s_1)(1-s_3), & \frac{\partial N_2(s_1,s_2,s_3)}{\partial s_2} &= -1/8(1+s_1)(1-s_3),\\
\frac{\partial N_3(s_1,s_2,s_3)}{\partial s_2} &= +1/8(1-s_1)(1-s_3), & \frac{\partial N_4(s_1,s_2,s_3)}{\partial s_2} &= +1/8(1+s_1)(1-s_3),\\
\frac{\partial N_5(s_1,s_2,s_3)}{\partial s_2} &= -1/8(1-s_1)(1+s_3), & \frac{\partial N_6(s_1,s_2,s_3)}{\partial s_2} &= -1/8(1+s_1)(1+s_3),\\
\frac{\partial N_7(s_1,s_2,s_3)}{\partial s_2} &= +1/8(1-s_1)(1+s_3), & \frac{\partial N_8(s_1,s_2,s_3)}{\partial s_2} &= +1/8(1+s_1)(1+s_3),
\end{aligned} \tag{4.25}$$

$$\begin{aligned}
\frac{\partial N_1(s_1,s_2,s_3)}{\partial s_3} &= -1/8(1-s_1)(1-s_2), & \frac{\partial N_2(s_1,s_2,s_3)}{\partial s_3} &= -1/8(1+s_1)(1-s_2),\\
\frac{\partial N_3(s_1,s_2,s_3)}{\partial s_3} &= -1/8(1-s_1)(1+s_2), & \frac{\partial N_4(s_1,s_2,s_3)}{\partial s_3} &= -1/8(1+s_1)(1+s_2),\\
\frac{\partial N_5(s_1,s_2,s_3)}{\partial s_3} &= +1/8(1-s_1)(1-s_2), & \frac{\partial N_6(s_1,s_2,s_3)}{\partial s_3} &= +1/8(1+s_1)(1-s_2),\\
\frac{\partial N_7(s_1,s_2,s_3)}{\partial s_3} &= +1/8(1-s_1)(1+s_2), & \frac{\partial N_8(s_1,s_2,s_3)}{\partial s_3} &= +1/8(1+s_1)(1+s_2).
\end{aligned} \tag{4.26}$$

Having calculated the differential of the shape functions, we can start to construct

the Jacobian matrix. The Jacobian matrix is responsible for being the transformation key between the calculations carried out in parent space and the actual element in the model located in mapped space. The 3 x 3 Jacobian matrix is constructed via the following summation

$$J_{ij} = \sum_{a=1}^{UEL} \frac{\partial N_a}{\partial s_j} X_i^a, \tag{4.27}$$

which in its full form results in

$$\begin{aligned}
J(1,1) &= \sum_{a=1}^{UEL} \frac{\partial N_a}{\partial s_1} X^a, \quad J(1,2) = \sum_{a=1}^{UEL} \frac{\partial N_a}{\partial s_2} X^a, \quad J(1,3) = \sum_{a=1}^{UEL} \frac{\partial N_a}{\partial s_3} X^a, \\
J(2,1) &= \sum_{a=1}^{UEL} \frac{\partial N_a}{\partial s_1} Y^a, \quad J(2,2) = \sum_{a=1}^{UEL} \frac{\partial N_a}{\partial s_2} Y^a, \quad J(2,3) = \sum_{a=1}^{UEL} \frac{\partial N_a}{\partial s_3} Y^a, \\
J(3,1) &= \sum_{a=1}^{UEL} \frac{\partial N_a}{\partial s_1} Z^a, \quad J(3,2) = \sum_{a=1}^{UEL} \frac{\partial N_a}{\partial s_2} Z^a, \quad J(3,3) = \sum_{a=1}^{UEL} \frac{\partial N_a}{\partial s_3} Z^a,
\end{aligned} \tag{4.28}$$

where $UEL = 8$ as there are 8 Gaussian integration points in the element. The Jacobian is then numerically inverted by a further sub-routine written for the third dimension. Finally, the hydrostatic stress, S, is needed. This is calculated in parent-space by analogous means to the Jacobian just calculated.

$$\frac{dS}{ds_i} = \sum_{a=1}^{UEL} \frac{\partial N_a}{\partial s_i} \times S, \tag{4.29}$$

$$\frac{dS}{ds_1} = \sum_{a=1}^{UEL} \frac{\partial N_a}{\partial s_1} \times S, \quad \frac{dS}{ds_2} = \sum_{a=1}^{UEL} \frac{\partial N_a}{\partial s_2} \times S, \quad \frac{dS}{ds_3} = \sum_{a=1}^{UEL} \frac{\partial N_a}{\partial s_3} \times S. \tag{4.30}$$

A cross product of the hydrostatic stress vector in parent-space and the mapping Jacobian will allow the gradient of hydrostatic stress to be mapped element on to the element in the model

$$\begin{bmatrix} \sigma_{s,1} & \sigma_{s,2} & \sigma_{s,3} \end{bmatrix} \cdot \begin{bmatrix} J_{1,1} & J_{1,2} & J_{1,3} \\ J_{2,1} & J_{2,2} & J_{2,3} \\ J_{3,1} & J_{3,2} & J_{3,3} \end{bmatrix} = \sum_{a=1}^{3} \begin{bmatrix} \sigma_{s,i} J_{1,i} & \sigma_{s,i} J_{2,i} & \sigma_{s,i} J_{3,i} \end{bmatrix} \tag{4.31}$$

This results in the mapped stress gradient in 3-dimensions. This along with the hydrostatic stress is stored in the state variables to be read-in by the UMATHT sub-routine. In addition to this series of changes, the common-block, UHARD and UMATHT sub-routines need additional trivial changes added.

4.5 Summary

Over this chapter, the theory surrounding a coupled hydrogen transport subroutine was outlined, and the development undertaken in this thesis explored. In this thesis, the UMATHT subroutine will be used to determine the mechanical properties after hydrogen charging, and estimate the hydrogen concentration present in the sample. It is hoped that with a well calibrated model, it will be possible to better predict PWR component life-times with the detrimental effects of hydrogen.

Chapter 5

Preliminary Characterisation

5.1 Materials Microstructure

5.1.1 Chemical Composition

The chemical composition of the materials used was provided by EDF, and verified by EDX on a Zeiss Evo SEM. Point analysis was conducted at five randomly selected regions across the sample, the averaged results are displayed in Table 5.1. There is good agreement between the recorded compositions, and the supplier's reference across the major alloying elements. The sensitivity of the equipment limits the detection of some minor alloying elements, any element less than 0.1 weight% are not detectable. The enhanced aluminium signal is due to Al sample holder.

5.1.2 Grain Statistics

Grain characteristics were investigated using EBSD, completed on a Zeiss Evo SEM with a 20kV accelerating voltage and a 5nA probe current. Firstly, the inverse pole figures (IPF), displayed in Figure 5.1, show the crystallographic orientation normal to the sample surface. There is no obvious texture in the samples, with the exception of A182. This sample is taken from a weld and, as expected, there is a high level of texture in the material due to the directional flow of the metal during welding. It is also clear that there is twinning in the majority of the materials, some such as A800 and A690 exhibit extensive twinning, while others, such as

Table 5.1: The chemical compositions of alloys tested. A comparison between the experimentally determined EDX composition to the supplier provided composition.

Material	Ni	Fe	Cr	C	N	Mn	Al	Ti	P	Cu	Mo	Si	Nb
SS316	11.5	66.4	18.4	-	-	2.1	0.1	-	-		2.7	0.4	-
ref [287]	12.0	65.8	17.3	0.03	0.05	1.81	-	-	0.03	0.02	2.6	0.42	-
A800	31.9	45.2	21.1	-	-	0.9	0.2	0.2	-	-	-	0.2	-
ref [287]	32.7	45.4	20.0	0.07	0.02	0.76	0.24	0.25	0.01	0.20	-	0.27	-
A690	60.7	8.5	29.9	-	-	0.1	0.4	0.2	-	-	-	0.3	-
ref [287]	61.7	6.8	28.6	0.02	-	0.2	<0.5	<0.5	<0.02	0.01	-	0.3	-
A182	67.3	7.2	15.5	-	-	6.6	0.1	-	0.1	-	-	0.4	2.0
ref [287]	69.2	6.9	15.0	0.03	0.03	6.2	<0.07	0.05	<0.02	<0.05	-	0.35	2.0
A600	72.4	8.9	16.7	-	-	0.8	0.2	0.2	-	-	-	0.5	-
ref [287]	73.2	8.8	16.1	0.06	-	0.81	0.15	0.15	0.01	0.02	-	0.45	-

A182 display little to none. This microstructural difference is thought to be linked to the annealing process during manufacture.

Grain size statistics are summarised in Table 5.2. These values are generated by Oxford Instruments' software *Tango Maps*, which used the mean lineal intercept (MLI) method. Twins were excluded from grain size analysis. The average grain size peaks at A800, i.e. 104 μm, and decreases as the nickel content changes. The minimum grain size belongs to A600 samples, i.e. 36 μm. The remaining alloys possess an intermediate grain size close to 80 μm. Cold-working in A600 appears to decrease the average grain size by 50%. This is likely due to the injection of dislocations which re-distribute, and form addition grain boundaries and sub-structures. These values fall within an accepted range in literature, for Steels a series of grain sizes has been reported by [121, 121], and for Ni alloys by [288, 227, 36, 17, 289].

Hall and Petch demonstrated that the yield stress σ (and hence the hardness) scales with the inverse square root of grain size, d, in poly-crystalline materials according to the following relation:$\sigma=\sigma_0+\mathrm{kd}^{1/2}$, where k is a measure of the local stress needed to initiate plastic flow at a grain boundary and σ_0 is the resistance to dislocation motion in the grain interior. Some people might argue that the CGR observed for all the alloys are not comparable because of the different grain size. If the grain size dominated or had a big effect on the CGR (i.e. by controlling

the yield-stress), you would expect the opposite of what you see in Table 5.2. The grain size of these materials has been investigated by Arioka et al [62], the presented results fall with in the size size ranges presented here giving confidence to the results, given some materials are from the same supplier.

5.1.3 CSL Boundary Types

Figure 5.2 shows the CSL, random and low angle (LAB) grain boundary types superimposed on top of the pattern quality maps. All boundaries with a $\Sigma < 29$ were considered, but only boundaries with a $\Sigma 3^n$ were readily observed across the samples. The other CSL boundaries ($\Sigma 7$, $\Sigma 11$, $\Sigma 13$ and $\Sigma 19$) had a boundary fraction <1%, are not included in the illustrations. The preference towards $\Sigma 3^n$ boundaries is inline with other published works on austenitic Ni-Fe-Cr alloys [181].

Figure 5.3 shows a complete boundary characterisation of the tested alloys. Figure 5.3a shows the density of boundaries in the material. There is a negative correlation between the average grain size and the density of grain boundaries; A600CW has the highest density of grain boundaries, and A800 has the lowest. The slope of the experimental curve is equal to -0.45, which is a value close to the slope of the Hall–Petch [290].

Figures 5.3b - 5.3d compare the fractional boundary length of low angle (LAB), random and CSL boundaries. The fraction of LABs is consistent across the materials (excluding welds) at <10%, this is due to the similar composition, thermal treatments and average grain size. The majority of boundaries can be categorised

Table 5.2: Summarises the average grain size of the tested alloys. The grain size increases as the Ni-content approaches 40% from either direction.

Material	Number Tested	Average Grain Size (μm)
SS316	475	79 ± 54
A800	321	104 ± 196
A690	701	88 ±62
A600	8931	36 ±25
A600 CW	248	16 ±20
A182	560	60 ±103

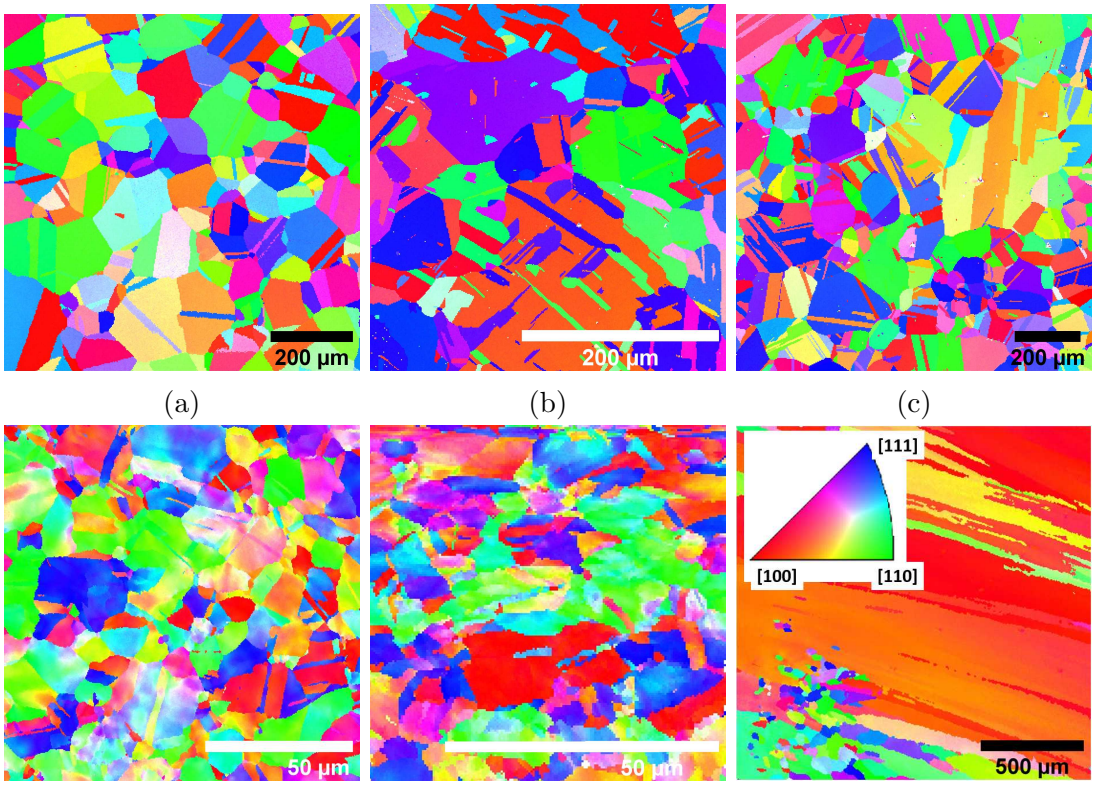


Figure 5.1: Normal inverse pole figures collected from each alloy by EBSD. The figures show (a) SS316L, (b)A800, (c) A690, (d) A600, (e) A600CW and (f) A182+IPFZ key. Tango maps was used to analyse these maps to determine the average grain size and grain boundary fractions. All scale bars (expect for A600 and A600 CW) denote 200μm to allow comparison given the changes in magnification between the maps.

as either CSL or random, because of this, there is an inverse correlation between these boundary types. The results indicate that larger grains promote the formation of CSL boundaries. This is because the larger distance between boundaries better facilitates the lattice rotation needed to form CSL boundaries. Analysis indicates that A800 and A600 possess the highest/lowest fraction of CSL boundaries (86 vs. 40%), and random boundaries (12 vs. 52%).

Cold-working appears to increase the fraction of random and LAB boundaries. This suggests that the CW process disrupts the established CSL boundaries, and through the injection of dislocations, creates new sub-optimum boundaries. This

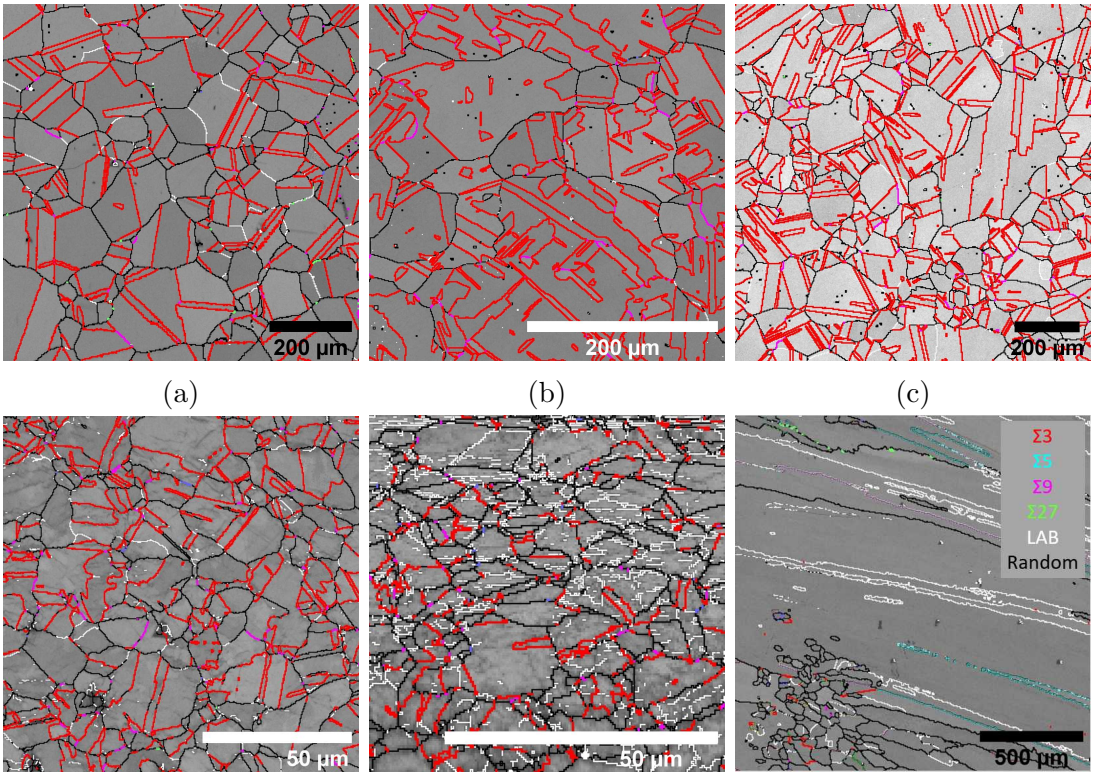


Figure 5.2: The band contrast of the EBSD scan is shown with the boundary information overlaid. The figures show (a) SS316L, (b)A800, (c) A690, (d) A600, (e) A600CW and (f) A182+ key. Σ3 is shown in red, Σ9 in green, Σ27 in blue. Low angle boundaries are highlighted in white and random boundaries are black.

redistribution of boundaries weakens the corrosion resistance. A182 is an anomaly in these results. It is from a weld, and has a low fraction of CSL boundaries. This arises from the fast cooling process which locks in dislocations and results in a majority LAB and random boundary material.

5.1.4 Inclusions

Some of the tested alloys have inclusions throughout the lattice, these are erroneously introduced during the manufacture or heat treatment process. They are important to characterise as they show the segregation of important minor alloying elements. EDX maps were conducted using a Zeiss Evo SEM, the beam was left

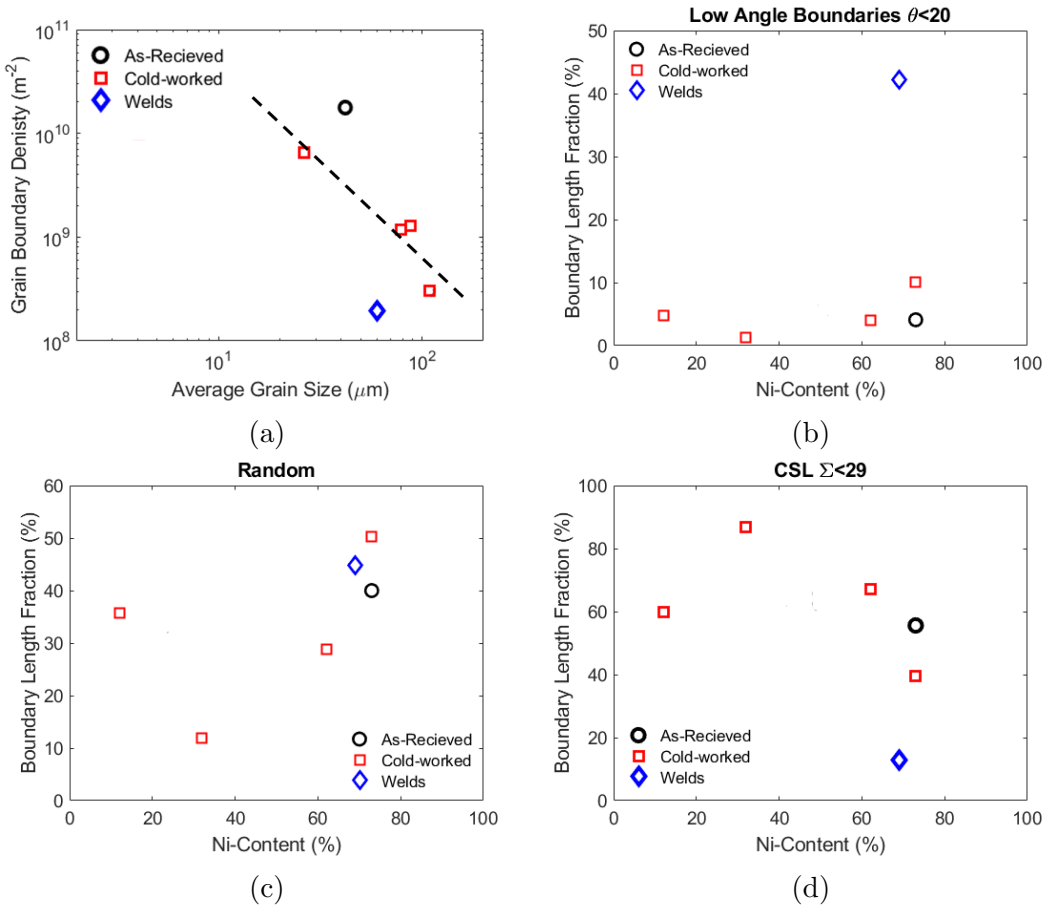
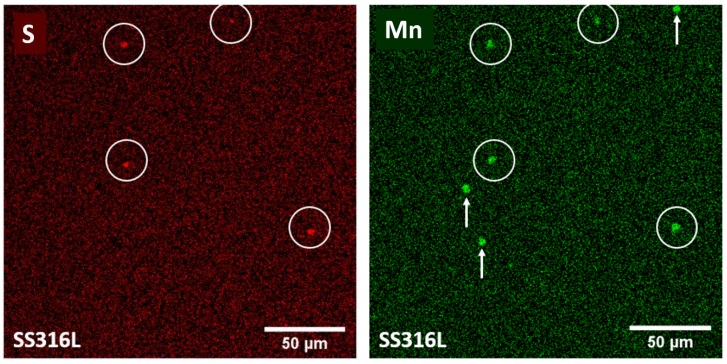


Figure 5.3: Comparing the fraction of grain boundary categories across the different materials tested. (a) is the number of low angle boundaries, (b) the number of random boundaries, (c) the number of CSL boundaries and (d) the density of grain boundaries present in the material as a function of the grain size.

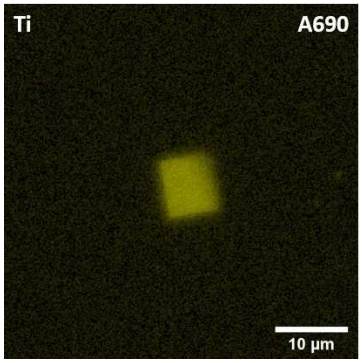
to raster the selected areas for 10 minutes. Figure 5.6 a & b shows what is likely to be MnS inclusions in chromium-depleted regions of SS316L. These particles are typically 3 - 4 μm in diameter, and do not correlate to the boundary regions. Particles are automatically identified as MoO by commercial EDX software. However, given that MnS regularly forms in steels and the Mo and S peaks overlap, it is highly likely that MoO is a miss-identification and the true identification is MnS.

Figure 5.6c shows a large cubic inclusion of Ti found in A690. Due to the 10 μm size and its faceted shape, these inclusions are likely linked to insufficient temperatures during the arc-melting process. As the Ti has not been able to



(a) (b)

Figure 5.4: EDX chemical analysis of SS316L, showing the localised enrichment of (a) Mn and (b) S in particle form. Region of interest are highlighted.

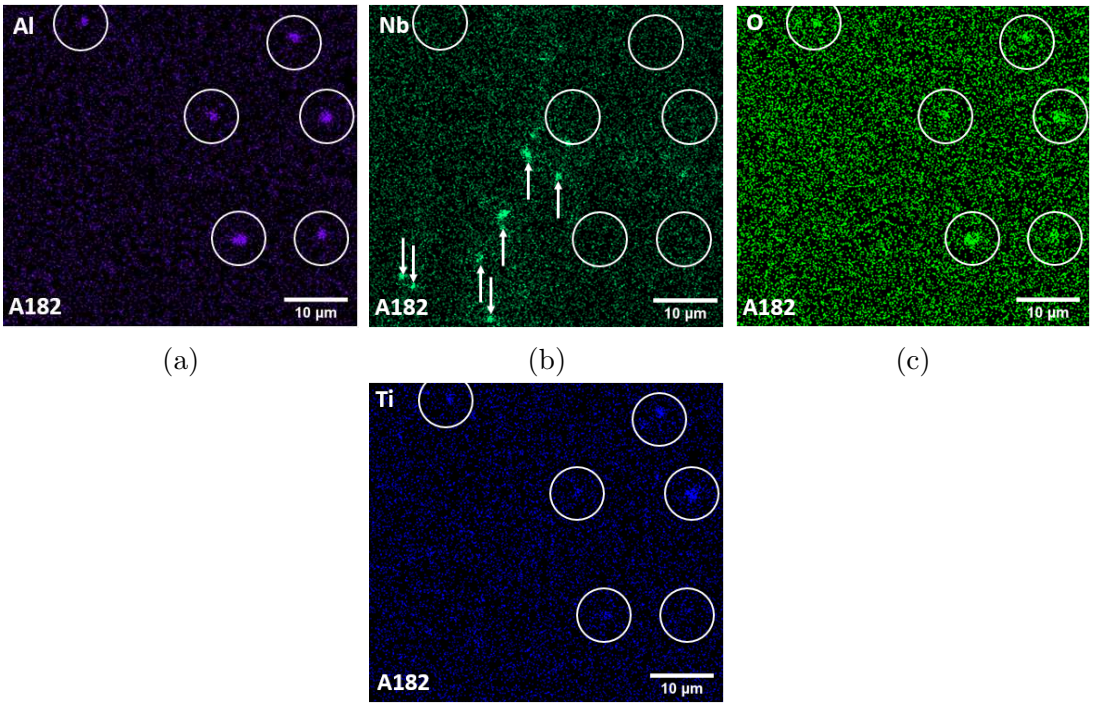


(a)

Figure 5.5: EDX chemical analysis of a Ti particle in A690.

disperse throughout the matrix, however is Ti is an impurity, it does not play a consequential role in the alloy thermal stability.

Figures 5.6 d – g show Nb, Ti and Al oxide inclusions. All the detected inclusions are <5 μm in diameter. It is clear that the Al and Ti oxides share common sites, this is highlighted by the circling. The Nb inclusions are separate, they do no correlate with any other element. The remaining materials (A800, A600 and A600CW) were found to have a uniform distribution of the alloying elements throughout the matrixAs the inclusion are part of the factory alloy, the testing shall not discriminate against these inclusion and shall actively form part of the testing and discussion.



(a) (b) (c)

(d)

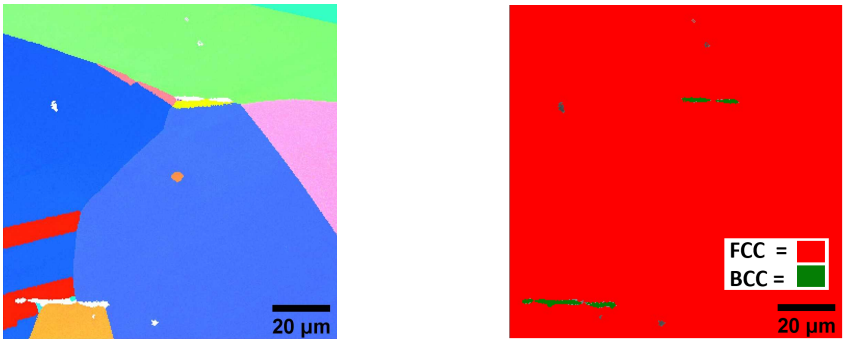
Figure 5.6: EDX chemical analysis of and A182, showing regions of (a) Al, (b) Nb, (c) O and (d) Ti. Region of interest are highlighted.

5.1.5 Phase Transformations

Figure 5.7 shows that SS316L has a small amount of a secondary B.C.C phase. It is suggested that this is delta phase, as in the steel phase diagram, delta stable at the higher temperatures and pressures used to make austenitic steels. EBSD has confirmed that the new phases are localised to a few grain boundaries in the material and should be avoided during mechanical testing.

5.1.6 Carbides Analysis

Nano-scale resolution of intergranular carbides was achieved using a back scatter detector (BSD) on a Zeiss Merlin SEM. The BSD was used as the lower mass of the carbides would make them clearly stand out on the surrounding matrix. A range of grain boundaries were imaged at ten random locations on the material surface, this was to minimise bias due to the preferential carbide precipitation that



(a) (b)

Figure 5.7: EBSD collected (a) IPFZ map and (b) phase map of SS316L after polishing (red=austenitic, green=ferritic). It is clear that there are unidentified regions in the IPF, thought to be delta-phase SS.

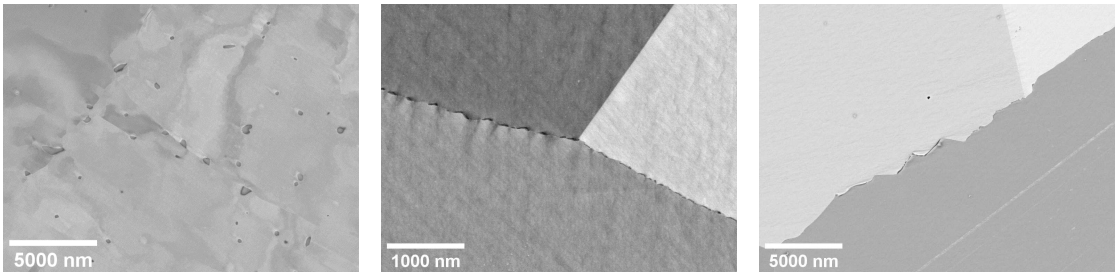
exists in some of the studied alloys.

ImageJ was used to analyse the images. Moreover, a trainable image segmentation tool was used [291]. This tool utilises machine learning algorithms to decompose the image, and return a probability map of an object being a carbide. A threshold was applied to the probability image. The threshold was set to a 90%-certainly, to ensure the results were reliable. The binary image was then analysed using a particle analyser to determine the average size of the carbides. The benefit of this method is that once trained, the image segmentation tool could be applied to multiple images rapidly. The length of the grain boundaries was calculated in a similar way. The carbide coverage is defined as the ratio of the total linear carbide length along the boundary, to the total boundary length.

No trace of carbides was found along the grain boundaries of SS316L and A182 alloys at 30,000x magnification. Very fine (<100 nm) continuous carbides were observed along the coherent grain boundaries of A800. Extensive carbide coverage was also found in A600, A600CW and A690. The sizes of carbides ranged from 100 - 1000 nm. A690 had a high fraction of large carbides, this is due to the higher Cr content of this alloy. Measured carbide coverage is reported in Table 5.3, and examples of carbides are visible in Figure 5.8. A600 and A600 CW also had a number of intragranular carbides, as seen in Figure 5.8a. These were typically smaller than the intergranular carbides. Intragranular carbides do not increase SCC resistance, so they are not characterised in this study.

Table 5.3: Carbide analysis of the materials with intergranular carbides.

Material	No. Analysed	Mean length ± StD (nm)	Coverage (%)
A600	397	600±50	20±5
A600CW	346	350±100	10±2
A800	128	200±100	80±10
A690	154	2000±1000	40±5



(a) (b) (c)

Figure 5.8: Examples of the carbides in the microstructure of (a) A600, (b) A800 and (c) A690.

Arioka et al [62] presented a comprehensive characterisation of these alloys, it was reported that the measured carbide coverage in A690 was 52.5%, no trace of carbide precipitation was not identified in Type 316 by 20,000X magnification and Alloy 800 in the solution-annealed condition displaced a very fine carbide precipitation. The size of carbide precipitate in A800 was very fine, usually less than 100 nm the precipitation in TT690 and MA600 was around 10 times larger. Shen et al [19] noticed a higher carbide coverage of 30% unlike the 10% reported in this work. This is thought to be due to differences in heat treatments. Zhai et al [22] noted for A690 from two different providers displayed different carbide precipitation, in one sample carbide precipitation was limited to a few isolated GBs in a mill annealed bar, while the other heat-treated samples exhibited a semi-continuous GB carbide coverage. The sample of the carbides ranges from 500 -2000 nm. This largely agrees with the very large carbides presented for A690.

5.1.7 Background Dislocation Density

Some of the alloys studied have have been cold-worked, increasing the number of dislocations in the material lattice. Increased dislocation content does not only affect the mechanical properties, such as yield stress, but also changes the apparent diffusion characteristics of a material. Therefore, it is important to characterise the dislocation distribution across the alloys. High resolution EBSD (HR-EBSD) was completed using an electron back-scattered patterns (EBSP) of 800x600 pxl. The SEM conditions were 20 kV accelerating voltage and a 5 nA beam current. All the maps were collected using a 125 nm step size.

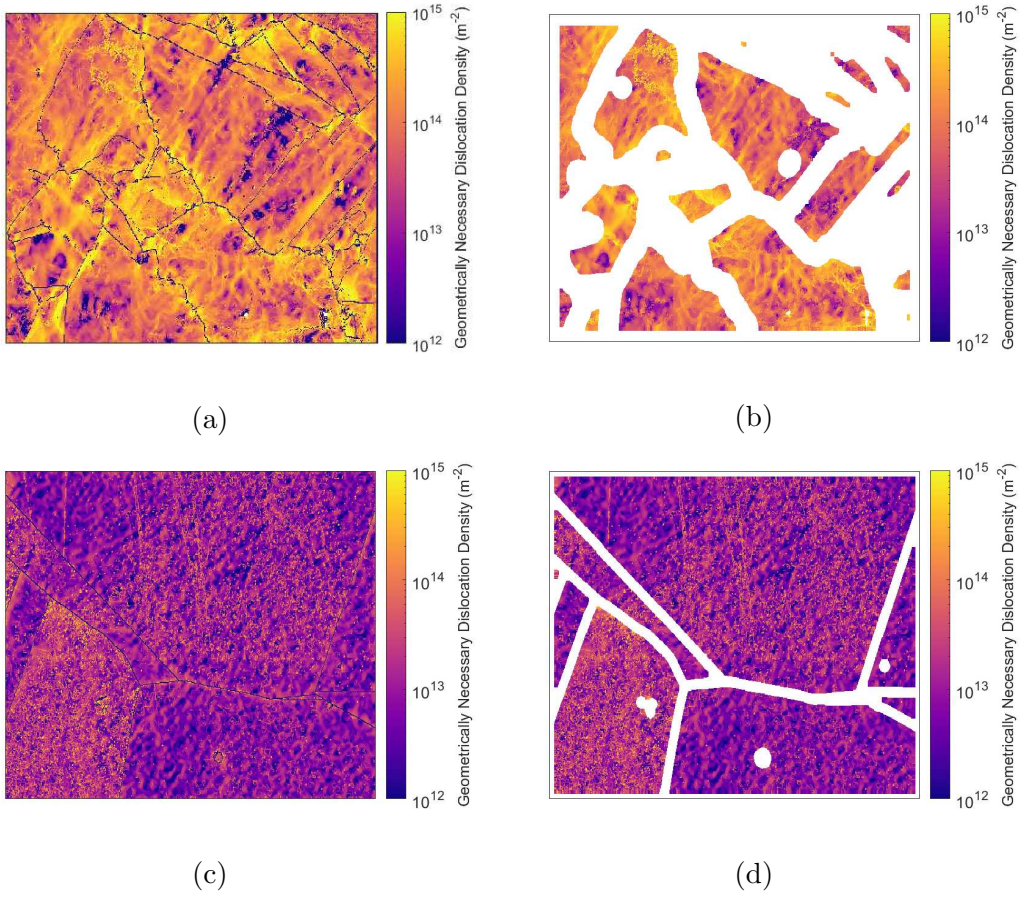


Figure 5.9: Examples of the calculated geometrically necessary dislocations in the microstructure of (a&b) A600 and (c&d) SS316L with and without the boundaries excluded.

A total geometrically necessary dislocation (GND) density is estimated from the Kernal average misorientation [292]. It is known that grain boundaries are regions of higher dislocation density. More representative bulk values were determined by excluding the data points within 2 μm of a grain boundary. A boundary is classified as a misorientation angle between neighbouring data points $\geq$10°. This value was chosen to include dislocations pile-ups. The resulting GND maps are shown in Figure 5.9.

Figure 5.10 summarises the mean calculated GND density in the tested materials. The error bars represent the inter-quartile range of the measured GND information, this was chosen to show any skew in the recorded densities. The small grain materials, A600 and A600 15%CW, have the greatest number of dislocations, approximately $1.2\pm0.2\times10^{15}$ m^{-2}. Large grain materials have a lower GND density, approximately $1.0\pm0.1\times10^{14}$ m^{-2}. The cold-working process injects additional dislocations to the alloy, what is surprising is that the GND density in both cold-worked and as-received alloys are the same, within error. This is thought to be due to a combination of effects. A significant number of GNDs are adsorbed by boundaries, which are excluded in this analysis. The calculated number of GNDs is a function of step-size, which means it is possible to under/over-report all dislocation densities using this technique. Finally, the sample of A600 came

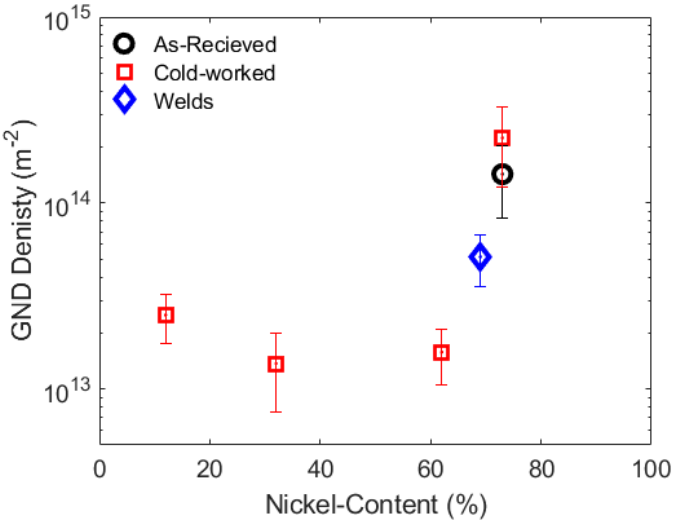


Figure 5.10: The calculated GND density against the nickel content.

from an in service component, so it may have picked up cold-work from subsequent installation and preparation.

Calculating the lattice curvature from the local misorinetation, instead of cross-correlation techniques, is a less computationally demanding method of estimating the GND density. Furthermore, this techniques is also a necessity, since the cross-correlation method doesn't work well on some cold-worked materials (i.e. 30%CW A690). As a consequence, this misorinetation based technique has an absolute resolution of 10^{12} dislocations/m^2. While, this is approximately ten-times greater than cross-correlation [281], it is more than adequate for this application.

5.1.8 Summary

The microstructural properties of austenitic nickel alloys have been characterised using predominantly SEM-based microscopy techniques. The results are summarised in Table 5.4 and will be referenced in later chapters.

5.2 Oxidation Characterisation

The protective oxide layers of austenitic alloys influence the hydrogen adsorption process under PWR conditions. For the SS316L, A800, A690 and A600 CW sample tested, the following analysis was completed: the surface morphology was determined by SEM imaging, the oxide thickness and chemical composition was determined by TEM-EDX line-scans, and the porosity was determined by Fresnel imaging. The sample preparation, analysis and findings are my own work, but

Table 5.4: Summary of the microstructural properties of the investigated austenitic alloys.

Materials	Grain Size (μm)	Boundary Density (m^{-2})	CSL Boundary Fraction	Random Boundary Fraction	GND Density (m^{-2})	Carbide Coverage (%)
SS136L	79±54	1.2x10^9	0.57	0.35	2.5±0.7x10^{13}	N/A
A800	104±196	3.1x10^8	0.86	0.12	1.4±0.6x10^{13}	80±10
A690	88±62	1.3x10^9	0.67	0.29	1.6±0.5x10^{13}	40±5
A600	36 ±25	1.7x10^{10}	0.55	0.40	1.4±0.6x10^{14}	20±5
A600CW	16±20	7.4x10^9	0.36	0.50	2.2±1.0x10^{14}	10±2
A182	60±103	2.0x10^8	0.13	0.44	5.3±1.6x10^{13}	N/A

the operation of the Jeol 2100 TEM was completed by Dr Guanze He. The next section is dedicate to presenting and discussing these findings.

5.2.1 Surface Morphology

Figure 5.11 shows an SEM analysis of the surface morphology of the oxide films. The SS316L specimen (Figure 5.11a) has a continuous distribution of highly faceted oxide particles across the surface. The sub-surface layer consists faceted polyherdal oxides, which are densely packed and generally smaller particles 300 ± 200 nm (n=145) with a 100% coverage. The surface layer contains much larger oxide particles, ranging up to 5 μm, but with a very low $\leq$5% surface coverage.

A800 displays a semi-continuous distribution of faceted spherical-like surface oxide particles (Figure 5.11b). The average particle size was found to be 700 ± 500 nm (n=165), and a high 50% coverage was found. The coverage of the surface oxide was found to be highly dependant on the grain orientation, on non-preferential grain orientation the coverage drops to $\leq$10%. The sub-surface layer of the outer oxide consists of much smaller particles, closely resembling those found in SS316L. The size of these was approximately 200 ± 100 nm, and the coverage was much lower, 40%. Due to the lower density the surface can be seen through the gaps in the outer-oxide.

The oxide morphology on A600 (Figure 5.11c), differs significantly from the other alloys. The surface has a low coverage, approximately 20%, of large discrete oxide particles. These large particles are located above grain boundaries. The mean size of these oxide particles was found to be 1900 ± 500 nm (n=122). The inner-grain oxide is much more homogeneous and taken on a pebble-like shape. It was not possible to examine the surface morphology of A690, as the sample is currently trapped in the NanoSIMS at the University of Oxford.

5.2.2 Oxidation Chemistry and Development

5.2.2.1 Post-Autoclave SS316L

Figure 5.12a shows the cross-sectional morphology of the oxide, which largely agrees with SEM observations. There are large faceted outer-oxide particles visible, but the cross-section has also revealed an inner-oxide layer which is composed of

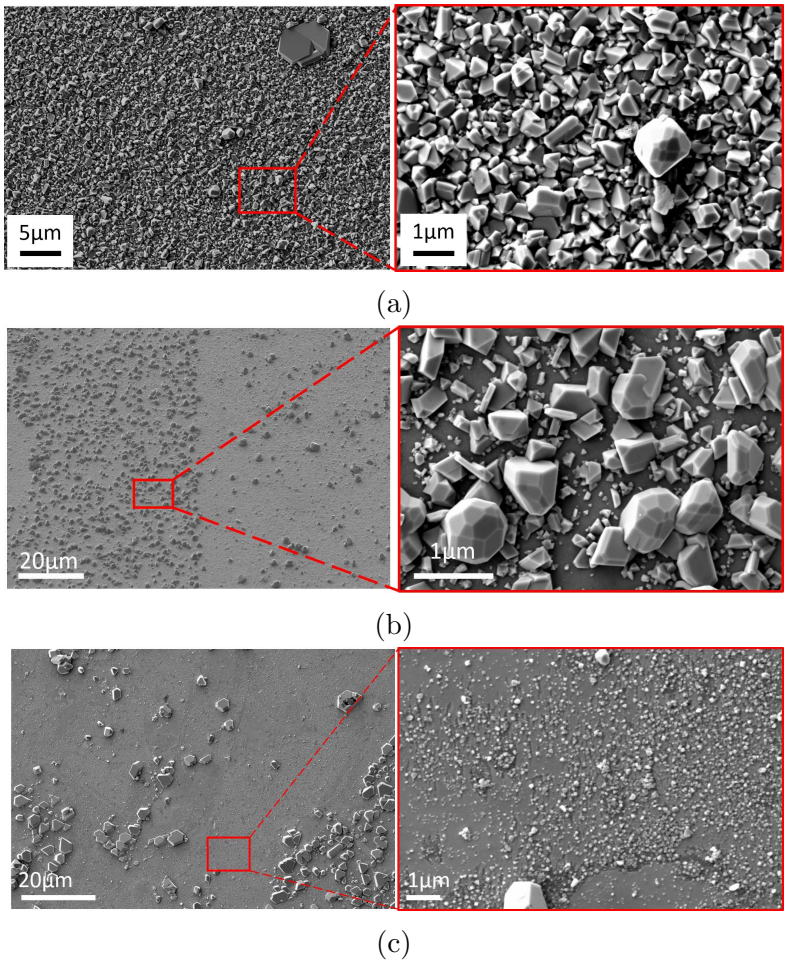
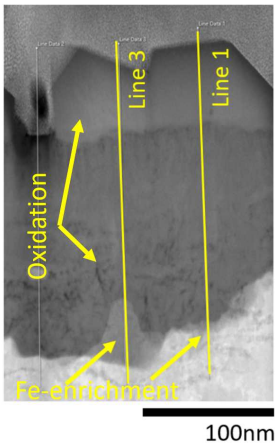


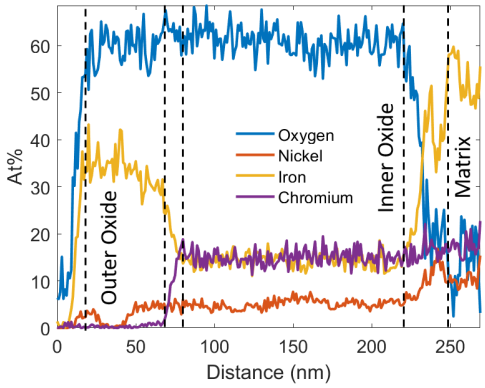
Figure 5.11: (a) Surface morphology of SS316L at 1000 times magnification and 10,000 times magnification. (b) Surface morphology of A800 at 250 times magnification and 15,000 times magnification. (c) Surface morphology of A600 at 250 times magnification and 15,000 times magnification.

dense and fine grain oxide. The thickness of the inner oxide layer was determined to be 140 ± 20 nm. It is clear to see from the image that the inner oxide is homogeneous, as there are brighter and darker areas that are labelled.

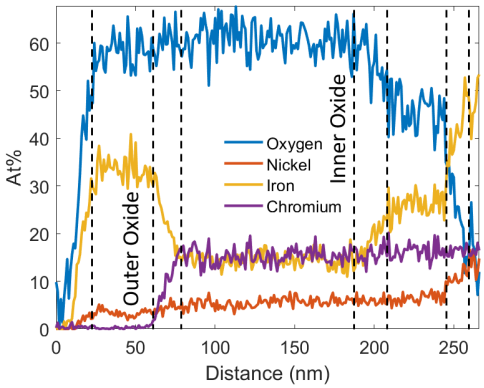
Figure 5.12 b & c show the elemental line profiles across the highlighted regions. The outer-oxide is enriched in iron, but depleted in chromium with respect to the inner-oxide. The outer-oxide comprises 35 ± 5% iron, 60 ± 5% oxygen and balance nickel. It has a typical thickness of 55 ± 20 nm. The chromium concentration in the inner-oxide is equivalent to that in the matrix, the other elemental concentrations



(a)



(b)



(c)

Figure 5.12: (a) TEM HADAF image of the oxide of SS316L (from top to bottom) are platinum protective layer, large outer-oxide particles, continuous inner-oxide and matrix. (b-c) EDX spectra of different locations of the oxide, (c) = Line 1, (d) = Line 3.

increase as you return to the matrix. The lighter regions in, and along the inner-oxide metal interface, are regions of iron enrichment (Figure 5.12c), in contrast the dark regions indicate iron depletion.

This material has been studied extensively in literature, here I summarise the common findings. Chen et al [293] investigated the oxide film formation of SS316L after exposure to deaerated PWR primary water at 310 °C for 1127 hours. EDS line scans show a binary oxide. The thickness of the inner oxide 143 ± 90 nm, and comprises a compact oxide film. The out oxide layer was composed of large

outer oxide grains and is enriched in Fe, and depleted in Cr with respect to the matrix. The Cr content in the outer oxide was similar to that of the matrix, and the Fe was lower than the matrix. Unlike in the results presented in this thesis diffraction pattern analysis indicates that the outer oxide particles had a spinel-type crystal structure, likely in the form of (Ni, Fe)Fe_2O_4, consistent with Raman spectroscopy results obtained from the same sample. Finally, it was noted that the outer oxide particle layer revealed that the atomic ratio of Fe/Cr/Ni was approximately 87.44: 1.50: 11.06 for particle A and 96.61: 0.76: 2.63 for particle B. The atomic percentage values of Fe, Cr, and Ni were non-stoichiometric according to TEM-EDS analysis.

Similar results are presented other authors [294, 295, 296]. Terachi et al [294] analysed a solution-treated CERT sample that was exposed to a simulated PWR primary water chemistries of the middle of the fuel cycle for approximately 500 hours. A bi-layered oxide was formed; the outer layer was composed mainly of iron oxide, while there was relatively chromium-rich fine grained inner layer. In addition, nickel enrichment was observed at the oxide/metal interface, at up to 70 nm in depth. Nickel is enriched in a matrix by more than twice its bulk concentration. Like Chen et al [293], EDS indicated that the outer oxide is composed of an iron-rich oxide with a spinel structure. And, it is concluded that the outer layer is composed mainly of Fe_3O_4, unlike Chen et al [293] who also list $NiFe_2O_4$ as an oxide product.

Han et al [296] published paper largely agrees with the observations mentioned above for SS316L exposed to simulated PWR conditions. Some additional observations are mentioned for the samples investigated after 500 hours of exposure. The oxide particles of the outer oxide were inhomogeneous, whereby large oxide particles were dispersed on the surface and the small oxide particles were observed in the sub-surface layer. The thickness of the spinel inner layer oxide film determined by TEM was about 450 $\pm$ 100 nm. Furthermore, dark areas (granular areas) of the inner oxide film were identified; they exhibited weaker Fe and Ni signals when compared with the non-granular areas. EDS characterised them with a low average atomic number indicating that the signal intensities of elements Fe and Ni in the dark areas were lower than that of the surrounding areas.

However, it is worth noting that as outlined by Was et al. [295] comparing oxidation on different grains should be conducted with great cautions, as he demonstrated that oxide thickness varied across different grain orientations in SS316 samples after exposure to BWR conditions.

5.2.2.2 Post-Autoclave A800

Figure 5.13a shows the cross-sectional morphology of the oxide layer on A800. The regions which were tested are highlighted by yellow lines, the direction of the scan is highlighted by the arrow-head. The location, from which this sample was taken from, was devoid of large outer-oxide particles. This is observed across other regions of the sample. In contrast to the SEM analysis, the cross-section has revealed an inner-oxide layer. The thickness of this inner-oxide layer varies

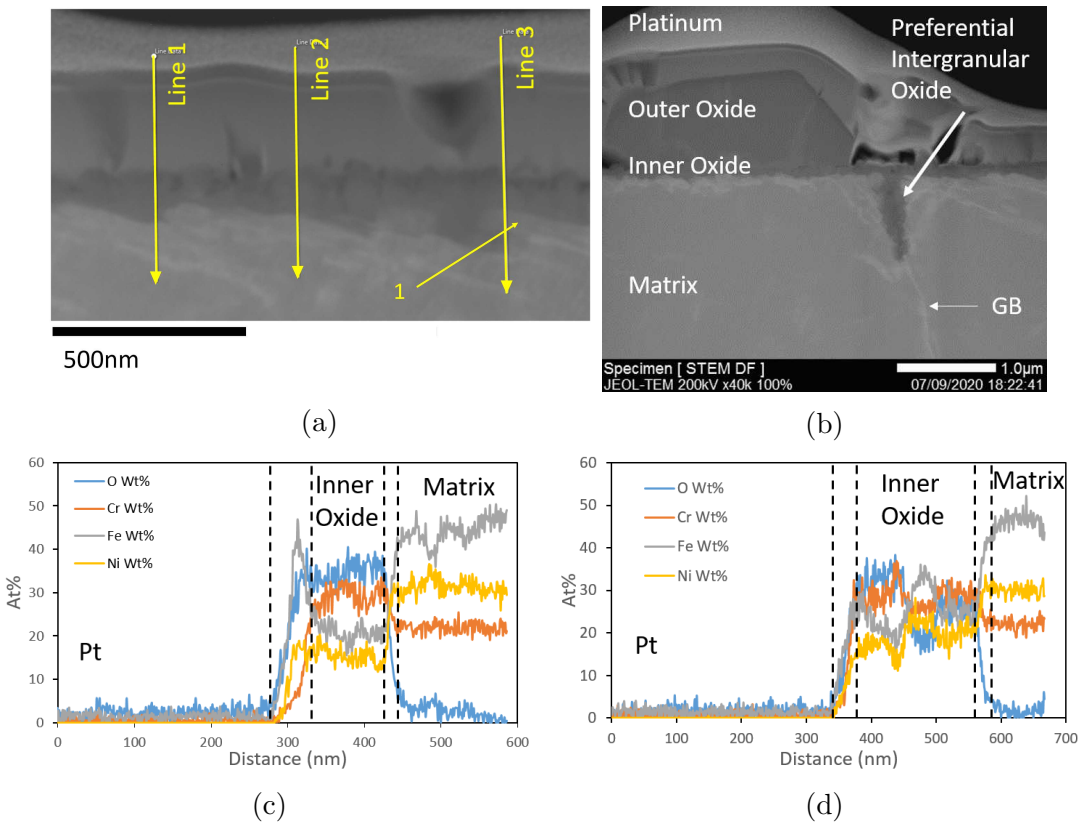


Figure 5.13: (ab) TEM HADAF image of the oxide in A800 (c-d) EDX spectra of different locations of the oxide. (c) = Line 1, and (d) = Line 3.

due to the inhomogeneities in the oxide. The average value recorded is 120 ± 40 nm, but this can range up to 200 nm. The varying thickness is due to preferential oxidation along certain directions, based on residual slip bands from the cold-work process (example label 1). The inner-oxide has equal concentrations of iron and nickel, and is rich in chromium. There is a high carbon signal from contamination from the TEM column.

Figure 5.13 b-d show the line scans from the highlighted regions. Despite there being no obvious outer-oxide particles in the bright field images, we still observe them in the EDX profiling. This is seen by the spikes in iron and delayed chromium concentration observed in Figures 5.13 b & c at approximately 300 nm. The outer-oxide is iron rich and chromium depleted compared to the inner-oxide. It is estimated that this iron-rich outer oxide is no more that 50 nm in thickness, and as seen in the EDX profiles, is highly inhomogeneous across the surface layer.

A800 has been less studied in literautre, however, it was noted by Choudhry et al [288] that the oxidation behaviour of A800 after exposure to oxygenated PWR water at 650 °C showed an outer oxide layer composition was a mixture of magnetite and hematite, and a very fine Fe-enriched (Fe_3O_4) layer with a small amount of dissolved Mn was observed in between the outer layer and the Cr-rich $(Cr,Fe)_2O_3$ innermost layer with small amount of dissolved Ni. Ni enrichment was observed below the oxide layers due to its low affinity for O to diffuse.

5.2.2.3 Post-Autoclave A690

Figure 5.14a shows the cross-sectional morphology of a large section of surface oxide. A duplex oxide structure formed. The outer-oxide particles are fine separate crystals of 30 - 50 nm in size that are inhomogeneously distributed across the surface. The inner-oxide is approximately 250 nm thick, continuous, and compact. This is attributed to the increased Cr content of A690. There is no observed intergranular oxidation along the grain boundaries.

Figure 5.14 b & c show the elemental line profiles along lines 2 and 4 respectively. It is observed that the outer-oxide is enriched in iron and nickel, and chromium depleted with respect to the inner-oxide. The outer oxide comprises 15 ± 3 wt% iron, 40 ± 5 wt% oxygen, 15 ± 3 wt% nickel and balance other impurity elements. Due to the high availability of chromium in the lattice, it is likely that

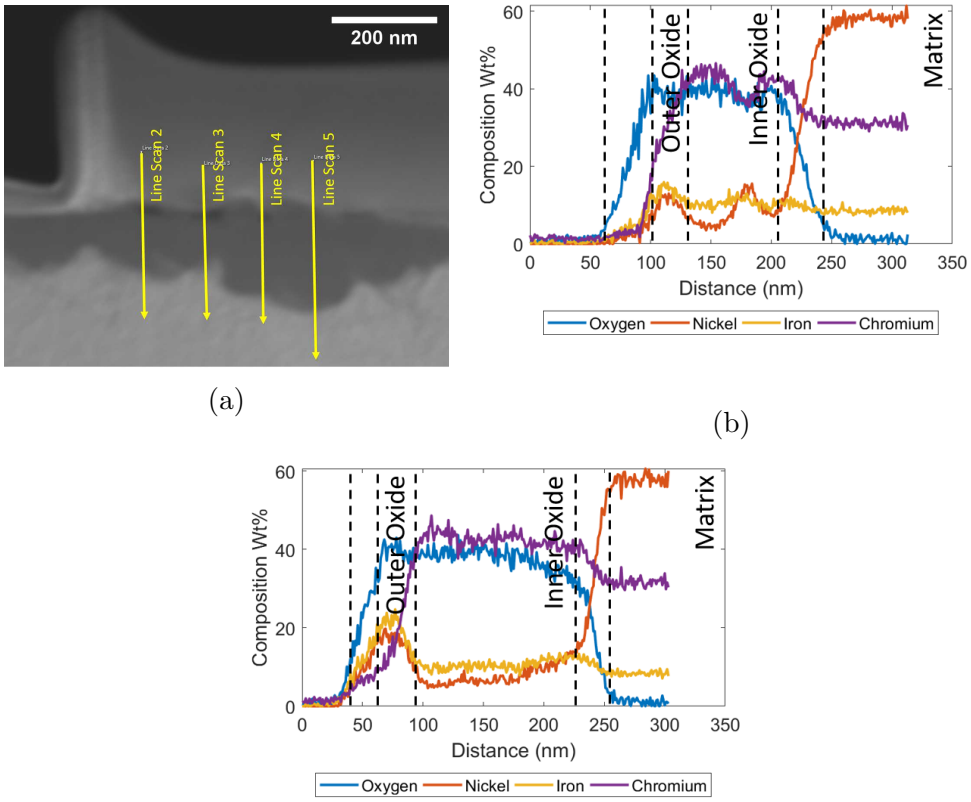


Figure 5.14: (a) TEM HADAF image of the A690 oxide (b,c) EDX spectra of different locations of the oxide. (b) = Line 2, (c) = Line 4.

the iron and nickel content in the outer oxide layer originate from dissolved species in the autoclave.

The inner-oxide is distinctly different from that of the other materials - it is chromium-rich. The inner oxide comprises 45 ± 5 wt% chromium, 40 ± 5 wt% oxygen, 10 ± 2 wt% iron and balance nickel. The chromium enriched inner-oxide is consistent with (Ni,Fe)Cr_2O_4 observed by Sennour et al [297]. The nickel content is slow to recover to bulk concentrations (67 wt%), this is due to increased chromium diffusing to the inner oxide.

Perrin et al [298] has investigated the oxide films generated on samples of Alloy 690, after exposure to simulated PWR primary media (B=1,000 ppm, Li=2 ppm,

H=1.39x10^{-3} mol^{-1}) at 325 °C for 1,024 hours. TEM-EDS reported a dual layer oxide. The external layer is composed of crystallites rich in Fe, and the internal layer appears to be continuous spinel oxide and richer in Cr. The thickness of this layer measured on different TEM images has been evaluated to 90 nm. It is reported that an enrichment in nickel (associated to an impoverishment in iron) was observed in the alloy just under the oxide scale. In this enriched zone, the concentration of nickel is about 20% (weight) on a thickness of 50 nm. This zone enriched in nickel seems to be linked to the presence of defects area observed under the oxide. Fresnel contrast) in order to estimate the grain size of the internal layer.

In another paper by Lafaix-Jeuland et al [299], A690 with simulated radiation damage from Xe was exposed to simulated PWR water at 325 °C for 304 hours and investigated. The oxide of Xe-A690 exhibited a compact and polycrystalline dual-layer oxide, but unlike the sample reported by Perrin et al [298], there was a large density of structural defects. The outer oxide was 10–15 nm in depth and richer in Fe, while the inner oxide was enriched in Cr and continuous. EDS also revealed a Cr depletion below the oxide/alloy interface. A FFT of the HRTEM images showed that the inner oxides were consistent with $NiCr_3O_4$ and Cr_2O_3 crystallographic structures. However, EDX profile highlighted a composition of the continuous oxide layer consistent with nickel–iron mixed chromite $Ni(1\text{-}x)Fe_xCr_2O_4$.

In a final study by Moss and Was [300], on A690 after exposure to hydrogenated water at 360 °C for up to 2,000 hours. It is reported that the inner oxide on Alloy 690 initially forms by internal oxidation before a protective layer of chromium-rich MO is formed with Cr2O3 at the metal-oxide interface. Grain boundaries in Alloy 690 act as fast diffusion paths for chromium to form a protective Cr2O3 layer at the surface, preventing internal oxidation from occurring. However, the migrated chromium-depleted boundary may be susceptible to oxidation like that observed in Alloy 600 if the surface oxide is ruptured.

5.2.2.4 Post-Autoclave A600 CW

Due to the prevalence of IGSCC in A600, a GB region is examined. ROI 1 in Figure 5.15a shows an overview of the area surrounding a grain boundary, while ROI 2 shows a close-up of the intergranular oxidation. In Figure 5.15 a (ROI 1), a large faceted outer-oxide particles is shown. It is homogeneous and, in this case, 1

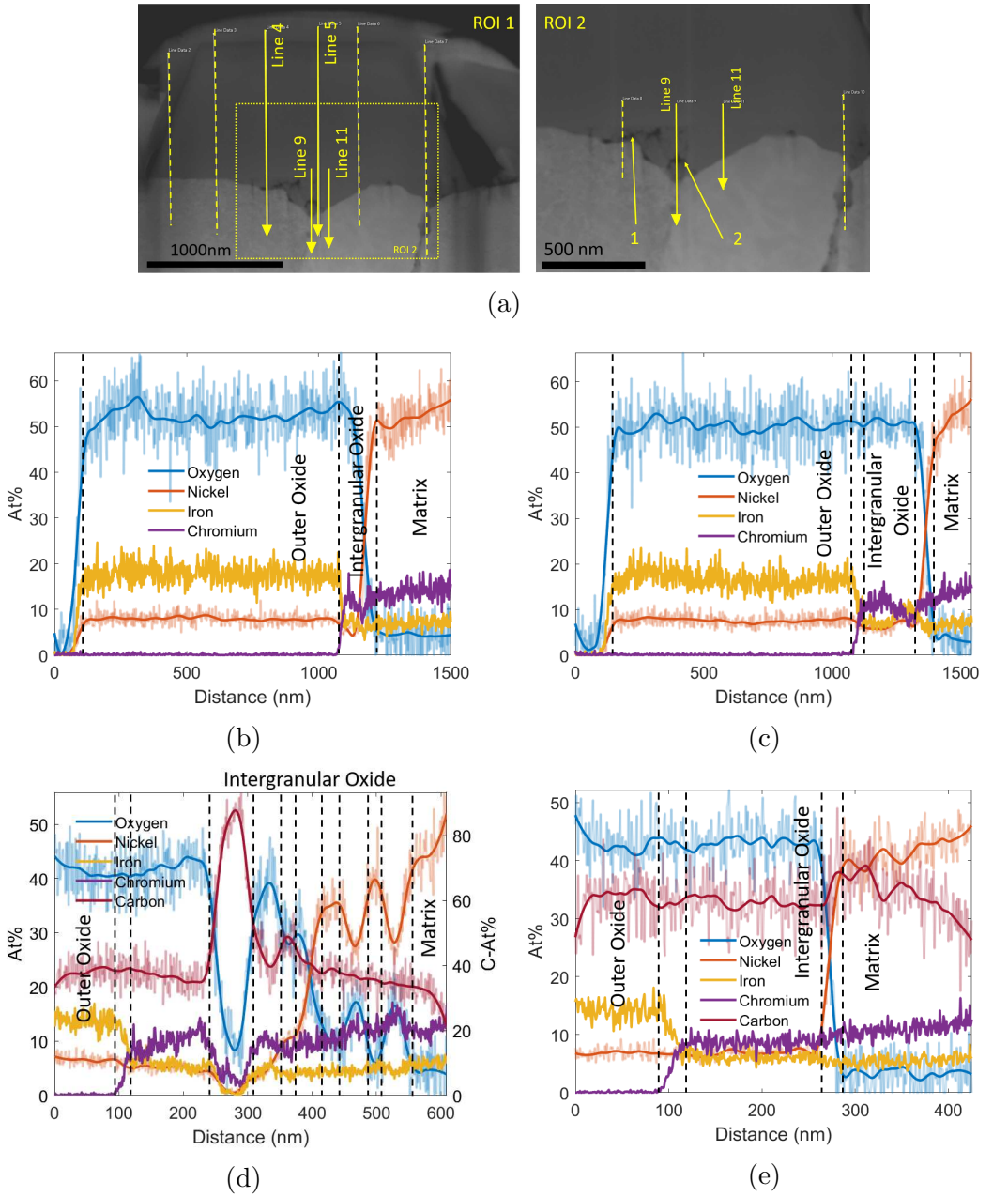


Figure 5.15: (a) TEM HADAF image of the A600CW oxide (b-e) EDX spectra of different locations of the oxide. (b) = Line 4, (c) = Line 5, (d) = Line 9 and (e) = Line 11.

μm thick. The inner-oxide, that is seen in previous materials, is not readily visible in EDX as it is too thin. Therefore, this analysis will focus on the intergranular

oxidation (IGO). ROI 2 shows a close-up of the IGO growing along the boundary. The IGO has penetrated 350±20 nm at its deepest point.

Figures 5.15 b & c show the elemental line profiles across the outer-oxide particle, lines 4 and 5 respectively. The outer-oxide is enriched in iron, but depleted in chromium with respect to the intergranular oxide. The outer oxide comprises 17 ± 5% iron, 50 ± 5% oxygen, 8 ± 3% nickel and balance other impurity elements. The IGO is chromium-rich and depleted of both nickel and iron. The darker regions visible, labelled 1 & 2, in the IGO indicate carbon-rich regions that are depleted in the major alloying elements. It is thought the carbon could be from the dissolution of an intergranular carbides.

Figures 5.15 d & e show the elemental line profiles along the boundary region and intergranular oxidation, line 9 and 11 respectively. The transition from outer to intergranular oxide occurs at approximately 100 nm, signified by the increase in chromium to approximately 10 ± 2 at%. Along and close to the grain boundary, there is a large carbon signal of 35 ± 10 at%. This carbon signal is thought to be due to the oxidation and dissolution of large intergranular carbides. Preferential oxidation around the carbide-boundary interface has been previously reported by Shen et al [58], and could explain why this site developed this IGO. The measured composition of the IGO with carbon is 10 ± 2 wt% chromium, 8 ± 2 wt% iron, 8 ± 2 wt% nickel, 45 ± 5 wt% and balance other impurity elements and carbon. The IGO is nickel depleted, and the iron and chromium compositions remain constant when compared to the bulk. The grain boundary (Figure 5.15d) finds further carbides along the boundary, this is seen by the inverse correlation between nickel and chromium in the 250 - 600 nm region of the scan. There is a high carbon signal originating from the bulk, this is likely contamination from the TEM.

Chen et al [19], reported the oxide structure of A600 after exposure to simulated PWR primary water (500 ppm B +2ppm Li +30 ml H2/ kg water) at 340 °C for 2000 h, with an applied stress via a 40° twists in a specially designed rig. The A600 sample was mill-annealed for 30 min at 930 °C and water-cooled. EELS was used to investigate the effect of intergranular oxidation along boundaries with carbides. It was concluded that along all four boundaries investigated the IGO terminates at intergranular carbides. The oxide around the upper carbide was enriched in Cr and Fe and depleted in Ni, a Cr-rich oxide is consistent with wider literature.

The signal intensities of Fe and Ni in the oxide were nearly uniform while there was a Cr composition gradient in the oxide, decreasing from the original matrix-carbide interface towards the matrix. The termination of IGO at IC is linked to the locally reduced oxidation rate in these regions, which become a rate limiting process. Conversely, a fast oxidation rate in the Cr depleted grain boundary region is expected, since Cr-depletion has been reported to significantly enhance oxidation rate.

In another study by Chen et al on A600, [301] a double-layer oxide film was reported on the exposed surface post-auto-clave exposure. TEM-EDS results showed that the outer oxide particles were rich in Fe and Ni, and the inner oxide film was rich in Cr. A narrow Cr-depletion zone was found in the matrix near the inner oxide film/metal interface with a width of approximately 20-30 nm. The diffraction patterns obtained by FFT (fast Fourier transformation) treatment from HRTEM, revealed that the oxide particles could be (Fe, Cr)Ni_2O_4 spinel-type oxide, and the inner oxide film could be a nano- crystalline Cr_2O_3 or $CrNiO_3$ chromia-type oxide.

5.2.3 Quantification of Oxide Nano-Porosity

To best characterise the oxide porosity, imaging has been focussed on three distinct regions, the inner-oxide/matrix interface, the inner-oxide, the inner-oxide/outer-oxide interface. The shift in focal plane ranged between ±500 nm to ±1000 nm depending on the material. The defects and porous regions were determined by contrast thresholds in ImageJ.

5.2.3.1 Post-Autoclave SS316L

The inner-oxide and matrix interface is shown in Figures 5.16 a - c. In this example, the porous nature of this oxide is evident in all images. The under focused image (Figure 5.16a) shows severe levels of porosity and nanocracking across the inner-oxide, highlighted by arrows and parallel lines. The additional dark speckling in the matrix, ahead of the inner-oxide, represents defects created by the forward diffusion of metallic elements to the oxide layer.

The inner-outer oxide interface, seen in Figure 5.16 d - f, shows more limited porosity. The large outer oxide particle, seen on the RHS of the image, has no

porosity. This is because these particles grow form the surface outwards from the dissolved cations in the autoclave environment. However, there are porous regions and channels under the outer-oxide particles in the inner oxide, as highlighted by the yellow arrows. These are remnants of an old oxide growth into the material, they now act as fast diffusion paths, and facilitate the movement of oxygen and hydrogen across the oxide boundary.

Figure 5.16 g - i continues to highlight the porous regions and nano-cracks the inner-oxide. These defects have generated an extensive network across the entire oxide layer from matrix (*left*) to outer-oxide (*right*), aiding in the fast transport of ions by providing defects-rich pathways to the oxidation front.

5.2.3.2 Post-Autoclave A800

The inner-oxide and metal interface is shown in Figures 5.17 a - c. The focused image shows that the oxide is highly unhomogeneous, and features finger-like oxide regions. In general, there there is little porosity at the oxide-matrix interface, but in the defocused image (a & c) it is possible to see pores and channels along these finger-like structures where the oxide is not yet established.

Figure 5.17 d - f, shows little to no porosity in the outer-oxide particles, or at the outer-oxide boundary. The inner-oxide, as seen in Figure 5.17 g - i, shows many nano-cracks along the length of the inner oxide. These defects act as fast-diffusion paths for adsorbed elements. The bright regions in (i) are thought to be dense clusters of porous oxide or dissolving carbides. However, the density of such defects are low when compared to the other alloys.

5.2.3.3 Post-Autoclave A690

Figure 5.18 show that the inner oxide of A690 is continuous and compact. There are no connected defect channels across the oxide layer that could facilitate fast-diffusion of elements. This can be attributed to the abundance of Cr, which forms a dense chromia oxide. This is not to suggest that defects do not exist, Figures 5.18 a - c highlight some areas could be linked to pores or nano-cracking generated during oxidation. However, unlike the other materials these defects are isolated and small compared to the oxide thickness. Figure 5.18 d - f includes a grain boundary

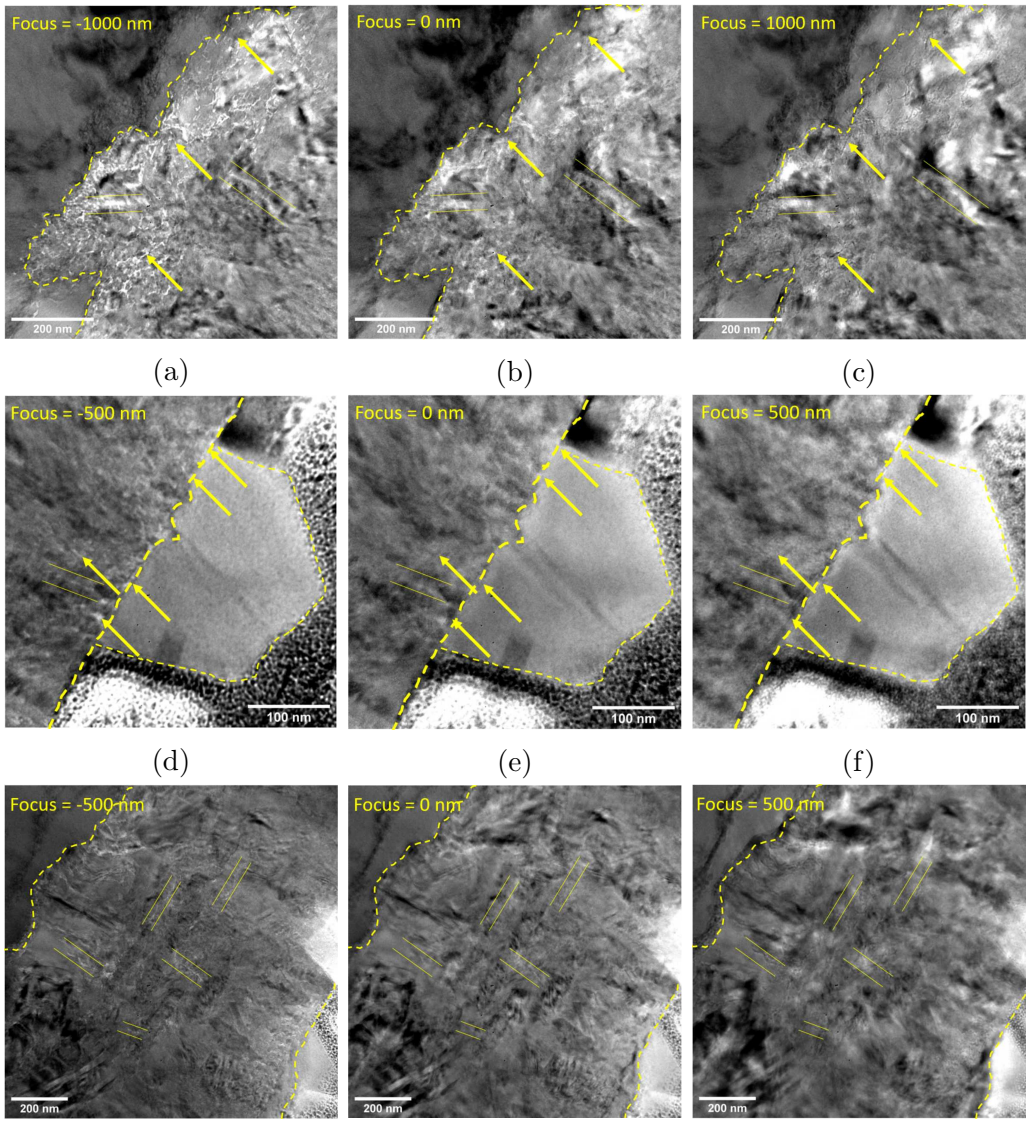


Figure 5.16: Fresnel imaging completed in the TEM is used to highlight the porosity and cracking in SS316L oxides. (a-c) focuses on the inner-oxide matrix interface, (d-f) the inner- outer-oxide interface and (g-i) the inner oxide. ROIs and nano-porosity are highlighted by arrows and nano-cracks are highlighted by parallel lines.

(labelled) that displays the initial stages of intergranular oxidation. Still, fewer bright regions associated with porosity are seen near or ahead of the IGO.

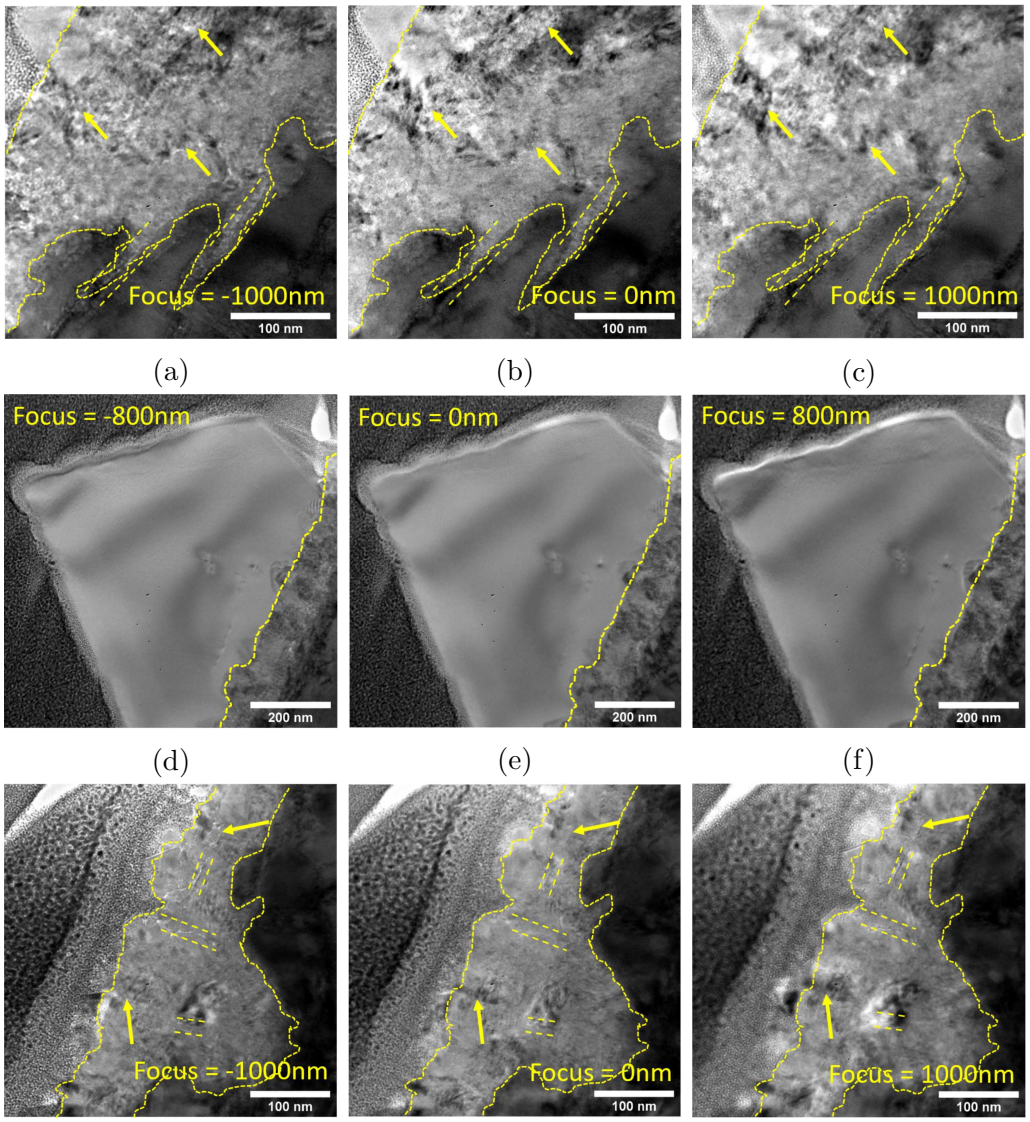


Figure 5.17: Fresnel imaging completed in the TEM is used to highlight the porosity and cracking in A800 oxides. (a-c) focuses on the inner-oxide matrix interface, (d-f) the outer-oxide interface and (g-i) the inner oxide. ROIs and nano-porosity are highlighted by arrows and nano-cracks are highlighted by parallel lines.

5.2.3.4 Post-Autoclave A600 CW

Fresnel imaging of intergranular oxidation along a grain boundary is captured in Figures 5.19 a - c. The arrows highlight bright regions in the foil. These

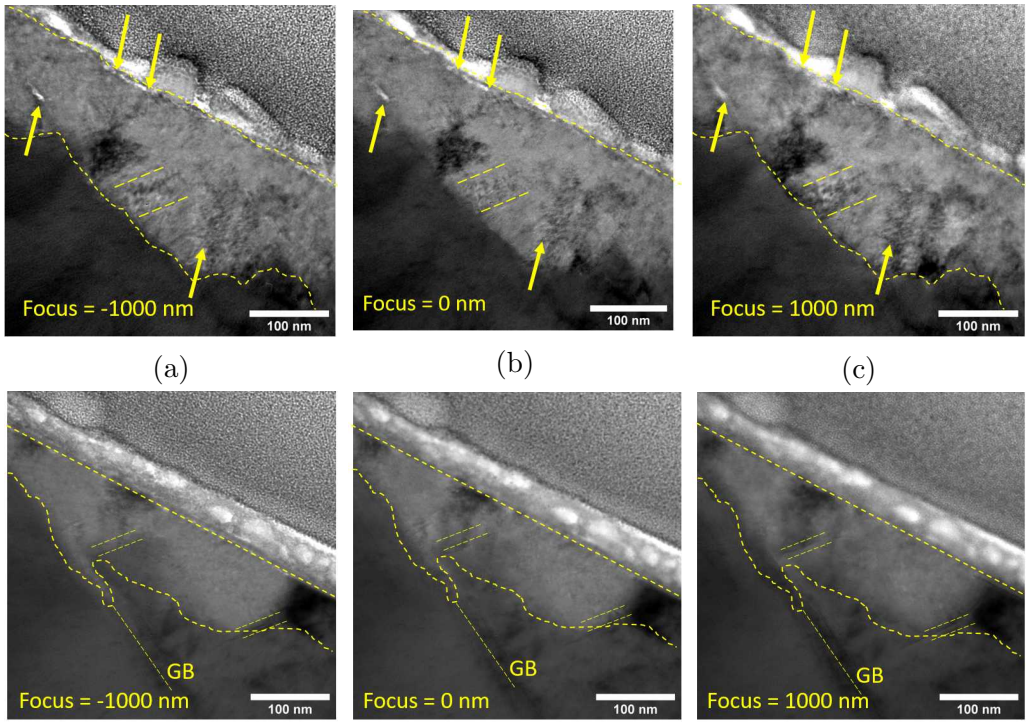


Figure 5.18: Fresnel imaging completed in the TEM is used to highlight the porosity and cracking in A690 oxides. (a-c) focuses on the inner-oxide, (d-f) examines the boundary between the inner oxide and matrix interface, including at a grain boundary. ROIs and nano-porosity are highlighted by arrows and nano-cracks are highlighted by parallel lines.

bright regions coincide with strong carbon signals (Section 5.2.2), suggesting that these areas could be from intergranular carbides. In Fresnel imaging, contrast is generated by structures satisfying the Bragg condition. As any structure different to the matrix can satisfy this condition, it is not possible to determine the origin of this defect, but is inferred through context.

Figures 5.19 d - f shows oxidation 1 - 2 μm away from the oxidised GB. There is still abundant porosity and nano-cavitation in these regions. The granular structure of the inner oxide becomes much clearer in the defocused images (d & f) as the boundaries are full of defects. The combined defects from carbides and boundaries provide an extensive network of channels to increase fast-diffusion across the oxide layer.

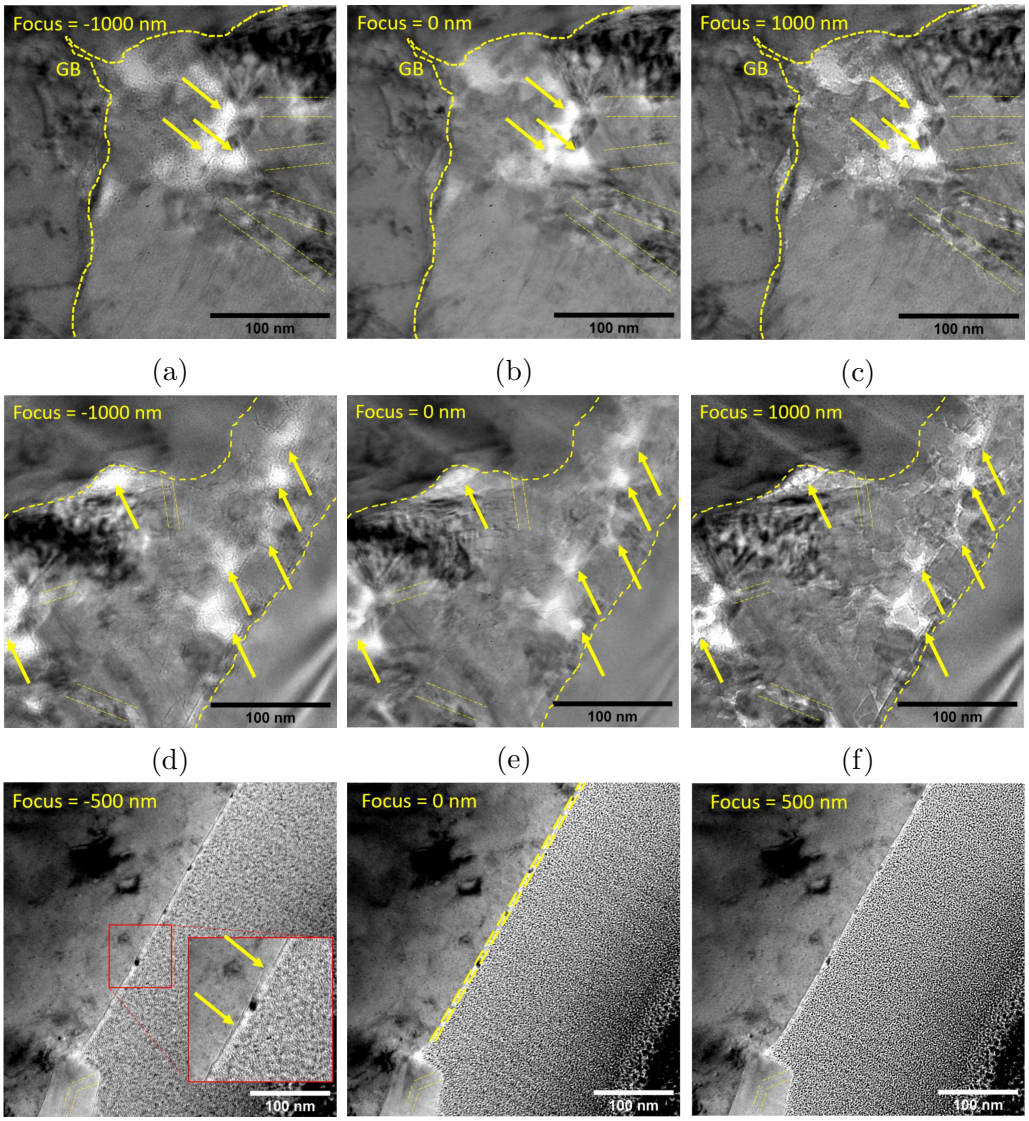


Figure 5.19: Fresnel imaging completed in the TEM is used to highlight the porosity and cracking in A600 CW oxides. (a-c) focuses on the intergranular oxide, (d-f) the boundary between intergranular oxide and oxide interface and (g-i) the inner oxide away from grain boundaries. ROIs and nano-porosity are highlighted by arrows and nano-cracks are highlighted by parallel lines.

Figures 5.19 g-i shows the typical inner-oxide layer across the majority of the sample. This oxide layer is very thin, $\leq$20 nm, and has no outer-oxide particles. Distinguishing any features in the defocused images is challenging, in a higher

magnification image some features are highlighted which appear match the porosity imaged in other regions of the material. The porosity in regions such as these is small and thought to be inconsequential when compared to other regions of thicker oxide. As the oxide is so thin, the diffusion of species across it is not thought to be severely hindered by the absence of fast-diffusion pathways.

5.2.4 Summary

The austenitic alloys were exposed to heavy water at 340°C, to simulate PWR operating conditions. The resulting oxide growth has been investigated using TEM-based microscopy tools. The findings from this preliminary study are summarised in Table 5.5, and referred to in later chapters.

Table 5.5: Summary of the oxidation properties of the investigated austenitic alloys.

Material	Inner Oxide Thickness (nm)	Inner Oxide Porosity (%)	Intergranular Oxidation Depth (nm)	Outer-Oxide Coverage (%)	Outer Oxide Thickness (nm)
SS316L	140±20	4±1	0	≥95	55±13
A800	120±30	2±1	500±100	35, otherwise ≤5	615±262
A690	110±20	1±1	0	N/A	40±10
A600 CW	5±10	2±2 (at GBs)	3000±2000	20 (at GBs)	930±350

Chapter 6

Room-Temperature Micromechanical Testing of Nuclear Alloys

6.1 Introduction

SCC propagation and crack initiation in metals are well documented in literature [17, 302, 303, 304, 12], but the mechanisms and precursors which lead to cracking need further investigation. A better understanding of the deformation mechanisms that lead to crack initiation will allow for improved models of SCC, and a more robust ability to predict material degradation. In this chapter, nanoindentation is used to determined the base-line deformation behaviour of nickel-based austenitic alloys, facilitating comparative studies to investigate the effects of temperature and hydrogen.

To meet the objectives of this chapter the following three factors, which can be attributed to crack initiation, will be examined. Firstly, the mechanical properties will be investigated. This includes the modulus, yield and deformation mechanisms, as these factors have shown to influence and affect the SCC crack initiation time in austenitic alloys [41]. Secondly, geometrically necessary dislocations (GND) will be studied, as they can prevent crack initiation and influence the stress distribution in deformed regions [305]. Finally, lattice rotation will be characterised. Strain heterogeneities increase when lattice rotations are prevented, which in turn leads to higher stresses. This is of interest as dislocation interac-

tions and entanglements can develop into sub-grain structures that influence the rotations when the lattice is deformed.

I will first discuss the mechanical properties of austenitic alloys by spherical indentation at room temperature. I will then present lattice rotations and GND analysis of comparable orientations, calculated from transmission Kikuchi diffraction (TKD) analysis. The materials selected for this investigation are SS316L (12% -Ni), A800 (32% -Ni) and A600 (73% -Ni). This selection is based on the findings of Coriou et al and Arioka et al [306, 12], in which A800 was reported to have an enhanced resistance to SCC over SS316L and A600 at certain temperatures. Through this comparative study, I aim to evaluate the likelihood that a mechanical deformation mechanism plays an influential role is promoting SCC resistance observed in certain austenitic alloys.

6.2 Converting Load-displacement data to Stress-strain

The method of analysis relies on essentially finding two parameters: the effective point of contact and the radius of contact area a. The method of finding these will now be explained using fused silica indents. First we have to find the effective point of contact. This is defined as: the first point in which the measurements in the loading segment are consistent with Hertzian theory [245]. The automatic surface detection does not function for aqueous testing, so the raw data is collected. In order to significantly speed-up the computation, an initial estimate of the elastic regime is taken, as seen in Figure 6.1. It is assumed that the elastic behaviour resides in this reduced data set.

Using the reduced data-set the effective zero-point con be determined for spherical nanoindentation using the following relationship

$$S = \frac{3P^0}{2h_e^0} = \frac{3(P - P*)}{2(h_e - h*)}, \tag{6.1}$$

where X^0 are the measured true values, X are the measured values and $X*$ are the values at the point of effective contact. This means that a simple linear regression of the elastic section can be used to determine the effective contact point. It

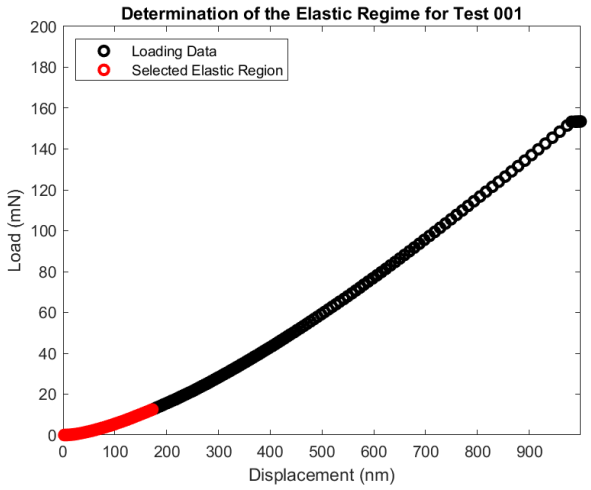


Figure 6.1: Graph illustrating the initial guess of the elastic region in the Load-displacement data

is emphasised that this step assumes no information about the tip. Figure 6.2 illustrates the linear regression fitted to the elastic region (red) of the data. The segment below the linear regime is influenced by surface artifacts, such as surface roughness and the non-ideal indenter shape, which causes the observed deviation from Hertzian theory. The segment above the linear regime deviates from Hertzian theory due to plastic deformation.

The zero-point correction shifts the data towards a Hertzian fit, which depending on the sample can be drastic. The resulting shift in the load-displacement curve from the analysis can be viewed in Figure 6.3.

After competing the zero point correction, the next step in the analysis is to find the radius of contact area. To find the radius of contact area the elastic properties of the material need to be known. If the properties aren't known then certain properties, i.e the Young's modulus, can be calculated from the data. To calculate the Young's modulus the yield point must be determined. The default is the load after the pop-in. If the material exhibits no obvious pop-ins, then this can be completed using a method by suggested by Hackett et al [307] or by Pathak and Kalidindi [246]. For simplicity, the method taken is from Pathak and Kalidindi and refers to the point at which the material continuously yields, as seen in Figure 6.5.

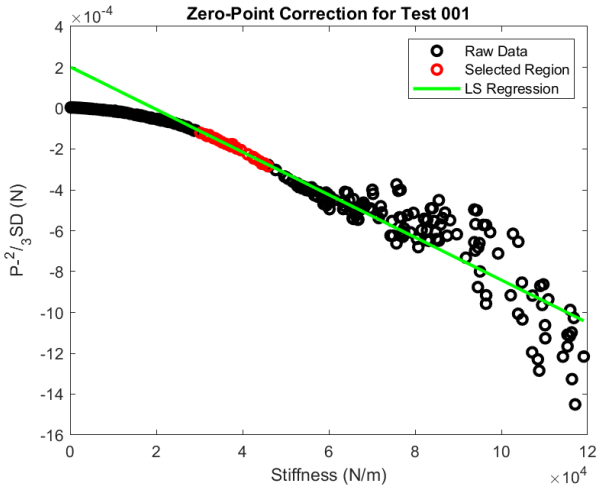


Figure 6.2: Determining the zero-point correction constants using linear regression (green) of the elastic region (red). The raw data is all the data in our initial guess of the plastic region (black).

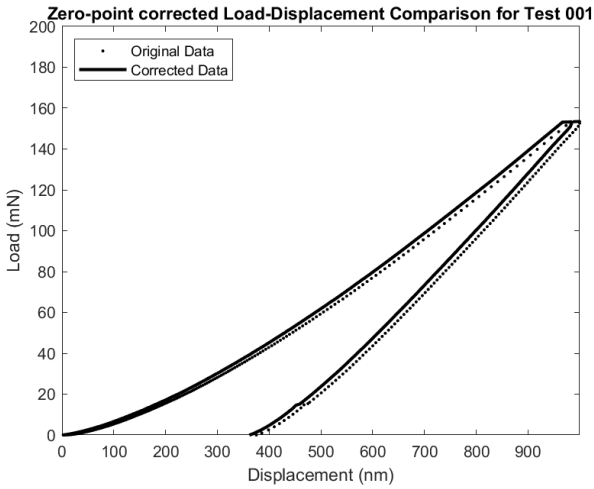


Figure 6.3: Comparison of the load-displacement before (dotted) and after (solid) the corrections have been applied.

Having ranged the elastic region the Young's modulus can now be determined by applying Hertzian theory

$$P = \frac{4}{3} r(h_e)^{0.5} H_e^{1.5}, \tag{6.2}$$

where $r(h_e)$ is the radius of the tip as a function of displacement. The gradient

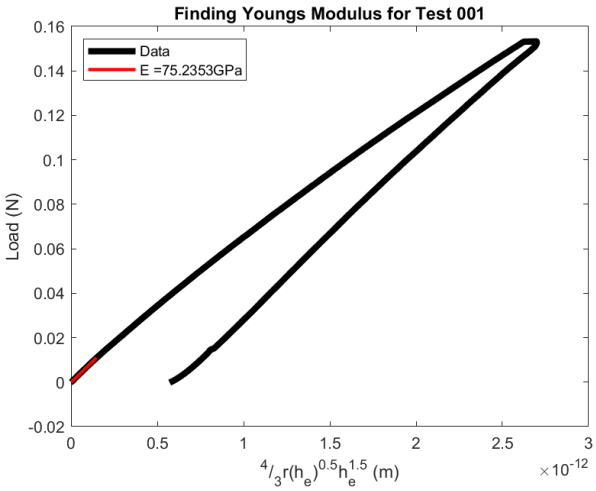


Figure 6.4: Finding the Young's Modulus of the sample. The red line marks the elastic regime that was used for fitting.

of the resulting linear section plotted in Figure 6.4 returns is the effective Young's modulus. The indent analysed had a Young's modulus equal to 75GPa, slightly above the accepted 73GPa but acceptable for nanoindentation.

Knowing the Young's modulus, the radius of contact area a can be determined. A CSM method greatly simplifies this calculation to $a = S/2E$. This relies on the assumption that E remains constant during the deformation. This is a reasonable assumption for Nickel as it is an isotropic material. However, materials with anisotropic properties should be treated with care, as lattice rotations and changes in material texture can influence the elastic properties.

Having undertaken the zero-point correction and found the radius of contact area, the indentation stress strain conversion, as defined by Pathak and Kalidindi [308], can be applied. The resulting indentation stress strain calculation can be viewed in Figure 6.5.

This analysis was repeated for every indent. The indents were individually evaluated to highlight any poor stress strain conversions. This is particularly apparent as the strain approaches zero, and results from the definition of the effective tip radius. The averaged results from the analysis of fused silica is displayed in Figure 6.18. The load-displacement curves are highly consistent with each other indicating that the zero-point corrections worked. The stress-strain curves have

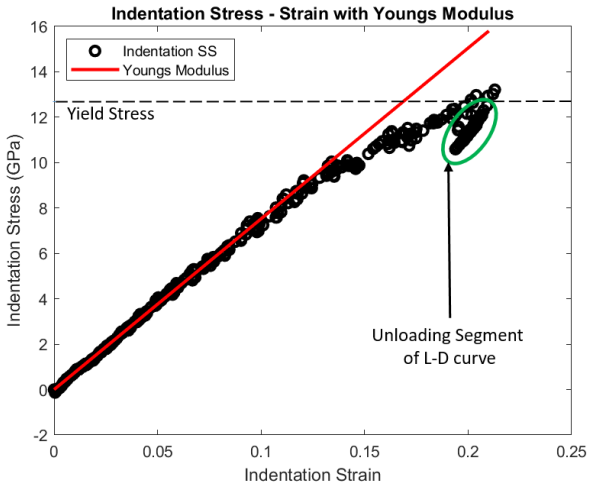
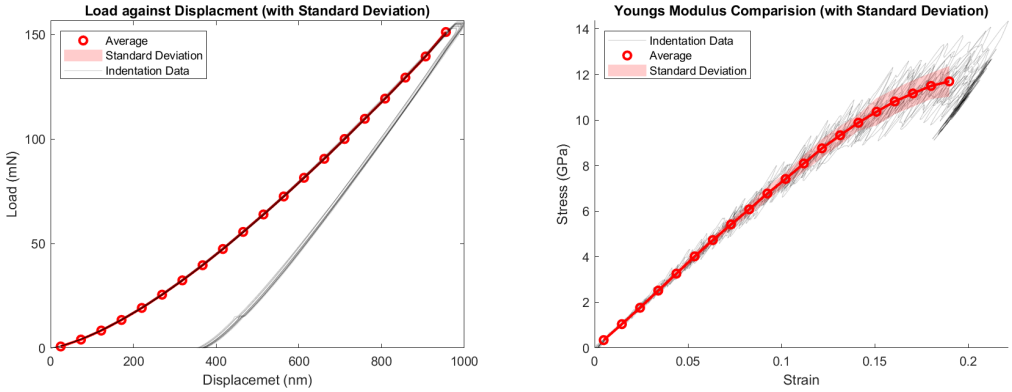


Figure 6.5: Stress-strain conversion of the load-displacement data, with Young's modulus superimposed



(a) (b)

Figure 6.6: Load displacement (a) and indentation stress strain (b) for fused silica.The bold red reflects the average of the 16 indents, with the shaded area being the standard deviation and the light grey plots represent the data from individual indents.

an average values of Young's Modulus of 74 $\pm$ 2 GPa. The yield stress, as read form the figure, is 12 $\pm$ 1 GPa. These calculated ranges encompass the accepted values of Young's Modulus and yield stress of 73 GPa and 12 GPa, suggesting that the analysis presented is reliable and accurate.

6.3 Results

6.3.1 Room-Temperature Mechanical Testing

There are three main grains selected for testing, near <001>, <101> and <111> orientations. The load-displacement of 36 spherical indents were collected on each orientation, converted to indentation stress-strain, and analysed using an in-house script based on the methods of Pathak and Kalidindi [245, 237]. The depth of each nanoindent was 300 nm. This is not ideal as shallow indents carry lower experimental reliability; but the priority of this chapter is comparing mechanical data with high magnification lift outs, which necessitated shallow indents. Target grain orientations were determined by EBSD, and co-ordinates for indentation were generated prior to testing. Indents are discarded if they are near microstructural features such as grain boundaries or carbides.

6.3.1.1 SS316L

Figure 6.7 shows the load-displacement and stress-strain results from spherical indentation. Load-displacement and stress-strain data can be broken down into four main stages. In the first phase, elastic behavior is observed up to displacements of 75 nm, or 0.05 strain. This elastic behaviour is characterised by Hertzian fitting (blue dashed) plotted over the load-displacementIn the stress-strain plot the elastic portion is initial linear portion of the curve, and extends in some cases to high near theoretical stresses. These stresses are plausible as they are less than the shear stress/2π, and arise due to the small testing volume and sparse distribution of dislocation sources. As the shear stress increases, there is a sudden increase in displacement. In the stress-strain this is the sudden plateau in high stress, before a retracement to the yield stress, as defined by Pathak and Kalidindi. This sudden displacement is referred to as a pop-in event and is linked to the initiation of plastic deformation. Following the pop-in, elasto-plastic behavior can be seen for the remaining loading segment. Unloading of the alloy is seen to be approximately elastic. As mentioned in the previous section, the unloading portion of the load-displacement curve does not translate well to the stress-strain curve. It is therefore not shown.

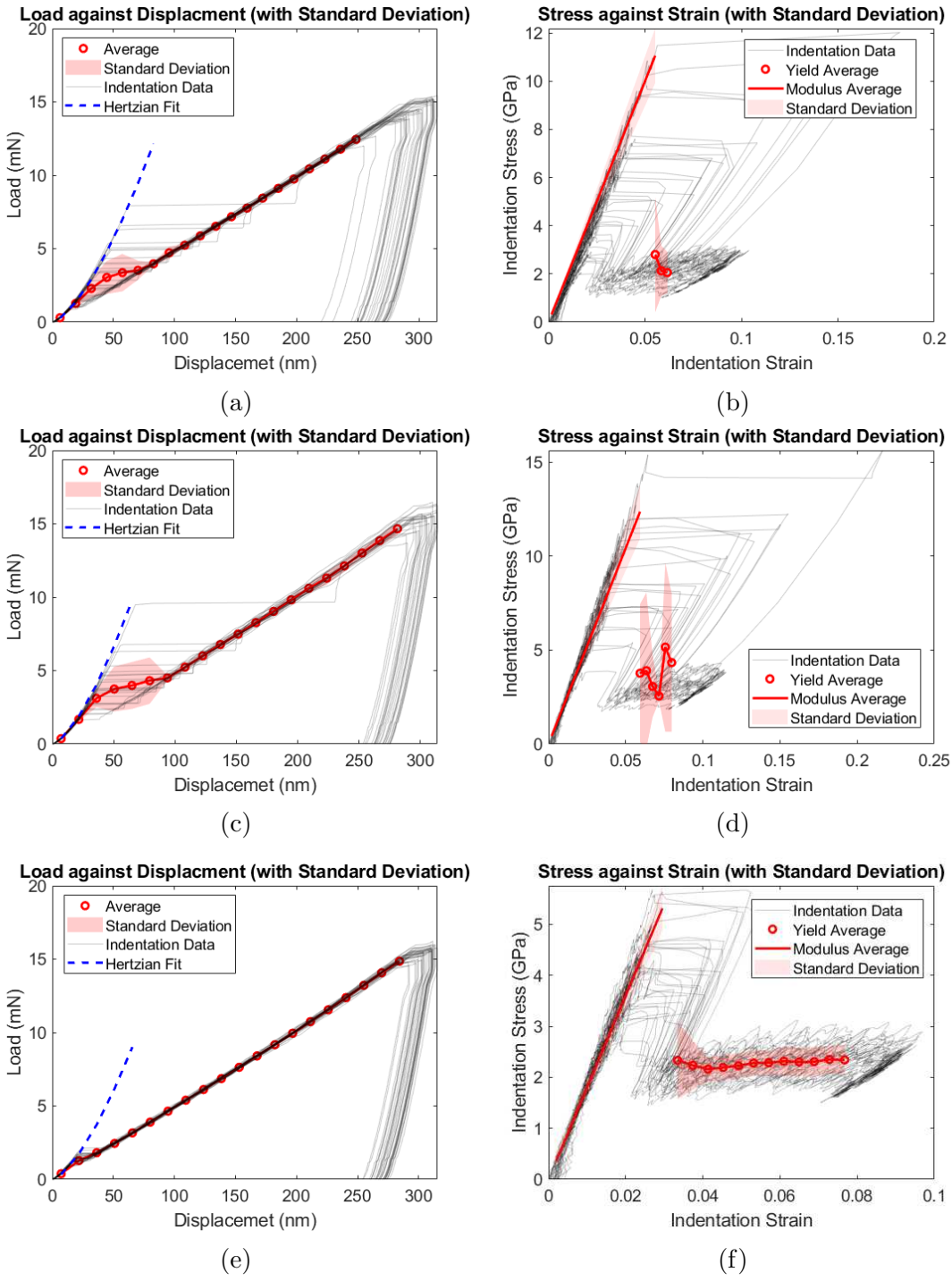


Figure 6.7: Averaged load-displacement and indentation stress-strain data from spherical indentation of SS316L. (a) and (b) are from the <001> orientation, (c) and (d) are from the <101> orientation, and (e) and (f) are from the <111> orientation.

Table 6.1: Summary of the Young's modulus and yield stress of S316L, alongside the Euler angles of the tested grains.

Orientation	Euler Angles ($[\phi_1, \theta, \phi_2]$)	Young's Modulus (GPa)	Yield Stress (GPa)
<001>	[351.4, 10.5, 157.2]	183±23	2.4±0.5
<101>	[169.0, 41.4, 353.0]	208±23	2.1±0.3
<111>	[75.1, 47.5, 131.9]	184±11	2.3±0.5

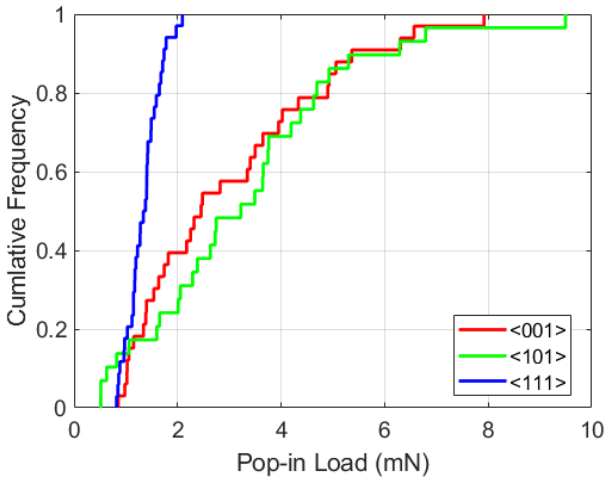


Figure 6.8: A cumulative frequency plot of the loads associated with pop-in phenomena in SS316L. This is the onset of a sudden burst of plasticity, indicating the generation of dislocations, in the load-displacement curves.

The values of Young's modulus and yield stress are summarised in Table 6.1. The modulus ranges from 183 to 208 GPa depending on orientation, the moduli of the three orientations can be considered equal given the scatter associated with the data. The yield stress is defined as the stress required to continuously deform the material. The yield stress of all orientations converge on to a small range of values centered on 2.2 GPa. The yield stresses are within error, and can be considered isotropic.

Figure 6.8 shows the cumulative frequency of the pop-in loads for the three orientations. The mean pop-in loads are 3.0±1.9, 3.3±2.0 and 1.3±0.3 mN of the <001>, <101> and <111> orientations respectively. Indents placed on <111> orientations have smaller pop-in loads (<2 mN) compared to the other orientations. In comparison, 60% and 75% of the recorded pop-ins along <001> & <101>

orientations respectively, occurred at loads greater than the maximum pop-in load recorded along the <111> orientation (i.e. 2 mN).

6.3.1.2 A800

Figure 6.9 shows the load-displacement and indentation stress-strain conversion. The load displacements can again be characterised by four principle regimes. Initial elasticity, denoted by Hertizan fitting; the end of elasticity, marked by a sudden burst of displacement occurring at a pop-in load; elasto-plastic deformation; and elastic unloading. The load-displacement curves show good alignment post-corrections.

A summary of the mechanical properties can be viewed in Table 6.2. The values of Young's modulus range from 175 to 189 GPa. There is no sign of anisotropy as the modulus of the three orientations can be considered equal within error. The yield stresses are consistent across the three orientations tested, and range between 2.1 - 2.3 GPa.

Figure 6.10 shows the cumulative frequency of the pop-in loads for the three orientations. The mean pop-ins loads are 1.8±1.1, 1.6±1.2 and 1.5±0.6 mN of the <001>, <101> and <111> orientations respectively. The pop-in behaviour of all orientations are comparable at lower loads (<1.5 mN), after which divergence between the <001> & <101> and <111> orientations is observed. Along <001> & <101> orientations, a skew towards higher loads is observed, while the frequency of pop-ins along <111> orientations is a linear continuation of the low-load behaviour. The maximum pop-in load of the <001> & <101> orientations is approximately double that of the <111> orientation.

Table 6.2: Summary of the Young's modulus and yield stress of A800 in the three listed orientations.

Orientation	Euler Angles ($[\phi_1, \theta, \phi_2]$)	Young's Modulus (GPa)	Yield Stress (GPa)
<001>	[91.7, 5.1, 126.7]	175±12	2.3±0.3
<101>	[35.5, 43.2, 170.5]	189±16	2.2±0.7
<111>	[237.4, 54.1, 319.6]	178±16	2.1±0.6

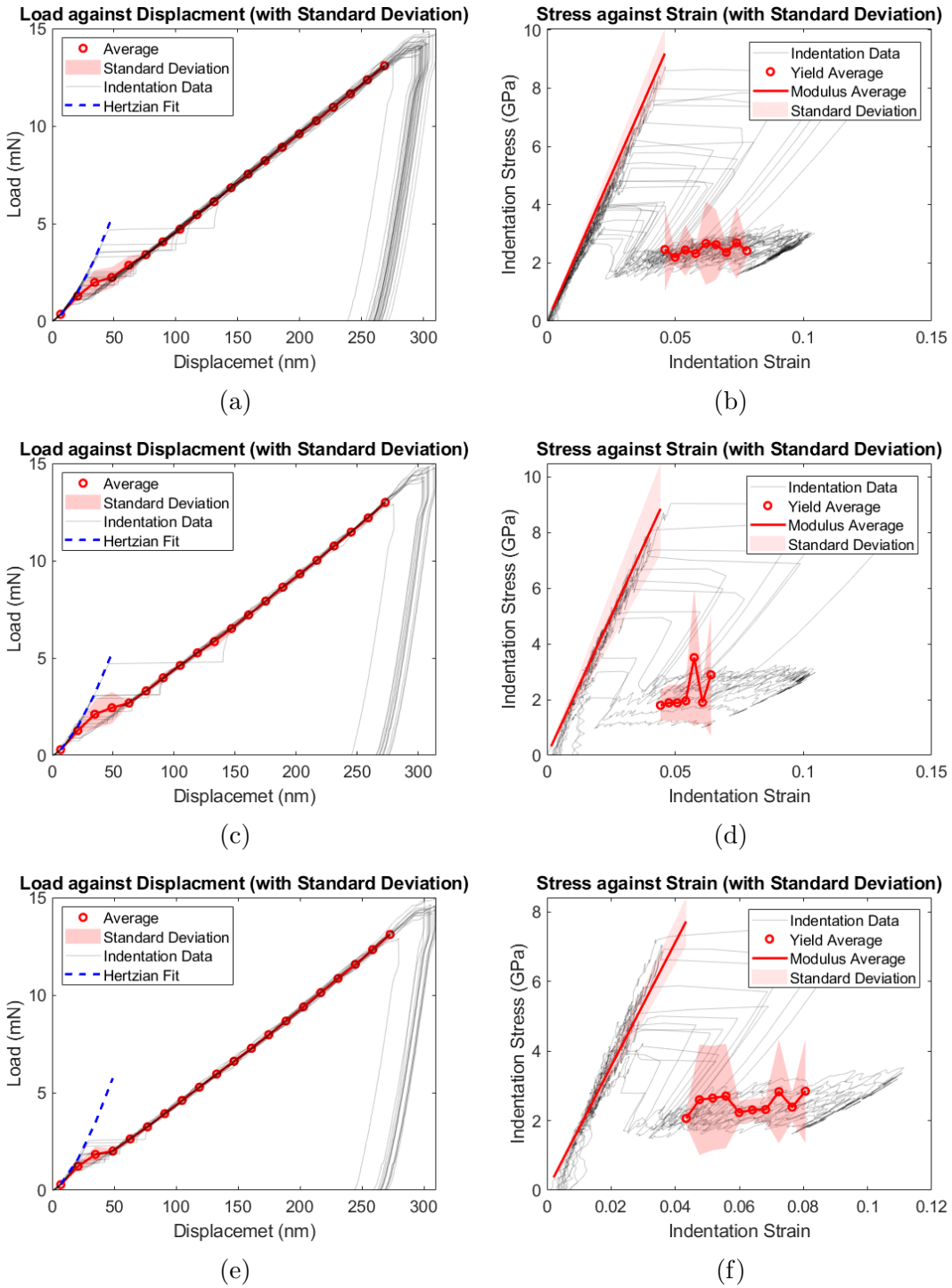


Figure 6.9: Averaged load-displacement and indentation stress-strain data from spherical indentation of A800 in air on a minimum of 16 indents. (a) and (b) are from the <001> orientation, (c) and (d) are from the <101> orientation, and (e) and (f) are from the <111> orientation.

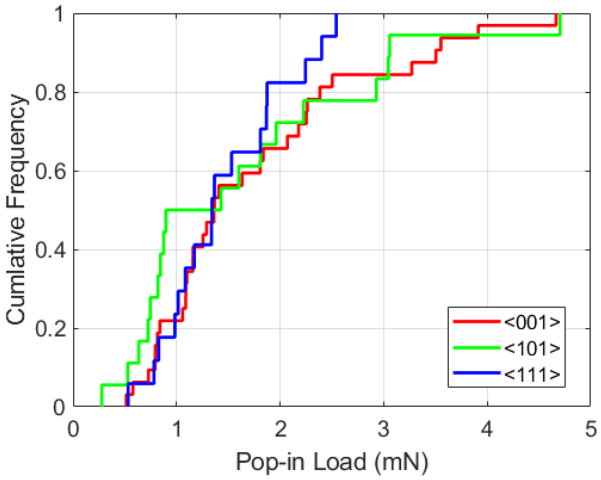


Figure 6.10: A cumulative frequency plot of the loads associated with pop-in phenomena in A800.

6.3.1.3 A600

Figure 6.11 shows the load-displacement and indentation stress-strain resulting from spherical indentation. Unlike the other materials sampled, the load-displacement data of A600 can be characterised by only three regimes. First, a brief initial elastic response is found at depths of up to 20 nm. Plasticity is soon initiated, and there is a smooth transition from elastic to elasto-plastic behavior. The remaining loading segment consists of elasto-plastic behaviour. The unloading of the alloy is seen to be approximately elastic. The indentation stress-strain conversion is poor, resulting in the the stress-strain missing the origin by a considerable amount ($\leq$ 0.005 strain). To make matters worse, the average grain size is small, $\leq$5 μm, and the number of indents discarded due to grain boundary interference is over 60%. Typically, 9-15 of the 36 indents are unaffected by boundaries for each orientation.

A summary of the extracted mechanical data is presented in Table 6.3. The Young's modulus reports values ranged from 97 to 142 GPa. The modulus values show some anisotropy, with <001> being lower than both <101> and <111> orientations. However, these values are between 46 - 78% of the expected bulk values. The yield stress is measured in the 600 - 800 MPa range. A600's data

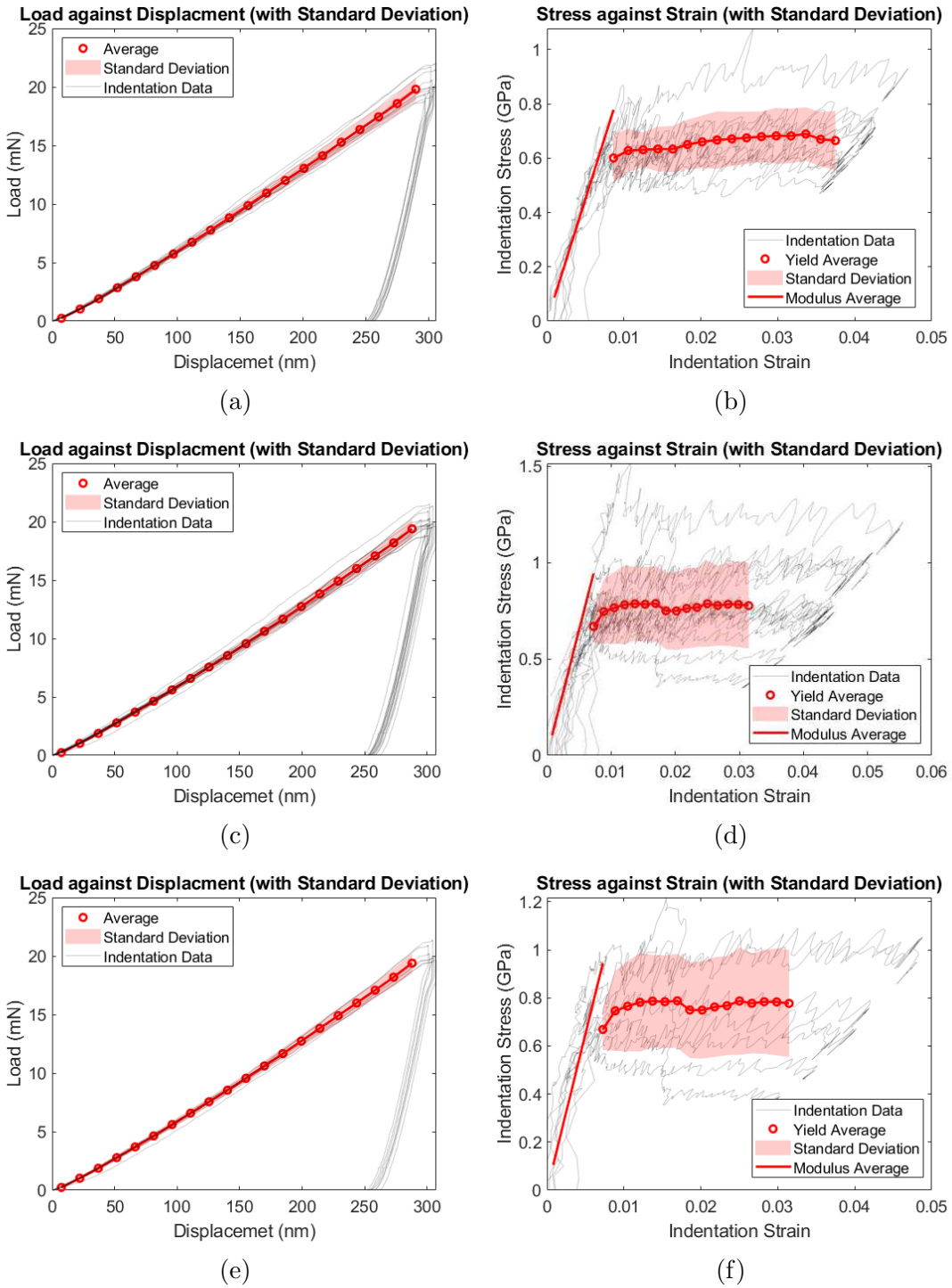


Figure 6.11: Averaged load-displacement and indentation stress-strain data from spherical indentation of A600 in air on a minimum of 9 indents. (a) and (b) are from the <001> orientation, (c) and (d) are from the <101> orientation, and (e) and (f) are from the <111> orientation.

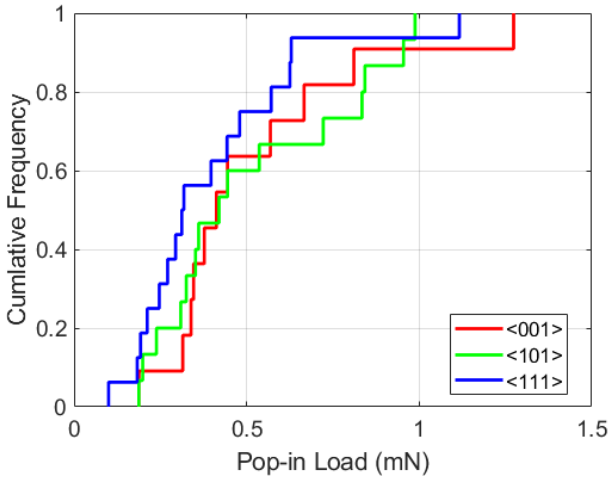


Figure 6.12: A cumulative frequency plot of the loads associated with pop-in phenomena in A600.

is less reliable as a larger elastic region is required for an accurate zero-point correction.

Table 6.3: Summary of the Young's modulus and yield stress of A600, alongside the Euler angles of the tested grains.

Orientation	Euler Angles ($[\phi_1, \theta, \phi_2]$)	Young's Modulus (GPa)	Yield Stress (GPa)
<001>	[140.0, 8.1, 45.4]	97±19	0.6±0.1
<101>	[202.2, 34.6, 0.2]	134±15	0.8±0.4
<111>	[217.1, 48.2, 317.2]	142±17	0.7±0.2

Figure 6.12 shows the cumulative frequency of the pop-in loads for the three orientations, which occur at loads between 0.1 - 1.5 mN. The mean pop-in loads are 0.5±0.3, 0.5±0.3 and 0.4±0.2 mN of the <001>, <101> and <111> orientations respectively. The pop-in behaviour is the same for all orientations. The errors are associated with both a larger noise-signal ratio and surface roughness.

A comparative summary of the mechanical properties determined by spherical nanoindentation is presented in Figure 6.13. These materials are explored and compared in detail in the discussion section.

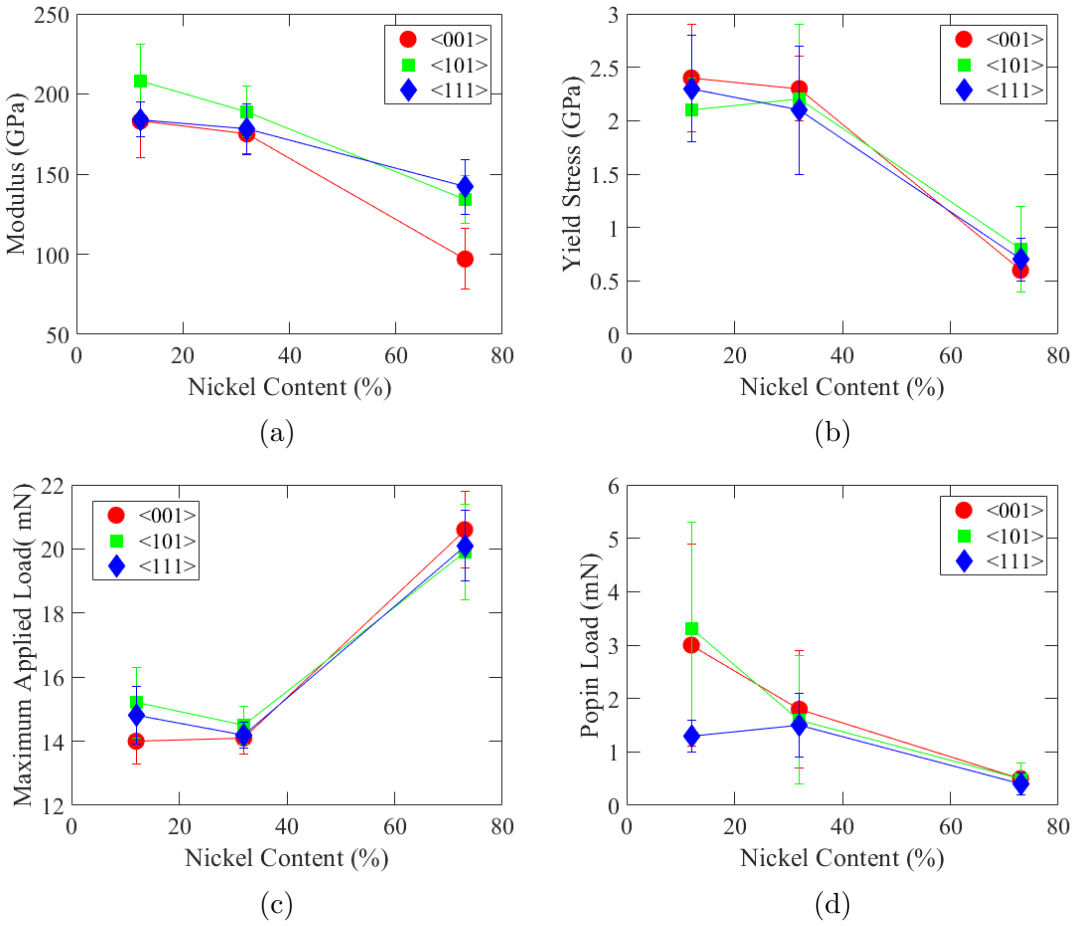


Figure 6.13: A summary of determined (a) modulus, (b) yield stress, (c) maximum applied load and (d) pop-in loads mechanical properties for the three austenitic alloys.

6.3.2 High-Magnification Analysis

Cross-sectional lift-outs of the spherical indents on the three alloys were taken from similar crystallographic orientations. The selected indents were on surface <001> normal, and the lift-out was made with a <101> plane normal. The high magnification results have been collected using transmission kikuchi diffraction (TKD). Pseudo-bright field and dark field images were collected using fore-scattered diodes [272], and the GND and lattice rotations surrounding the indent were also mapped [271, 272]. GND calculations were performed using a correlative technique [309]. Fore-scattered diode images were collected using 20 kV & 1 nA, and the EBSD maps were collected using 20 kV & 5 nA. The step size of the collected maps is 10 nm.

6.3.2.1 Localised Deformation Zones

Figure 6.14 shows the average misorientation (MO) map surrounding a spherical indent. To measure the extent of the localised deformation region around the indent, two MO profiles were used along the slip traces, and the results averaged.

The average lattice rotation angle in SS316L was measured to be 1.5±0.3°, and the deformation zone size extend up to 1.4±0.2 μm. For A800, the peak lattice rotation is 3.5±0.4°, and the length of the deformation zone is on average 1.6±0.3 μm. The RHS possesses an additional component from shadowing noted in the MO profile, providing additional lattice rotation. However, this is inconsequential as it is sufficiently distant from the indent. The average misorientation in A600 was measured to be 8.5±2.1°, and the deformation zone is on average 0.5±0.1 μm. There is some sample bending present, indicated the gradual change of lattice rotation across the sample, but this does not affect the indentation induced rotations. The results are summarised in Table 6.4 along with the deformation intensity.

6.3.2.2 Deformation Mechanisms and Dislocation Analysis

Deformation, in both the previous indentation experiments and SCC crack growth, requires the generation and movement of dislocations throughout the matrix. Figures 6.15, 6.16, and 6.17 show highlighted dislocations in a combined pseudo-bright and dark field image of the region directly underneath an indent.

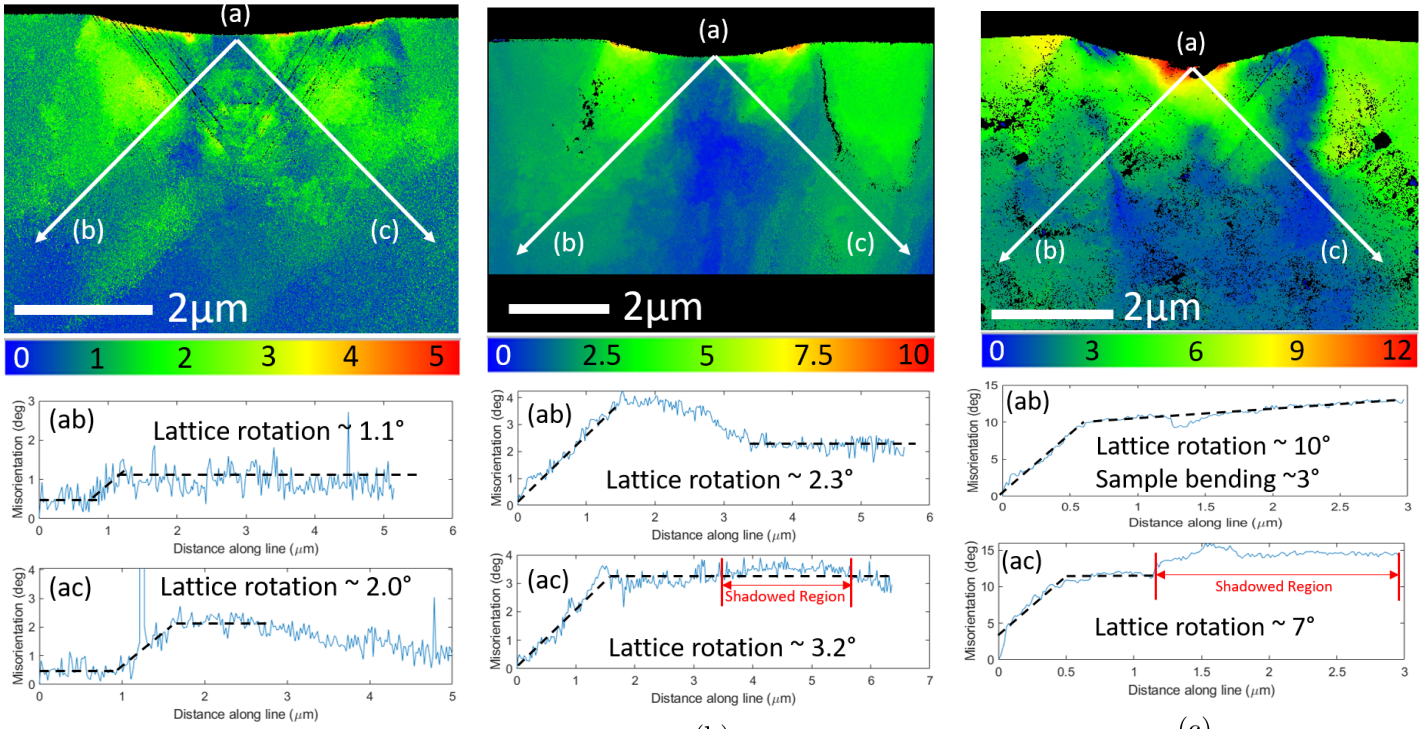


Figure 6.14: The average misorientation map from the TKD in (a) SS316L, (b) A800 and (c) A600. In addition a misorientation profile from the center of the indent showing the lattice rotations.

Table 6.4: Summary of the average length of the localised deformation zone (LDZ), the lattice rotation, and deformation intensity. Colour bar shows lattice rotation from neighbours in degrees.

Materials	LDZ (μm)	Lattice Rotation (°)	Deformation Intensity (°/μm)
SS316L	1.4±0.2	1.5±0.3	1.1±0.3
A800	1.6±0.3	3.6±0.5	2.3±0.5
A600	0.5±0.1	8.5±2.1	17.0±3.0

Figure 6.15 shows the plastic zone underneath a spherical indent (centre-top) in SS316L. During indentation dislocation generation has occurred. Dislocations are visible as black or white features in the bright- and dark- field images respectively. There is also FIB damage present in the material, despite low energy cleaning. This is seen in the vertical striping present in the results, not to be confused with dislocations. The numerous dislocations have resulted in multiple visible slip traces. The normal of the slip traces have been determined to fall along the <111> directions from the pole figures. The slip traces are 55.3° and 125.2° from the horizontal axis and extend approximately 3.4±0.3 μm into the material from the base of the indent. The dislocation field extends to approximately 4.3±0.5 μm underneath the surface. In addition to dislocation generation, there is deformation twinning observed directly underneath the indent. The twins are confirmed $\Sigma 3$ by a 60° lattice rotation in the MO profile that runs along the normal of the twinning plane. The mean separation of the deformation twins is on 110±30 nm.

Three regions of interest (ROI) have been highlighted. ROI 1 provides a closer view of the the deformation bands. ROI 2 and 3 are on the outer edges of the plastic zone, a band pass filter has been applied to minimise the FIB damage. The dislocation densities have been estimated to be at least 7.2×10^{13} and 3.2×10^{13} m^{-2} in regions 2 and 3 respectively. Region 1 has too much deformation and can not be easily counted.

The GND map suggests that there are high GND concentrations of at least $5x10^{15}$ m^{-2} localised to the slip planes and deformation bands under the indent. The regions further from the indents see a reduction of the GND density to below $5x10^{14}$ m^{-2}. This represents a ten-fold reduction in the dislocations between the

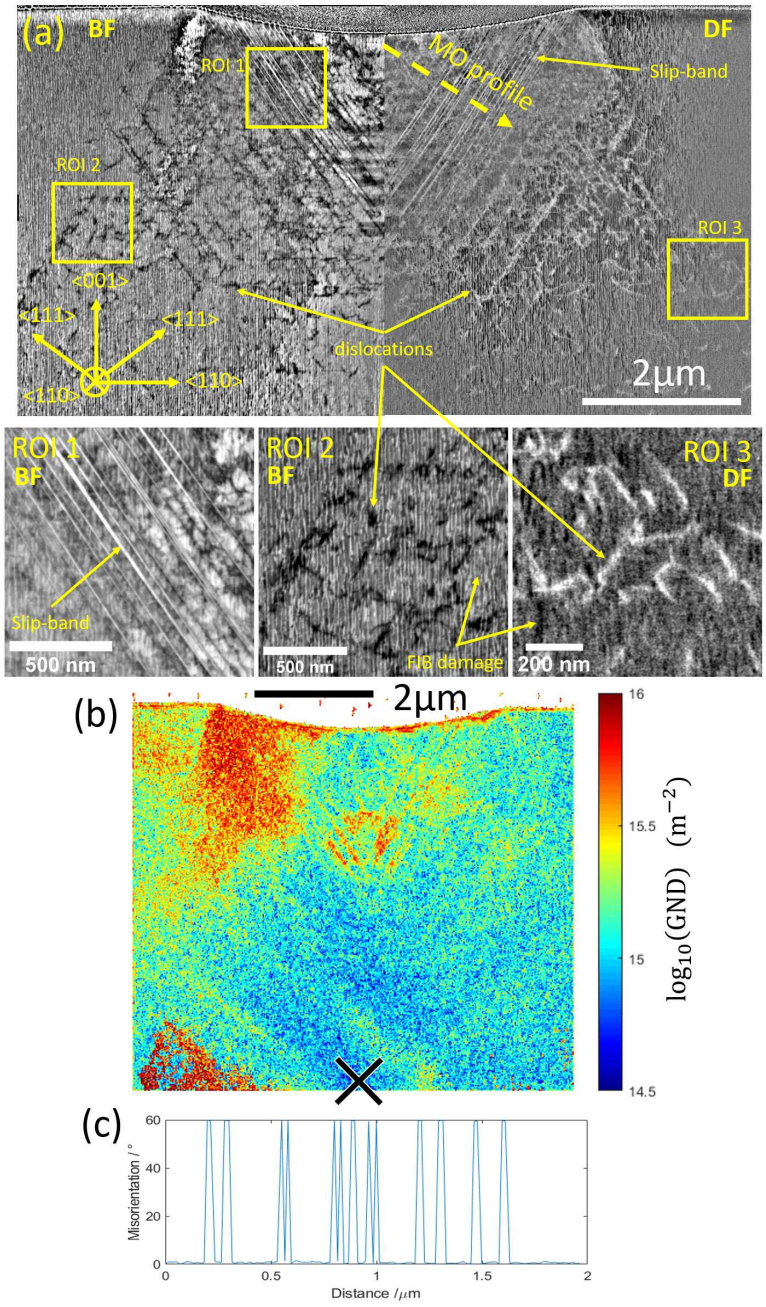


Figure 6.15: (a) Forescattered cross-sectional images (both pseudo bright- and dark- field) of a spherical indent in SS316L along a near <101> zone axis. Higher magnification images of regions of interest, selected from the fore-scattered images. (b) A calculated GND density map using the Kikuchi patterns captured from TKD.(c) A misorientation profile, of the dashed yellow line in the fore-scattered image. This profile confirms the deformation twinning, through the 60° orientation changes.

"strain-free" reference point (black-cross) and deformed matrix. High GND counts in SS316L displays a strong localisation to the slip bands, in the regions between these band, it is seen that the GND density falls to almost background levels, with the observed count being between 7x10^{14} – 2x10^{15} m^{-2}. There is a left-right mismatch in GND, this is thought to be due to slight sample bending. Comparing the estimated and calculated dislocation density in the regions of interest, there is an order of magnitude difference between the results. The calculated GND density is a function of the step size. As the step size is ten-times smaller than mean the dislocation lines length it is likely that the calculated GND density is likely an over estimate of the true value.

Figure 6.16 shows the deformation-induced dislocation network in A800. Dislocations are generated along slip planes and defined dislocation channels approximately 100 nm wide. From the bright field images, the anticipated <111> slip plane normal has been identified, and an additional slip trace with a <211> normal is also observed at a further distance from the indent. It is not clear if the origin of this addition slip trace is from background dislocations or the indent. The deformation from the indent extends to depths of 4.2±0.4 μm into the bulk. At the centre of the indent, there is a very compact dislocation network. As the distance from the indent increases the spacing between these dislocation channels increases from 100±20 to 600±100 nm. The dark field images are less clear, due to shadowing and interference from the copper grid on the RHS of the image.

Three regions were selected in the bright-field images to represent near, intermediate and long distances from the indent to count dislocation densities. The estimated densities were 2.1±0.3×10^{14}, 6.6±0.2×10^{13} and 2.8±0.2×10^{13} m^{-2}. The calculated GND values are 5×10^{15}, 4×10^{14} and 1.5×10^{14} m^{-2}. Both methods show a similar trend in dislocation densities and show reasonable correlation between the fore-scattered images and GND maps.

Figure 6.17 shows a high magnification pseudo- bright and dark field view of the deformation region in A600. The fore-scattered images show a highly dense and tangled dislocation network underneath the indent. Some evidence of slip bands can be seen in the bright-field images, but when compared to previous samples, the dislocations in A600 do not form distinct slip bands. This ambiguity may arise from a 26° misalignment in the normal of the cross-sectioned plane, pointing in

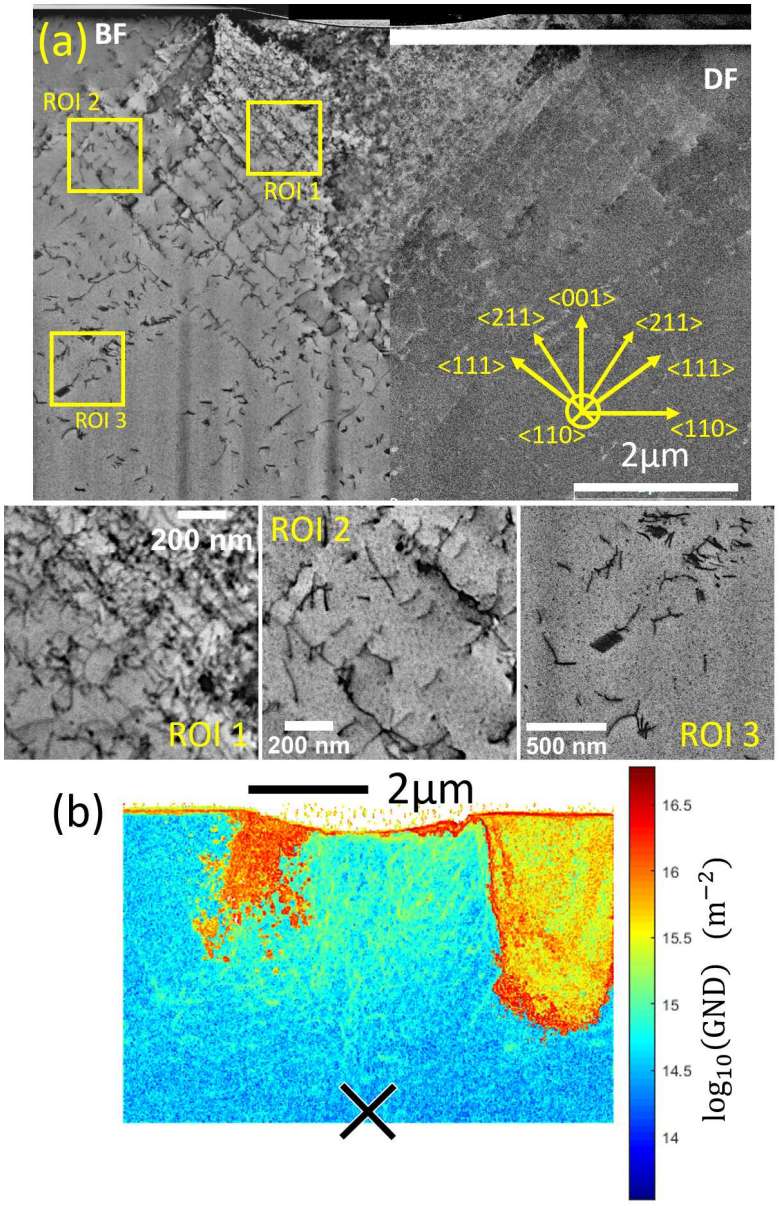


Figure 6.16: Forescattered cross-sectional images (both pseudo bright- and dark-field) of a spherical indent in A800 along a near <101> zone axis.

<103> instead of <101>. The <103> orientation makes dislocations going into the plane visible (appear as dots for <101>), increasing the appeared density. A600 also displays Σ3 deformation twinning, determined by 60° misorientation profiling shown in Figure 6.17 c. The dislocation density is determined from regions

1 and 3. The counted densities were 3.1×10^{14} and 1.2×10^{14} m^{-2} respectively. The GND calculations in Figure 6.17 b show that there is an extremely high dislocation density across a large area underneath the indent. The GND map shows regions of high dislocation density, that maybe linked to pile-ups interacting with carbides present in the sample. The background density is estimated to $5\pm4\times10^{14}$ m^{-2}, compared to $3\pm2\times10^{16}$ m^{-2} near the indents.

6.4 Discussion

Three different austenitic alloys, SS316L, A800 and A600, have been tested using nanoindentation, and the resulting strain fields examined using TKD. The aim was to extract the yield stress, compare the GND density, and determine the lattice rotations in each material in order to discuss their implications on the crack growth rate and SCC mechanisms.

6.4.1 Mechanical Properties in Austenitic Alloys

6.4.1.1 Young's Modulus

The Young's modulus values for SS316L are in good agreement, the three orientations cover a range between 183 - 208 GPa. This compares well to the specification value of 190-200GPa [310] and literature values [311, 312]. However, more anisotropy was observed by Weaver et al [313], who reported expected modulus values of 197, 218, and 225 GPa for respective <001>, <101> and <111> orientations. Similarly for A800, the reported moduli are consistent, ranging from 175-189 GPa, they are also inclusive of the reported bulk value of 196 GPa [314]. The modulus values for each orientation are within error, demonstrating no anisotropy in either material.

The accepted elastic modulus of A600 is 214 GPa [315], and previous nanoindentation studies have reported values of 180 GPa [316, 73]. Single crystal investigations conducted by Li et al [317] have shown that A600 is anisotropic and can stray from this macroscopic value 290–320 GPa in <111>, 115–130 GPa in <001>and 210–230 GPa in <011> direction. The results presented here do not

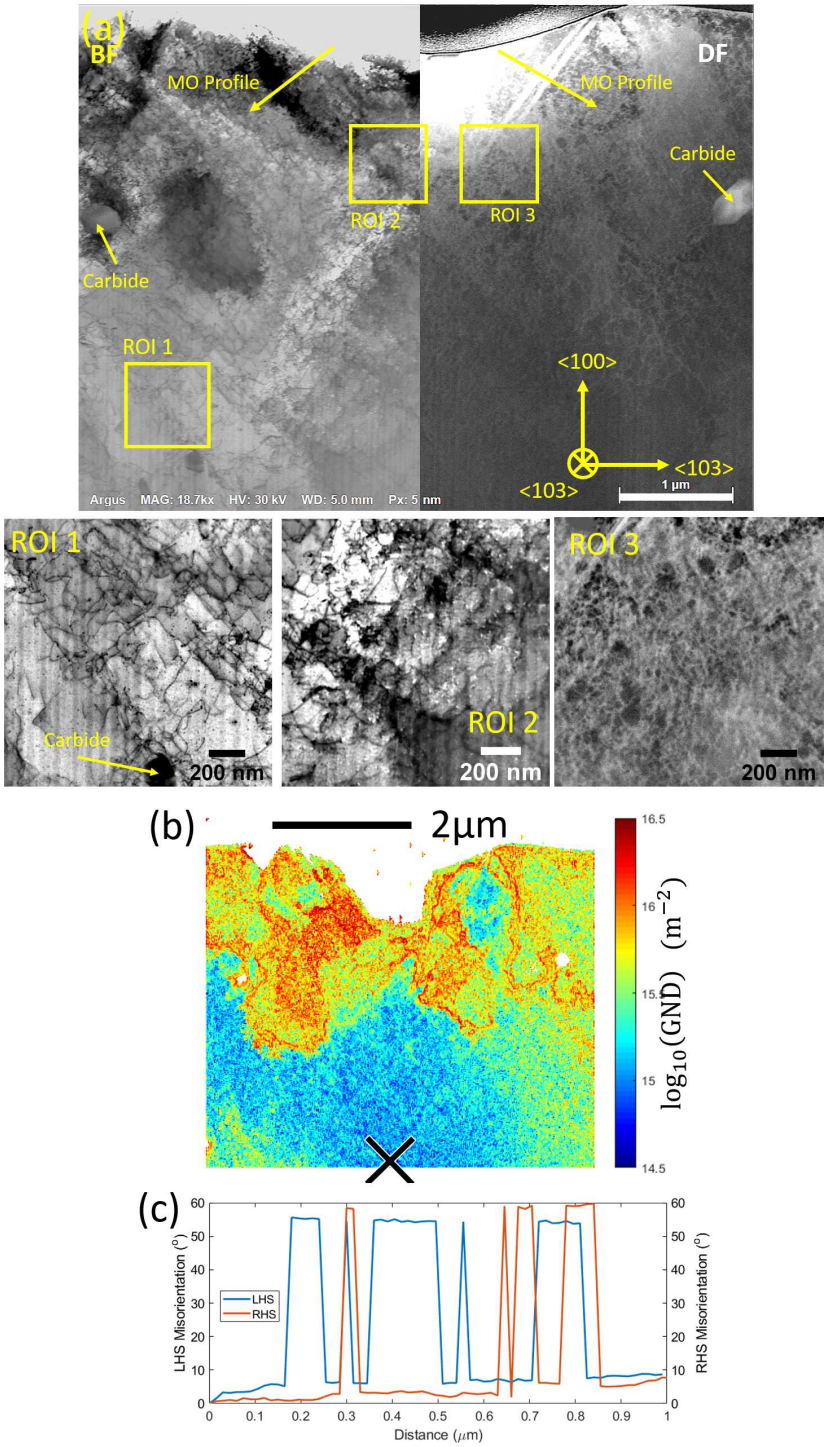


Figure 6.17: (a) Fore-scattered cross-sectional images (both pseudo bright- and dark- field) of a spherical indent in A600 along a near <101> zone axis. (b) Calculated GND map is shown for comparison. (c) Misorientation profile collected along the pathways shown.

show this level of anisotropy, and are only 62% the reported bulk values. The errors in calculating the modulus of A600 can be linked to two main effects. Firstly, the elastic field is larger than the plastic zone and thus impinges on multiple orientations [318], this is highly likely given the 25 μm grain size. Secondly, the small elastic response limits the accuracy of the zero point correction, which disproportionately affects the modulus value.

6.4.1.2 Yield Stress

Pathak and Kalidindi define values of yield stress as the stress required for continuous plastic deformation. This value for SS316L was found to be 2.1 - 2.4 GPa, which is in good agreement with the 2.4±0.5 GPa nanoindentation yield stress found in literature [319]. A800 is measured to be between 2.1 - 2.3 GPa. While no spherical indentation data on A800 has been found in literature, a comparison is made to the hardness determined by 200 nm Berkovich indents, which is reported to be 5.2 GPa [312]. Taking macroscopic rules of Yield = Hardness/3, we find that the predicted yield stress would be 1.7 GPa, which is within the error range of the experimental yield stress. The nanoindentation yield stress of A600 is 600 - 800 MPa. This value is distinct from the other materials as it is comparatively low, indicating that A600 is softer than the other austenitic alloys. This result is incompatible with the maximum applied load which suggest that the A600 is harder than the other alloys. This magnitude of yield is more typical of micro-tensile or micro-pillar compression tests [320] rather than nanoindentation.

The yield values determined by nanoindentation are higher than the bulk values, typically 230, 183 and 205 MPa for SS316L, A800 and A600, that have been reported. The mechanism responsible for the increased yield stress is Nix-Gao size-effect, which suggest that the 300 nm indents are significantly stronger than bulk values. Finally, data from shallow indents are known to be less quantitatively reliable than deeper indents, however the priority of this chapter was comparing mechanical data with high magnification lift outs, which necessitated shallow indents.

Comparing mechanical tests to autoclaved SCC studies is difficult. This is because the yield stress has become a proxy term for quantifying the resulting microstructural changes introduced by cold-work [321, 322, 323, 324, 41], and there

are large variations in materials and testing conditions. It was suggested that an empirical relation third-power law can be established between the CGR and yield strength [41, 325]. Using this as an approximate relationship, would predict A600 to be the most resistant alloy, which is not true [15].

Figures 6.8, 6.10 and 6.12 show the pop-in loads for the austenitic alloys. Pop-ins originate when dislocation movement or nucleation occurs. Nucleation results in stresses that are near the theoretical limits of the material, while movement occurs at lower stresses. As the pop-in load is greater in SS316L it suggests that generating dislocations requires greater energy, or that dislocation sources are more distant. As reported in the preliminary characterisation, the background dislocation density in A600 is an order of magnitude higher than the other samples. As the availability of dislocations is greater, this means that new dislocations do not need to be created to initiate plasticity, and plasticity can occur by the movement of dislocations at a lower stress. However, the reported pop-ins for A600 are not thought to be reliable, this is due to the small elastic zone present, which could be influenced by the surface roughness.

Two observable trends are suggested from the pop-in data. First, as the nickel content increases the mean pop-in load decreases from 3.0±1.9 mN, to 1.8±1.1 mN, to 0.5±0.4 mN (Figure 6.13). However, the errors that are associated with these values - the standard deviation of the recorded pop-in loads - show heavy overlap. The second is that <001> and <101> orientations display pop-ins at higher loads than <111> orientations. This orientation-based dependency is thought to link to the Schmit factor, which is minimised along the <111> normal grains.

6.4.1.3 Experimental Reliability

While some of the absolute values presented in Table 6.1, 6.2 and 6.3 agree with those published in literature. There is concerning absence of anisotropy presented in the results, anisotropic properties are commonly reported for austenitic alloys. It is the purpose of this section to determine if this method is capable of detecting such changes in the underlying mechanical properties. I summarise the three main concerns surrounding this experimental procedure, and the steps taken to quantifying reliability and accuracy.

Firstly, the experimental results are sensitive on the surface finish and quality. In cases of inadequate colloidal silica, the yield stress can be artificially boosted by up to 30% [237]. Secondly, the determination of the zero-point, where the tip makes contact with the surface is crucial. In materials with distinct pop-ins, this is trivial. However, for others with a smooth elastic-plastic transition, this becomes highly challenging, and can amount to guess work through trail and error. An immediate improve to this method can be made by employing a simple python script that could automatically find the zero-point correction, reducing user error. An automated script would at least introduce some reproducibility between users. It is commented by Pathak and Kalidindi that the zero point correction can make the Young's modulus change by many 10's of GPa is incorrectly completed. This should sit uneasily with those who are familiar with this method of analysis. In the opinion of the author, this introduces a critical flaw in the method that, as it currently stands, is hard to avoid. Finally, the definitions of stress, strain and yield are debated in literature, where different formulations result in significantly altered stress-strain conversions. In addition to this obvious experimental problem, the definitions of stress, strain and yield do no easily equate to the definitions used in other micromechanical experiments. The definitions used in this project are, at the time of writing, the most appropriate. But, this makes comparisons to the limited pool of spherical indentation data challenging at best and impossible at worse.

In the absence of a routine method for characterising experimental errors, such as that for regular nanoindentation, a bench-marking test is completed on a reference sample of Fused silica. This is completed to show the highest achievable accuracy of the method under the most opportune circumstances. The experiment consists of 36 indents, spaced apart 15x the maximum depth. These indents are far enough apart to guarantee there is no overlap in plastic zones, and should mimic the conditions used on metallic samples. Figure 6.18 shows the load displacement and stress-strain conversion for the fused silica indents. It is clear that the zero point correction step is completed well. There is little deviation between curves, and all trace an almost identical L-D curve. The conversion tells a different story. The Modulus, starts to flare out, and values are reported between 69 - 78 GPa, centered on the 74 GPa. The yield stress shows greater variation, at yield, it is

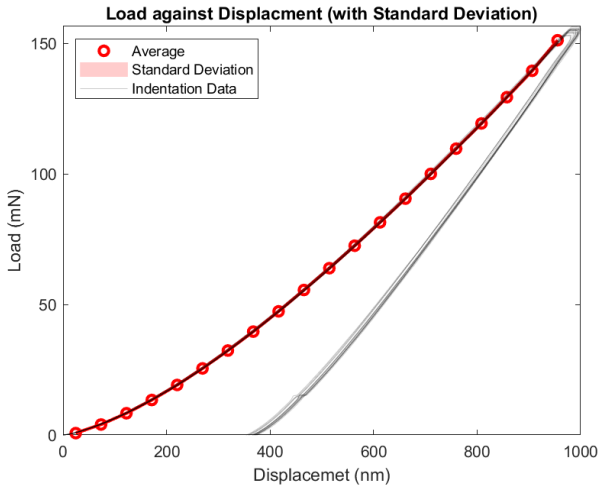
estimated that there is a 2 GPa range, again centered on 12 GPa. This benchmark shows that for ideal materials, the average tends to the accepted values, but a wide variance should be expected. This issue is compounded when we consider that the metallic samples are far from ideal, and the granular structure cannot guarantee that the plastic zones do not overlap.

6.4.2 Lattice Rotations

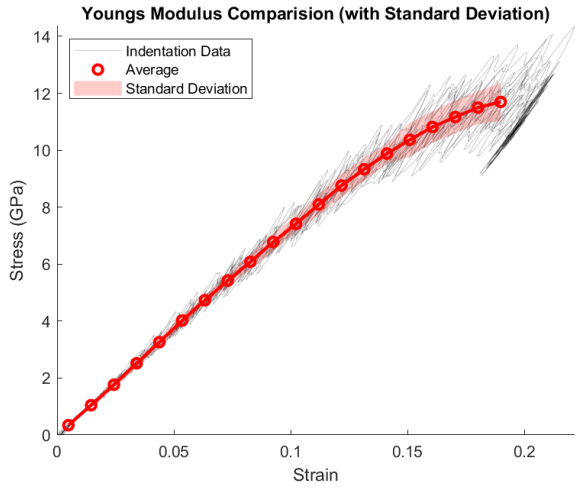
It is important to establish if spherical indentation creates a comparable mechanical response to an SCC crack tip. To achieve this, the lattice rotations created by indentation were compared to those reported from a crack tip using the same method published by Shen et al [18]. It was reported that the average the misorientations of 2.7 ± 1.1^o for SS316L and 2.55 ± 1.1^o for A600 were found from SCC tips. This rotation is highly comparable to that generated by indentation. The deformation zone generated by nanoindentation is an order of magnitude greater than that of an SCC crack tip, i.e. 237±77 nm compared to 500±100 nm, and 226±31 nm against the 1400±200 nm for A600 and SS316L respectively. The larger deformation zone reflects the blunt nature of the spherical tip. It is assumed that further analysis is comparable to published SCC propagation data. The lattice rotations in Table 6.4 appears show a drastic increase in deformation intensity with nickel content (Figure 6.19). I believe that the trend displayed is physically correct, however the magnitude of the maybe misrepresented given the anomalously low results achieved mechanically for A600. It also assumes that the plastic deformation is independent on load, which is hard to justify.

6.4.3 Deformations and Dislocations

There is an excess of dislocations generated during deformation to accommodate plasticity in the three tested austenitic alloys, however, there are stark differences between measurable factors. The dominant mode of deformation in the nickel-rich samples is dislocation glide, while Fe-rich SS316L undergoes considerable deformation twinning. This result can be rationalised by conventional theories of stacking fault energies (SFE). SS316L has the lowest SFE, which literature estimates to



(a)



(b)

Figure 6.18: Load displacement (a) and indentation stress strain (b) for fused silica.The bold red reflects the average of the 16 indents, with the shaded area being the standard deviation and the light grey plots represent the data from individual indents.

be between 14-17 mJm^{-2} [326, 327]. SFE theory predicts martensitic transformations and deformation twinning are the dominant deformation mechanisms [328], but only twinning is observed in this sample. This agrees with published data [329]. The SFE of both A800 and A600 are more ambiguous, and aren't as well

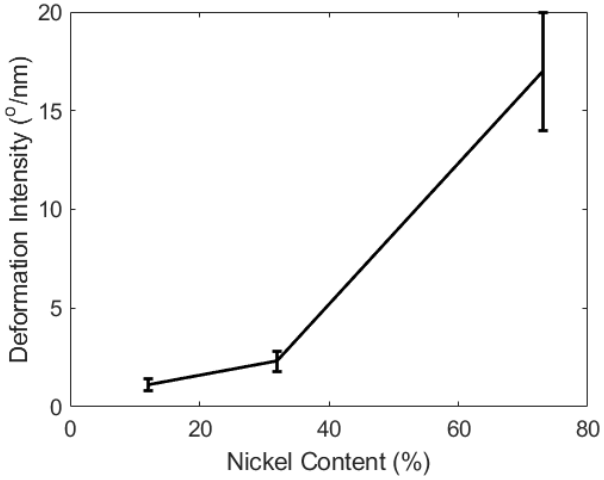


Figure 6.19: The deformation intensity as a function of nickel content.

Table 6.5: Summary of the background, counted and calculated GND dislocation densities from the three samples. Dislocation ratios are presented to normalise for increase in dislocation density.

Materials	ρ_{BG} (m^{-2})	ρ_{Cnt} (m^{-2})	ρ_{GND} (m^{-2})	ρ_{Cnt}:ρ_{BG}	ρ_{GND}:ρ_{BG}
SS316L	2.5±1.1x10^{13}	7.2±0.4x10^{13}	5.6±4.1x10^{15}	2.9±1.3	224±191
A800	1.3±0.6x10^{13}	2.1±0.3x10^{14}	5±3x10^{15}	16.2±7.8	384±290
A600	2.3±0.8x10^{14}	3.0±0.3x10^{14}	6.2±3.1x10^{16}	1.3±0.4	269±163

studied as that of SS316L. Computational simulations report that the SFE of A800 is 29 mJm^{-2} [326]. While TEM observations calculate the SFE of A600 is at least 28 mJm^{-2} [330]. The GND observations support the trends in SFE of the materials. The SFE of A800 is an intermediate of SS316L and A600, but deforms by dislocation glide instead of deformation twinning. As a result of no twins, there is more strain localization along {111} planes.

The GND calculations and bright-field images show similarities with results from Cackett et al [331], who mapped GND densities in cross-sections of spherical indents in copper. An observed trend across both GND and counting methods is that as the distance from the indent increases, the density of dislocations decreases. A summary of the dislocation densities are summarised in Table 6.5. It is unlikely

that there is an strain-free region in these samples, so a background dislocation density was estimated from a relaxed region at the bottom of the lamella, i.e. dislocations can exit the thin film. The counted dislocations, ρ_{Cnt}, is the greatest density observed in the ROIs. The ROIs selected are of equal size. Finally, the ρ_{GND} values are taken as the average GND value directly under the indent, representing the theoretical maximum measured dislocation density. Ratios are present to normalise against the variation in background dislocation densities. A800 shows the greatest normalised increase in dislocation density. Dislocation generation is the primary deformation mechanism seen in A800, and as such the number of dislocations to accommodate the deformation has increased the most.

Table 6.6 shows the localisation of GNDs to the slip bands, or channels, which have formed in the alloys different alloys. In absolute terms, A600 and SS316L have the highest GND densities localised to their slip bands, but relative to the GND between the slip bands, A800 displays a much greater localisation to slip bands. Due to the nature of this method, there is great spatial sensitivity on the GND density. The values presented are based on an average of five-regions. The dislocation channels come with benefits, dislocations are easily transported away from the crack tip, preventing a stress build up and rapid crack propagation. This could in part help attribute A800's improved SCC resistance.

HR-TKD is a powerful tool to image dislocations [270], however there are limitations to this methodology. 1) As noted by Liu et al [273], the rotations and shift in the Kikuchi pattern is a function of both sample thickness and step size. This error was minimised by using identical TKD conditions, 10 nm step size, in the data collection process. 2) The process of creating a sample results in data loss, due to relaxation of the elastic strain, while this is non-negligible it is measured

Table 6.6: The calculated GND density at slip-bands, the spaces between them, and the background regions. The ratios of GND density are presented to normalise for increase in dislocation density.

Materials	Slip-band ρ_{GND} (m^{-2})	Not Slip-Band ρ_{GND} (m^{-2})	Background ρ_{GND} (m^{-2})	ρ_{GND}^{SB}:ρ_{GND}^{NSB}
SS316L	3.6±1.4x10^{15}	1.3±0.3x10^{15}	1.2±0.5x10^{15}	2.9±1.3
A800	1.9±0.7x10^{15}	4.1±1.8x10^{14}	2.8±1.1x10^{14}	4.6±2.7
A600	3.8±1.7x10^{15}	2.4±1.1x10^{15}	1.2±0.7x10^{15}	1.6±1.0

by Karamched et al to be approximately 20% [271]. Due to consistent sample preparation, this is assumed to be constant across the samples. 3) The correlative techniques only capture GNDs, and statistically stored dislocations (SSDs) should not be ignored, as $\rho_{total} = \rho_{GND} + \rho_{SSD}$. Implications of this can be seen in the comparability of the bright-field images and the GND maps. 4) Unlike TEM, the stage is less versatile and the sample can not be tilted. This limitation places a high burden on precise sample preparation for comparative studies, as no corrections can be made in the chamber. 5) Accurate GND calculations rely on a suitable "strain-free" reference pattern. In the results reported for cold-worked and indented samples, a strain-free region should be treated skeptically, because the materials have undergone prior cold-work and already contain significant deformation. The best compromise is to select a central point at the bottom of the lamella. The thinned sample edge, is thought to provide the lowest possible levels of deformation, as the dislocations can escape the lamella.

6.4.4 Quantifying a Mechanical Deformation Mechanism in SCC

Two main conclusions are drawn from the investigations into austenitic alloys. First, the material yield stress shows an inverse correlation with the alloy's nickel-content. As A600 is the softest alloy, it would make strain localisation and therefore crack propagation easier. Secondly, the normalised increase in dislocation density and the normalised dislocation localisation along slip-bands suggest that A800, more so than the other alloys, has increased dislocation activity. This enhanced activity could prevent stress localisation, and require the addition of oxidation to embrittle the material to facilitate meaningful crack growth.

This mechanically focused study has ignored various corrosion-based phenomena to simplify the comparison. In SCC, the propagation at the crack tip is driven by defects, which increase the inwards diffusion of oxygen and outwards diffusion of elements such as Cr and Fe. The increased diffusion of oxygen leads to increased oxidation, and the increased outwards diffusion of Cr and Fe can lead to a more complete protective oxides. These play an important role in the development of SCC, but are not included in this analysis.

These experiments are conducted at room temperature, which is not the same as reactor conditions. To better comment on the temperature-dependent resistance behaviour of A800 [12] testing under more realistic under PWR conditions is needed. The next two chapters are dedicated to improving the testing conditions. The first will introduce electrochemically hydrogen charged nanoindentation, so that the effect of hydrogen on SCC can be directly studied. The second will complete nanoindentation at "cold" (280 °C) and "hot" (360 °C) reactor conditions, to determine the thermal stability of the mechanical properties.

6.5 Summary

Nanoindentation is postulated to generate similar mechanical conditions to that of an SCC crack tip, and can be used to isolate the mechanical properties of nuclear alloys, without the chemical complications associated with autoclave experiments.

Nanoindentation has produced the yield stress from stress-strain conversions. It was found that the yield stress of SS316L and A800 is approximately 2 GPa, while A600 is softer, with a yield stress of 700 MPa. The lower yield stress has resulted in a larger plastic zone in this alloy.

TKD was used to analyse the dislocation structures generated during indentation. Dislocations were counted from bright-field images, and the GND were calculated from the EBSD patterns recorded. These results demonstrated that A600 had the greatest number of dislocations and lattice deformation, but when normalised against the background, A800 has undergone the most drastic deformation.

Chapter 7

Room-Temperature In-situ Hydrogen-Charged Micromechanical Testing of Nuclear Alloys

7.1 Introduction

Hydrogen is known to effect the mechanical properties of metals, commonly resulting in hydrogen embrittlement (HE). There are several theories that attempt to explain HE [95, 92, 88], none of which address the role of hydrogen in stress corrosion cracking (SCC). The purpose of this chapter is to fill this gap in literature, and evaluate the role of hydrogen in SCC. This will be completed by investigating the effect of hydrogen on the deformation of austenitic alloys, and correlating the changes in material properties with Arioka's reported temperature-dependent crack growth rate (CGR) [12]. Data will be collected using a synergistic combination of novel in-situ hydrogen charged nanoindentation and finite element analysis (FEA).

In the previous chapter, the mechanical properties and deformation mechanisms of SS316L, A800 and A600 were characterised in air and at room temperature. In this chapter, the mechanical degradation of hydrogen is determined by re-testing the same SS316L, A800 and A600 samples after they have been electrochemically charged with hydrogen, and comparing the properties to the in-air

results. The FEA presents a 3-dimensional UMATHT user-subroutine that models the coupled mechanical deformation and hydrogen diffusion throughout a sample.

7.2 Experimental

Nanoindentation is well suited to this method for two reasons. Firstly, experiments are completed on a length-scale that is relevant for SCC. Secondly, relatively little sample preparation is needed for completing the parameter studies, i.e. a flat surface. To electrochemically introduce hydrogen there are two options: ex-situ and in-situ hydrogen charging. Ex-situ charging was attempted but due to the mobility of hydrogen and long set up time of the nanoindenter, no experimental differences were reported. This leaves in-situ charging the only option. In-situ hydrogen charged nanoindentation is a novel and highly non-standardised technique, therefore, suitable testing conditions and work-flow have to be established for these austenitic nickel alloys. Over the next chapter, parameter studies are presented, followed by some results achieved by in-situ hydrogen charged nanoindentation.

7.2.1 Results

7.2.1.1 Electrochemical Potentiodynamic Polarisation

Potentiodynamic polarization tests were conducted to determine appropriate charging conditions for the in-situ electrochemcial charging tests. The electrochemical measurements were taken using a variety of solutions. The electrolyte solutions tested are 0.1M sodium hydroxide (NaOH) and 0.1M sodium hydroxide with 5 g/L thiourea (0.1M NaOH + 5 g/l CH_4N_2S) both with a pH 12. The tests were completed at room temperature. All measurements were made vs. the open circuit potential, which was measured over the first 120 seconds of each test, and used a sweep rate of 2 $mV{\cdot}s^{-1}$.

Table 7.1 shows that the corrosion potentials and current densities of SS316L, A800 and A600 are highly comparable. This means similar electrochemical conditions can be used to charge samples with hydrogen during experiments. The addition of thiourea (CH_4N_2S) causes an increase in current density, indicating an increased corrosion activity, and a shift toward cathodic potentials.

Table 7.1: The corrosion current density and voltage determined by potentiodynamic polarisation of SS316L, A800 and A600 in 0.1M NaOH with and without 5g/L thiourea (CH_4N_2S).

	0.1 M NaOH		0.1M NaOH + 5g/L CH_4N_2S	
Material	$\log_{10}(i_{corr})$ ($\mu A \cdot cm^{-2}$)	V_{corr} (mV)	$\log_{10}(i_{corr})$ ($\mu A \cdot cm^{-2}$)	V_{corr} (mV)
SS316L	-2.4	-650	-2.1, -2.4	-950, -650
A800	-2.4	-650	-1.9	-1000
A600	-2.5, -2.5, -1.8	-700, -800, -1000	-1.9	-1000

Figure 7.1 shows the potentiodynamic polarisation of SS316L in the two electrolytes. In the anodic branch of the diagram, SS316L undergoes passivation in the potential ranges of -500 to 200 mV, and the break-through potential of the passive film on the surface occurs at potentials of 600 mV in both electrolytes. The cathodic branch shows that the current does not excessively rise with increasing over-potential, and is suitable for a variety of charging cathodic over-potentials.

Figure 7.2 shows the potentiodynamic polarisation of A800 in the two elec-

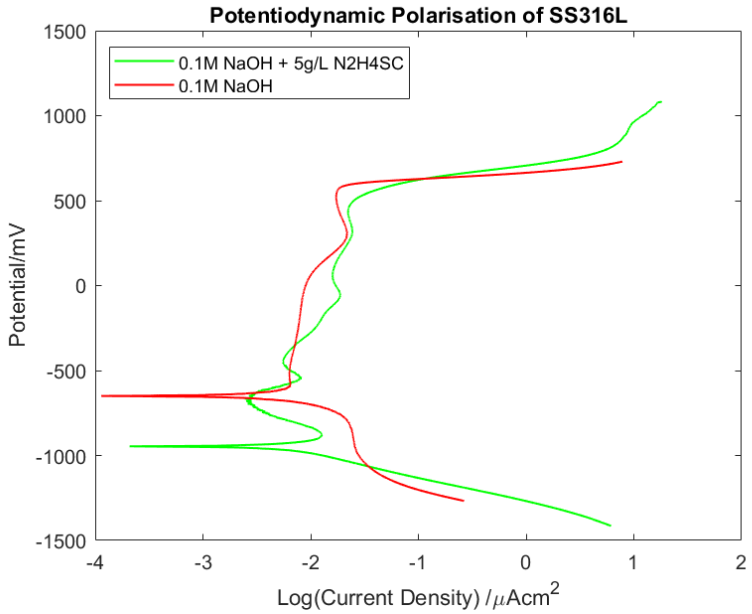


Figure 7.1: Potentiodynamic polarisation of SS316L in 0.1M NaOH with and without 5g/L thiourea (CH_4N_2S).

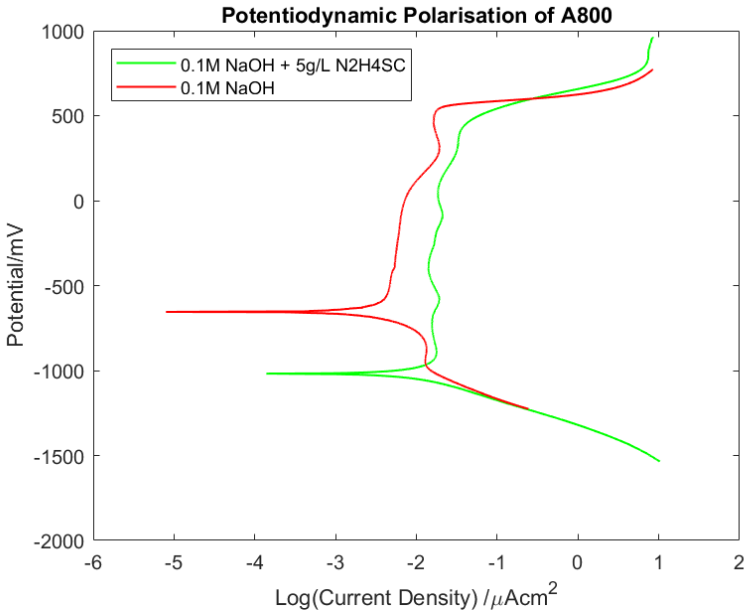


Figure 7.2: Potentiodynamic polarisation of A800 in 0.1M NaOH with and without 5g/L thiourea (CH_4N_2S).

trolytes. In the anodic branch there is a passive region from -500 to 400 mV and -900 to 400 mV for the 0.1M NaOH and NaOH + 5 g/L CH_4N_2S electrolytes respectively. Both electrolytes have a break-through at 600mV. The cathodic side appears to briefly plateau in NaOH, but corrosion activity increases at greater cathodic potentials.

Figure 7.3 shows the potentiodynamic polarisation of A600 in the two electrolytes. In the anodic branch of the figure, there is a region of passivisation extending from -500 to 0 mV for both electrolytes, and the break-though potential is 300 mV. The cathodic branch shows increased dissolution with increasing over potential. There are multiple corrosion potentials observed, this is in part linked to the free corrosion of the multiple oxides that can be formed in A600.

7.2.1.2 Effects of Charging Conditions on the Sample Surface

The effect of localised corrosion and deposition on the surface during charging was investigated in a comparative study. Maintaining a flat and unmodified surface is crucial, as any hydrogen charge results achieved with a modified surface can

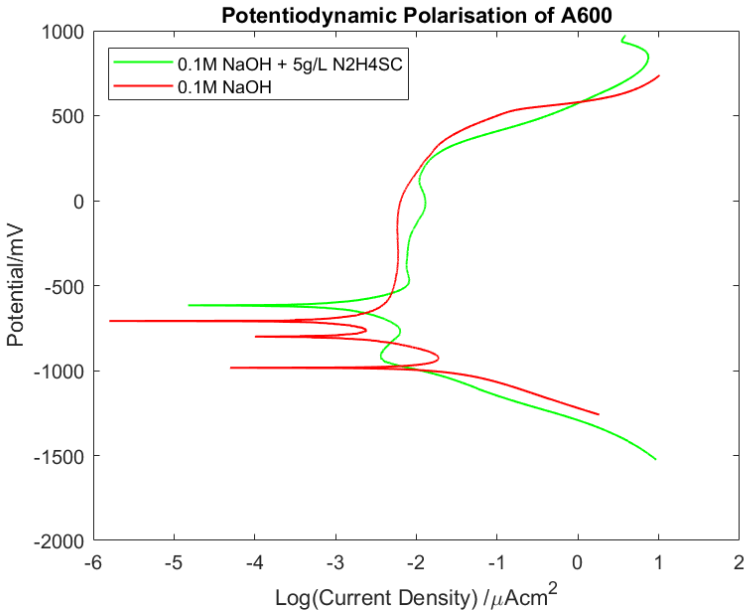


Figure 7.3: Potentiodynamic polarisation of A600 in 0.1M NaOH with and without 5g/L thiourea (CH_4N_2S).

not be attributed to only hydrogen. Nine identically prepared samples of A600 were charged at a 500 mV cathodic over-potential at potentials of -1500, -1540 and -1480 (corresponding to current densities of 2, 5 and 10 mA/cm^2), for several hours (2, 4, 8 hours). The electrolyte used is a standard 0.1M sodium hydroxide (NaOH) solution with a pH 12. The surfaces were imaged using a scanning electron microscope at 200 - 15,000 times magnification. Representative images are shown in Figure 7.4.

Figure 7.4 shows the surface conditions after charging compared to a uncharged reference sample. The sample surfaces charged at 2mA/cm^2 are largely unaffected. No large corrosion products are visible, and the surface has remained flat over all charging times. There are some fine and sparsely distributed spherical particulates on the surface with a diameter <100nm, but given their absence on the majority of the samples, this is thought to be from alternative sources, such as colloidal silica for polishing.

The surface conditions after charging at a current density of 5mA/cm^2 show an increased level of damage. After 2 hours, fine structures can be seen covering

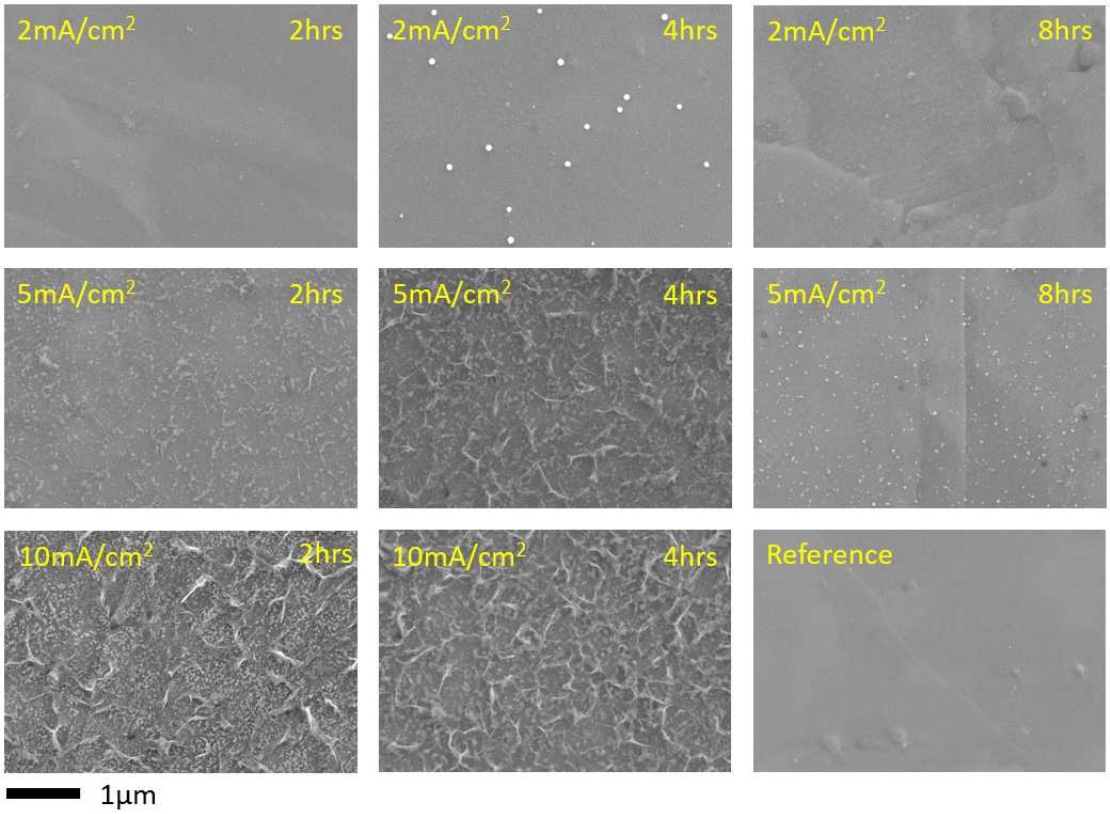


Figure 7.4: A comparative study of the surface conditions after charging at different conditions for different times at 15,000 times magnification.

the majority of the surface. After 4 hours, these fine structures coalesce to form string-like structures across the surface which extends up to ≈500 nm in length. The absence of any corrosion products after 8 hours is believed to be an anomalous result.

The surfaces charged at 10mA/cm^2 display the highest levels of surface deposition and corrosion. Hydrogen charging has introduced a surface coverage of long string-like corrosion deposits. There appears to be enhanced texturing underneath these corrosion structures, indicating that the surface has been irreversibly damaged and can not be tested by nanoindentation. This comparative study has demonstrated that as the current density, and to a lesser extent exposure time, is increased, the surface corrosion also increases and can lead to permanent damage. To minimise surface damage, the best charging condition to use is 2 mA/cm^2, as

this can be maintained for a long period of time.

During these investigations, it was noted that if the current density is too high, or the electrolyte is too aggressive, then the sample surface can crack. Figure 7.5 shows the hydrogen-induced surface cracks in a sample of A600 in a 0.5M H_2SO_4 electrolyte. These cracks are formed due to the increased lattice strain, caused by the high concentration of hydrogen in the lattice. Samples that undergo such surface cracking can not be used in nanoindentation experiments. For this reason, alkaline electrolytes are preferred as they are more gentle on the material surface, both in this investigation and in literature [223, 227, 160, 176].

7.2.1.3 Nanoindentation in a Liquid Environment

Resolving the buoyancy and meniscus forces acting on the indenter tip during testing is not possible. However, it is possible to demonstrate that testing in liquid environment does not significantly interfere with the results. 25 indents were completed in air and in a 0.1M NaOH liquid environment (with no applied potential) on a single grain of A800. Figure 7.6 shows that the liquid environment increases the maximum load by approximately 3-4%. This systematic error introduced by the liquid environment is small compared to the 20%+ load changes recorded by hydrogen in literature [332, 121]. The forces introduced by the liquid are thought

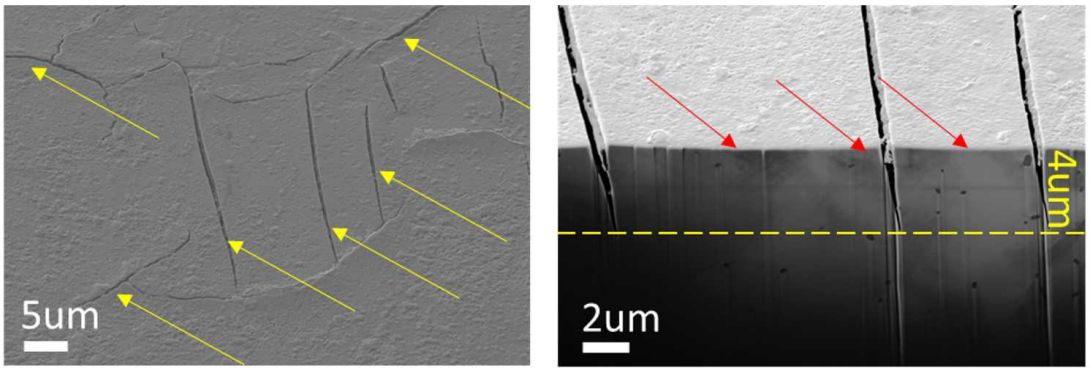
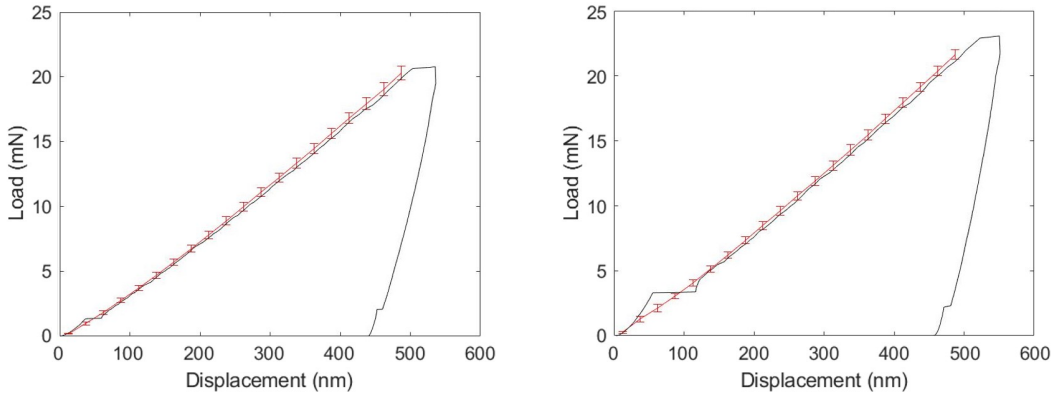


Figure 7.5: The surface (Left) and depth profile (right) of an A600 sample after a total charging time of 8 hours in an 0.5MH_2SO_4 electrolyte. Yellow arrows highlight inter- and intra-granular cracks that extend 4μm into the surface. Red arrows highlight changes in contrast due to lattice straining and relief, support an idea that a large hydrogen concentration was established.



(a) (b)

Figure 7.6: Spherical indentation on a single grain of A800 (a) average of 25 indents (red) in air (b) average of 25 indents in liquid. Black data curve shows a typical load-displacement curve. The sudden increase in load (pop-in) is unique to each test and is not comparable.

to be negligible compared to those required to deform the stiff alloys, and therefore can be ignored.

7.2.1.4 In-situ Electro-chemical Hydrogen Charged Nanoindentation

In the previous sections, suitable electrochemical charging parameters have been determined, and the effect of the liquid environment investigated. The indents were completed on the MTS XP with the custom made in-situ charging cell. The indents were a depth of 300 nm and completed in 4x4 arrays on a single grain. The indent spacing was 1 μm. This depth and spacing of the indents was chosen to match the conditions used in the previous chapter.

Figure 7.7 shows representative load-displacement and nanoindentation stress-strain curves collected on a similar <001> grain orientations to increase comparability between SS316L pre- and post- hydrogen charging at 2mA/cm^2 for 8 hours. The air indents can be broken in to four stages: initial elastic loading, a sudden increase in displacement (pop-in) which indicates the on-set of plasticity due to the activation of dislocation sources, subsequent elasto-plastic loading and elastic unloading. However, the indents collected under hydrogen charged conditions forego the pop-in, and transition directly from elastic to elasto-plastic deforma-

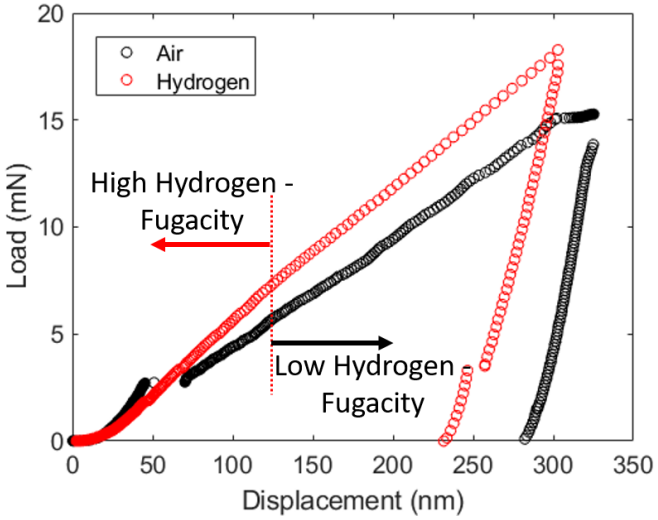
Table 7.2: A summary of the material properties of SS316L in the <001> orientation, collected under in-air and hydrogen charged conditions.

Material	Environment	Max Load (mN)	Modulus (GPa)	Yield Stress (GPa)	Pop-in Load (mN)
SS316L	Air	14.0±0.6	183±23	2.4±0.5	3.1±1.2
SS316L	Hydrogen	18.8±1.3	154±29	2.3±1.0	0.5±0.3

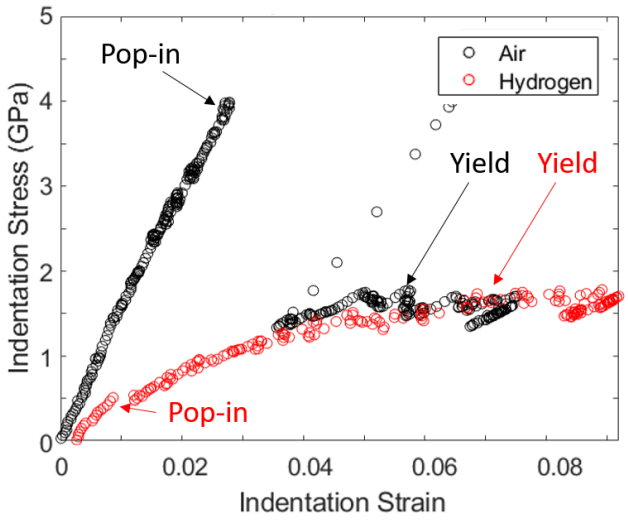
tion. The L-D curves show that the hydrogen charged sample is harder than the air sample, indicated by a 4.8 mN (28%) increase in the maximum applied load. This increase is significantly greater than the 1 mN (4%) increase in load caused by the liquid environment, and can therefore be attributed to hydrogen. As seen in the figure, there is an inflection point (large change of gradient) in the hydrogen charged L-D curve at 110±10 nm. Such inflection points are characteristic of a regime change, the decreased hardening suggests that the hydrogen fugacity has decreased at greater indentation depths, and the material properties recover to the underlying bulk values.

Table 7.2 summarises the material properties of ten air and ten charged indents. The average maximum applied load at deep indentation depths increases by approximately 4.8 mN, indicating that the hydrogen charged material is harder than the bulk sample. The recorded moduli are distinctly different, but the error bars overlap between air and hydrogen charged samples. This is in contrast to the reported literature which states that hydrogen has no effect on the material modulus [121, 333]. The yield stresses are also within error. This is limited by the definition of yield, which is heavily weighted towards the properties at greater depths. As seen in Figure 7.7b, the material properties recover deeper into the bulk. The pop-in load also decreases by approximately 2 mN, this indicates that plasticity is on average initiated at lower loads. The reduction of pop-in load could suggest that austenitic alloys are susceptible to hydrogen enhanced localised plasticity at lower loads.

Results for A800 and A600 were not achieved, this is because after several attempts at longer charging times, corrosion of the indenter shaft was observed. As a precautionary measure to prevent permanent damage, further experiments were halted. With no clear path to achieving further hydrogen charging results, a computational approach was explored. During this project, it was possible to



(a)



(b)

Figure 7.7: (a) Representative load-displacement and (b) indentation stress-strain curves achieved on <001> in SS316L under air and hydrogen charged conditions.

develop a 3-dimensional fully coupled hydrogen transport sub-routine (i.e both mechanically and diffusion driven), based on the works of Barrera et al [282]. The motivation for developing a finite element model is to extract experimental values of hydrogen fugacities, and understanding the diffusion of hydrogen in the sample. The results of this coupled model are presented and discussed in the next section.

7.2.2 Discussion

The electrochemical behaviour of austenitic alloys was investigated, and shown to be similar in across multiple electrolytes. The addition of a hydrogen-promoter, such as Thiourea, drives activity and results in higher current densities during corrosion tests. The effect of electrochecmial charging on the surface samples of austenitic alloys has been explored qualitatively. It was determined that the best charging condition to use was 2 mA/cm^2, as this was the highest current that best maintained the sample surface over a range of charging times. Alkaline electrolytes are preferred over acidic electrolytes to minimise surface damage.

Figure 7.6 has demonstrated that the liquid environment effects the recorded load-displacement negligibly, and therefore no special considerations need to be accounted for in the analysis of the hydrogen-charged data. These observations on the effect of a liquid environment agree with previously published works of Barnoush [111, 121] and Mann [334].

7.2.2.1 Limitations of In-situ Nanoindentation

Figure 7.7 has demonstrated that hydrogen charged nanoindentation was successfully conducted on SS316L. The main effect of hydrogen is to significantly increase the hardness of the material by approximately 30% at deep indentation depths, and to enhance the onset of plasticity from 3.1±1.2 to 0.5±0.2 mN at low loads. This change seems to be purely driven by the presence of hydrogen and its variation throughout the material. This is in agreement with the HELP mechanism, and the findings of Wang et al on TWIP steels [121] and Yao et al on iron alloys [335]. To realise the potential implications, consider a SCC test. The crack tip region would have a higher concentration of hydrogen, as it is directly injected from the environment by corrosion processes. The hydrogen will preferentially diffuse to high stress regions (as shown in Section 7.3.1), and cause the pre-mature deformation, a smaller plastic zone would be expected overall.

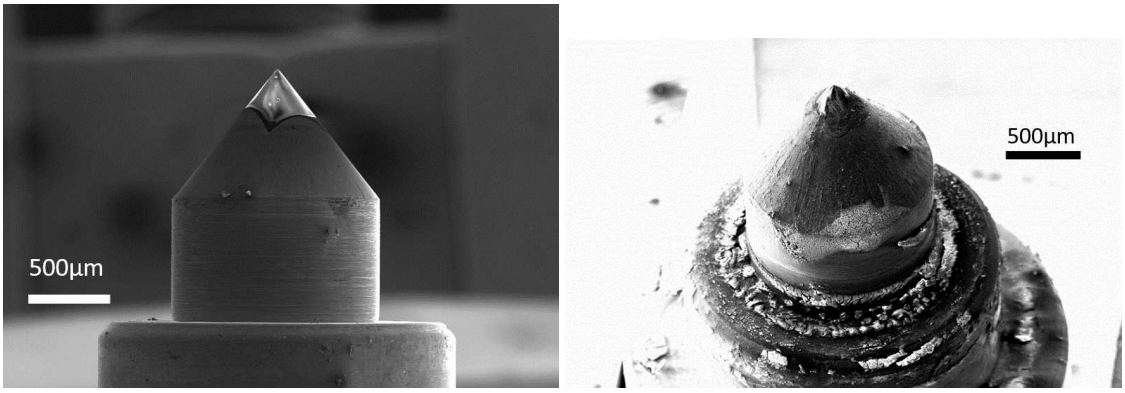
The nanoindenter started to show signs of corrosion around the indenter shaft, with increased in-situ charging times. It is unclear what part of this experiment caused this corrosion. As the nanoindenter relies on fine components to operate with nanometer accuracy, any potential damage was unacceptable, and in-situ

charging could no longer continue in its current form. A solution to this issue is provided by Kim et al [336], who has developed a method of back-charging a sample with hydrogen to avoid corrosion of the tip, surface, or nanoindenter. Manufacturing such a testing cell was considered, but disruptions due to the coronavirus halted all progress. It is therefore left for future work. It was not possible to establish a correlation between Arioka's reported SCC CGR [12] and the effect of hydrogen on mechanical properties. This was due to instrumental limitations.

The greatest challenge faced by this methodology is sufficiently charging the material with hydrogen, while maintaining the testing surface. The L-D curves suggest that after 8 hours of charging a large hydrogen fugacity was established in the first 100 nm of the bulk. The 8 hour charging time used was the longest supervised charging period managed, but it is clear that this is insufficient for the 300 nm indents attempted. There are two solutions, (1) decrease the indentation depth or (2) increase the charging time. (1) In literature, it is highly uncommon to indent over 100 nm into a hydrogen charged material, let alone the 300 nm indents attempted in this project [332, 111, 337, 333, 121]. It is believed these shallow depths are chosen to avoid long periods of charging. However, shallow indents return less reliable mechanical data, as they are more susceptible to size-effects, such as the nano-jackhammer effect [338]. (2) It is estimated from Fick's law that a charging time of at least 24 hours is needed to generate a sufficient hydrogen environment throughout the indentation depth. To hydrogen charge a sample unsupervised for 24 hours would require a method of monitoring the electrolyte, as the controlled humidity and temperature conditions for required by the nanoindenter cause evaporation of the electrolyte. Prior to reporting corrosion on the nanoindenter, I was pursuing longer charging times, as the experimental challenges are favoured over unreliable data from shallow indents.

7.2.2.2 Tip Condition

Figure 7.8 shows the nanoindenter tip after several hydrogen charging experiments. It is clear to see that it is ruined from deposition, and can no longer be described by a sphere, voiding the calibrations. EDX shown in Figure 7.9 suggests that the deposited materials are copper, silver, sulphur and nitrogen. The copper is from an earlier cell design, in which lacquered copper wires were connected the anode and



(a) (b)

Figure 7.8: A macroscopic view of the tip (a) before in an SEM, and (b) after using optical microscopy.

cathode to the power supply through the electrolyte. It is clear that the copper was attacked through this lacquer, and deposited on the sample and indenter tip. Similarly, silver paste, which is used to establish a strong electrical connect between the sample and the mounting stub, is attacked through the lacquer. This means that a minimum amount of metallic components should be exposed to the electrolyte, as protecting them is not simple. Finally, both sulphur and nitrogen are from the thiourea (N_2H_4SC) used to promote hydrogen absorption. These cannot be prevented so long as thiourea is used. This analysis serves as an illustration as to how quickly deposition can occur on the tip. This has certain implications to the method of data analysis which assumes the tip is fully described by the calibration and the deposition changes the shape, effective radius and elastic values.

7.3 Computational Analysis of In-situ Hydrogen Experiments

7.3.1 Results

A model nanoindenter simulation is considered, Figure 7.10 shows a 2D cross-section of the 3D tip and bulk material. In the analysis, it is assumed that there is full coupling between the mechanical and diffusive processes, and that the constitutive assumptions made are appropriate for a stainless steels. All boundaries

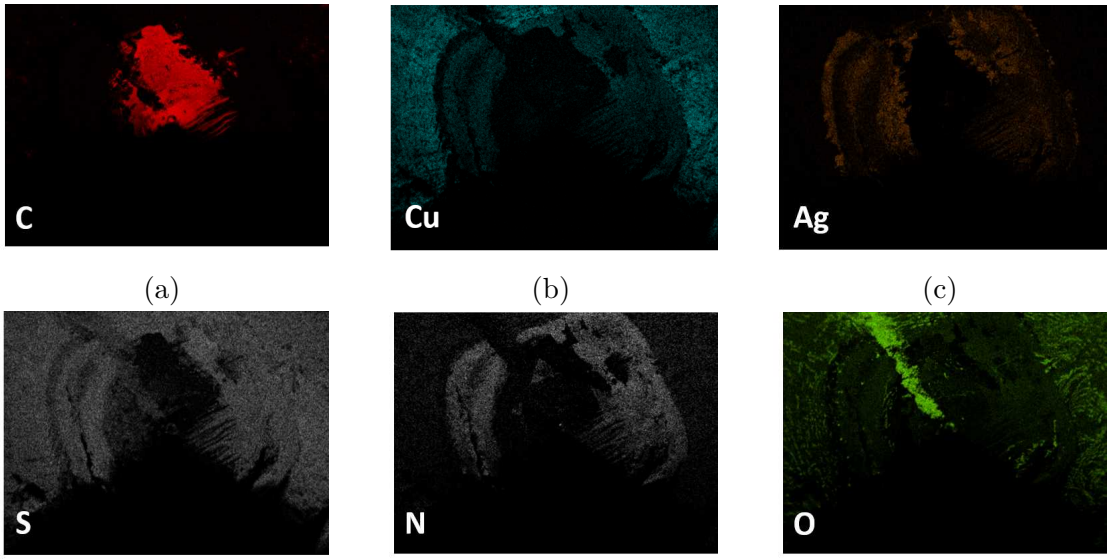


Figure 7.9: Elemental analysis via quantified EDX revealed that several impurities are deposited on the indenter tip during in-situ hydrogen experiments.

are insulted, meaning hydrogen can not leave the volume, or diffuse into the tip. The tip is gradually driven into the bulk at a rate of 180 nm·s^{-1} until the desired depth is reached to replicate experiments (i.e. 120 nm for air, 100 nm for hydrogen charged). Different depth are simulated as the experimental data is collected using a load-controlled method (i.e. indenting until 2000 μN loads are achieved). Load controlled indents are not as simple to model, so it is assumed that a displacement equivalent is appropriate. In total the experiment lasted 1.1 s.

The coupled hydrogen diffusion is achieved by solving the diffusion equation in Eq 4.16, by its UMATHT implementation given in Eq 4.17–4.20. Additional material parameters are taken from literature and summarised in Table 7.3. The bulk material was modelled using 20-noded thermally coupled brick with tri-quadratic elements and a reduced number of integration points (C3D20RT). A biased mesh was applied, decreasing from 5000 nm at the edge of the sample to 100 nm at the point of first contact under the tip. The indenter tip was modelled as three-dimensional quadrilateral rigid object (R3D4). A similar biased mesh size was applied, decreasing from 2000 nm to 200 nm. The total number of elements used

Table 7.3: Material Parameters used in the simulation of TWIP steel with source.

Parameter	Value	Citation
N_L number of solvent atoms per unit volume	9.24x10^{28} mol m^{-3}	[282]
N_A Avogadro's Number	6.023x10^{23} atoms mol^{-1}	[282]
D_L Lattice hydrogen diffusivity	1.8x10^{-16} m^2s^{-1}	[121]
β Number of interstitial sites per atom	6	[282]
ρ Background dislocation density	1x10^{-10} m^{-2}	[121]
a Lattice parameter	2.86x10^{-10} m	[282]
V_H Partial molar volume of hydrogen	2x10^{-6} m^3 mol^{-1}	[282]
W_B Binding energy to a dislocation	-18 kJ mol^{-1}	[282]
A Young's modulus/yield stress	309.9	Fitted

was 4936.

The time step dt is optimised in the ABAQUS programme, but initial conditions need to be provided. To ensure that the time step initially chosen is sensible, the characteristic time for diffusion is calculated $t_c = l^2/D_L$. The characteristic length l is the total indenter depth, i.e. 100 nm. The characteristic time is 5x10^{-3} s, so an initial dt of 5x10^{-6} s is selected, with a maximum allowed dt of 5x10^{-4} s. This demonstrates that the total experimental time, T=1.1 s, is sufficient for hydrogen to diffuse, as T=200t_c.

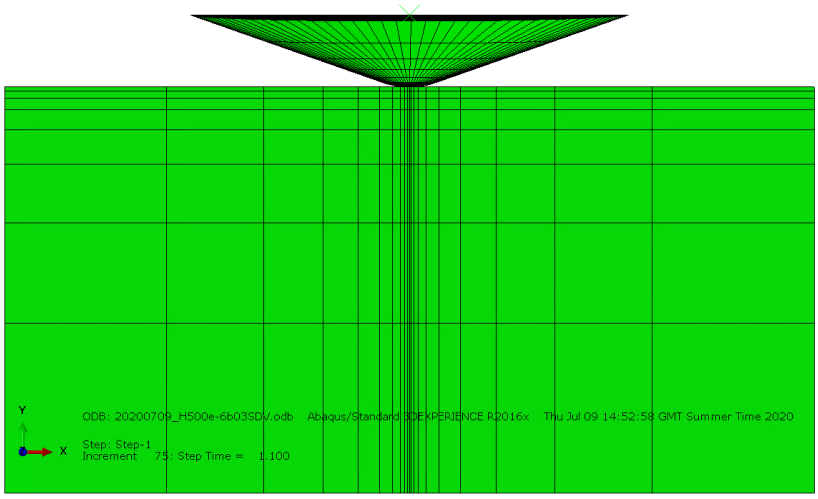


Figure 7.10: Schematic drawing of the conical nanoindenter model.

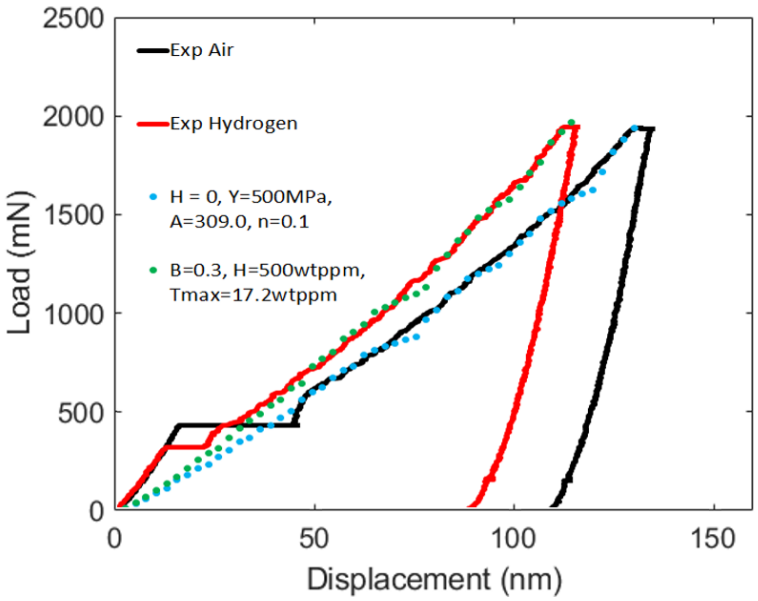


Figure 7.11: Fitted hydrogen charged results for TWIP steel using UMATHT script. Experimental data provided by Dr Wang, from [121].

Figure 7.11 shows the load-displacement curves of in air and hydrogen charged TWIP steel, with the fitted UMATHT-FEM results superimposed. The in-air results are fitted first, to determine the underlying bulk material properties. During fitting, the hydrogen field is set to zero everywhere, i.e. H = 0 wtppm. The elastic properties are fitted to the Hertzian response initially observed in the first 20 nm, the Young's modulus E = 155 GPa and Poisson's ratio $\mu = 0.27$, the same as the values reported in [121]. In these simulations swelling due to the introduction of hydrogen is ignored for simplicity. An assumption of the model is that the current yield strength of the material is a function of both the plastic strain and lattice hydrogen concentration, i.e $\sigma_Y = \sigma_0^H(\bar{C_L})(1+\epsilon^p/\epsilon_0)^n$, where $\sigma_0^H(\bar{C_L}) \propto (\mathrm{H}/\mathrm{H}_{max})^B$ by an isotropic hardening law. More information can be found in an article by Barrera [282]. The initial yield strength is fitted to the plastic segment of the L-D curve, $\sigma_Y^0 = 500$ MPa, and the hardening exponent n = 0.1. This hardening exponent is not considered to be affected by hydrogen. This is common practice in literature to facilitate reasonable computation times, but it is likely that the plastic flow leads to increased strain hardening. It is assumed $\epsilon^p = 0.2$ [282].

With the underlying material properties fitted, the UMATHT subroutine can be activated by setting H > 0 wtppm. The experimental results show that hydrogen causes the TWIP steel to become harder, and the pop-in values are reduced. It is determined through fitting, that the initial uniform hydrogen concentration in the lattice is 500 wt ppm, i.e $\bar{C_L} = 785$ mol$\cdot$ m^{-3}, which is an order of magnitude above the hydrogen concentrations at which hydrogen embrittlement in nickel-base alloys has been observed [339]. The initial hydrogen concentration in the lattice, H, was fitted to be H = 500 wtppm. For nickel alloys and steels typical values range between 3.5 wtppm [305] and 2.3×10^6 wtppm [340], with many more in between [341, 342, 343, 282, 341]. The UMATHT subroutine cannot predict pop-ins, as they do not conform to the continuous model of plasticity implemented.

The distributions of hydrostatic stress and lattice hydrogen concentration at the end of the nanoindentation simulations are shown in Figure 7.12. The hydrogen concentration in the region 20-80 nm ahead of the indenter tip is 30 wt. ppm greater than the lattice mean, the concentration peaks at 50 nm. The increased hydrogen concentration is supplied to this region from the volume 100-250 nm ahead of the indenter tip. The hydrostatic stress similarly peaks at 50 nm and drops off as the distance to the tip is increased.

It appears to be possible to model the type of hydrogen-charged nanoindention results presented in this chapter and in literature using a fully coupled hydrogen transport sub-routine. This is because hydrogen enhanced localised plasticity (HELP) is the most commonly reported mechanism responsible for the micromechanical observations in literature [121, 337, 333]. To achieve the experimental hardening, the model is highly constrained, and requires large values of hydrogen concentration to achieve the desired hardening. Such aggressive constraints can be problematic and indicative of additional mechanisms that are not considered, i.e. hydrogen induced decohesion (HID).

Hydrogen-charged stainless steels, Figure 7.7, display similar experimental results to hydrogen-charged TWIP steel, suggesting these alloys are subject to the same mechanisms. This indicates that it is likely that the simulated hydrogen response in austenitic alloys would also be similar to that of TWIP steel. The diffusion coefficients of TWIP steel and austenitic alloys are roughly comparable [121, 120], so the effects of diffusive hydrogen should be similar. Amongst the

three austenitic alloys investigated in previous chapters, there are several fundamental parameters that differ, i.e. lattice parameter and background dislocation density. So while the simulations of the three alloys would show similar trends, the numerical values could differ significantly. The relation to an SCC study is explored in the discussion.

7.3.2 Discussion

A 3-dimensional User-MATerial coupled Hydrogen Transport (UMATHT) sub-routine has been generated from a 2-dimensional version supplied by Barrera et al [282]. The purpose of this sub-routine is to analyse and explain experimental results, in the framework of the HELP mechanism. The HELP mechanism implies

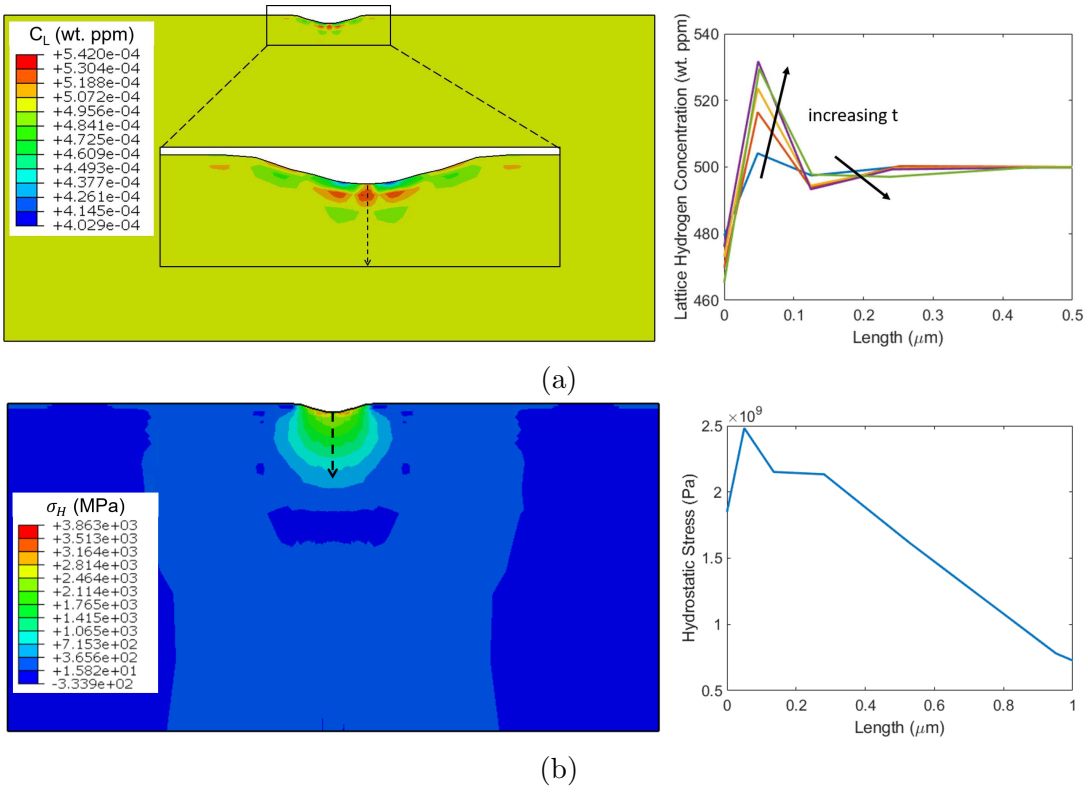


Figure 7.12: (a) The resulting lattice hydrogen concentration, and a profile of the lattice hydrogen concentration ($\bar{C_L}$) underneath the indenter tip during the simulation. (b) The resulting hydrostatic stress (σ_H), and a profile of the hydrostatic stress underneath the indenter tip at the end of the simulation.

that hydrogen reduces the applied stress required to move a dislocation past an obstacle, increasing mobility. The two main features of this mechanism are (1) materials softening, and (2) localisation of plastic flow in regions with high hydrogen concentrations. It is assumed that hydrogen either occupies interstitial lattice sites (NILS), or trapping sites, following Oriani's assumptions.

The response of hydrogen-charged nanoindentation has been analysed, which contains a blunted tip driving into a bulk material. It is observed that (1) hydrogen accumulates ahead of the indenter tip in regions of high hydrostatic stress, and (2) the plastic flow leads to increased strain hardening and a locally increased yield strength [282]. The model parameters are highly constrained, which is indicative of other active mechanisms that are not accounted for here. Literature, provides little assistance, most values reported vary wildly (3.5 to 2.3×10^6 wtppm [305, 340]) due to the immaturity of this emerging field of study. This does how ever make extracting meaningful hydrogen concentrations challenging. The challenges faced in the HE community resemble those in the SCC community, and it is emphasised that a single prescribed solution to HE is highly unlikely. A more pragmatic approach is to consider materials on a case-by-case basis.

During reproducing experimental nanoindentation L-D curves, there was an issue with tip geometry. It was reported in literature that the Berkovich tip had a contact radius of 1 μm. This is highly spherical for a Berkovich tip. Simulating a changing tip geometry is not simple in ABAQUS, so a way around this problem was to model a conical tip with a half angle of 70.3° to match the Berkovich geometry. This method, first suggested by Moore et al [344], was highly successful in this application and a useful for future simulations.

There are two competing effects in this HELP model that may be of interest to the SCC community, enhanced initial localised plasticity and strain hardening. In SCC it is known that cracking only occurs if the stress intensity factor is sufficiently large [15], and that an increased yield stress leads to increased the crack growth rate in austenitic alloys [41]. The hydrogen-induced enhanced plasticity could assist reducing the stress intensity factor, until the plastic flow is reduced and strain hardening becomes the dominant term in the localised yield stress. It is important to emphasise that this is observation is based on limited experimental

and computation data, and further examination of hydrogen charged samples and SCC crack tips would be needed to fully determine the effect of hydrogen on SCC.

7.4 Summary

In this investigation there have been two key findings. Firstly, when compared to in-air nanoindentation studies, hydrogen charged samples are harder and have an enhanced onset of plasticity. This is what the HELP mechanism predicts. Secondly, the UMATHT suggests that hydrogen accumulates in regions of high stresses. In the context of SCC, this is ahead of crack tips. From these findings it is difficult to determine if hydrogen has a dominating influence over SCC behaviour, but these results have consequences, i.e. changing the size of the plastic zone, that needs to be accounted in SCC models if hydrogen is in a sufficient concentration. The hydrogen concentration required to introduce impactful changes is simply not known. It is suggested by Fukai [163], that the observed superabundant vacancy theory requires a high concentration of hydrogen. This suggests that the reported hydrogen concentration in the nanoindentation model, which is 35 times the hydrogen required to observe HE on a macroscopic sample, is potentially possible on a localised level.

Chapter 8

PWR-Temperature Micromechanical Testing of Nuclear Alloys

8.1 Introduction

In the previous chapters, nanoindentation has been used to study the material properties of austenitic alloys at room temperature and in a hydrogen charged state. However, It is not currently known if room temperature experiments are a fair reflection of the material behaviour at PWR operating temperatures between 280 - 360°C. It has been demonstrated by Arioka et al [12] that environmental temperatures effect the crack growth rate (CGR) of SCC in austenitic Ni alloys exposed to PWR reactor conditions. To summarise these results, a 20 °C temperature increase from 320 $\rightarrow$ 340 °C, caused the CGR of SS316L, A600 and A690 to increase by approximately an order of magnitude, and the CGR of A800 to drop by two orders of magnitude. This chapter aims to use nanoindentation to investigate the temperature-dependence of the mechanical properties in these austenitic alloys tested by Arioka et al, and to determine if room temperature experiments are a good approximation for high temperature operating conditions.

Inspired by Arioka's findings, high temperature nanoindentation was completed on samples of SS316L, A800, A600, and A690. A690 is a commercially available austenitic alloy, with a high chromium and a similar Ni/Fe ratio to A600. Temperature-dependent investigations have been previously published [345, 41],

but these experiments were conducted over a large temperature range (i.e. 300 - 1200 K) with large intervals (i.e. 100 - 200 K) which are unable to characterise the subtle changes relating to Arioka's findings. The experiments were completed by Kathryn Kumamoto on the X-treme high temperature nanoindenter. Three temperatures were investigated. The result are collected at room temperature, 280°C and 360°C ($0.25T_{melt}$). These temperatures are designed to represent the "cool" and "hot" temperatures tested by Arioka et al.

8.2 Results

Nanoindentation was carried out on polished sample of SS316L, A8090, A690 and A600, mounted on the same heating stage using cement. Both load and displacement-controlled tests were carried out. The target load and displacement was 50 mN and 1μm respectively. Indents were completed in 2x8 arrays, with a spacing of 100μm. This large spacing was used to mitigate anisotropic effects by sampling multiple crystal orientations. The samples were tested at room temperature before being heated to 280 °C and 360 °C. No thermal cycling occurred. The samples were mounted using omega Bond 600 cement, and heated at a rate of 1.6 °C·m^{-1} until the target temperature was achieved. A carbon-boron nitride (cBN) Berkovich tip was used as diamond has a tendency to react with ferrous and carbide forming materials [346]. Once at temperature, the indentation started when the tip and sample were at thermal equilibrium ±1 °C, as measured by thermo-couples in the tip and stage. The data collection method used is described by Oliver and Pharr [241] with no continuous stiffness measurement (CSM). This means only a single value of hardness and modulus is achieved for each indent.

8.2.1 Room Temperature

Figure 8.1 shows the load displacement curves of the four materials at room temperature. The curves shown comprise two-sets using the two testing methods. The load-displacement curves show good agreement between the two methods and trace out a common mechanical response. In the initial 25 - 50 nm we observe a sudden burst of displacement. This is thought to be the initiation linked to the

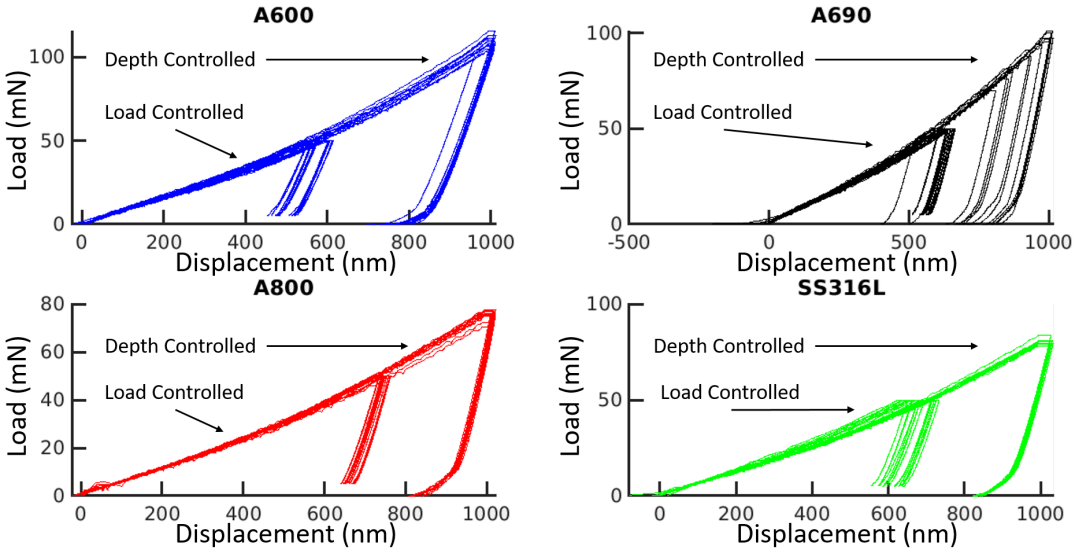


Figure 8.1: Load-displacement curves of the tested alloys at room temperature.

Table 8.1: Hardness and Young's modulus values (mean ± standard deviation) at room temperature, measured by indentation. Literature values are included for comparison. Modulus calculated from reduced modulus using cBN properties (E=524 GPa, μ=0.07).

	Displacement-Controlled		Load-Controlled		Literature	
Material	Hardness (GPa)	Modulus (GPa)	Hardness (GPa)	Modulus (GPa)	Hardness (GPa)	Modulus (GPa)
SS316L	2.4±0.1	195±6	2.5 ± 0.1	186±12	2.4±0.5 [319]	200 [310]
A800	2.3±0.1	197±10	2.3±0.1	167±9	5.2 [312]	196 [314]
A690	3.0±0.1	196±7	2.8±0.1	196±12	3.1±0.1 [347]	206 [348]
A600	3.4±0.1	190±7	3.2±0.2	205±13	3.4 [316]	214 [315]

onset of plasticity, referred to as a pop-in, and the activation of dislocation sources.

The calculated hardness and modulus values are shown in Table 8.1. The reported ranges for hardness measurements are inclusive of the published values found in literature. The previously reported hardness values, found by nanoindentation, are in good agreement with the experimental results (Table 8.1). The values found in literature for A800 are much larger than those presented here. The differences in these values are thought to arise from the indentation depth used, the 200 nm indents are susceptible to size-effects increasing the reported hardness, unlike the 1000 nm indents used in this study. Furthermore, it is also likely that

Table 8.2: Hardness and modulus values (mean ± standard deviation) at 280°C, measured by indentation. The percentage decrease in hardness is reported from room temperature. The reported values are the mean and standard deviations from both load & displacement controlled measurements.

	Displacement-Controlled		Load-Controlled		
Material	Hardness (GPa)	Modulus (GPa)	Hardness (GPa)	Modulus (GPa)	RT % decrease
SS316L	2.00±0.1	139±12	1.7±0.1	140±15	24±9
A800	1.80±0.1	138±11	2.0±0.1	128±13	17±3
A690	2.40±0.1	149±13	2.3±0.1	144±12	19±1
A600	2.60±0.2	145±9	2.6±0.1	146±10	21±2

the nano-jackhammer effect, described by Cordill [338], has increased uncertainty in the recorded values at low displacements.

The moduli are largely constant across the materials using both methods, but some anisotropy is observed in A800. The ranges reported are in good agreement with bulk methods and other nanoindentation studies, which have also reported below-bulk modulus values in the 180-185 GPa range [311, 312] (Table 8.1). The modulus values suggest that there is minimal compliance arising from the use of mounting cement.

8.2.2 Cool Operating Temperature - 280°C

Figure 8.2 shows the load displacement curves of the four materials at 280°C. The indentation was completed in low vacuum, approximately 0.05 ATM. The tip and sample temperatures, deviated from 280°C by no more than ± 1°C. The recorded load-displacement curves show greater variation at 280°C than room temperature. The increased variation is due to resulting thermal drift, which becomes exacerbated by higher temperatures. The thermal drift introduces a non-linear displacement component, which is hard to remove in post-processing. The displacement-controlled experiments show a stepped behaviour in the 800 - 1000 nm range, this is the PID system varying the applied loads.

The hardness and modulus are displayed in Table 8.2. The hardness of these austenitic alloys is shown to decrease with increasing temperature. The observed reduction is between 17 - 24% of the room temperature values, and the deviation in results remains constant from RT. The absolute reduction in hardness is inline

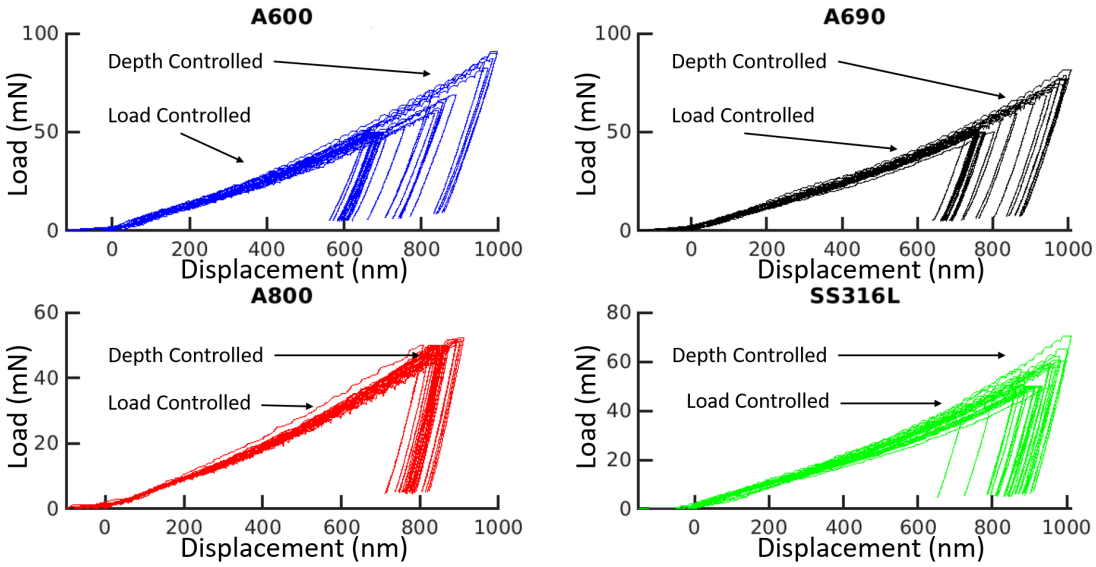


Figure 8.2: Load-displacement curves of the tested alloys at 280°C.

with published values from Torres et al [349], who reported a 14 - 28% drop in the hardness of austenitic steels between RT and 300. It was suggested that the softening resulted from increased dislocation glide, and greater mechanical degradation was observed in alloys with a lower fraction of thermally stabilising elements, such as molybdenum.

The Young's moduli are decreased compared to those reported at room temperature. It is estimated that the Young's modulus should fall by 10% for the alloys [315, 348, 314, 350, 311], instead a fall of 20 - 30% is recorded. The reduction in modulus values is assumed to be linked to an increased compliance in both equipment and mount cement at temperature [254]. The uncertainty, or standard deviation, on the results increasing by a factor of two from RT, this is linked to thermal drift that is more pronounced at higher temperatures.

8.2.3 Hot Operating Temperature - 360°C

Figure 8.3 shows the load displacement curves of the four materials at 360°C. The load-displacement curves show the greatest variation at 360 °C when compared to room temperature or 280 °C results. At 360 °C, the max load shows a variation of ± 10-20 mN. A kink is observed in the load between 100 - 300 nm of the alloys, in

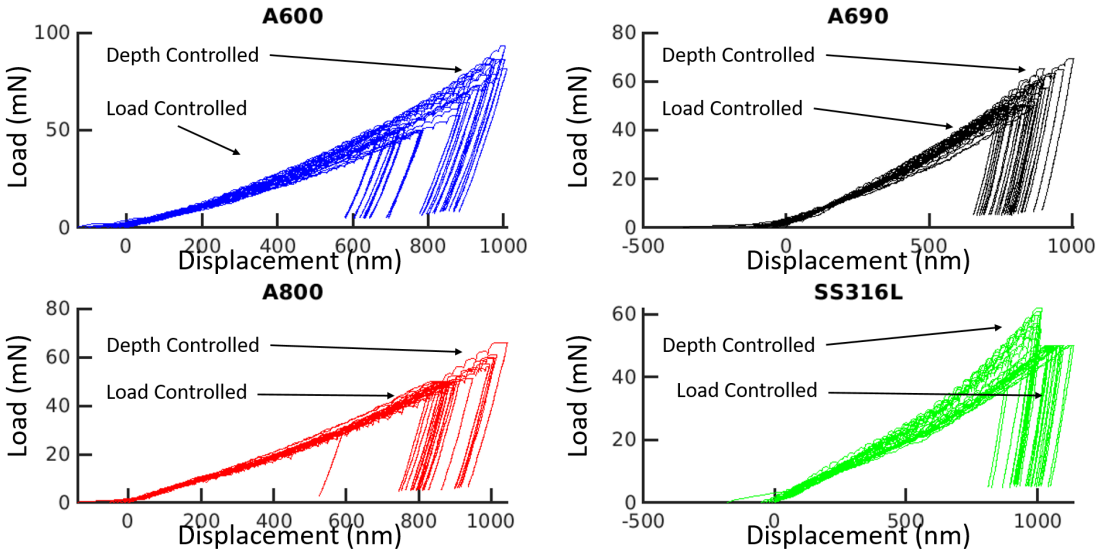


Figure 8.3: Load-displacement curves of the tested alloys at 360°C.

Table 8.3: Hardness and modulus values (mean ± standard deviation) at 360°C, measured by indentation. The percentage decrease in hardness is reported from room temperature and 280°C. The reported values are the mean and standard deviations from both load & displacement controlled measurements.

	Displacement-Controlled		Load-Controlled			
Material	Hardness (GPa)	Modulus (GPa)	Hardness (GPa)	Modulus (GPa)	RT % decrease	280°C % decrease
SS316L	1.7±0.1	131±25	1.4 ±0.1	128±18	36.0±12.0	16.0±2.0
A800	1.8±0.1	123±18	1.9±0.1	133±15	19.7±0.6	2.5±3.6
A690	2.2±0.1	128±11	2.1±0.2	142±11	25.8±0.8	8.5±0.3
A600	2.6±0.2	142±13	2.4±0.2	141±14	24.3±0.7	3.8±5.5

particularly SS316L. As anisotropic mechanical properties decrease with increasing temperature in nickel austenitic alloys [351], the increase variation in load is linked to thermal drift and other factors. In this instance, other factors include surface oxidation, which was observed post-testing. This is discussed in more detail later.

The hardness and modulus values are shown in Table 8.3. The hardness of austenitic alloys were shown to further decrease with increasing temperature. Austenitic alloys soften at moderate reactor temperatures [349, 351]. The observed softening results in a 20 - 33% drop in hardness when compared to room temperature values, and a 2.5 - 16% drop when compared to compared values col-

lected at 280°C. This is shown in Table 8.3, the standard deviation is determined from the two results from both load and displacement controlled methods. The moduli recorded at 360°C are comparable to the values recorded at 280°C, but significantly lower than room temperature.

A potential issue with this experimental design, was the development of surface oxide particles during the heat process. These oxides were only prominent post-testing, as the total experimental time was over a week. Figure 8.4 shows the surface of the alloys post-heating. SS316L and A800 have formed a fine semi-continuous particle oxide across the surface of the material. The mean diameters were determined from scanning electron micrographs, the results are summarised in Table 8.4. Due to a low iron content, A690 and A600 have formed a continuous oxide layer formed across the surface. The thickness of this oxide was <50 nm, as determined by FIB cross-sectional analysis.

On close examination of the top-down and cross-sectional imaging, there is little evidence to suggest that oxide particles have been crushed or punched in the material. There are two possibilities as to why. Either the oxides particles are hard [351] and do not deform under these applied loads, or the oxide particles are formed post-indentation. To help determine which case is correct, the 360°C indents are compared to the RT indents, as no oxide was present at RT. In A800 and A600, the RT indents look very similar, while SS31L and A690 do not. The reason why this trend occurs is unknown, it cannot be explained in terms of composition, time at temperature or location on stage.

Table 8.4: Measurements of the oxide particle size on both the faces of the indent in contact with the Berkovich tip and surrounding surface.

	Oxide Particle size (nm)	
Material	Indent	Surface
SS316L	250±70	75±10
A800	145±40	165±70
A690	180±70	115±40

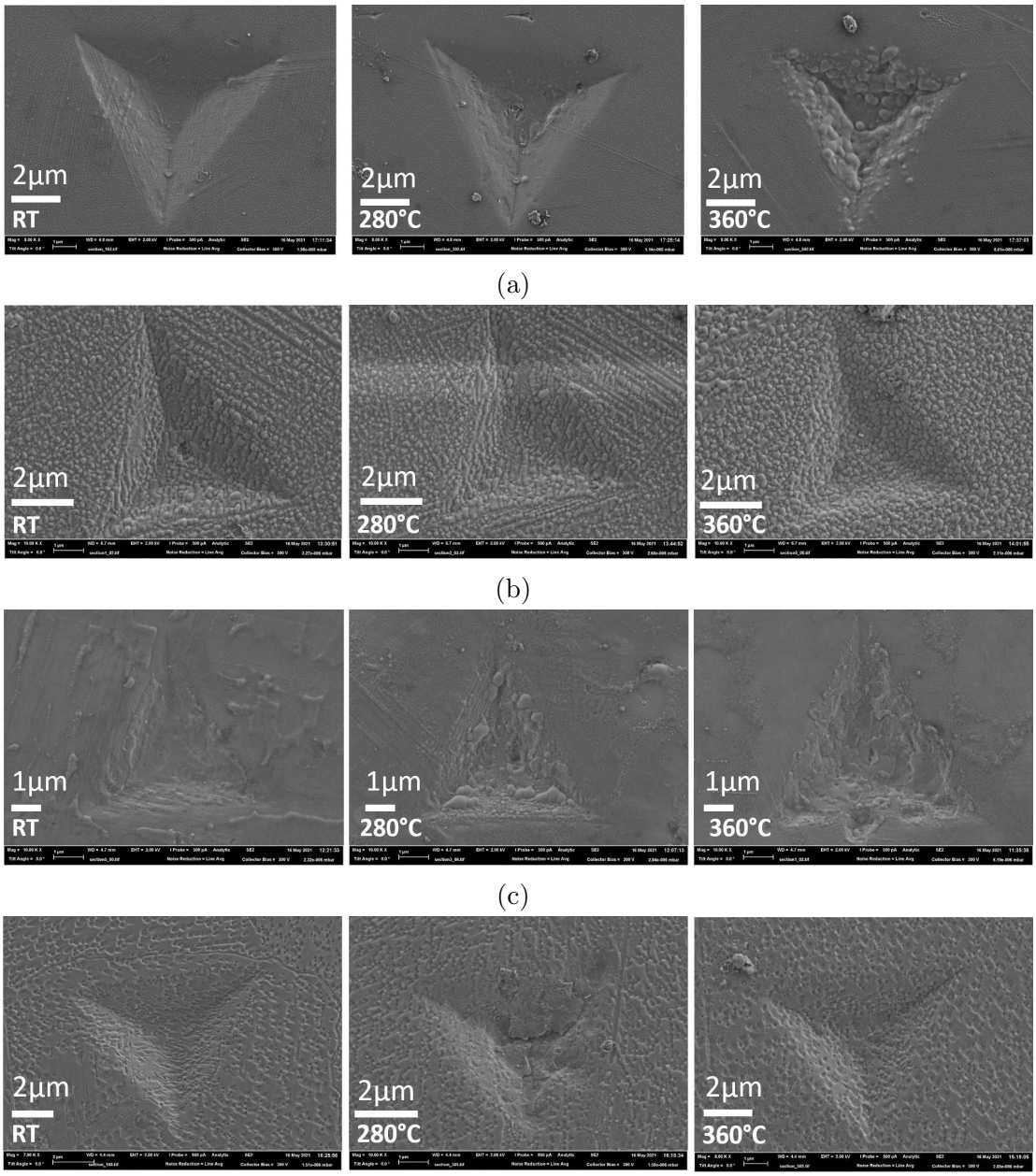


Figure 8.4: Scanning electron microscope images of the indentation surface post-testing for materials (a) SS316L (b) A800, (c) A690 and (d) A600. Comparison between the indentation surfaces at different temperatures are shown to determine the role of oxidation on the results. Oxidation is enhanced in the indents, this is due to the increased dislocation and slip band density in this region which increases oxidation rate compared to the surrounding surface.

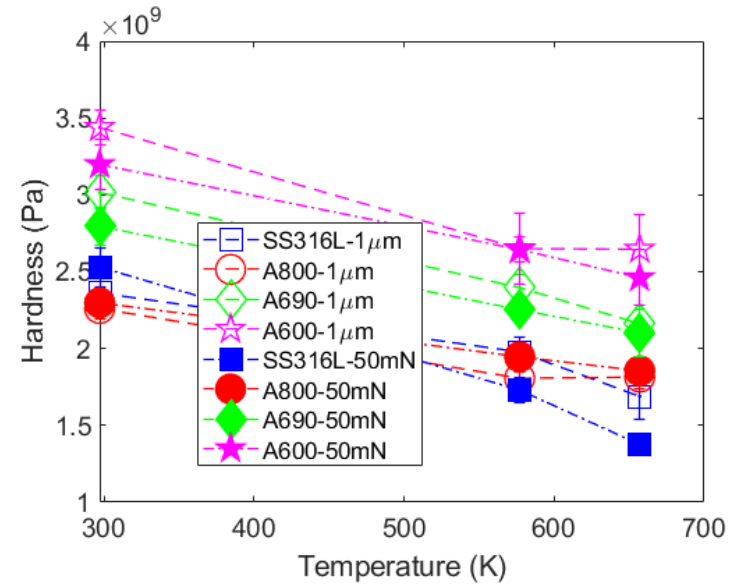
8.3 Discussion

Nanoindentation of four common, nuclear grade, austenitic alloys were tested at low and high PWR operating temperatures. The hardness and modulus was reported for the temperatures tested. The temperature-dependence of the mechanical properties will be examined, and from this a comparison to the CGR of these materials.

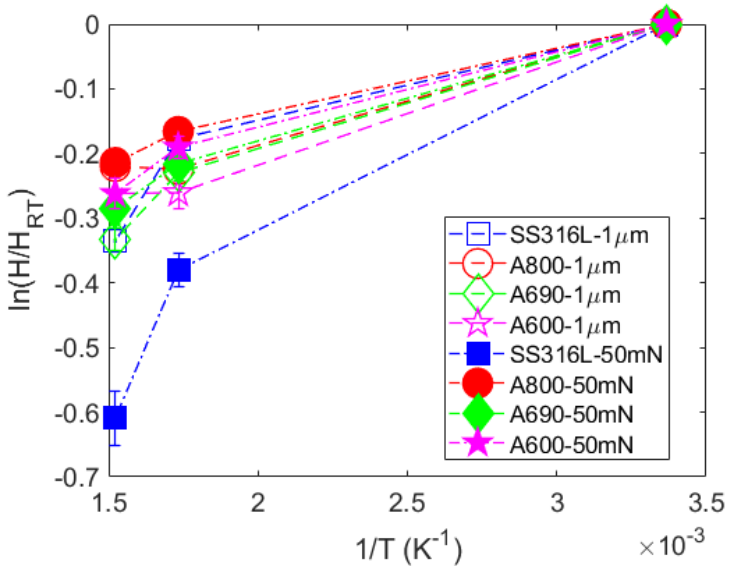
8.3.1 Temperature Dependence of Mechanical Properties

Figure 8.5 shows the absolute material hardness and an Arrhenius plot, displaying the logarithm of the normalised hardness against the inverse temperature measurements for the different alloys. Generally, there are no large drops in the recorded mechanical properties of austenitic alloys at these tested temperatures. In absolute terms, we see that A600 is the hardest alloy present. Its measured hardness drops of 19% from 3.2 GPa at room temperature to 2.6 GPa at 280°C. The alloy is relatively thermally stable showing a small decrease, a further 7% in hardness, to 2.4GPa at 360°C. The next hardest alloy is A690, with a room temperature hardness of 2.8 GPa. The alloy loses 18% of its initial hardness to 2.3 at 280°C, and a further 9% loss to 2.1 GPa at 360°C. At room temperature, the softest alloy is A800 with a hardness of 2.3 GPa. However, the alloy is undergoes little softening with increased temperature, dropping 13% in hardness to 2.0 GPa at 280°C and a further 5% to 1.9 GPa at 360°C. Finally, SS316L experiences a large reduction in hardness from 2.5 GPa to 1.7 GPa at 280°C (32% reduction) and undergoes a further 17% reduction in hardness to 1.4 GPa at 360°C. At PWR temperatures, SS316L is the softest alloy by approximately 500 MPa.

In the austenitic alloys tested, an incremental drop in hardness was observed between RT, 280 and 360°C. This is in line with other high temperature testing of austenitic alloys [349]. A800 was the most resistant alloy to softening and SS316L was the worst, these characteristics were determined from the gradient of the Arrhenius plot in Figure 8.5b. The observed softening is due to a reduction in the lattice resistance to dislocation motion [352], this is characteristic of FCC metals. As the SFE increases with temperature by 0.048 - 0.11 mJm^{-2} per Kelvin [328, 353]. From the findings of Molner et al [328] on SS316L, it is thought that at higher



(a)



(b)

Figure 8.5: (a) Absolute hardness (b) Semi-logarithmic plot of the normalised hardness against the inverse of temperature.

temperatures all the materials deform by dislocation glide. It could be possible that a different deformation mechanism (i.e. twinning to glide) could account for the rapid degradation of some alloys. Other softening mechanisms, such as low

temperature creep and enhanced dislocation climb aided by increased dislocation mobility, are typically observed at higher temperatures than those investigated in this study, i.e. 0.3-0.4 T_m.

There are microstructural differences in the alloys that need to be considered. Firstly, the measured background dislocation densities of SS316L, A800 and A690 are an order of magnitude lower than A600. The pre-existing dislocation network can contribute to the increased hardness, requiring more force to move dislocations. Secondly, the hardness at room temperature correlates with the measured grain size. This is known as the Hall-Petch effect [354, 355]. This states that in smaller grains, smaller pile-ups are possible, so a greater external force must be applied to overcome the energy barrier preventing dislocation transfer across the boundary. Figure 8.6 confirms the Hall-Petch effect in common samples.

It has been reported that molybdenum can increase the thermal stability of hardness measurements in austenitic alloys [349]. The results from this investigation do not support this claim in either absolute or relative comparisons, and suggests that other factors, such as Fe/Ni ratio or microstructure, are more influential. Out of the materials tested, SS316L was the only alloy tested with a significant molybdenum content of 2.6 wt%, above the 2% threshold for noted by Torres et al [349].

The effect of Cr is determined by comparing the performance of A600 and A690, as they have a comparable Fe/Ni ratio but different Cr-contents. There is no evidence to suggest that the thermal stability of austenitic alloys is affected by additional chromium over the PWR temperature range investigated. The Cr-rich alloy is, in this example, 300 - 400 MPa softer at every temperature. However, this may be related to other factors, such as microstructure differences and background GND values, which differ between the alloys.

There are errors associated with high temperature nanoindentation, as it is a method still in development. Recent publications by Wheeler et al [254, 356, 357] summarise the technical issues surrounding high temperature hardness testing, focusing on thermal drift, surface oxidation, and tip conditions. I will address these in the context of this experiment. First, minimising contact thermal drift is key to reliable results. The temperatures of both indenter and samples were matched using independent heaters and thermo-couples. It is given that the temperatures will

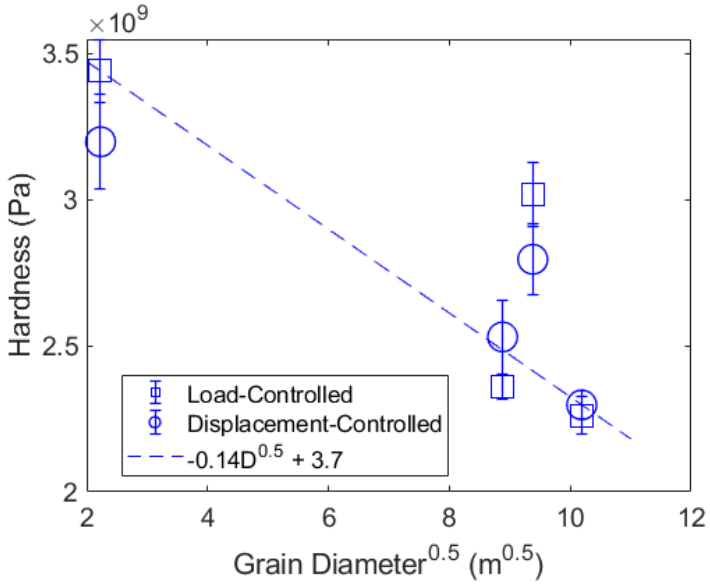


Figure 8.6: Shows a plot of hardness against the square-rooted grain size. The resulting linear correlation demonstrates a grain size hardening effect, called the Hall-Petch effect. A690 is a Cr-rich alloy, and has twice the Cr of all other alloys. As Cr decreases the hardness, it has been ignored in the regression plot.

not match exactly, and will become worse at higher temperatures, but the thermal gradient between stage and tip was minimised. An issue with the experimental design is that all samples were mounted simultaneously on the heating stage, but this may have increased the drift due to a larger thermal mass and irregularities in the sample positioning on the stage and increased the time for samples to oxidise. This decision was taken to minimise variation in the testing temperatures, as while the thermo-couples between the tip and stage temperatures differ by no more than a degree, the error to the target temperature is estimated to be $\pm$ 20°C. Another criticism of high temperature indentation is tip reactivity and wear. The indenter tip was held at temperatures cooler than 400 °C, therefore it is not thought that any oxidation has occurred [358]. The mechanical properties of cBN are stable in this temperature range, to within $E_{err} < 0.5\%$ [346]. An insufficient quantity of indents were undertaken to cause considerable wear to the tip. Fused silica indents were completed post-testing using the original area function, a negligible change in the Young's modulus of 68.8 to 68.2 GPa was recorded. Finally, despite the low vacuum, the samples partially oxidised, which will be discussed next.

8.3.2 Oxidation

Nanoindentation is a highly surface sensitive method, and the oxides formed indubitably influenced the measured hardness and modulus. This can happen in one of two ways, either the oxide particles increase the force measurements, as they are harder than the surrounding matrix, or they effect the area calibration of the tip.

In post-testing SEM analysis, no indents were observed to have compressed oxide particles impressed on the sides of the indent, or irregular indenter shapes. This suggests that the area function of the tip remained constant. The oxides, possibly Cr_2O_3, are very hard 20-30 GPa [326]. This additional resistance could be responsible for the irregularities observed in the sub-250 nm regions of the load-displacement curves at 360°C (Figure 8.3). However, the oxide particles are small compared to the indent.

The overall impact of the oxides on the results is due to a combination of the oxide particle size, and the number density. In some materials, such as A800, there was a very high number density and therefore the influence of oxide is thought to be greater than on A690, which had a thin oxide layer. To confirm any results prior to publication, it would be beneficial to repeat these experiments either under high vacuum, or in an inert argon, environment to prevent oxidation.

8.3.3 Comparison to Crack Growth Rate

Meisnar et al. [359] and Shen et al. [16] investigated the similarities in CGR between SS316L and A600 and the effect of temperature, and suggested that a "thermally-activated elemental diffusion and oxidation" mechanism and a "localized deformation" mechanism controlled the crack behaviour. A mechanical rate limiting mechanism is supported by the results published by Terachi et al. [41] on austenitic steels, as the yield strength and pre-existing cold work impact the CGR. The weightings of these mechanisms are evaluated for the tested alloys, by correlating the normalised drop in hardness against the reported CGRs [12], as seen in Figure 8.7.

Figure 8.7a shows there is an inverse correlation between the normalised drop in hardness and the CGR of SS316L. Implying that crack growth is heavily weighted

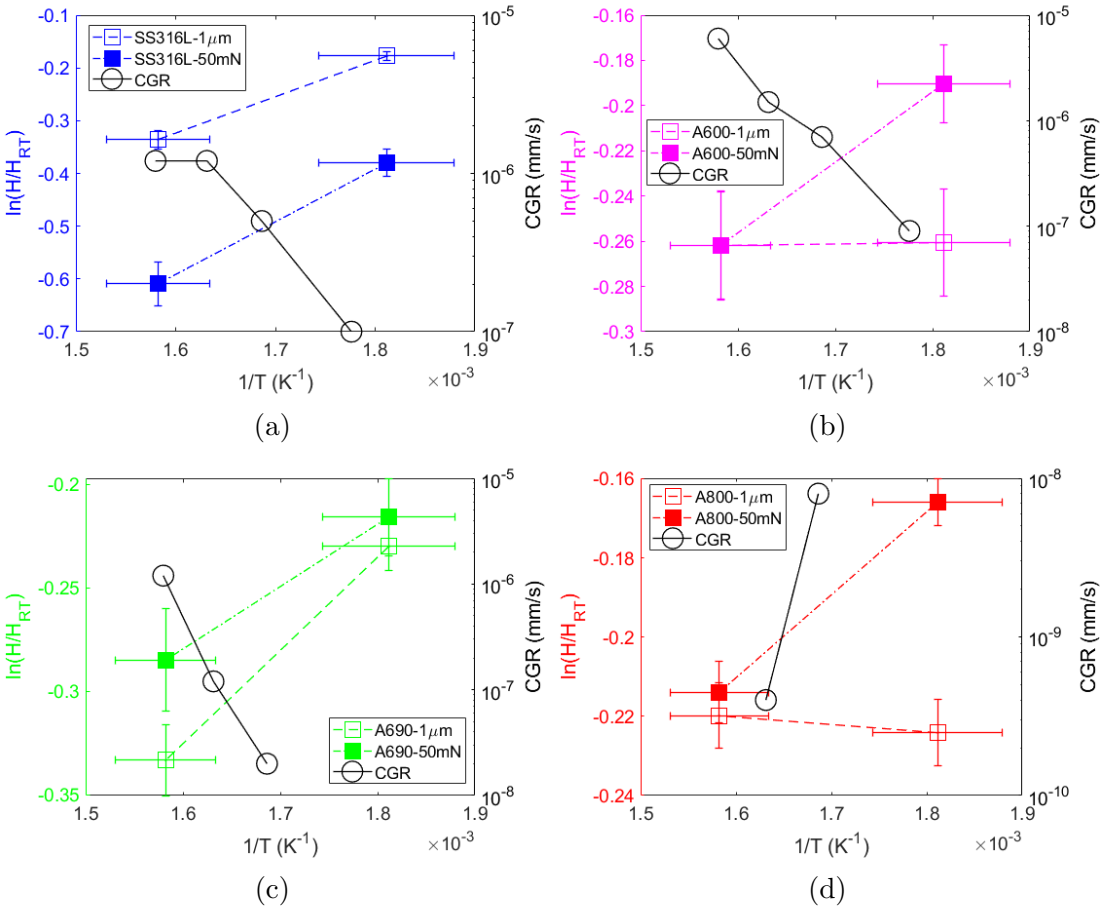


Figure 8.7: A dual plot showing the semi-logarithmic plot of the normalised hardness against the inverse of temperature on the left axis and the measured crack growth rate on the right. CGR results from [12]. The sub figure show (a) SS316L, (b) A600, (c) A690 and (d) A800.

towards localized deformation. The drop in hardness is a result of increased dislocation mobility due to a reduction in the lattice resistance to dislocation motion [352]. Similar results have been achieved by Meisner et al. [359] and Shen et al. [16], who also noted that a "localized deformation" mechanism played a dominant role in restraining CGR of SS316L.

Figure 8.7b shows that normalised hardness measurements of A600 are weakly correlated with the reported CGR. This indicates that a "thermally-activated elemental diffusion and oxidation mechanism" is more dominant in the CGR. This observation is supported by Shen et al. [16] who found greater Fe/Cr-depletion zones ahead of SCC crack tips in A600, by high-resolution electron energy loss spectroscopy (EELS).

Figure 8.7c shows that normalised hardness measurements of A690 are also weakly correlated with the reported CGR. The softening of A690 and A600 are within error, indicating that a "thermally-activated elemental diffusion and oxidation mechanism" is more dominant in the CGR. It has been observed by Wang et al [360] that in A690 the localised deformation enhances "thermally-activated elemental diffusion and oxidation mechanism"; similar to observations by Shen et al.'s in A600, and the results reported from this study. As the reported CGR of A690 is 100 times slower than that of A600, the enhanced corrosion resistance provided by additional Cr is thought to out-weigh any potential mechanical disadvantages noted. The additional Cr is so beneficial that a new SCC mode, grain boundary cavitation, has been reported [22, 13]; this has been determined in Chapter A to be a coupled "mechanical-diffusion" mechanism that weakens the grain boundaries.

Figure 8.7d shows that normalised hardness measurements of A800 are weakly anticorrelated with the reported CGR, similar to A600. The oxidation surrounding an SCC crack tip was investigated by Persaud et al. using atom probe tomography, and a Cr-rich oxide was observed to extend into the surrounding matrix along dislocation lines [361]. It was suggested that cracking is controlled by mechanical factors; however, the presented results suggest that A800 has the smallest weighting towards a "localized deformation" mechanism and is softest. This conflict implies that a third unknown mechanism could be activated, i.e. film-rupture/dealloying or hydrogen to cause embrittlement and generate critical stresses.

The temperature-dependence of the CGR, as observed by Arioka [12], is not thought to be a purely mechanical phenomenon. The enhanced resistance to crack growth in A800 is at least partially reflected in the low levels of softening of the alloy across the investigate temperature range. It is suggested that the enhanced resistance of A800 comes from a much more complicated mixture of diffusion and oxidation mechanisms [362]. However, finding high-resolution EDX or EELS support for this argument is challenging, as SCC is scarce in A800 samples. In future work, it would be beneficial to include an additional selection of temperatures, given the thermal accuracy and reliability of the system 320 °C would be a suitable candidate.

8.4 Summary

Room temperature experiments do not necessarily reflect the material behaviour at high temperatures and testing should be completed at PWR temperatures to eliminate the ambiguities introduced by room temperature approximations. SS316L and A690 display similar softening behaviour as temperature increases, as such we suggest that there is a thermally activated deformation-based mechanism that leads to accelerated crack propagation. A800 and A600 display similar mechanical behaviours at temperature. As there is minimal thermally activated deformation, this suggests that crack growth rate is dominated by another mechanism, potentially diffusion-based, which is enhanced by the temperature increase.

It is not possible to explain the temperature dependence of the CGR obseved by Arioka et al. [12] with the mechanical deformations at PWR temperatures. A800 is the softest alloy tested, and should display increased localised strain and CGR. However the opposite is reported, and it is deducted that a pure deformation based mechanism is not responsible for these observations.

Chapter 9

Hydrogen Uptake and Trapping Under PWR Conditions

9.1 Introduction

The investigation of hydrogen uptake in austenitic alloys under PWR reactor conditions has seen little development in recent years. This chapter aims to complete a comparative NanoSIMS and thermal desorption spectroscopy (TDS) study which will investigate the hydrogen adsorption and trapping ability of different austenitic alloys. The samples used in this chapter are SS316L, A800, A690, A600 and A600 CW that were exposed to heavy water (D_2O) for 1572 hours at 340°C. These materials were chosen as they contain various nickel and chromium contents that represent the crack growth rate (CGR) under PWR conditions reported by Arioka. A correlation will be presented between the hydrogen trapped and the SCC susceptibility to determine if hydrogen is a precursor to SCC under more realistic PWR operating conditions.

9.2 Thermal Desorption Spectroscopy

Calibration experiments were first completed to establish the effects of heating rates on the recorded desorption peaks in unoxidised austenitic alloys. The effects of oxidation and surface oxides on the desorption was investigated. Finally, the effect of cold-work levels and chemical compositions on the trapping of hydrogen was explored. As the Culham Centre for Fusion Energy was closed to external

researchers during the coronavirus pandemic, the TDS data was collected by Dr Yevhen Zayachuk. The analysis, figures and findings are my own work. In all presented figures the deuterium counts are normalised against the sample volume (Table 9.1).

9.2.1 Preliminary Findings and Calibration Tests

To calibrate the TDS system, samples of A600 in the as-received condition without autoclave exposure were tested at heating rates of 5, 10, 15 and 20 K/min. An emission current (which changes the detector sensitivity) of 20 μA was selected, this value was chosen as it avoided saturating the mass quadrapole (i.e exceeding a mass-to-charge ratio of over 10^7). This value was then kept constant over every test to make the experiments comparable. The selected heating range was from 293 - 1100 K, this was determined from literature of TDS testing on austenitic alloys [227, 160]. The resulting hydrogen desoption is shown in Figure 9.1. Decreasing the ramp-rate delays the desorption peak, while reducing and broadening the spectra. In the temperature domain, this results in a peak shift to a cooler temperature, as a slower heating rate gives more time for hydrogen to outgas before the temperature changes significantly.

The absolute peak position is the temperature that hydrogen would desorb at

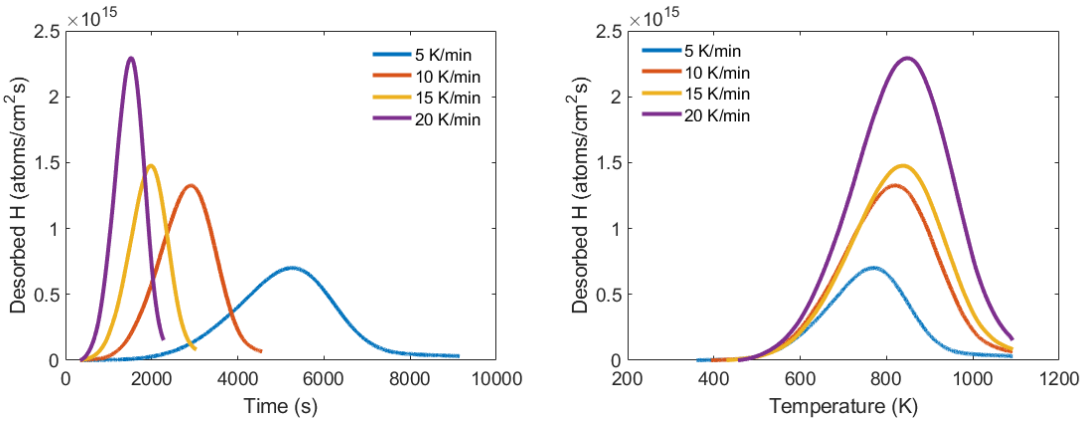
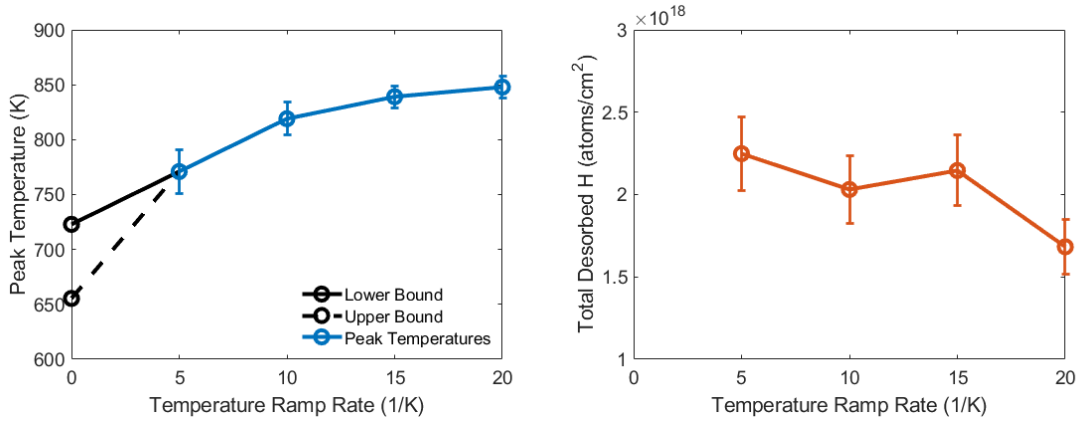


Figure 9.1: Recorded desorption of hydrogen (mass 2) at different temperature ramp rates plotted against (a) time and (b) temperature.

using an infinitesimally slow ramp-rate. This value can be estimated from the peak positions collected. Figure 9.2 displays the peak positions plotted against ramp-rate. An estimated absolute peak position is between 650 - 725 °C. These bounds were determined by extrapolating the shift in peak position from 10 K/min to 5 K/min in the case of the lower bound, and the sequential difference in peak positions for the upper bound. These results can be used to compare my results to experiments using a different heating rate. The total amount of hydrogen desorbed is within error, and does not significantly change with heating rate. This is estimated by calculating the area under the desorption curve in Figure 9.1.

9.2.2 Impact of oxide on hydrogen desorption

Figure 9.3a shows the desorption spectra for samples of A600 CW in two states, as removed from the autoclave, and with the top surface oxide ground off prior to TDS heating. The heating rate across the two samples are largely unchanged. The recorded temperature of the sample with an oxide is delayed with respect to the sample with no oxide (i.e. separation between the two heating curves is seen).



(a) (b)

Figure 9.2: (a) The peak temperature-position of recorded hydrogen desorption against the ramp rate. The lower bound is a linear extrapolation from 10K/min to 5K/min. The upper bound is found using the sequence of changes in peak positions i.e. deltas are 10, 20, 40 and an estimated 80 K.
(b) The total amount of hydrogen desorbed from the sample during each test, with a typical 10% error associate with sample variation.

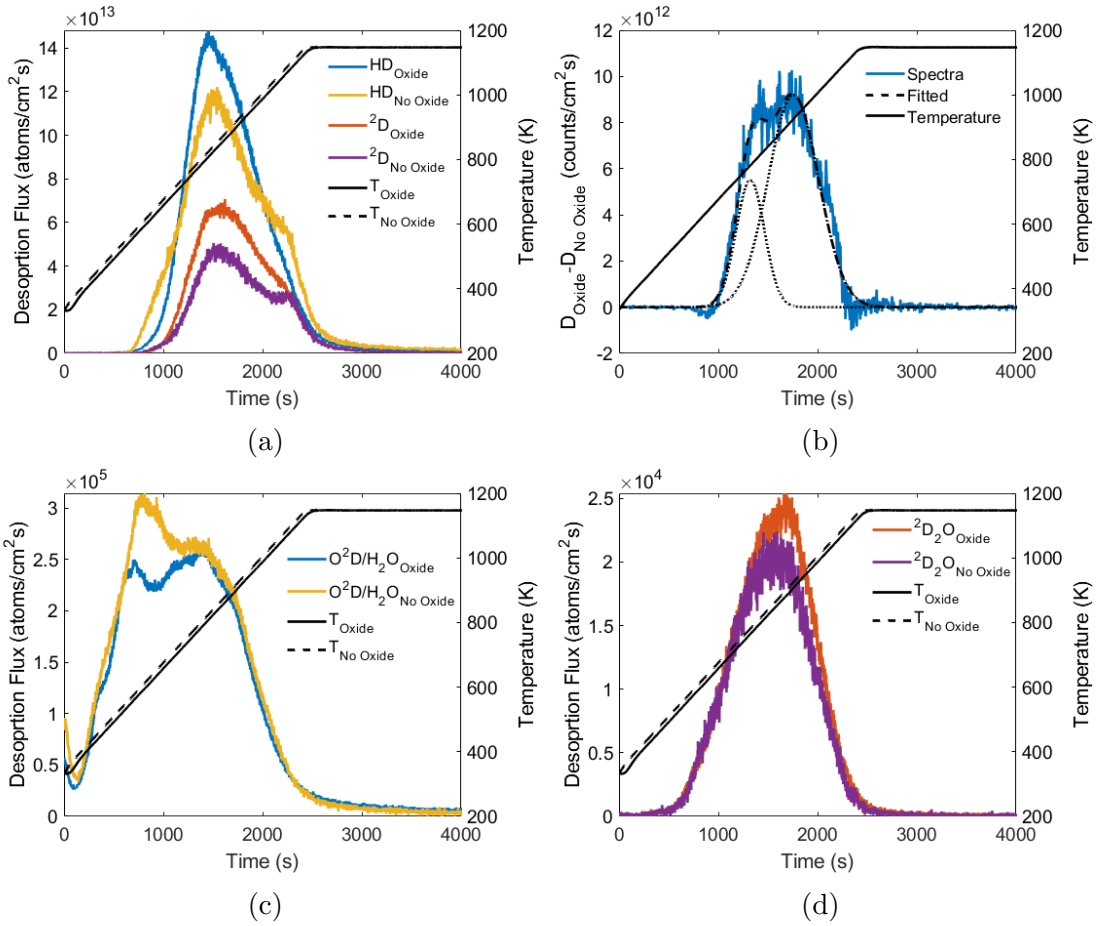


Figure 9.3: (a) The scaled deuterium containing HD and ^{2}D desoprtion spectra for A600CW with a surface oxide and a removed surface oxide layer. Sample volumes are 90 mm^3 and 40 cm^3 respectively. (b) Difference between spectra from A600CW with and without the oxide layer. The resulting spectra is a double peaked Gaussian fitted. The scaled (c) ^{2}DO/H$_2$O and (d) ^{2}D$_2$O desoprtion spectra for A600CW.

This is because the sample with no oxide has a smaller thermal mass (40 vs. 90 mm^3) and is more responsive to heating. The sample size variance is due to the oxide remove sample being an off cut, or fraction of a larger oxidised sample of A600CW.

In the absence of the surface oxide (purple), the main hydrogen desorption peak occurs at 800±25 KThis is some 20 K lower than the unexposed A600CW samples (Figure 9.1). The main desorption peak of the sample with a surface

oxide layer (orange) is significantly shifted to a higher temperature 850±25 K. A secondary desorption peak is seen at 1000±25 K which was not reported in the non-autoclaved samples shown in Figure 9.2, indicating that new trapping sites are generated by the oxidation process. This peak is present in both samples with and with out a surface oxide, and is therefore not associated with oxidation, but a deeper trap being saturated with hydrogen from the autoclave process.

During the removal of the oxide layer, the recorded deuterium content falls 15%, from $5.6\pm0.5\times10^{16}$ to $4.7\pm0.5\times10^{16}$ atoms/cm^2 in A600CW (Table 9.1). These values are within the experimental error, and therefore cannot be attributed to the removal of the oxide layer. The assumption moving forward has to be that most of the recorded deuterium is in the metal and not the oxide. This is likely due to the high solubility of the lattice in austenitic alloys [363, 364].

There are still observable differences between the two recorded spectra. The most pragmatic method for determining differences is called a residuals spectra. This plots the differences between two area normalised spectra, i.e. Spectra A - Spectra B. This is beneficial as it fits only a few Gaussian peaks to specific traps, instead of reproducing an entire spectra. Gaussian peaks are not the most suitable choice, but given the outgassing speed they do not limit the accuracy.Figure 9.3b shows the difference between the two deuterium spectra presented in Figure 9.3a. The residual deuterium spectra can be characterised by two Gaussian peaks centered on T_{abs}= 680±25 and 830±25 K. These peaks are thought to be associated with the desorption of deuterium from the oxide. The same double oxide peak centered on 703 and 803 K was reported by Lee and Lee, and attributed to the formation of iron oxides in spring steel [139]. The dual oxide peaks originate, in part, due to the different oxide structures formed on the surface. It is not possible to identify individual peaks without further experiments.

Figure 9.3a also shows the desorption spectra of H-D. The observed desorption peaks are similar to those found in ^{2}D spectra. However, greater H-D release is reported at the beginning and end of the experiment with the sample containing no surface oxide. This H-D out-gassing is associated with additional hydrogen bound to the freshly prepared surface. The H-D is shifted to lower temperatures, this is a discrepency when compared to the D-D peaks shown in the same figure.

Table 9.1: The normalised deuterium concentration of the tested alloys. *= with removed oxide. The number of detected deuterium counts is normalised against the surface area of the samples, as is the convention in literature. The sample thicknesses are all constant.

Material	Raw ^{2}D Content (atoms)	Normalised ^{2}D Content (atoms/mm^3)
SS316L	2.1±0.2 x10^{17}	2.3±0.2x10^{17}
A800	2.1±0.2 x10^{17}	2.3±0.2x10^{17}
A690	2.1±0.2 x10^{17}	2.3±0.2x10^{17}
A600	6.2±0.6x10^{16}	7.7±0.8x10^{16}
A600 15%CW*	1.9±0.2x10^{16}	4.7±0.5x10^{16}
A600 15%CW	5.0± 0.5x10^{16}	5.6± 0.6x10^{16}

This could be in part due to the fact that more H-D is released in the early stages of desorption that will naturally shift the peak to lower temps.

Figure 9.3 c&d show the desorption for masses 18 ($^2DO/H_2O$) and 20 (^2D_2O). These spectra are largely consistent, but there are some observable differences. The $^2DO/H_2O$ signal has additional desorption at approximately 550±25 K, due to the early emission of H-D associated with additional hydrogen bound to the surface. As this is a low temperature peak, the additional counts are thought to be evaporating H_2O instead of additional ^2DO [211]. The ^2D_2O desorption peak is shifted to a higher temperature in the sample with no surface oxide, this could imply that the oxide is a barrier to diffusion. As this oxide layer is thin, this is difficult to determine. Finally, the quantity of oxide products is consistent across both sample conditions. This suggests that the majority of the detected oxygen originates from a dissolved concentration in the lattice instead of being stored in the oxide.

9.2.3 Cold-worked Samples

Figure 9.4a shows the H-^{2}D and $^2D_2$ desorption spectra for two samples of A600, one is in the as-received condition and the other has undergone 15% cold-work. Both samples were subjected to identical autoclave conditions. The as-received sample desorbed more deuterium than the cold-worked sample. The total des-

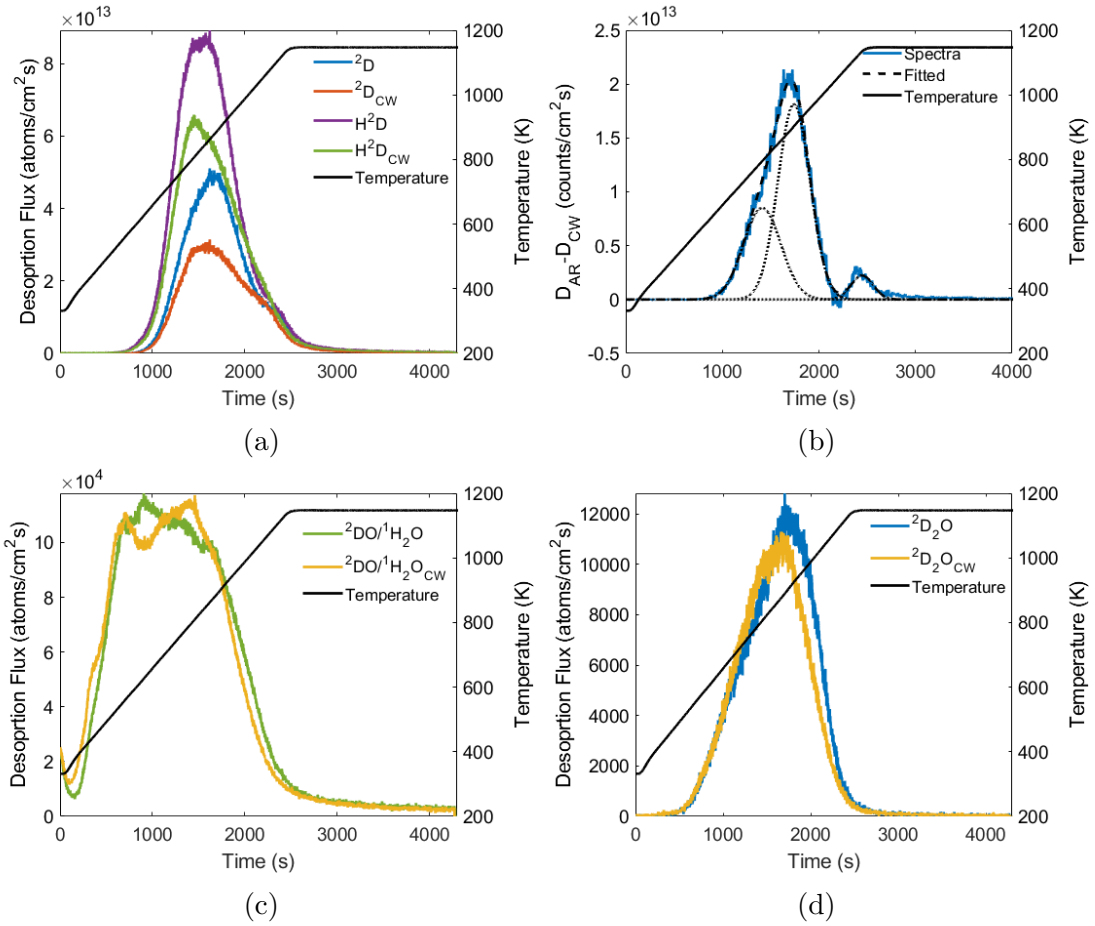


Figure 9.4: (a) Deuterium desorption of A600 in as-received and in CW form collected by TDS at 20K/min ramp rate. (b) Residual spectra from A600 with and without the cold-work. The resulting spectra is a triple peaked Gaussian, fitted using cftool in MATLAB. (c) $^2DO/H_2O$ spectrum and (d)^2D_2O desorption spectra.

orbed deuterium is 38% greater in the as-received sample compared to the cold-worked sample. This is a significant increase from $5.6\pm0.5\times10^{16}$ to $7.7\pm0.8\times10^{16}$ atoms/cm^2.

Figure 9.4b shows the residuals plot between the spectra shown in Figure 9.4a. The residual deuterium can be fitted by three Gaussian's centered at T_{abs}= 700±25, 810±25 and 1020±25 K. The peak at 700 K is thought to be due to changes in both the surface oxide and carbide precipitates. This is based on three key observations. (1) Back of the envelope calculations show that the total carbide

interfacial area is 30% greater in the as-received alloy. (2) The ratio of peak heights is inconsistent between this experiment and literature [139], it is also broader indicating multiple traps maybe present. (3) The reported range of desorption peaks for carbides (370–650 K) and oxides (460–800 K) overlap. The peak at 810 K is due to changes in the surface oxide thickness. The peak at 1020 K is unidentified, but could relate to the decomposition of the surface oxide.

Figures 9.4 c&d show the desorption spectra of $^2DO/H_2O$ and ^2D_2O. The $^2DO/H_2O$ spectra are essentially identical and the total molecular counts are unchanged. The ^2D_2O spectra consist of a single peak that is shifted to lower temperatures by the addition of cold work, the same behaviour was observed by removing the surface oxide. The cause is likely a combination of these two factors, the CW sample has a thinner oxide layer and a reduced barrier effect, and the dislocations provide fast-diffusion pathways to facilitate the early out-gassing of deuterium products.

The increased hydrogen content in the as-received alloy is counter-intuitive, as dislocations are trapping sites [365, 142]. There are three factors which could influence these results, and they are discussed. (1) Due to the corona virus, there was a 9-month storage period before TDS testing, which has allowed the out-gassing of weakly bound deuterium in low energy traps. (2) The measured geometrically necessary dislocation (GND) density of both A600 in cold-work and as-received condition are similar (Section 5.1), therefore dislocations should play a negligible role in trapping deuterium. (3) Cold-work has increased the grain boundary area and increased the number of random boundaries in the material. The increased hydrogen diffusion caused by a boundary area increase of 50%, is thought to outweigh the increased trapping from 10% more random boundaries. Therefore it is thought that a greater fraction of deuterium in the CW sample has out-gassed prior to testing.

It has not been possible to test as-received and cold-work variations of every material. A challenge of this study is to understand how the other alloys may behave under similar as-received conditions. It is established that cold-work increases the density of dislocations, resulting in a network of slip bands and pile-ups. The behavioural differences in dislocations, and therefore cold-work, are estimated using the stacking fault energy (SFE). A600 has the highest SFE of the materials

tested, and therefore the other alloys are more planar, increasing the dislocation pile-ups surrounding microstructural features such as grain boundaries, carbides and inclusions. The increased pile-ups in all other alloys should, in theory, increase the effect of cold-work, i.e. increasing the effective trapping energy, as documented by Symons et al [142].

To conclude the effects of cold-work on hydrogen uptake in PWR conditions, the 15% level of cold worked introduced into the A600 sample is greater than the 10% CW required to observe a significant increase in the susceptibility of A600 to IGSCC [38]. This result shows that trapping in non-oxide sites is not significantly affected at high deformation levels, aside from known microstructural differences. Therefore, increased hydrogen trapping due to lower levels of cold work is not thought to be the cause of increased SCC susceptibility observed by Arioka et al [12]. Unless during SCC, high vacancy densities ahead of the crack tip act as hydrogen trapping sites, increasing its concentration locally and only during SCC or SCC testing, and therefore not detectable during ex-situ investigations.

9.2.4 Effect of Cr-content

Figure 9.5a shows that by increasing Cr content from 15 to 30%, the total trapped of deuterium increases by approximately five-times, from $5.6\pm0.5\times10^{16}$ to $2.3\pm0.2\times10^{17}$ atoms/cm^2. All desorption peaks have been reached prior to the isothermal hold. A residuals plot is not presented in this section, as large differences in microstructure and oxidation would not result in reliable peak fitting. Instead the differences are qualitatively described. The initial dehydrogenation starts at around 600 ± 10 K for both materials, indicating that the same trap is present. This is assumed to be carbides, as both material have a large carbide coverage, and carbides have the lowest binding energy energy of non-reversible traps [142]. The spectra is significantly broadened when compared to A600, and desorption typically occurs at higher temperatures. The broadening of the peaks is thought to reflect A690's large granular structure, carbide coverage and thick inner-oxide layer, these factors are discussed in the next section.

Figures 9.5 b & c show that the A690 has a lower hydroxide desorption spectra than A600. The A600 sample desorbed significant counts of $^1H_2O/^2DO$ compared

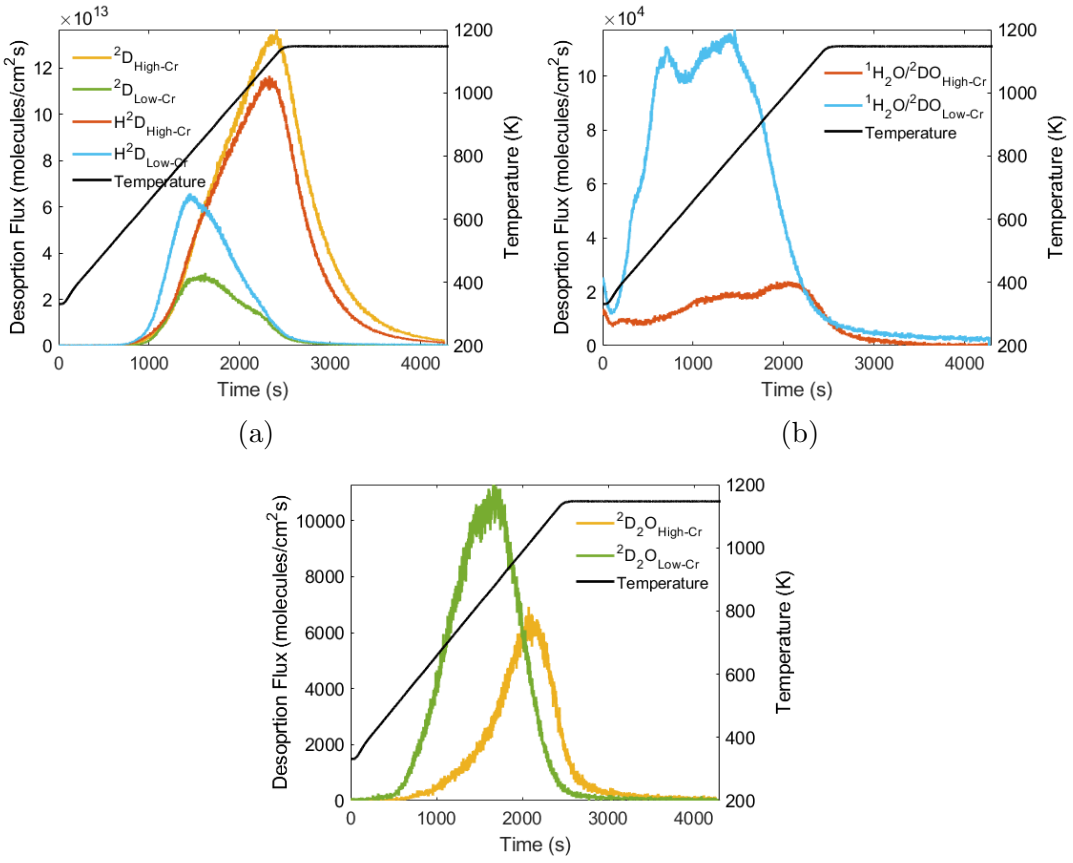


Figure 9.5: The scaled (a)^{2}D and H^{2}D, (b) ^{2}DO/H_2O and (c)^2D_2O desorption spectra for high and low chromium alloys (A690 and A600 respectively).

to A690. A690 has the ^2D_2O desorption peak shifted to hotter temperatures.

Oxides heavily influence the adsorption of hydrogen in austenitic alloys. These results suggest that chromia, formed in A690, is more efficient barrier than chromite spinel in A600. This is in part due to the increased oxide thickness, density and uniformity of A690, at approximately five-times thicker ($\approx$ 90 vs 15 nm in agreement with literature [297, 366]), but also the hydrogen environment created during oxidation. It was found by Rummery & Macdonald and Symmons that oxidising chromium produces a hydrogen fugacity three orders of magnitude greater than iron or nickel. The higher fugacity drives more deuterium into the material and trapping sites. The porosity, determined by Fresnel imaging, of both oxides are

low.

There are several microstructural differences in the alloys, notably differences in carbides, GNDs, GB and grain size. The total carbide interfacial area in A600 is much greater than that of A690, due to the higher boundary density. The increased area suggests that more deuterium is stored at this trapping site. The GND density of A600 is approximately ten times greater than A690. CW vs AR A600 suggests that the increased GNDs will promote diffusion, not trapping, which could account for the decreased deuterium in A600. The fraction of boundary types (CSL, random, or low angle) is similar between both alloys, and not considered important in this comparison. Finally, the large granular size of A690, means that a network of fast-diffusion pathways and additional trapping sites does not exist. This is similar to the GND argument, and the diffusion of deuterium through the matrix is thought to be a limiting step in the desorption process of A690.

An important factor to consider in PWR applications is that A690 develops grain boundary cavities under accelerated PWR tests. These cavities form as vacancies coalesce on carbides. These cavity regions are thought to be strong hydrogen trapping sites [211]. This is particularly of concern as the greatest cavity density coincides with the greatest stress gradient in the material [61], this is also where hydrogen is also likely to accumulate [367].

Alloys with chromium contents greater than 15-17% are highly resistant to SCC [368]. The changes in hydrogen uptake between A600 and A690, while dramatic, are thought to reflect the change in oxide composition to a Cr-rich spinel. The change in composition is not thought to affect the hydrogen-related corrosion resistance of the alloys, as the greatest deuterium content is found in the alloy with known superior SCC resistance. Therefore, chromium is not thought to significantly effect the role of hydrogen in SCC.

9.2.5 Effect of Nickel Content

Figures 9.6 a & b show the H-^{2}D and ^{2}D-^{2}D desorption spectra for SS316L, A800 and A600. The total deuterium counts from SS316L and A800 are comparable, approximately $2.3\pm0.2\times10^{17}$ atoms/cm^2, and A600 has a substantially lower count

Table 9.2: The total hydrogen and deuterium oxides species desorbed from post-autoclave samples of SS316, A800 and A600CW.

Sample	$^{1}H_2O/^{2}DO$ (counts/cm^2)	$^{2}D_2O$ (counts/cm^2)	O_2 (counts/cm^2)	$^{2}D_2O/^{2}D$
SS316L	1.55×10^{8}	2.35×10^{7}	3.50×10^{5}	0.14
A800	5.76×10^{7}	7.04×10^{6}	1.15×10^{5}	0.04
A600 CW	1.80×10^{8}	1.07×10^{7}	3.41×10^{5}	0.23

at $5.1\pm0.5\times10^{16}$ atoms/cm^2. This corresponds to 80% reduction in the desorbed deuterium.

The desorption spectra are unique, but there is a macro-trend; as the Fe-content of the alloy increases the desorption temperature increases. This is likely a combination of several factors including the oxide thickness and the apparent activation energy of diffusion. SS316L has both the thickest oxide layer and the largest barrier to diffusion, 63.5 kJ/mol [369], both these factors decrease as the nickel content increases. A800 and A600 have an activation energy of 58 kJ/mol [370] and 44 – 50 kJ/mol [370, 142, 146] respectively.

Figures 9.6 c&d show the desorption spectra for the hydroxides. These spectra show greater variation, numerically summarised in Table 9.2. SS316L and A600CW degas similar quantities of hydroxides, water and oxygen. The hydroxides, water and oxygen degassed from A800 is approximately half that of SS316L or A600CW. Table 9.2 shows that A600CW desorbs a significant fraction of its total hydrogen content as hydroxides. These results indicate that the traps responsible for trapping these species, voids in the oxide and GBs, are not as numerous in A800. This is supported by Section 5.2, which shows that A800 forms a complete and compact inner oxide layer. This is in contrast with A600 and SS316L which have more porous structures, and out-gas a greater fraction of trapped hydrogen as a hydroxide [371].

Figure 9.7a compares the published crack growth rate (CGR) in PWR conditions at 340°C reported by Arioka et al [12], to the total desorbed hydrogen from the alloys. There is a weak inverse correlation between Arioka's results collected at 340°C and the TDS deuterium signal, A600 with the fastest CGR has the lowest deuterium counts, and A800 with the slowest CGR has the highest deuterium

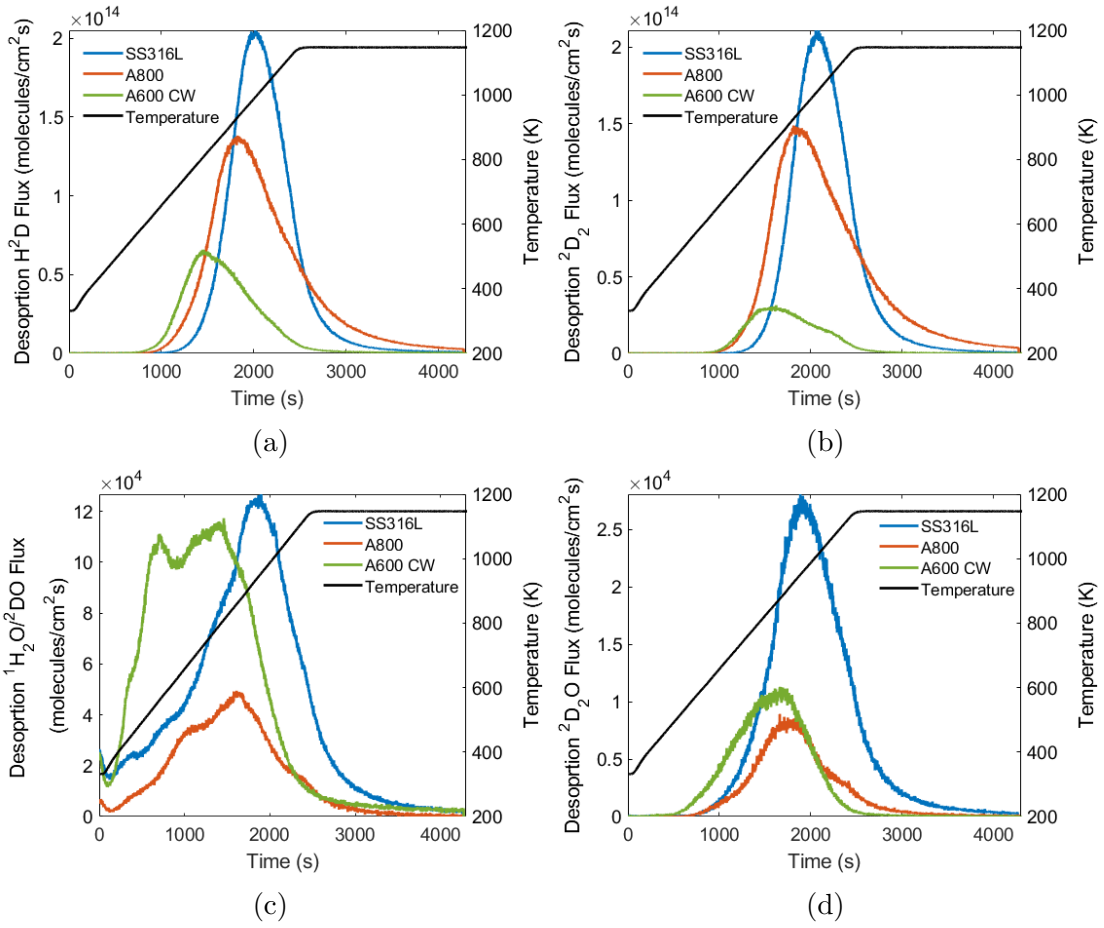


Figure 9.6: The desorbed (a) ^{2}DH, (b) ^{2}D (c) $^1H_2O/^2$DO and (d) ^2D_2O spectra from SS316L, A800 and A600CW.

counts [372, 12]. This weak correlation may be observed because the samples used in this experiment were exposed to pure heavy water – not hydrogenated water typical of PWR applications and used by Arioka. Therefore, included in the same plot is a comparison to Coriou's original SCC experiments in pure water conditions [9, 306]. There is now an inverse correlation between SCC failure and bulk deuterium content resulting from pure heavy water.

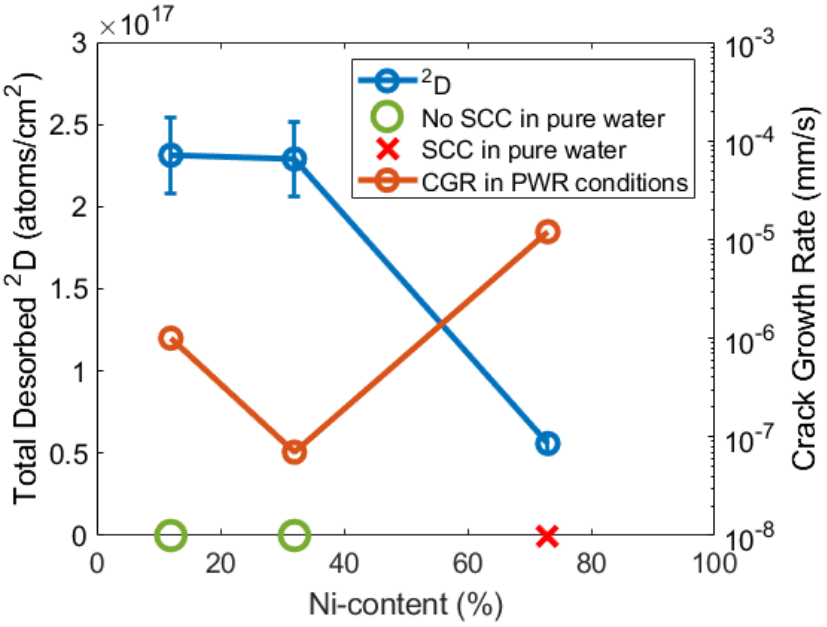


Figure 9.7: A comparison between the total desorbed deuterium for the alloys and the experimentally observed crack growth rate found from exposure to PWR water at 340°C, from [12]. In addition, a comparison to Coriou's initial SCC findings after exposure to pure water, from [9].

To conclude the effects of nickel content on hydrogen uptake under PWR conditions. The alloys tested are low, medium and high nickel content, representing the three regimes observed by Arioka et al [372, 12]. Alloys with a nickel content between 20 -50% are the most resistant under PWR conditions at temperatures above 340°C. The observed hydrogen content show an inverse trend with reported CGRs, i.e. most susceptible to SCC has the least hydrogen. It is clear to see that high nickel alloys are worse at trapping hydrogen, which suggests that they are less weighted towards a hydrogen-based SCC mechanism.

9.3 NanoSIMS

During autoclave exposure the hydrogen must diffuse through the oxide that has developed on the alloys to become trapped in the material. Similarly, during TDS the hydrogen must be liberated from its trapping sites, and diffuse across the oxide. The NanoSIMS is able to determine the origin and relative intensity of trapped deuterium recorded in the TDS. Two sets of experiments were conducted at two facilities. Top-down analysis was completed in Oxford by Dr Junliang Liu, and the cross-section analysis was completed at the University of Manchester by Dr Kexue Li, with funding from the Royce Institute. The analysis, findings and generated figures are my own.

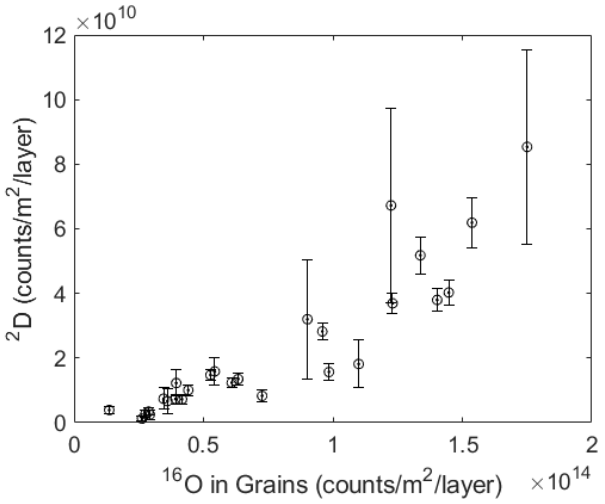
9.3.1 Normalisation Process

The analysed material in a NanoSIMS is sputtered from the bulk. The intensity of the detected signal is therefore dependent on the sputtering rate of the material. This process is subject to influential factors, this includes crystal orientation, the primary beam current, and aggregates of atoms i.e. the signal may be affected by the presence of the other atoms such as oxygen and metals. In order to qualitatively compare samples, these factors must be controlled, and the results normalised. Normalising the deuterium counts against oxygen signal vastly improves the signal changes due to crystal orientation and atom aggregates. This greatly improves the comparability across materials. This normalisation is completed on both top-down and cross-sections of samples. The oxygen-normalised data is then aggregated into a single value for each material. All the values presented in this chapter have been normalised for oxygen detection. Figure 9.8 shows the recorded deuterium signal and the oxygen-normalised deuterium signal, which is more consistent across different grains in a single sample.

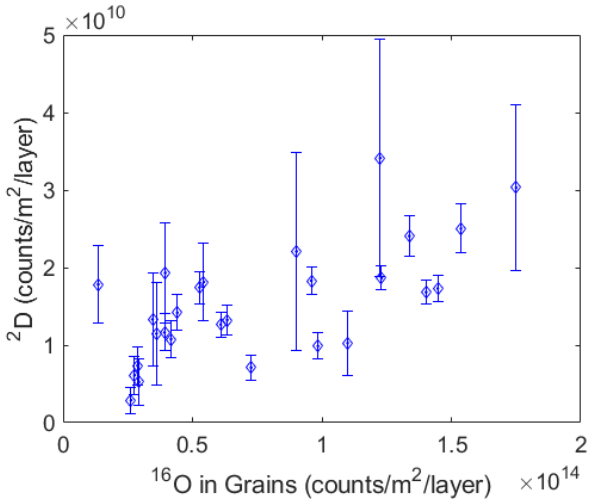
9.3.2 Cross-section Analysis

9.3.2.1 Matrix Concentration

Figures 9.9 and 9.10 show the mean and standard deviation of the normalised deuterium content and the ^{2}D:^{1}H ratio for SS316L, A800, A690, A600 and A600CW,



(a)



(b)

Figure 9.8: Normalisation method demonstrated on SS316L using the grain oxygen signal for cross-sectional imaging (a) before and (b) after.

excluding grain boundaries and precipitates. Table 9.3 summarises the data numerically. The sample have a ^{2}D:^{1}H ratio that is an order of magnitude above the natural abundance of deuterium, 10^{-4}, showing that there is still a significant amount of deuterium stored in the samples. There are three main observations to be discussed, the effects of nickel and chromium composition, and cold-work.

The first observation is that the ratio of D/H is the same within error across all

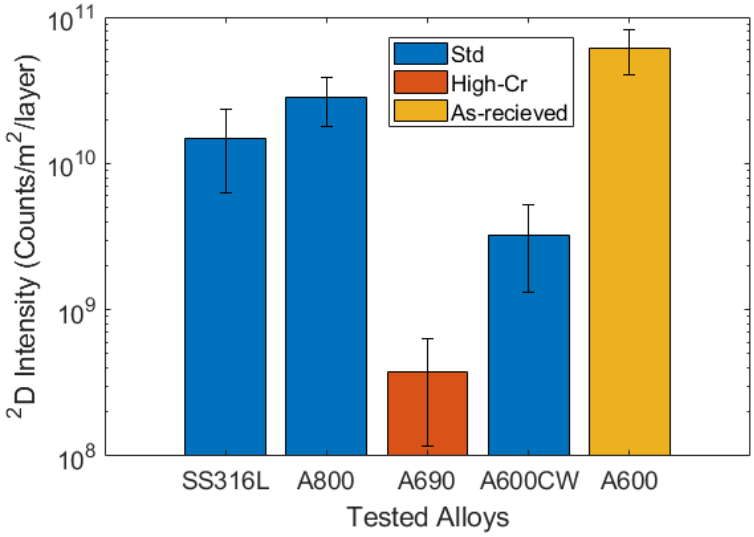


Figure 9.9: Graphed version of ^{2}H content as seen in Table 9.3, the error bars are the standard deviation of all the grains examined.

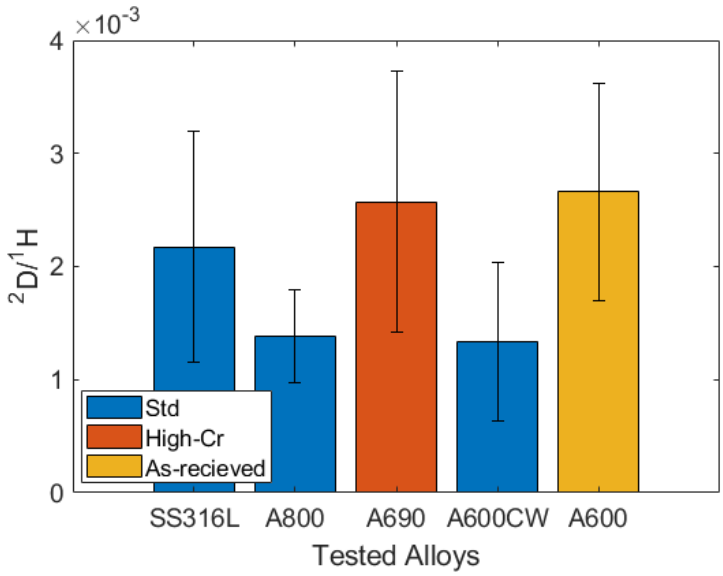


Figure 9.10: Graphed version of ^{2}H/H ratio as shown in Table 9.3, the error bars are the standard deviation of all the grains examined.

tested alloys. This suggests that the variation between the alloys is linked to the number of trapping sites in a material, and not an increased hydrogen up-take. The higher number of trapping sites is the result of increased M-H bonding in

Table 9.3: The normalised deuterium concentration of the tested alloys.

Material	Ni- Content (%)	Normalised ^{2}H Intensity (cts/m^2/slice)	^{2}H/^{1}H (x10^{-3})
SS316L	12	15 ± 9x10^9	2.0 ± 1.0
A800	32	3 ± 1x10^{10}	1.5 ± 0.5
A690	67	4 ± 2x10^8	2.5 ± 1.2
A600	73	6 ± 2x10^{10}	1.3 ± 0.7
A600 15%CW	73	3 ± 2x10^9	2.5 ± 1.0

the lattice. Simonetti [373] computationally determined that interstitial hydrogen caused the Fe-Fe local bond strength to diminish by 60%, and that Fe-H bonds are formed at the expense of the metallic nearest neighbors. A690 and A600 have approximately a quarter of the iron content of A800, this explains why the deuterium content is a quarter of A800. The observed differences are not due to microstructural changes, as SS316L, A800 and A690 all have a consistent microstructure and background GND count.

The second observation is that the addition of chromium has little effect on the the deuterium in the lattice. A690 and A600CW represent alloys with high and low chromium contents and similar nickel contents. Table 9.3 shows that by increasing Cr content from 15 to 30%, the D/H ratio in the lattice is within error. The effect of additional Cr in austenitic alloys is to change the protective inner-oxide from a chromium spinel to chromite. The chromite in A690 is 20-times thicker than A600, 110±20 vs. 5±5 nm, and less porous. As a result, it takes approximately 55 times longer for hydrogen to diffuse across the oxide under PWR conditions [114, 299]. However, as seen in the results this has no effect on the hydrogen in the lattice.

The final observation is that cold-work reduced the number of trapping sites for deuterium in the lattice. The sample with cold-work shows a 95% decrease in the deuterium recorded from the lattice from 6±2x10^{10} to 3±2x10^9 counts/m^2/layer. This result is unexpected, as it has been reported in literature that a 15-20% increase in the binding energy of a trapping site is expected for a 15%-CW material [142]. There are two main reasons why this is not observed in these CW samples. Firstly, despite CW raising the lattice binding energy (36 kJ/mol), it

is still insufficient to store hydrogen over long periods of time at room temperature. Secondly, the dislocations introduced by cold-working act as fast diffusion pathways that increase the apparent hydrogen mobility and out-gassing at room temperature [374, 15]. As there was a long period between charging and testing it is not possible to determine the initial deuterium content, and therefore the fully understand the effect of CW on these samples.

9.3.2.2 Grain Boundaries and Oxidised Grain Boundaries

Figure 9.11 displays the hydrogen concentration found at non-oxidised and oxidised grain boundaries. Oxidised grain boundaries are boundaries where the number of Oxygen counts is above 100/pxl. The mean hydrogen concentration for all tested alloys measured at grain boundaries is between 2 - 4 x10^{10} counts/m^2/layer, and within error in Table 9.4. The distribution of GB types differ in each alloy, CSL boundaries and low angle boundaries enhance diffusion and have a much lower binding energy (20 - 26 kJ/mol), while random boundaries which trap deuterium have a higher binding energy (53 - 58 kJ/mol) [134] due to higher dislocation densities. A800 has the lowest fraction of random boundaries (10%), followed by A690, SS316L and A600 (30–40%), and A600CW has the highest fraction of random boundaries (<50%), as determined in Section 5.1.3. Microstructural changes due to alloy composition and treatments (including cold-work) do not appear to significantly influence the trapping of deuterium at grain boundaries.

Table 9.4: The normalised deuterium concentration of the tested alloys.

Material	GB ^{2}H Intensity (cts/m^2/slice)	Matrix ^{2}H Intensity (cts/m^2/slice)	$^2H_{GB}$:$^2H_{Mat}$
SS316L	3.2±1.5x10^{10}	1.5±0.9x10^{10}	2.1±1.5
A800	3.8±0.5x10^{10}	3.0±1.0x10^{10}	1.2±0.4
A690	–	4.0±2.0x10^{8}	–
A600	1.5±0.6x10^{10}	6.0±2.0x10^{10}	0.3±0.1
A600 15%CW	2.3±1.5x10^{10}	3.0±2.0x10^{9}	7.6±7.2

Figure 9.11 shows that oxidised grain boundaries have a significantly higher deuterium content than their unoxidised counterparts, by approximately two orders of magnitude. The deuterium content along the oxidised boundaries is within

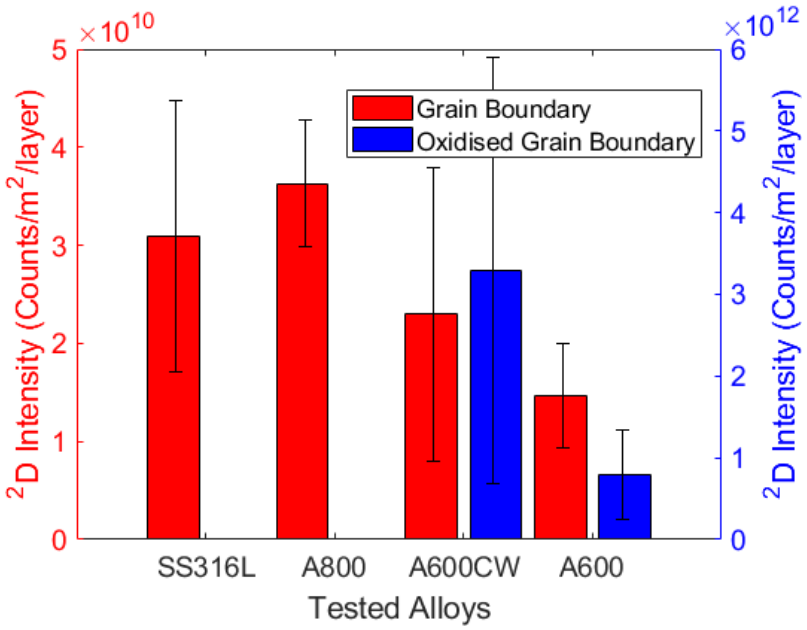


Figure 9.11: The hydrogen concentration found at grain boundaries and oxidised grain boundaries. A690 is excluded due to its low deuterium count.

error. This shows that cold-work does not increase the trapping of deuterium along these boundaries. There is a large uncertainty associated with these values, this due to rounding of the sample as we approach the exposed edges where the oxidised boundaries are located. This variation is an uncontrollable variable, from a change in surface height which affects the collection of ions.

Figure 9.12 shows that there is a strong correlation between intergranular oxidation and hydrogen. The regions ahead of the oxidation provide no evidence for a hydrogen-rich environment, necessary for hydrogen-based SCC mechanisms to be effective. These observations do show that a continuous supply of hydrogen from the environment has been established. This is no surprise, the hydrostatic stress fields are not trapping sites and any hydrogen accumulation will have dissipated over the corona-virus pandemic. The oxide pathways shows that it was possible for hydrogen to migrate to the tip of intergranular oxidation from the environment.

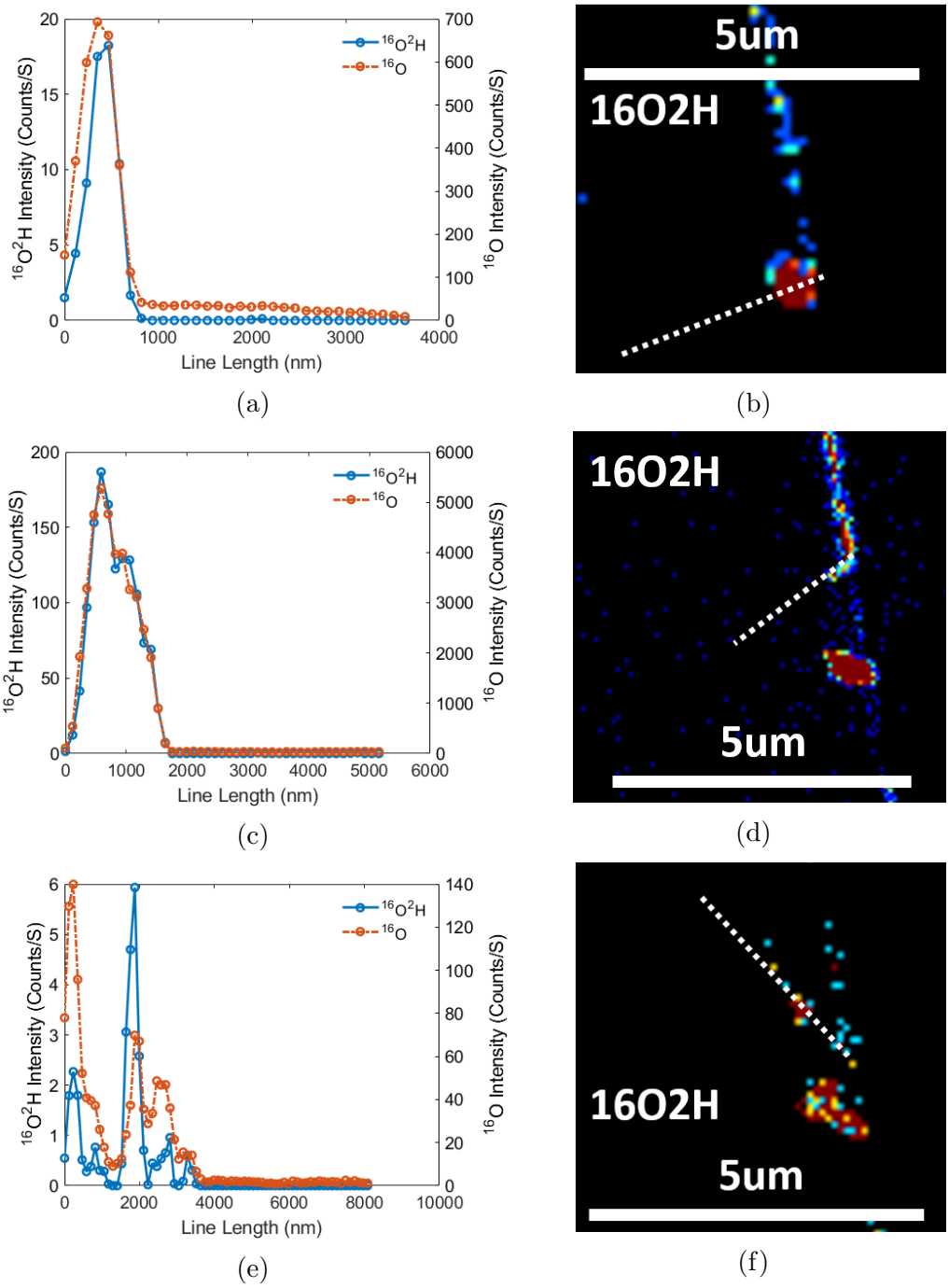


Figure 9.12: The line intensity profile and $^{16}O^2D/^{16}O^1H$ image along grain boundaries displaying intergranular oxidation for (a, b) A800, (c, d) A600 and (e, f) A600 CW.

9.3.2.3 Carbides

Carbides are major trapping sites for hydrogen, due to a high binding energy and regularity throughout the lattice. Of the materials studied, A600, A600CW, A690, and A800 are known to have intergranular carbides. To determine if carbides still trap deuterium, line profiles were collected across the carbides. Figure 9.13 shows that there is not a clear correlation between the position of deuterium in a single slice and carbides in A600 as-received. The line profile along individual carbides start to show trapping of deuterium at carbides, but the low deuterium count is insufficient to draw any conclusion. To overcome limitations due to low counts, a statistical approach is employed, as presented by Chen et. al [116], where the oxygen-normalised line profiles across 52 carbides and the surrounding matrix are combined to form a single profile. To accomplish this, the length of the carbide is normalised from 0→1, where 0 is the start of the carbide and 1 is the end. The mean normalised length of the carbides is 830±150 nm. The data is binned and combined by superposition.

Figure 9.13b shows that in the resulting combined line-profile, there is on average 50% more deuterium across the carbide region (0→1) compared to the surrounding matrix. This reveals that carbides could be a significant trapping site in A600. Deuterium is found across the total width of the carbide [375], and not just the interfaces [376]. This result is in agreement with that published by Chen et al [192], who found deuterium restricted to the inside of carbides using atom probe. The measured deuterium is not so strongly localised to the carbides as previously reported [192, 375], this maybe due the time between charging and testing, that could of resulted in the removal of deuterium from the carbide, and the spatial resolution, which is starting to push the limitations of the NanoSIMS.

Similar analysis has been conducted on A600CW, the results showed a 30% increase in deuterium content between the matrix and carbides. Figure 9.14 compares the ratio of carbon, from the carbides, to the deuterium signals for each of the 20+ test regions investigated in each sample. It is shown that both samples trap the same amount of deuterium, and that the dislocations from cold-working have not affected the hydrogen content associated with these sample features. A800 and A690 were investigated, but their carbides could not be clearly defined in the

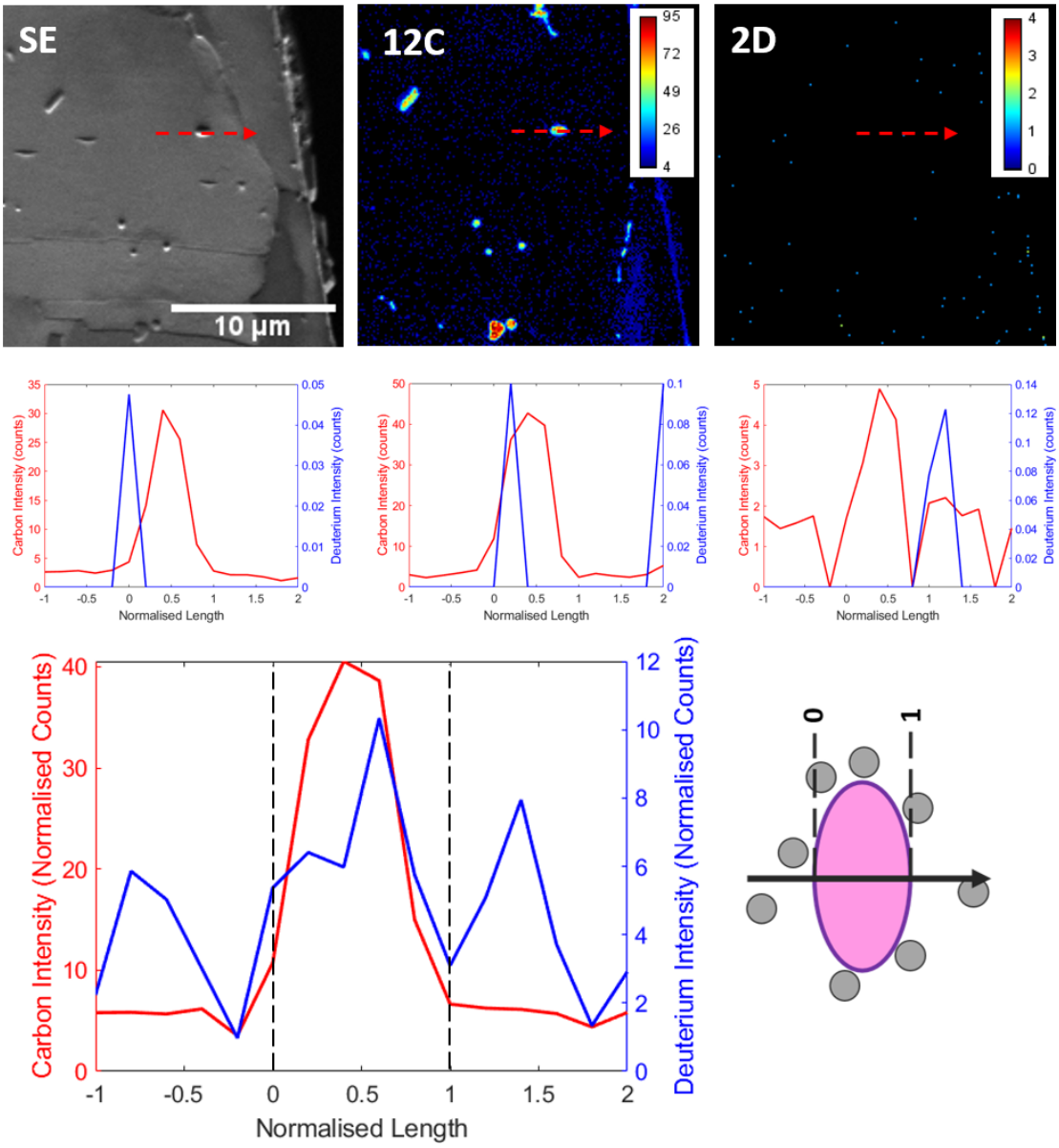


Figure 9.13: Superimposed profile of carbides, generated by combining multiple normalised individual profiles from each carbide as shown in the three individual line profiles. Number of carbides tested >50. NanoSIMS images of A600 example of carbides.

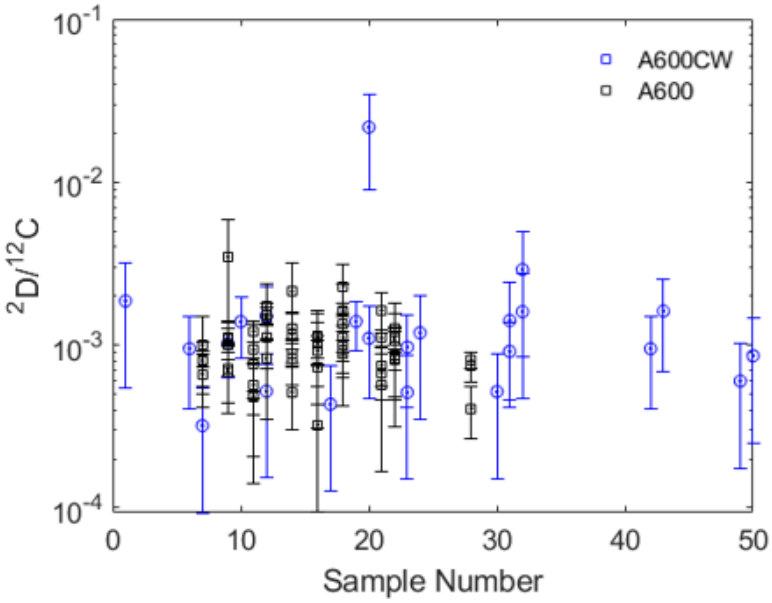


Figure 9.14: The ratio between deuterium to carbon from intergranular sources.

elemental maps, and due to their large grain size not enough carbides were tested.

9.3.3 Top-down Analysis

9.3.3.1 Depth Profiling - Hydrogen Diffusion

Figures 9.15 - 9.17 show the depth profiles of trapped deuterium obtained by NanoSIMS for samples of A600, A600CW and A690. The black dotted lines show the oxide-metal interface, determined as the depth at which the change in the ^{2}H:^{16}O ratio is zero, i.e. d(^{2}H:^{16}O)/dl $\rightarrow$ 0. The trapped deuterium follows Fick's law, the fitted solution is the error function $c_H(x) = k{\cdot}\text{erfc}(\text{x}/\sqrt{4DT})$, from which the short circuit diffusion coefficient, D, can be determined. The exposure time, T, is the time in the autoclave (1572 hours), and k is a scaling factor that represents the hydrogen concentration at the surface.

Internal oxides have been identified in all three samples, with an additional outer oxide on A690. The fitted diffusion coefficients are presented in Table 9.5. This shows that A690 has the greatest measured diffusion coefficient, at least

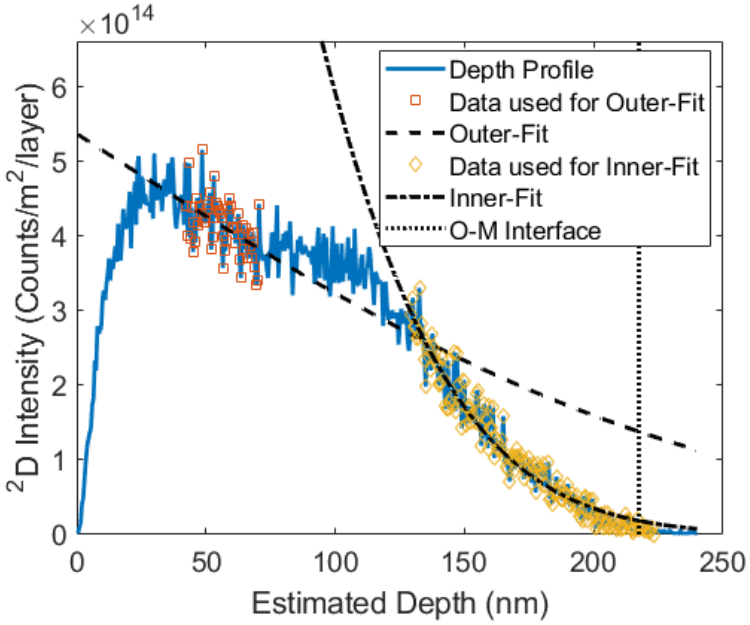


Figure 9.15: Depth profile from A690 after autoclave exposure in deuterated water, the diffusion across the barrier is shown for the inner (yellow) and outer (orange) oxides. $1ms$ pixel time and FCp 18.3nA.

double that of A600CW, and that cold-work in A600 increases the diffusion by five-times. The measured values of A600 are compared to values presented in literature. Jambon et al [114] reported by NanoSIMS profiling, that the effective hydrogen diffusion coefficient in single-crystal A600 was $5.2\pm1.2\text{x}10^{-21}\text{m}^2/\text{s}$ at PWR temperature. The slower measured diffusion coefficient in this experiment is linked the introduction of random GBs, which trap hydrogen and decrease the

Table 9.5: The short-circuit diffusion coefficients of hydrogen across the oxides of the tested alloys.

		Diffusion Coefficient (m^2/s)		
Material	Oxide Type	Sample 1	Sample 2	Literature (m^2/s)
A690	Inner	$5.4\text{x}10^{-22}$	$3.8\text{x}10^{-22}$	$2\text{x}10^{-22}$ [114]
A600	Inner	$8.4\text{x}10^{-23}$	$4.5\text{x}10^{-23}$	$5.2\pm1.2\text{x}10^{-21}$ [114]
A600 15%CW	Inner	$1.8\text{x}10^{-23}$	$1.4\text{x}10^{-23}$	–
A690	Outer	$3.3\text{x}10^{-21}$	$2.4\text{x}10^{-21}$	–

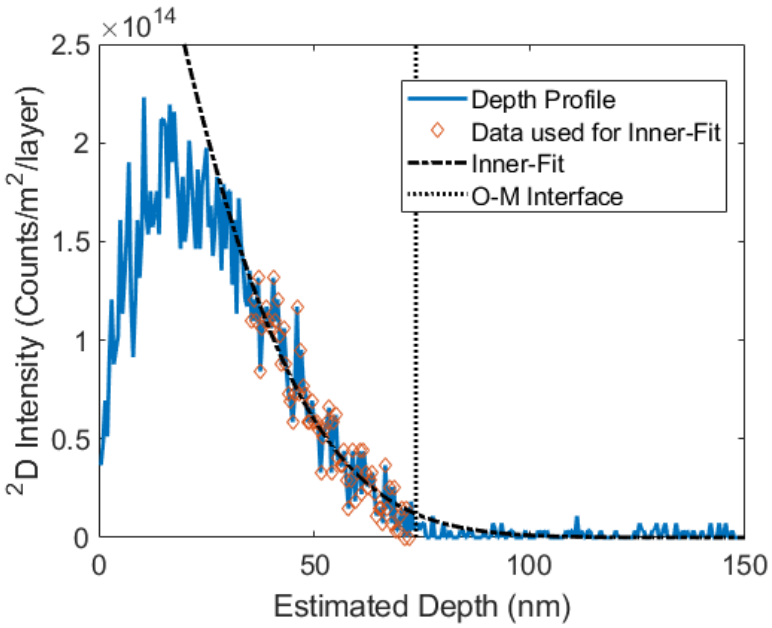


Figure 9.16: Depth profile from A600 after autoclave exposure in deuterated water, the diffusion across the barrier is shown for the inner (orange) oxide. $1ms$ pixel time and FCp 17.9nA.

apparent diffusion. The inner oxide diffusion coefficient of A690 agrees well with $2\text{x}10^{-22}\text{m}^2/\text{s}$ reported in literature [114] at PWR temperature. Gas-absorption methods have reported diffusion coefficients ten-orders of magnitude higher than those determined by nanoSIMS [377]. This suggests that the transport of deuterium across the oxide scale developed during PWR exposure is a rate limiting step for hydrogen adsorption in a passivated austenitic alloy.

9.3.3.2 3D Reconstruction

Three-dimensional maps of deuterium and oxygen have been generated, and displayed in Figures 9.18–9.20. The same regions were used to determine the depth profiling presented in Figures 9.15–9.17. Deuterium is displayed in green, oxygen in blue, and carbides in red. The deuterium signal can further be broken down in to low counts (counts$\leq$4) in light green, and high counts (counts$>$4) in dark green. The depth of each image is scaled to increase visibility, the depth is estimated using an average slice thickness of 0.5 nm.

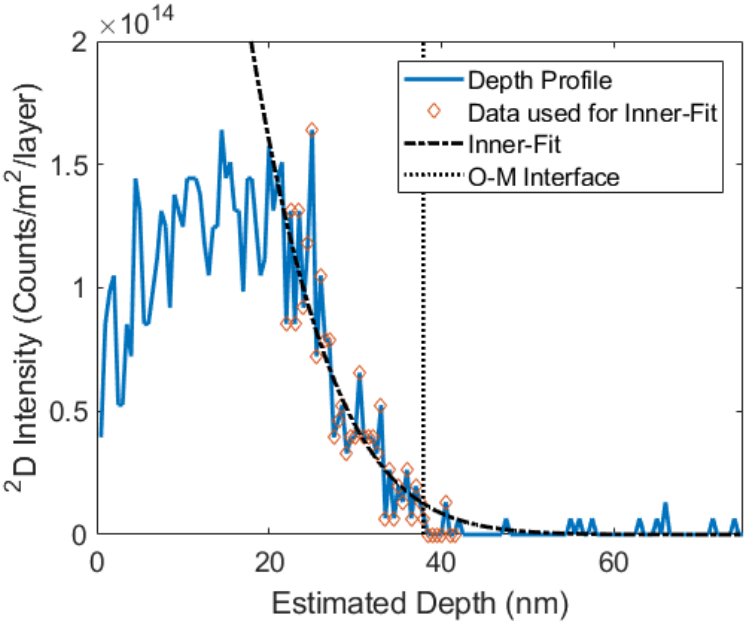


Figure 9.17: Depth profile from A600 cold-work after autoclave exposure in deuterated water, the diffusion across the barrier is shown for the inner (orange) oxide. $1ms$ pixel time and FCp 19.4nA.

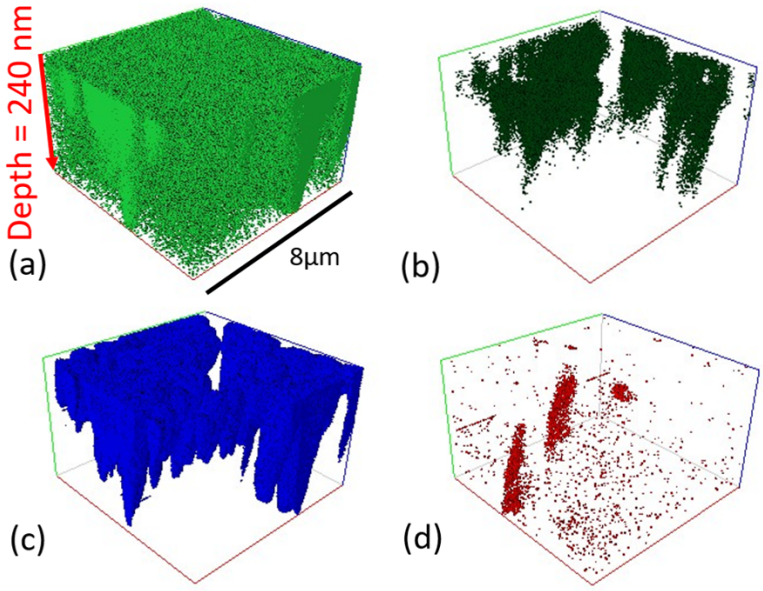


Figure 9.18: 3D reconstruction of low deuterium (light and dark green), oxygen (blue) and carbides (red) from the depth profile of A690 used in Figure 9.15.

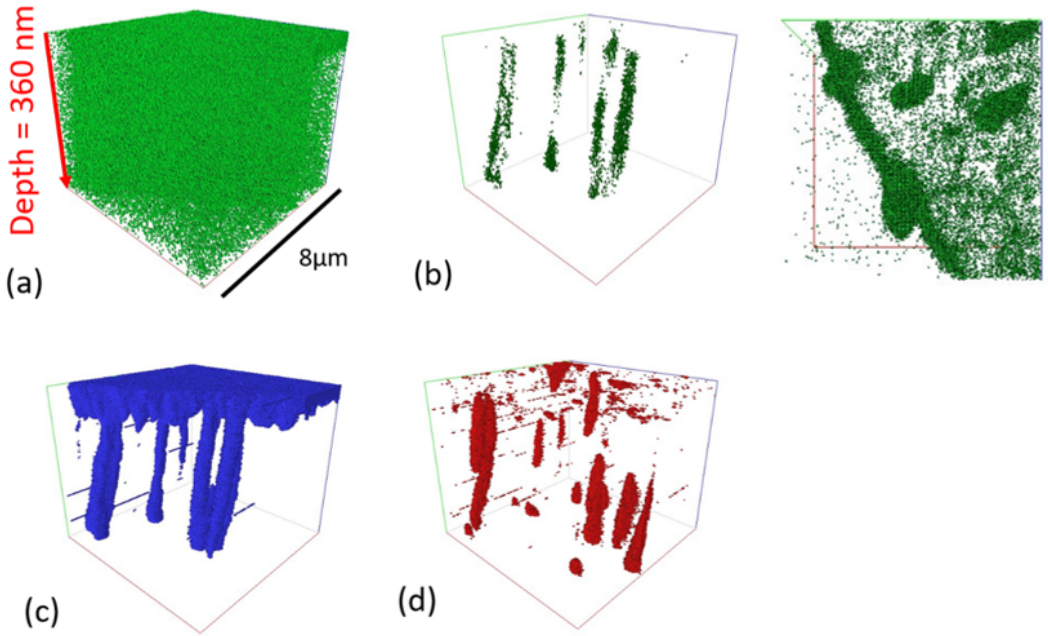


Figure 9.19: 3D reconstruction of deuterium (light and dark green) and oxygen (blue) and carbides (red) from the depth profile of A600 CW used in Figure 9.17. (b) is a top down view to show the strong deuterium signal originating in the grain boundary oxide.

Figure 9.18 shows the 3D depth profile of A690. There is a clear correlation between high deuterium counts and the location of oxide, suggesting that deuterium is trapped in high densities in the oxide or at oxide particle interfaces. The oxide has a very low measured porosity from the Fresnel analysis (Section 5.2.3.3); therefore, the slow deuterium diffusion across the boundary is thought to be linked to this high signal, instead of free surfaces from porosity trapping hydrogen. There are low deuterium counts uniformly distributed across the remaining volume, showing there is a significant deuterium content in the lattice. Trapping occurs at carbides that exist along the GB. There are no clear signs of oxidation due to a higher Cr content.

Figure 9.19 shows that high deuterium counts are located near to oxides along a grain boundary and near intergranular carbides. Intragranular carbides are present, but do not correlate with high deuterium counts and they are thought

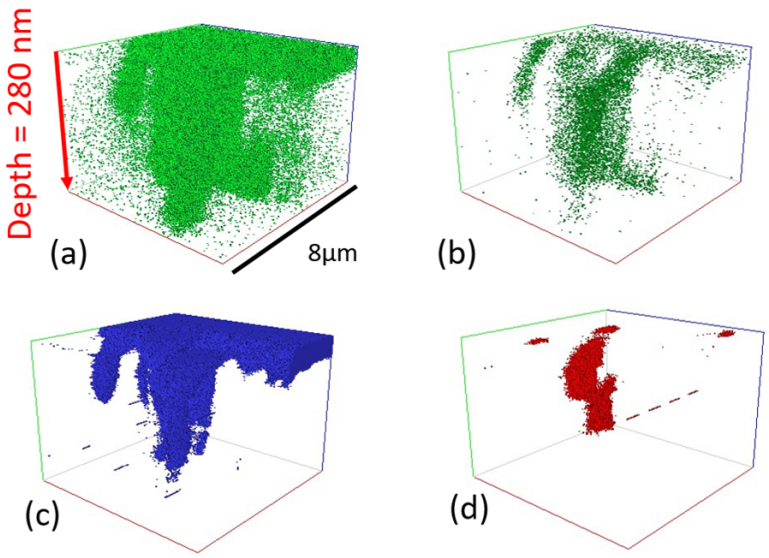


Figure 9.20: 3D reconstruction of deuterium (light and dark green) and oxygen (blue) and carbides (red) from the depth profile of A600 used in Figure 9.16.

not to be oxidised. There is an orientation dependence of the deuterium content on the exposed surface, however, low deuterium counts are recorded uniformly throughout the bulk.

Figure 9.20 shows the 3D depth profile of A600. There is a correlation between high deuterium counts, oxide, and carbides in the sample. Unlike the previous sample, there is a low level of deuterium connectivity, indicating these observations could be associated with particles, not a layer. In both low and high counts we see a strong orientation dependency from the growth of the surface oxide. The deuterium signal is uniform in the oxide layer. The low deuterium counts correlate with a grain boundary in the sample.

These three austenitic nickel alloys show that deuterium is trapped strongly in the same sites, but in different concentrations. The main observed trapping sites include grain boundaries, surface oxide, intergranular carbides and bulk. The goal of the following discussion is to take a holistic view of hydrogen uptake and trapping in austenitic alloys by combining the presented TDS and NanoSIMS observations.

9.3.3.3 Depth Profiling - Hydrogen Concentrations

Table 9.6 shows the mean deuterium content, with standard deviation, for both the oxide layer and metal matrix. The mean D content in the oxide layer is defined as the half-height of the deuterium peak, and in the matrix as the mean deuterium value after the oxide-metal interface. A690 has the greatest normalised deuterium content in the oxide and the lowest in the matrix, this is due to the thicker chromite protective oxide layer that has prevented D diffusing into the bulk. The concentration of D in the oxide layer of A600CW and A600 are within error. This is inline with expectations, cold-work should only influence the thickness of the oxide, so similar D contents are expected. The D content measured in the bulk of A600CW is similar to A600. The low deuterium concentration found in the bulk likely makes these results indistinguishable.

There are three points to consider when comparing the two NanoSIMS methods. Firstly, the top-down analysis has had no prior sample preparation. The cross-sectional samples had to be cut, polished, and mounted. The polishing exposes the analyzed surface before the measurement, with the potential loss of trapped volatile species that might outgas. The mounting process will have induced thermal diffusion as the samples are heated to 100 — 150 °C. Secondly, cross-sectional analysis is sensitive to surface conditions as it the sampling depth is 10 nm. The top-down analysis samples over 300 nm. Finally, top-down method has a smaller pixel size 500 nm^2, than the cross-section method which used a 1.875 μm^2 pixel size.

Table 9.6: The normalised deuterium concentration of the tested alloys.

	Normalised ^2H Intensity (cts/m^2/slice)	
Material	Matrix	Oxide
SS316L	-	-
A800	-	-
A690	$1.11 \pm 0.02 \times 10^{12}$	$3.7 \pm 0.4 \times 10^{14}$
A600	$2.7 \pm 0.2 \times 10^{12}$	$1.3 \pm 0.2 \times 10^{14}$
A600 15%CW	$5.3 \pm 0.1 \times 10^{12}$	$9.6 \pm 0.6 \times 10^{13}$

9.4 Summary and Discussion

In section 9.2.1, Figure 9.1, the hydrogen desorption from an unexposed autoclave sample of as-received A600, was characterised by a single desorption peak centered at an absolute temperature of 675±25 K. The effect of changing the temperature ramp-rate was determined, delaying the desorption peak, reducing and broadening the spectra. Finally, the investigated temperature range (298–1150 K) was demonstrated to be sensible for the hydrogen desorption of A600.

Section 9.2.2 reveals that additional desorption peaks associated with the autoclave exposure were found at 1000±25 K in samples of A600. Desorption peaks were recorded to shift to higher temperatures after exposure, indicating that the protective oxide acts as a barrier to diffusion.

The effects of alloy composition and cold-working on deuterium trapping have been quantitatively explored in Section 9.2. Figure 9.3 demonstrates that in A600CW, the majority of deuterium originates from the bulk, not the surface oxide layer. Deuterium desorption peaks from the oxide layer were identified at temperatures of 680±25 and 830±25 K, by comparing samples of A600CW with and without a surface oxide layer. These results agree with Fe-oxide peaks identified by Lee and Lee [139]. It is assumed that the majority of deuterium is stored in the bulk for all investigated alloys. Back-of-the-envelope calculations suggest this is true. The oxide layer in A690 contains 400 times the bulk deuterium (Table 9.6), and accounts for 0.012% of the sample of the sample volume. Therefore, the deuterium counts attributed to the oxide should be <5% of the total detected deuterium.

The total deuterium desorption recorded by TDS (Table 9.1), shows that the total hydrogen content of SS316L, A800 and A690, $2.3\pm0.2\text{x}10^{17}$ atoms/cm^2, is five-times greater than that of A600CW, $5.5\pm0.5\text{x}10^{16}$ atoms/cm^2. In all materials the recorded deuterium to hydrogen ratio is at least ten times the natural abundance. The deuterium content correlates with the enthalpy of diffusion. A600 has the lowest boundary to diffusion in the lattice, 46 kJ/mol. The other alloys have activation enthalpies of at least 50 kJ/mol, and upto 63 kJ/mol in the case of SS316L, which is considered a non-reversible trap. The importance of the enthalpy of diffusion increases the longer the samples are stored. Table 9.1 shows the

as-received sample of A600 has a higher deuterium content than the cold-worked samples. The increased deuterium is associated with both increased intergranular carbide coverage, and the lack of fast-diffusion pathways caused by dislocations throughout the sample.

The residuals plot is a convenient way of fitting key difference in spectra. Currently, the confidence interval of the automated MATLAB scripted used is approximately 25 K. To reduce the uncertainty in the peak positions. To reduce the uncertainty, a ramp-rate of 5 K/min is recommended for future experiments.

Section 9.3 documents deuterium trapping at common sites in austenitic steels. The resolution of the cross-section (C-S) scans (117 nm/pxl) and Top-Down (T-D) scans (30 nm/pxl) means that dislocations and microvoids cannot considered individually, but collectively in different regions of the scans such as the matrix, grain boundaries, oxides, and carbides. These investigations will be compared between both top-down and cross-sectional methods.

Firstly, the matrix regions shown in Table 9.3 and 9.6, comprise of interstitial, dislocation, void, and inclusion trapping sites. The deuterium content of individual grains was estimated using both top-down and cross-section methods. These techniques provide mixed results, with the cross-section methods suggesting that A690 has a lower deuterium count than A600, and the top-down methods suggest the A690 has a greater deuterium count than A600. It is possible that both techniques are correct. The cross-section records a lower deuterium content in the CW sample, because the deuterium diffuses outwards along fast-diffusion pathways caused by the extra dislocations from the cold working process. The T-D method records a higher deuterium content as deuterium is slow to diffuse through the oxide layer so a greater deuterium content is recorded. As previously discussed, the sample preparation of the cross-sectional method causes concerns, especially with the low count rate in the first 5–20 nm layer imaged by the NanoSIMS. This demonstrates that one technique is not necessarily enough to develop a full picture of hydrogen, and great care should be taken when interpreting results. SS316L and A800 were not analysed using the T-D method as the NanoSIMS in Oxford failed and is still awaiting repair.

Secondly, Figure 9.13 shows that carbides trap 50% more deuterium compared to the surrounding matrix. This is in agreement with atom probe tomography

results published by Chen et al [198]. Deuterium is found across the total width of the carbide [375], and not just the interfaces [376].

Thirdly, Figure 9.11 and Table 9.3 show that in the tested austenitic alloys grain boundaries have a greater deuterium content than the surrounding matrix. This is due to two factors. (1) Random boundaries are in all the alloys and due to increased dislocation densities, have a higher trapping potential [227, 138, 142, 150]. (2) Intergranular carbides are present along the grain boundaries, which trap deuterium. As neither random boundary fraction or carbide coverage correlate with the total measured deuterium content, it is likely that both these two traps are active.

Finally, as shown using both T-D and C-S methods in Figure 9.12 and Table 9.6, deuterium is highly correlated with oxide formation on the surface and along boundaries, supported by 3D constructions and depth profiling (Figure 9.18, 9.19 and 9.20). When compared to the deuterium content of random grain boundaries, no additional deuterium was detected ahead of the oxidised grain boundary in any of the alloys. After this investigation it is not possible to determine if this is due to the outwards diffusion of deuterium from the hydrostatic stress field, or that no detectable hydrogen content was found ahead of the oxidation front with the conditions used.

Assigning peaks to TDS spectra assumed that reversible traps will not contain hydrogen, eliminating dislocations, boundaries and some carbides with binding energies < 48 kJ/mol from the analysis. It is revealed by NanoSIMS that deuterium is not just limited to deep traps (inclusion, oxide and carbides), but exists uniformly throughout the matrix. This questions the validity of the TDS peak fitting presented in this chapter. The elimination of lower energy traps was used to help deconvolve the measured spectra, if it is indeed true to lower energy traps contain hydrogen, then a peak fitting approach will fail as there are too many variables and unknowns. A slower temperature ramp-rate would help decovolve deuterium from overlapping trapping sites and identify peaks.

Despite the combined approach, there are still some unidentified high energy traps in the TDS spectra. I am reluctant to attribute these sites to inclusions, as they occupy a negligible volume of the overall sample [195, 376, 378]. Furthermore, Zhang et al [379] found no such trapped deuterium at high energy inclusion

interfaces in SS304, because inclusions have a low solubility over prolonged periods of hydrogen up-take in austenitic alloys. To help identify the source of deuterium thermal desorption modelling software TMAP should be used. Using such software was outside the scope of this project, but examples of TMAP are provided in the following publications [211, 380].

Given the difficulty associated with interpreting results, a single technique is often insufficient and potentially misleading when investigating hydrogen. Confirmation of an observation by multiple techniques on independent samples allows us to be confident in the observations reported and discussed in this chapter. These results have been affected by the coronavirus pandemic, yet there is still much to take away and the deuterium detected is still significant compared to as-received samples. Therefore, repeating these experiments would be invaluable, as there is a demonstrated success using these complementary techniques.

Chapter 10

Conclusions and Future Work

The aim of this thesis was to investigating the role of hydrogen in the stress corrosion cracking (SCC) of austenitic nickel-based alloys under pressurised water reactor (PWR) conditions. In particularly, evaluating the effect of hydrogen on the temperature-dependent crack growth rate (CGR) observed by Coriou and Arioka [12, 9]. To achieve this, a multi-technique approach was employed: micromechanical tests evaluated the effect of hydrogen on the mechanical properties, and thermal desorption spectroscopy (TDS) and NanoSIMS were used to map and determine the uptake and trapping of hydrogen during PWR operation. The key findings from each chapter will be summarised, and used to make informed recommendations for future work.

10.1 Conclusions

I have applied a series of micromechanical and high magnification methods to compare the micro-mechanical properties of austenitic alloys, and the hydrogen uptake of the same alloys under PWR conditions

- Room temperature micromechanical testing has been used to compare the mechanical properties of austenitic alloys on a length-scale that is relevant to SCC. The mechanical properties of all austenitic alloys are highly comparable at room temperature, and show no deviation with changing nickel content. High-magnification cross-sectional analysis shows that the deformation mechanisms in A800 differs from SS316L and A600 at room temperature.

A800 does not undergo Σ3 deformation twinning, but instead deforms by dislocation glide. This is unexpected as the stacking fault energy of A800 is an intermediate of the other alloys. Deformation is a main SCC mechanism, and the observed alloy deformation correlates with Arioka's reported SCC CGR in PWRs, i.e the slowest CGR undergoes no twinning. As the mechanical properties of alloys with a 25-40% nickel content do not differ significantly from other austenitic alloys, it is thought that their corrosion resistance is weighted towards diffusion-based SCC mechanisms.

- High temperature micromechanical testing was used to validate that room temperature experiments are a good approximation for PWR temperature experiments, and to test the degradation of material properties at the "cool" (280°C) and "hot" (360°C) PWR temperatures investigated by Arioka et al [12]. The softening observed in both SS316L and A690 suggests that SCC is more heavily weighted towards a mechanical deformation-based mechanism. While, A800 and A600 maintain their mechanical properties, and it is likely that SCC crack growth is weighted more towards diffusion-based mechanisms.

- NanoSIMS and TDS were used to quantitatively and qualitatively explore the hydrogen trapping in austenitic alloys exposure to pure heavy water at PWR temperatures. Hydrogen is found trapped by various microstructural features, such as carbides, grain boundaries and oxides by NanoSIMS. The total hydrogen content of SS316L and A800 is five-times greater than that of A600, which correlates with the enthalpy of diffusion in the alloys. These results show an inverse trend with the SCC failure reported by Coriou, and a weaker inverse correlation to Arioka's results. The weaker correlation with Arioka's results could be due to a change in the corrosive medium, from simulated PWR water to pure water used in this study and by Coriou. It is suggested that the inverse relationship could be due to the elastic shielding provided by the hydrogen enhancing dislocation motion, and preventing the stress intensity factor reaching a critical values that will initiate crack propagation. However, as no correlation is found between hydrogen and CGR,

it is thought that hydrogen is not a dominant mechanism in SCC. The disagreement between different experiments suggests that analysing hydrogen is highly challenging, and that a multi-technique approach is essential for through characterisation.

10.2 Future Work

To fully understand the effect of hydrogen on stress corrosion cracking, and to help understand long-term environmental degradation in pressurised water reactors. Some suggestions for future work are listed:

- Hydrogen-charged nanoindentation results have been simulated using a fully coupled hydrogen transport subroutine. This model suggests that hydrogen accumulates in regions of high hydrostatic stress, and causes strain hardening. The role of hydrogen ultimately can not be determined without further experimental observations. To achieve this, a back-charging cell need to be designed and created for the XP system to avoid the unforeseen corrosion of the nanoindenter system, that has prevented further characterisation from being undertaken during this project.

- A comparative study of more complex mechanical properties, such as high temperature creep, would help better understand the behaviour of austenitic alloys held a sub-critical stresses for long periods of time.

- To better understand the up-take and trapping of hydrogen after autoclave exposure in austenitic alloys, further NanoSIMS experiments would be desirable. Future experiments should have little time between leaving the autoclave and NanoSIMS analysis, to avoid the lower counts experienced in this project, due to the corona-virus pandemic. Higher count rate would reduce errors and help determine trapping at features and identify trends in the alloys.

- Similarly, further TDS results should be collected. A question still to be full answered is the effect of cold-work on hydrogen up-take. The results

presented in this thesis are counter-intuitive, and further experiments would give greater confidence to the current observations.

- The diffuse lattice hydrogen was not investigated in the NanoSIMS or TDS, due to the cryogenic temperatures needed to freeze hydrogen in place. Cryo-atom probe tomography (c-APT) is currently used to examine diffusive hydrogen at microstructural features, and would provide the last piece of the hydrogen puzzle that is currently not explored in this project.

Appendix A

Testing the Effect of Intergranular Carbides and Cavities on Grain Boundary Cohesion in A690 by Microcantilever Fracture

A.1 Introduction

Alloy 690 is widely used as a replacement material for alloy 600, due to its superior resistance to intergranular stress corrosion cracking (IGSCC). After over 30 years of operational service in pressurized water reactors (PWRs) there has been no documented failure of A690. However, accelerated autoclave laboratory tests have shown that IGSCC cracks can grow in highly cold-worked (CW) alloy 690 samples by grain boundary cavity formation.

Cavity formation in A690 was initially observed by Arioka et al [14], who reported that creep cavities and cracks could form at grain boundaries in high cold-worked samples. An observation that was successfully replicated in other laboratories [381, 382, 22]. Arioka proposed a connection between the observation of cavities and the failure of A690 [13, 289]. The stress concentrations surrounding GB carbide precipitates attract diffusing vacancies that are injected into the bulk by surface oxidation and the mechanical deformation of cold-working. Vacancies condense on the carbide-matrix interface, which acts as a nucleation site. The accumulation of excessive vacancies develops into a cavity. These cavities are

thought to promote SCC initiation and propagation by weakening the bonding strength of the grain boundary.

This appendix departs from the findings of Airoka and Coriou, but follows the core theme of this thesis: understanding of SCC initiation and propagation to better degradation management. Developments in this area of SCC research are stalling, as traditional autoclave experiments are unable to investigate specified region of interest. So in this chapter, a site-specific micromechanical cantilever test is presented to directly investigate the bonding strength of boundaries with intergranular cavities and carbides. In addition, a finite element model, that can be calibrated against physical experiments, is used to develop a rounded understanding of the effects of boundary precipitates on the bonding strength in alloy 690. We will show its validity in this application, and consider case studies of carbides and cavities along an idealised boundary.

A.2 Experimental Micromechanical Cantilevers

A.2.1 Autoclave Testing

Autoclave experiments and sample preparation were completed by INSS, Japan. I will outline the sample preparation that was used. The alloy 690 used in this study was taken from an industrial ingot, the chemical composition of which is 0.019 C, 0.30 Si, 0.32 Mn, 0.04 Cu, 0.009 P, 0.0006 S, 30.18 Cr, 9.42 Fe, and balance Ni (wt. %). During manufacture the ingot was thermally treated, this formed a semi-continuous distribution of carbides along the grain boundaries. The grain size of this material was about 100 μm. Prior to tests, the material was cold-rolled to a thickness reduction of 30%. This process will be referred to as 30% cold-work. The IGSCC initiation testing was conducted by the Institute of Nuclear Safety Systems (INSS). The details of the autoclave procedure and slow strain rate tensile tests (SSRT) is explained in detail by Terachi et al [383]. Post IGSCC initiation test, a cross-section was taken from the sample. This sample was then ground with SiC paper and polished with diamond suspensions until an EBSD-quality surface finish was achieved.

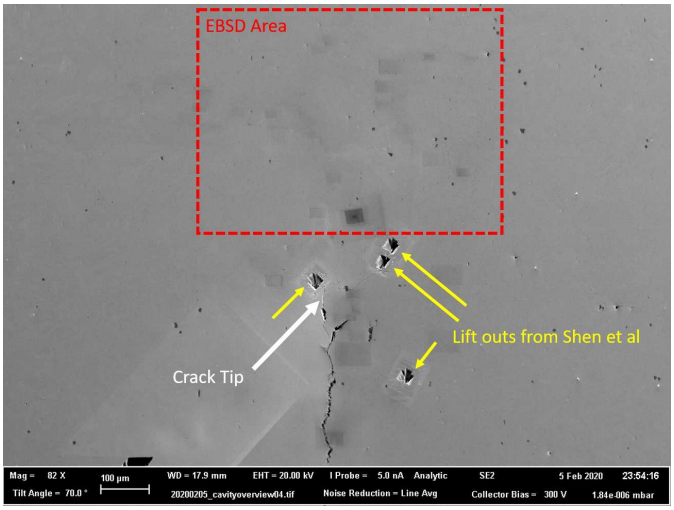
A.2.2 Methodology

In total, three boundaries with a carbide and cavity coverage were tested alongside two control boundaries with just a carbide coverage. Due to the thermal treatment every boundary had a distribution of carbides. A scanning electron microscope (SEM) was used to locate cavities ahead of the crack tip (CT). The method used to locate and image cavities is documented by Bruemmer et al [382, 22]. The local crystallography and boundary orientation were determined using EBSD.

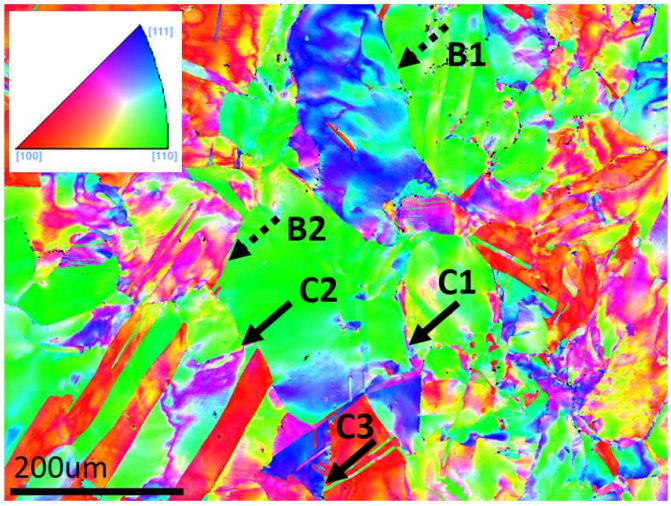
Figure A.1 displays an IPFZ map of the region ahead of the crack tip, and a macro-scopic view of the cracked sample. The prefix C denotes a boundary with cavities and B denotes a reference boundary. The loading axis is horizontal and the crack tip is 50 μm south of the location shown in the EBSD map. Cavities were found in high densities on grain boundaries up to distances of 400 μm away from the observable crack tip. Their density decreased gradually further away. The peak of population of cavities is located at the peak of the stress gradient from SCC. This is because the diffusion of vacancies are driven to regions of high stress gradients. Once there, the vacancies are free nucleate and coalesce to form cavities along the grain boundaries [14, 289].

A dual beam Auriga FIB-SEM was used to prepare site specific micro-cantilevers. Coarse trenches were milled and undercut using 2 nA probe current. The sides were refined with a 600 pA and polished to their final dimensions using 240 pA. The micro-cantilevers were a triangular cross-section and had a target width and length of 3 and 15 μm. This ratio was maintained across the samples if their exact dimensions did not match, the measured dimensions of the cantilevers are displayed in Table A.1. The boundary plane was near orthogonal to the surface and was located in the first fifth of the beam to ensure the load was well applied.

Once prepared, the microcantilevers were tested in a Keysight nanoindenter G200 series using a diamond Berkovich tip. The indenter tip was placed near the end of the cantilever. The cantilever was deflected by the tip at a constant rate of 5 nm s^{-1}, during which a load–displacement curve was recorded simultaneously. More details about this micro-mechanical technique can be found in a series of papers by Armstrong et al. [384, 73, 385, 318]. A typical load-displacement curve produced during cantilever testing and analysis is shown in figure A.2.



(a)



(b)

Figure A.1: (a) Macro SEM image of the crack tip region, highlighting the EBSD area. (b) IPFZ map of the area ahead of a SCC crack tip in A690CW. The Regions highlighted mark the tested boundaries. The pre-fix B refers to a standard boundary with carbides and C refers to a boundary with cavities. The boundaries that had cavities were much closer to the visible crack tip. The loading axis is horizontal and the crack direction runs from bottom to top.

The load-displacement curve can broken down into 5 distinct regions A-E. Region A corresponds to the indenter tip making contact with the surface, and is not purely related to the bending of the cantilever. We observe that this region

Table A.1: Dimensions of the beams tested determined by SEM, the error on these measured values is ±5%. L indicates the distance from the cantilever base to the centre of indenter tip.

Beam	Width (μm)	Height (μm)	Length (μm)
B1	2.45 ± 0.10	2.10 ± 0.10	11.10 ± 0.55
B2	2.95 ± 0.15	2.55 ± 0.15	11.90 ± 0.60
C1	3.10 ± 0.15	2.75 ± 0.15	10.80 ± 0.55
C2	2.15 ± 0.10	1.85 ± 0.10	11.30 ± 0.55
C3	2.90 ± 0.15	2.50 ± 0.10	10.35 ± 0.50

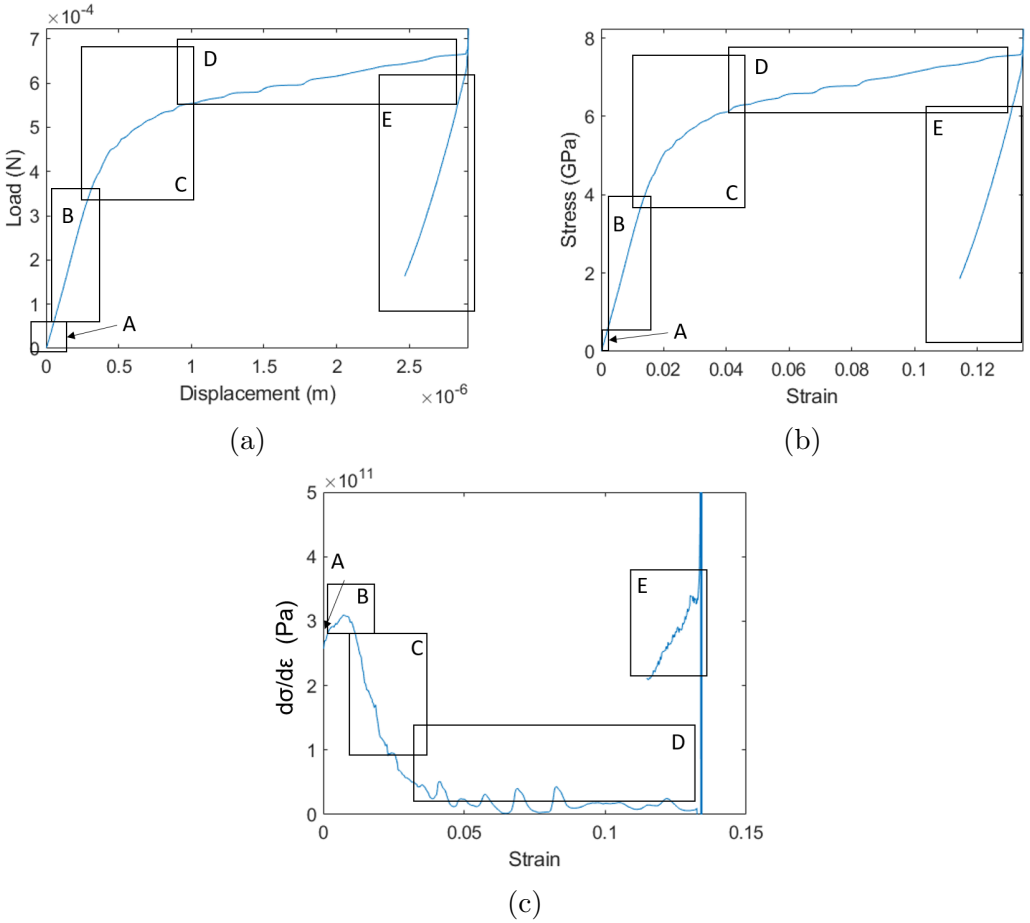


Figure A.2: Typical (a) load-displacement response, (b) stress-strain conversion using simple beam theory and (c) method of identifying elastic constants.

is not linear, but more parabolic. At displacements greater than 50 - 100 nm we enter region B, which is characterised by linear relationship between the load and displacement, this is due to elastic deformation. The transition to region C indicates the onset of elasto-plasticity, it is a gradual process and the exact yield point is not clear from the load-displacement curve alone. Region D is pure plastic deformation and is associated with displacements greater than 1000 nm. Region E is the unloading region of the curve. The indenter tip is withdrawn to 20% load where a thermal drift calculation is performed. The tip then full retracts.

The stress-strain conversion by simple beam theory [386], Figure A.2b, shows a similar regional break down to that previously mentioned. Regions B and/or E can be used to calculate the modulus, while the transition between regions b and c can be used to determine the yield stress. Figure A.2c shows the gradient of A.2b as a function of strain. The gradient is calculated by using a moving average of the nearest 10 points. The modulus can be determined by taking the mean value of the elastic region in Figure A.2c. This graph can too be split into 5 distinct regions. To evaluate the yield point, I use the definition created by Armstrong [318]. The onset of plasticity is defined as the point at which a 10% drop in mean value from the modulus is observed. While region E is meant to represent elastic unloading, the gradient plotted shows this is not the case. For this reason we use only the initial loading to calculate the material properties.

A.2.3 Results

A.2.3.1 *A690* with intergranular carbide coverage and no cavities

The boundaries decorated with only intergranular carbide coverage have not displayed fracture during testing. This is result is determined though an accumulation of recorded load-displacement data and electron imaging, shown in Figure A.3. The boundary remains continuous upon 20'000-times magnification and no large and instantaneous increase in displacement is recorded during mechanical deformation.

Table A.2 shows an overview of the results arising from the tests. The experimentally determined Young's modulus E was between 190-361 GPa. This was calculated using simple beam theory from the dimensions (Table A.1). Since the

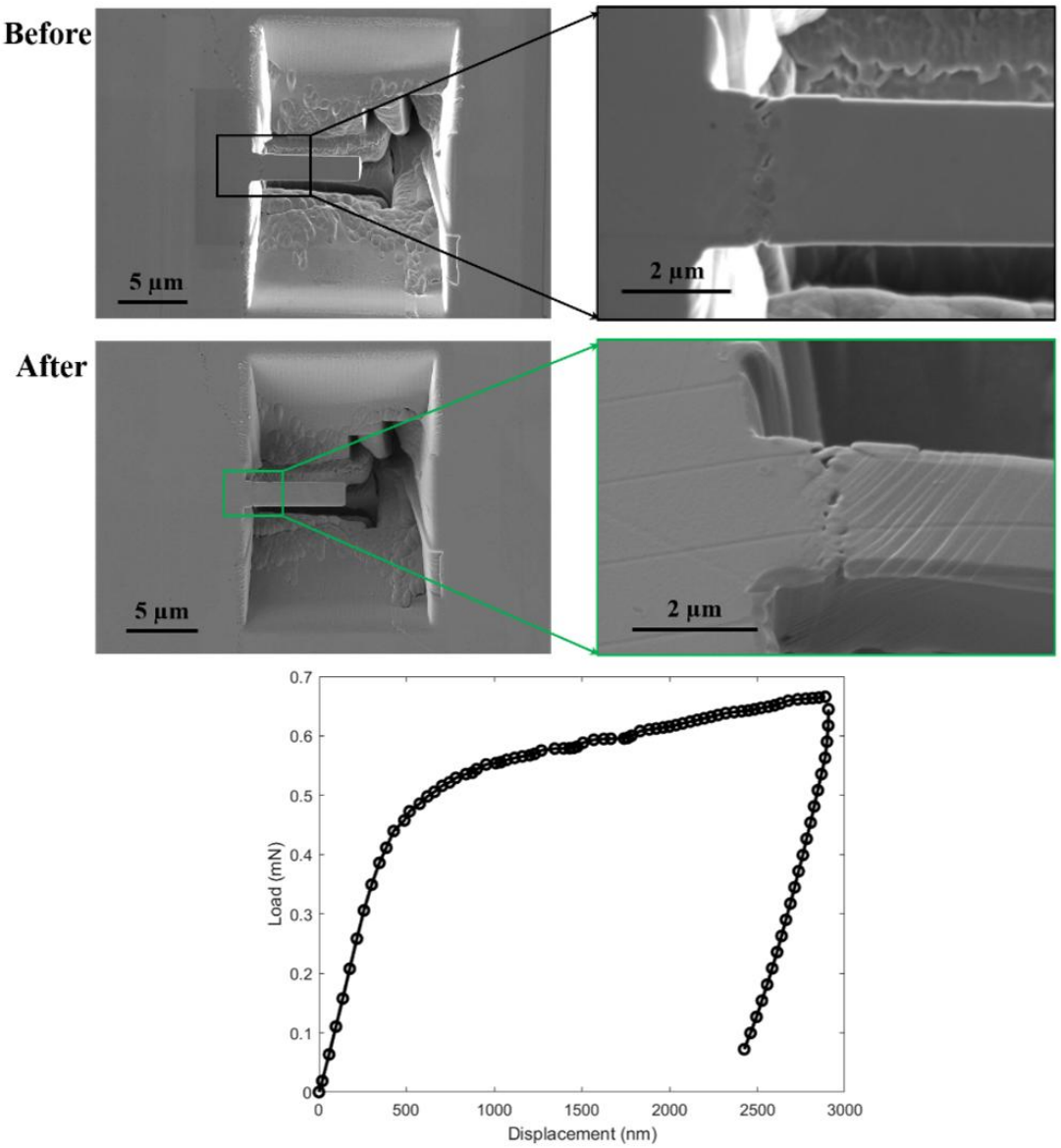


Figure A.3: Pre- and post-deflection experiment images of the beam B2. Close up images are shown of the base of the cantilever. The Load- displacement curve recorded is also displayed along side.

Table A.2: Overview of micro-cantilevers tested on A690 30%CW grain boundaries with no cavities at room temperature. The Young's modulus E was found to be anisotropic. Neither beam failed. The yield stress was calculated using simple beam theory, but lacks a sufficient sample size at the moment. The misorientation angle (MA) is also quoted between the two grains. This was calculated using the Euler angles. * = questionable experiment.

Beam	Fracture	Young's Modulus (GPa)	Yield Stress (GPa)	MA (°)
B1*	No	361	5.1	54
B2	No	190	2.9	44

boundaries did not fail during testing, the yield strength has been estimated. The reported yield stress was found to be $\sigma_Y = 2.9$ GPa. Post-deflection SEM examination of the cantilever beams has revealed that in beam B1, the indenter tip slip across the surface. This invalidates the assumptions of simple beam theory as the load is not being applied from a fixed length from the base. These results are not to be trusted.

The beams B1 and B2 have misorientation angles of 54^o and 44^o around the direction $[1\bar{2}\bar{2}]$ and [012] respectively. Under the coincidence-site lattice (CSL) framework, these are designated special boundaries, taking the values $\Sigma 15$ and $\Sigma 45c$.

A.2.3.2 *A690* with intergranular carbide coverage and cavities

Three grain boundaries with intergranular carbide and cavity coverage on the 30%CW A690 sample were tested with cantilever deflection tests. The cantilevers were deflected until either the boundary fractured, or until the indenter made contact with the sides of the cantilever site.

The boundaries exhibited one of two types of behaviour, either plastic formation or unstable fracture. The cantilevers C1 and C2 underwent plastic deformation. The final beam, designated C3, displayed unstable fracture. Figure A.4 shows a SE image of the beam C3 pre- and post-deflection. In the pre-deflection images, it is clear to see the high intergranular cavity and carbide coverage present in this test. The post-deflection images show the clear fracture of the boundary, which has opened up some 15^o. The Load-displacement curve for the fractured

Table A.3: Overview of microcantilevers tested on A690 30%CW grain boundaries with high cavity coverage at room temperature. The Young's modulus E was found to be anisotropic. One of the three most promising candidates failed. The yield stress was calculated to be 3.1±0.5 GPa. The fracture stress of the failed beam was 7.1 GPa. The misorientation angle (MA) is also quoted between the two grains. This was calculated using the Euler angles.

Beam	Fracture	Young's Modulus (GPa)	Yield Stress (GPa)	MA (°)	Cavity Coverage (%)
C1	No	260	3.4	51	17±3
C2	No	164	2.4	37	19±5
C3	Yes	169	3.6	48	32±6

sample is also shown, the large instantaneous increase in the displacement indicates fracture. The L-D curves of beam C1 and C2 resembled those of B1 and B2.

Table A.3 shows an overview of the results arising from the cantilever tests. The Young's modulus E for the deformed beams covers approximately 160 – 260 GPa. The yield stress can be calculated in C1, C2 and C3 using the load-displacement data pre-fracture. The yield stress was found to be $\sigma_Y = 3.1 \pm 0.5$ GPa. This figure agrees with the results previously presented in Table A.2. The fracture stress for C3 was found to be $\sigma_f = 7.1$ GPa. The beams C1, C2 and C3 all contain a random boundary of rotation 51°, 37° and 48° around the direction $[3\bar{2}4]$, $[11\bar{4}]$ and $[4\bar{3}1]$. All the boundaries are random and do not fulfill any CSL criterion. There is no enhanced resistance associated with any particular beam.

There is a large spread in the modulus values. To determine if this variation is linked to crystal orientation, the results are plotted over the anisotrpic modulus in Figure A.5. The modulus values are calculated using the elastic constants from [387]. As the cantilevers are a sum of two crystallographic orientations, both will influence the calculated properties. This elastic data follows the expected trend calculated [318], as the orientations approach the [111] direction the modulus approaches a maximum. The absolute values of E are between 11 - 27 % from the calculated values from literature.

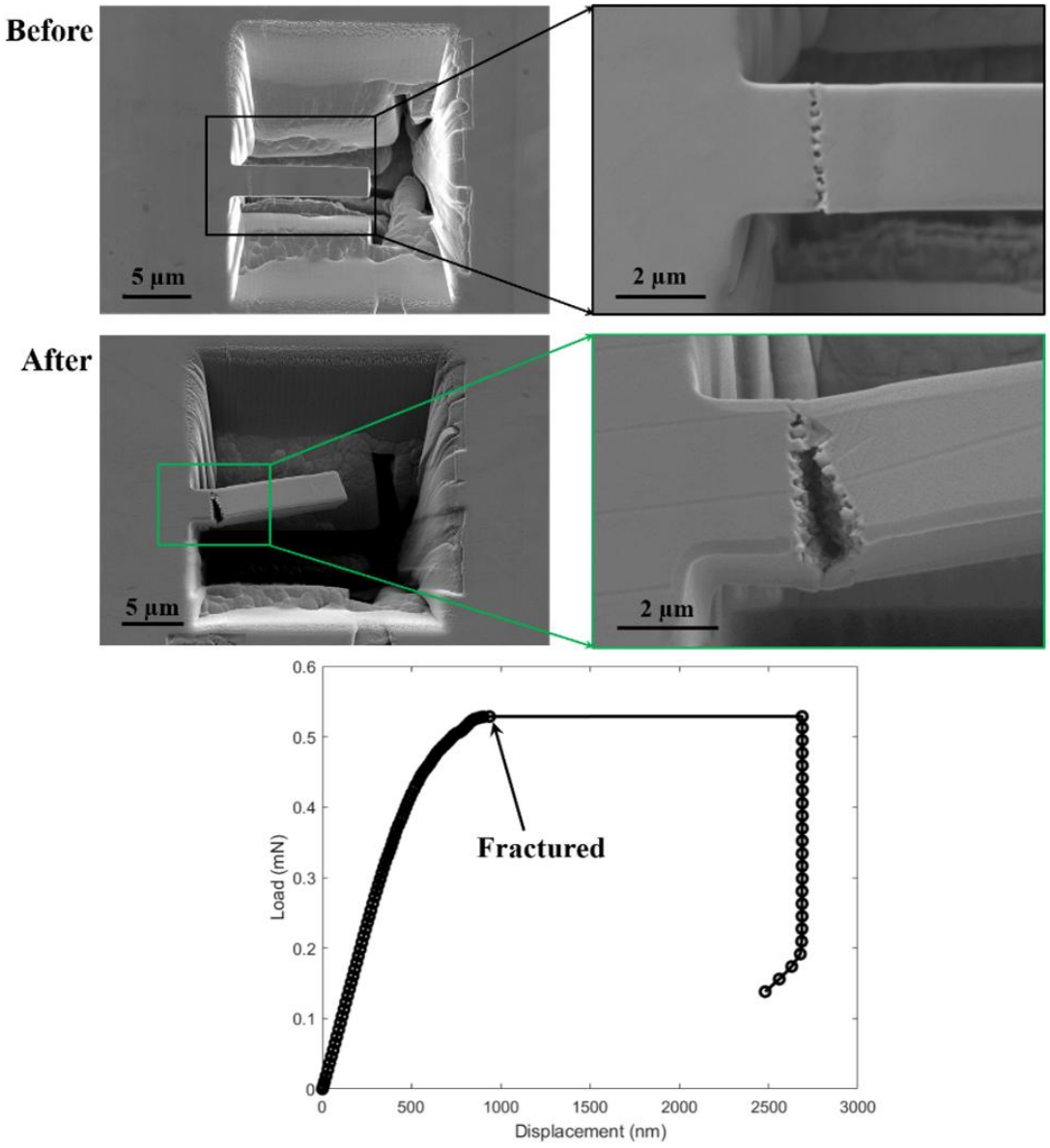


Figure A.4: Pre- and post-deflection experiment images of the beam C3. Close up images are shown of the base of the cantilever. The load-displacement curve recorded is also displayed along side.

A.2.3.3 Nanoindentation

Figure A.6 shows the hardness and modulus results determined by nanoindentation. We find that the bulk hardness, or yield stress, trends toward 4 GPa. The hardness displays a strong size effect, increasing by 50 % as the indent depth changes from 1 μm to 100 nm. The modulus is constant across the indentation depth and centred on 240 GPa. The standard deviation recorded across the 49 indents for the hardness and modulus is $\pm$300 MPa and $\pm$15 GPa respectively, this fluctuation arises from the crystal anisotropy of the material. The reported mean value is within 20% of the accepted bulk value, an accuracy that is typically expected of bulk nanoindentation.

A.2.4 Discussion

This work utilises the experimental techniques developed [73, 384] to test the effect of carbides and cavities on the bonding strength of the grain boundary proposed by Arioka et al [14]. Mechanical data has been collected from boundaries with

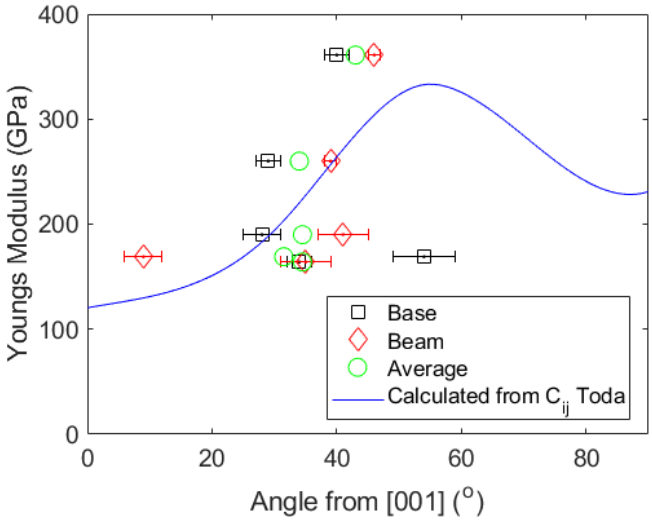
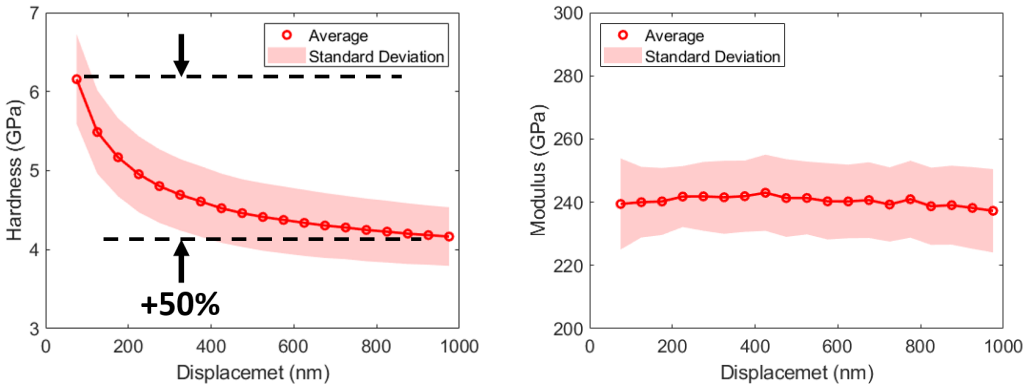


Figure A.5: Experimentally measured modulus as a function of crystallographic orientation. Solid lines represent data calculated using elastic constants found in literature [387]. The data points represent the experimentally determined Young's modulus, the error bars are associated with the uncertainty in orientation due to excessive cold-working.

only intergranular carbide coverage, and from boundaries with both intergranular carbide and cavity coverage. A single boundary has been shown to fail.

The Young's modulus was found to be highly anisotopic ranging from 164-360 GPa. This is inline with the high levels of anisotropy found in nuclear austenitic nickel alloys [73] and nanoindentation. The macroscopic value of 206 GPa [348] falls within the presented range, giving confidence to this result.

Regarding the mechanical behaviour results, this yield stress is significantly higher than the bulk values of as-received (205 - 345 MPa [388]) and 30% cold-worked (650 - 875 MPa [345, 389, 390]) A690. The yield stress is determined by classical beam theory. It is found that the elastic properties of the material are in line with theoretical calculations of the anisotropic Young's modulus [387]. As the elastic properties are reasonable, it can also be assumed that the plastic properties are reasonable due to the calculations being coupled. Therefore, the presented yield stress is thought to be elevated due to size effects typically associated with micro-mechanical tests [391, 392]. This is not uncommon. [73] reported a yield strength of 825 MPa for A600 by micromechanical testing, which is 4-times the accepted bulk value of 205 MPa. This was an annealed sample with low dislocation density. The mechanism driving this increase in the stress is thought to be dislocation pile-up [393, 394]. The dense dislocation network, induced through severe cold work, and pile-ups at the grain boundary inhibit the movement of dislocations. In turn,



(a) (b)

Figure A.6: The mean and standard deviation of hardness and Young's modulus values over a 1 μm depth range.

this requires a higher stresses to overcome the pinning and initiate plasticity.

The intergranular carbide coverage was assumed constant for all samples with a value of 45 %. Considering this, it is thought that the fracture of the boundary is directly linked to the cavity coverage along the boundary. This is because the failed boundary had the greatest intergranular cavity coverage. The measured intergranular cavity coverage of the fractured boundary was 50 % greater than the other boundaries.

The boundary that fractured had an MO angle of 48^{o}. It is the median MO angle reported, and is a random boundary. There is no obvious preferential strengthening or weakening associated with this boundary, and as a results the fracture is thought to be independent of MO [395].

The cantilever deflection tests are conducted on boundaries that are over 12 μm ahead of the crack tip. At this distance electron energy loss spectroscopy (EELS) has shown that no oxidation of the carbide interfaces or boundary is observed [396]. This is important for modelling.

The cantilever deflection tests presented have been achieved in air at room temperature (RT), while the operating temperature of a reactor is approximately 300^{o}C and in a hydrogenated environment. It is known that in austenitic alloys, the yield and ultimate tensile (UTS) strengths are reduced at high temperatures [328]. However, as fracture is possible at RT, the reduction of the UTS linked to high temperature PWR conditions is thought to enhance boundary fracture. Previous chapters have aimed to explore the mechanical properties at high temperatures. To explore boundary behaviour of A690 at PWR temperatures, it is possible to repeat this experiment using high temperature nanoindetation. Examples of this method have been published and are left from the reader to explore [397].

To test and further explore the role of cavities on the boundary strength, more cantilever fracture tests would be needed to test a range of conditions. However, finding suitable regions, e.g. 25% coverage, and cantilever fabrication is proved challenging and time consuming. To continue our investigations on the effects of both intergranular carbide and cavity coverage on the boundary strength, it was decided to model the conducted experiments using finite element analysis. Modelling the cantilevers would allow a range of intergranular carbide and cavity

configurations to be tested, including ideal case studies that would not naturally be found in the material. The results are presented in the next section.

A.3 Modelling Micromechanical Cantilevers

In the preceding experimental section we have discussed the results of cantilever deflection tests on 30 % cold-worked A690. Many interesting trends have been observed, linking high intergranular cavity coverage to intergranular failure. However, a more robust analysis is required. Due to the limitations of the experimental procedure, I will use finite element modelling to isolate and investigate the role of intergranular carbides and cavities on the failure of A690. Over the next chapter, I will discuss the methods used, the preliminary parameter studies and the simulation of the cantilever tests conducted.

A.3.1 Finite Element Methods

Modelling stems from the desire to understand physical processes. Continuum mechanics involves solving partial differential equations over a predefined body, subject to initial and boundary conditions. If the geometry of the object is simple, then analytical methods (e.g stress functions) can be used to determine (with-in limits) exact solutions. However, if the geometry of the object is more complex, then applying such methods is non-trivial. Finite element analysis (FEA) is a numerical method of breaking-down complex geometries into simple polyhedral elements that can be easily solved using analytical tools [398]. A solution to the FEA typically involves many thousands of calculations to achieve, and is therefore solved by a computer. The increased availability of powerful graphics processing units (GPU) over the past decade, has allowed more elaborate simulations (such as diffusion, heat transfer and fluid dynamics) to be completed quickly and efficiently on desktop computers [399].

As a result of the increased computational power and reduction in experimental sample size, there now exists a convergence between the length-scales of experiments and simulations. This enables virtual experiments to be undertaken, and directly compared to micromechanical tests [384, 73, 331]. The ability to calibrate

and verify predictive models through FEA is of great interest for wider SCC research [400, 401]. In this chapter the models and methods associated with finite element analysis will be further explored and outlined. This will start with an explanation of the crystal plasticity model, and finish with cohesive zone modelling.

A.3.1.1 Crystal Plasticity

Crystal plasticity (CP) is implemented in the commercial FEA software ABAQUS, via a user sub-routine. The motivation for using such a sub-routine is to reflect the plastic anisotropy typically associated with many crystalline materials and to capture orientation-depend phenomena, such as strain hardening and crystallographic slip [402].There are several different implementations of CP used throughout literature [403, 404, 405], but the CP model used is a user material (UMAT) variant designed by Tarleton [331, 406]. This formulation is based on the user element (UEL) model, first created and implemented successfully by Dunne et. al [407, 281]. For more information about the developed formulation and the underlying implicit integration scheme of this crystal plasticity model, please refer to the original work and the book published by Dunne and Petrinic [408].

When a crystal material becomes deformed beyond the yield criterion, a irreversible plastic deformation occurs in the form of slip activation. In the F.C.C austenitic alloys investigated in this project, there are 12 possible slip systems that might become activated depending on the Schmid factor. Upon activation, dislocations start to populate the slip plane. In sufficient numbers, this results in strain hardening and pile-ups upon the surface of the material. There are numerous methods to evaluate slip and dislocation generation. The method used in this is analysis is based on a strain gradient law.

The strain gradient law is now explained. Under the framework of crystal plasticity, the deformation of the crystal can be broken down into a multiplication of the elastic $\mathbf{F}^e$ and plastic $\mathbf{F}^p$ deformation gradients.

$$\mathbf{F} = \mathbf{F}^e\mathbf{F}^p. \tag{A.1}$$

The elastic deformation gradient is associated with stretching and rotating the atomic lattice, while the plastic deformation gradient is solely due to crystal slip

from simple shears. This plastic deformation gradient obeys a user defined flow law. It has the form

$$\dot{\mathbf{F}^p} = \mathbf{L}^p \mathbf{F}^p, \tag{A.2}$$

where $\mathbf{L}^p$, is the velocity gradient. The velocity gradient quantifies the deformation of the crystal that is caused by the movement of dislocations along the activated k^{th} slip system with normal $\mathbf{n}^k$ the direction $\mathbf{s}^k$. Formally, this is expressed as

$$\mathbf{L}^p = \sum_{k=1}^{N} \dot{\gamma}^k \mathbf{s}^k \otimes \mathbf{n}^k, \tag{A.3}$$

where N is the total number of active slip systems and $\dot{\gamma^k}$ is the crystallographic slip rate on the k^{th} slip system. The crystallographic slip rate is a constitutive equation that is physically-based on a power law. This introduces a strain-rate dependency in the material

$$\dot{\gamma}^k(\boldsymbol{\sigma}) = \begin{cases} 0, & \text{if } |\tau^k| < \tau_c^k. \\ A \sinh\big(B(|\tau^k| - \tau_c^k)\big) \operatorname{sgn}(\tau^k), & |\tau^k| \geq \tau_c^k. \end{cases} \tag{A.4}$$

where A and B are fitting constants with the following form

$$A = \rho_m \, b^2 \, \nu \exp\bigg(- \frac{\Delta H}{k_b \, T}\bigg), \quad B = \frac{V}{k_b T}, \tag{A.5}$$

where ΔH is the Heltholtz free energy, ν is the attempt frequency, k_b is the Boltzmann constant, V is the activation volume, T is the temperature and ρ_m is the density of mobile dislocations. As postulated by Schmid, the material will only yield once the absolute of the resolved shear stress is greater than the critical resolved shear stress (CRSS) i.e. $|\tau^k| = |\boldsymbol{\sigma} : (\boldsymbol{n}^k \otimes s^k)| \geq \tau_c^k$. Once plasticity is achieved, the CRSS is increased by the hardening law [331]

$$\tau_c^k(\rho_c^k) = \tau_c^0 + C \, \mu \, b \, \sqrt{\rho_c^k}, \tag{A.6}$$

where τ_c^0 is the strain-free CRSS, b is the Burger's vector, ρ_c^k is the dislocation density intersecting the k^{th} slip-plane, and C is a fitting parameter. The dislocation density comprises geometrically necessary dislocations (GNDs) and statistically

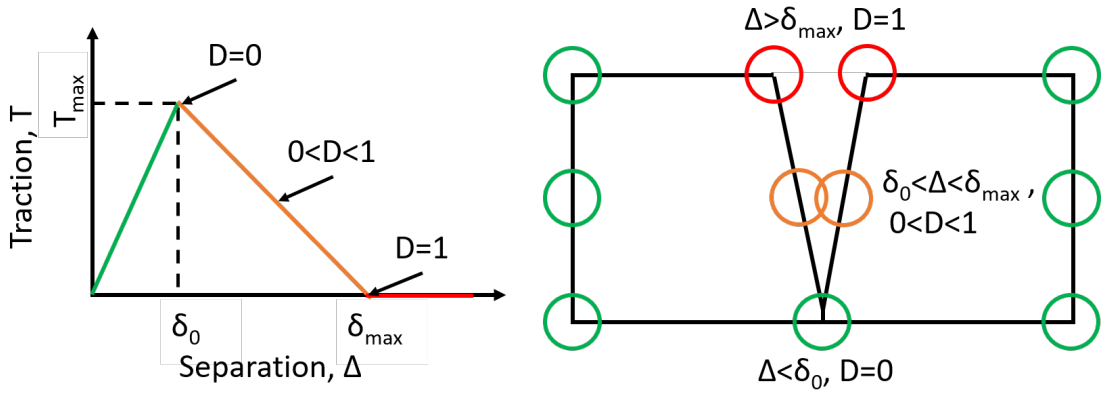


Figure A.7: The grain boundary cohesion law, as the properties decay after maximum traction is reached, and the visual representation of the nodes.

stored dislocations (SSDs), it can be related to experimentally measurable GND values by the following

$$\rho_c^k = \sum_{j=1}^{18} |\, \mathbf{l}^j \cdot \mathbf{n}^k |\, \rho_{GND}^j \tag{A.7}$$

where $\mathbf{l}^j$ is the direction of the dislocation line and $\mathbf{n}^k$ is the slip-plane normal.

A.3.1.2 Boundary Traction Law

In poly-crystalline materials, and models of sufficient complexity, it may be desirable to simulate weak interfaces. This can be achieved using a cohesive interface, which may separate or fracture when subjected to a sufficiently large stress [409, 410, 411]. The cohesive interface evaluates a traction-separation law (T-Δ), which relates the tractions (t_n, t_s, t_t), in normal and shear directions on the interface to the displacement discontinuity $(\delta_n, \delta_s, \delta_t)$ across the surface. One big advantage of this method is that it combines crack initiation and propagation within one model - making it ideal for SCC investigations [412].

The traction-separation law of the cohesive interface is illustrated in Figure A.7. The initial response of the interface is that of a linear elastic boundary. The stiffness along this boundary is defined as $K_i = \sigma_i/\delta_{0i}$. This is the assumed behaviour until the nominal stress reaches a critical threshold σ_{max}, and the max-

imum nominal stress ratio reaches one

$$\max\left\{\frac{\langle t_n\rangle}{t_n^0}, \frac{t_s}{t_s^0}, \frac{t_t}{t_t^0}\right\} = 1. \tag{A.8}$$

At this point, damage is initiated. Damage refers to the on-set of degradation in the material's response, i.e. the assumed elastic linear boundary is weakened. The damage evolution law describes the rate at which the material stiffness degrades once the damage initiation criterion is fulfilled. A scalar damage variable D is used to represent the degradation of the damaged elements. D increases from $0 \rightarrow 1$ as $\Delta = \delta_0 \rightarrow \delta_{max}$, where $\Delta = \sqrt{\langle\delta_n\rangle^2 + \delta_s^2 + \delta_t^2}$ is the effective nodal displacement. The effective traction is defined in similar way $T = \sqrt{\langle t_n\rangle^2 + t_s^2 + t_t^2}$. The damage effects the traction model according to the definition by Camanho and Davila [413]

$$D(\Delta) = \begin{cases} 0, & \Delta < \delta_0 \\ \dfrac{\delta_{max}}{\Delta}\dfrac{(\Delta - \delta_0)}{(\delta_{max} - \delta_0)}, & \Delta \geq \delta_0 \end{cases} \tag{A.9}$$

$$\mathbf{T} = (1 - D)\mathbf{K}\Delta. \tag{A.10}$$

Material models that exhibit material stiffness degradation often suffer from convergence issues. These arise from elastic snap-backs upon the initiation of damage. As described by Gao and Bower [391] a method of overcoming these instabilities is to include a viscous term. A small viscous term (small compared to the characteristic time increment of the model) can usually help improve the rate of convergence of the Newton-Raphson method used to solve the constitutive equations of the model. The solutions of the viscous system dependant on its implementation. The value of the viscous parameter should be minimised. As $t/\mu \rightarrow \infty$, where t is the characteristic time, the solutions of the viscous system tend to those of the underlying inviscid model.

In addition, to simulating the fracture and load-displacement of a mechanical test, several key parameters can be calculated. These include the critical fracture energy, G_c, which represents the total area underneath the traction-separation law

$$G_c = \frac{1}{2}\sigma_{max}\delta_{max}, \tag{A.11}$$

and the fracture toughness via the following relationship

$$K_{IC} = \sqrt{G_c E}, \tag{A.12}$$

where E is the Young's modulus of the material.

To ensure the accuracy and reliability of the model being used, there must be a suitable choice of mesh size to ensure the cohesive region is well captured. The length of the cohesive zone be estimated from a range of physical parameters inputted to the FEA model

$$l_{CZ} = ME\frac{G_c}{\sigma_{max}^2}, \tag{A.13}$$

where M is a parameter close to 1. Therefore, the necessary number of elements needed in the cohesive zone is given by

$$N_e = \frac{l_{CZ}}{l_e}, \tag{A.14}$$

where l_e is the mesh size along the cohesive zone. These equations are not exact, but they are useful to ensure suitable inputs are selected.

A.3.2 Material Definition, Model Specifications and Parameter Studies

The task presented is to re-produce the experimental observations achieved in Section A.2 and extract mechanical values such as boundary strength. The physical dimensions of the model are taken from electron micro-graphs presented in Section A.2. It was noted that the mechanical properties of A690 displayed a strong crystallographic dependence. To capture this anisotropic behaviour a crystal plasticity will be used to emulate the beam-specific elastic and plastic deformation. The crystal plasticity code used in this work was developed by Dunne et al [281, 408] and Tarleton [285]. The grain boundaries, centre to this investigation, are captured with a cohesive interface [391]. The parameters of both the crystal plasticity and cohesive interfaces will be calibrated against the collected experimental load-displacement data. Previous attempts at incorporating both crystal plasticity and cohesive boundaries have been unsuccessful [73]. However, in this study we present a fully implemented crystal plastic approach with cohesive surface law. This has been made possible by refinements to the UMAT crystal plasticity subroutine.

Table A.4: The elastic constants of A690, from [387].

C_{11}	C_{44}	C_{12}
258 GPa	136 GPa	172 GPa

A.3.2.1 Crystal plasticity Parameter Fitting

The anisotropic elastic material constants for the crystal plasticity model were calculated using the stiffness matrix of Alloy 690 published in literature [387]. The stiffnesses used are provided in Table A.4. In a cubic material, such as A690, there exists three mutually orthogonal planes of reflective symmetry, and four-fold (90°) rotational symmetry. This reduces the number of independent elastic constants to three, where $c_{11} = c_{22} = c_{33}$, $c_{44} = c_{55} = c_{66}$ and $c_{12} = c_{13} = c_{23}$. For such a material the Young's modulus, Poisson's ratio and the shear modulus can be calculated with the following relationships in Eq A.15 - A.17 [414]. This gives a calculated Young's modulus of $E = 120$ GPa, Poisson's ratio $\nu = 0.4$ and a shear modulus of $\mu = 136$ GPa as summarised in Table A.5.

$$E_1 = E_2 = E_3 = E = \frac{c_{11}^3 + c_{12}^3 - 3c_{11}c_{12}^2}{c_{11}^2 - c_{12}^2} \tag{A.15}$$

$$\nu_{12} = \nu_{13} = \nu_{23} = \nu = \frac{c_{12}c_{11} - c_{12}^2}{c_{11}^2 - c_{12}^2} \tag{A.16}$$

$$\mu_{12} = \mu_{13} = \mu_{23} = \mu = c_{44} \tag{A.17}$$

The Euler angles (ϕ_1, Φ, ϕ_2) were found from the IPFZ map collected by EBSD and extracted using m-tex [415]. They are displayed in Bunge notation (Z,X,Z') for the free and fixed end of the cantilevers in Table A.6. In order to input the crystal lattice orientation, the Euler angles had to be transformed into a (3x3) rotation matrix, this was calculated by using a script provided by Edmund Tarleton. The unique crystal orientation for both grains in the as-received conditions (before any displacement) were implemented into each individual model. This allows the UMAT to determine any slip activation and deformation that may arise during the beam loading.

The slip (Eq. A.18) and hardening laws (Eq. A.19) within the crystal plasticity framework have variables that require calibration, or fitting, against experimental

Table A.5: The parameter values used in the implementation of the crystal plasticity script.

Parameter	Symbol	Value	Source
Young's Modulus	E	120 GPa	[387]
Poisson's ratio	ν	0.4	[387]
Shear Modulus	μ	136 GPa	[387]
Burger's Vector	b	0.25 nm	[345]
Helmholtz Free Energy	ΔH	3.45x10^{-20} J	[417]
Boltzmann's Constant	k_b	1.38x10^{-23} Jk^{-1}	[417]
Temperature	T	293 K	[417]
Frequency of Attempts	ν	1x10^{11} s^{-1}	[417]
Dislocation Density	ρ_{SSD}	5x10^{10} m^{-2}	[417]
Critical Resolved Shear Stress	τ_{CRSS}	675MPa	Fitted
Mobile Dislocation Density	ρ^m_{SSD}	5x10^{10} m^{-2}	[417]
Probability of pinning	Ψ	1.45x10^{-4}	[417]
Fitting Parameter	A	0.064 s^{-1}	Calculated
Fitting Parameter	B	2.45x10^{-4} MPa^{-1}	Calculated
Slip-law Hardening Parameter	C	0.25	Fitted
Dislocation mobility Parameter	D	5x10^{3} μm^{-2}	Fitted

observations. These values are the critically resolved shear stress τ_{CRSS} and the hardening terms C and D. The parameters A and B are material specific. They are calculated using fundamental properties and held constant over all simulations [416]. The constants used elsewhere in the UMAT are summarised in Table A.5. These are taken from published works by Kartel et al [417].

$$\dot{\gamma} = A \sinh(B \left|\tau - \tau_C\right|) \operatorname{sgn}(\tau) \tag{A.18}$$

$$\tau_c = \tau_0 + C\,\mu\,b\,\sqrt{\rho}, \quad \text{where} \quad \rho = D\sqrt{\frac{2}{3}\dot{\epsilon}_{ij}\dot{\epsilon}_{ij}} \tag{A.19}$$

The fitting parameters can each be altered independently, and used to re-create a wide range of material responses. There are no unique solutions to fitting with this many parameters. It is therefore imperative to understand how each parameter affects the simulated load-displacement data. This has been completed through a

Table A.6: Euler Angles of the fix and free ends of the cantilevers simulated in Bunge notation.

Name	Fixed	Free
C3	(165,31,209)	(70,39,258)
B2	(38,56,307)	(53,16,293)

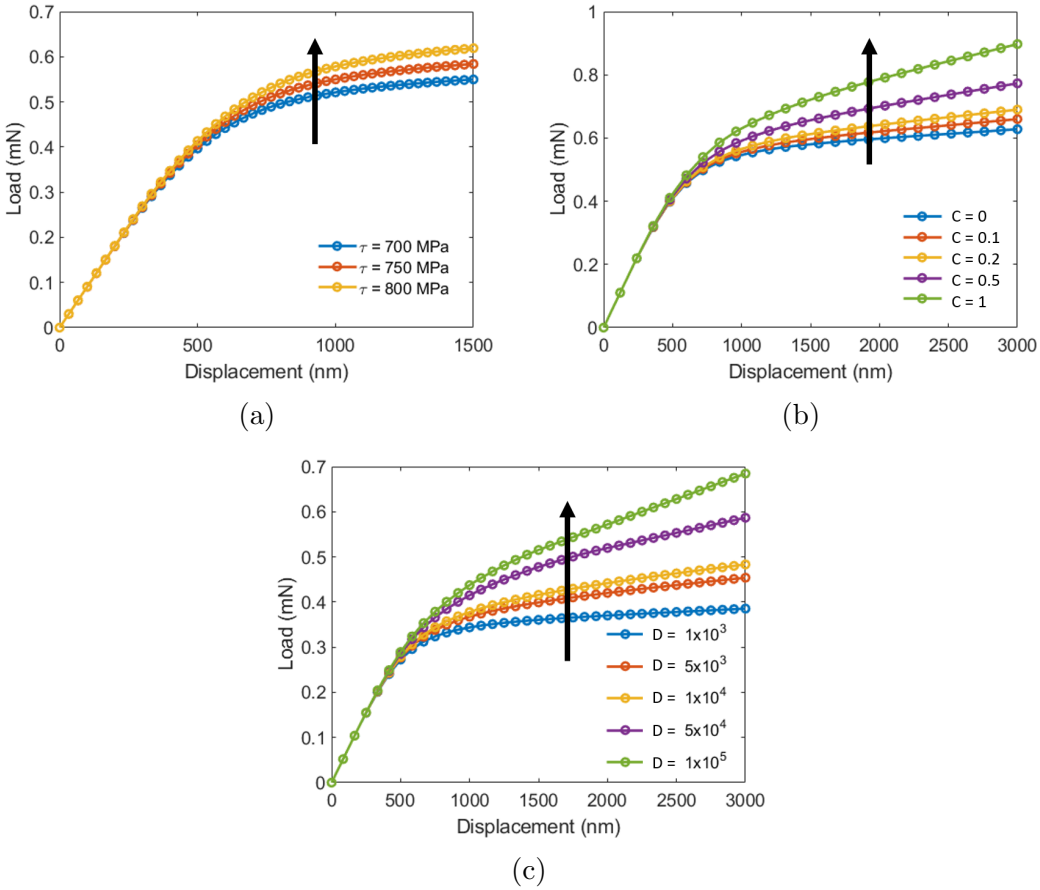


Figure A.8: (a) The influence of the critical resolved shear stress on the simulated load-displacement response. The hardening fitting parameter was held constant. Arrow shows the effect of increasing parameter value on the load-displacement. (b) The influence of the hardening fitting parameter on the simulated load-displacement response. The critical resolved shear stress was held constant. (c) The influence of the dislocation mobility hardening on the simulated load displacement. The critical resolved shear stress was held constant.

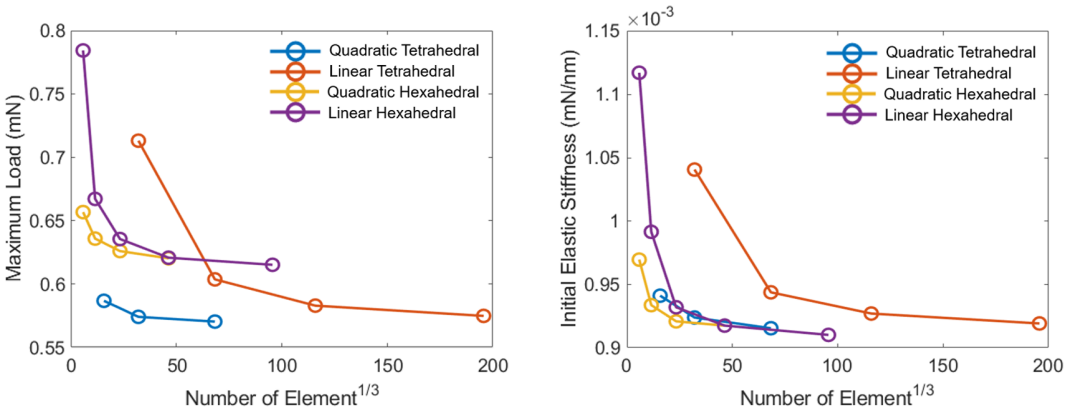
parameter study. A systematic approach was taken, each variable was individually changed and the effects on the load-displacement documented (Figure A.8).

The critical resolved shear stress governs the stress at which a slip-system activates. As illustrated in Figure A.8a, a higher τ_{CRSS} results in a longer linear elastic regime. The parameters C and D determine the strain-hardening rate of the material, or the rate that τ_{CRSS} increases once a slip-system is activated. Figure A.8b shows that as C increases, the load required to deflect the beam increases. It is apparent that there is a power-relation between this parameter and observed hardening. For the experiments conducted, C should have a value between $0 < C < 1$. It is also noted that as $C \to 0$ we recover the case of perfect plasticitySimilarly, Figure A.8c shows that as D increases, the hardening increases following a power-law. D links the dislocation density to the plastic strain. Therefore this value is large, typically on the order of 10^4 μm^{-2} [418, 331].

A suitable element choice is required for accurate modelling; each element type is situational. The investigated elements were tetrahedral (C3D4 and C3D10) and hexahedral (C3D8 and C3D20R) in both their linear and quadratic formulation (Figure A.9). The initial stiffness of all the element type was found to convergence at a similar value. In contrast, comparing the maximum applied load shows two emerging trends. The applied load in cubic elements is approximately 10% greater than that in tetrahedral elements. These results confirm that hexahedral elements are superior at stress calculations during bending [419], and that quadratic elements converge faster than linear elements. There is a trade off, quadratic elements converge faster, but linear elements are quicker to compute. Speed is crucial for efficient analysis and it is prioritised. An element size of 100 nm was found to be sufficient to converge the simulated response for cubic elements. These findings are in-line with results of Hardie et al [420] and Dohr et al[73] on CPFEM. Here on in, during simulations an element size of 100 nm can be assumed in regions where accurate stress information is necessary, unless otherwise stated.

A.3.2.2 Cohesive Boundary

In this study the cohesive boundaries are implemented with cohesive surfaces. Traditionally cohesive elements have been used to model boundaries. However, a cohesive surface is preferable, as it offers greater flexibility and greater numerical



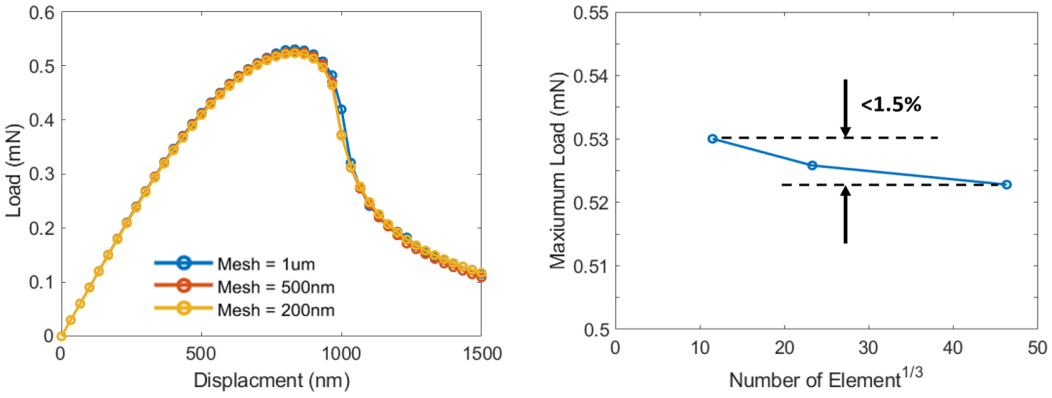
(a) (b)

Figure A.9: The effect of mesh size and element type on (a) the maximum applied load and (b) initial stiffness of the cantilever beam.

stability when compared to cohesive elements [421]. Within a cohesive surface there are various tracking and sliding options that are uniquely available. For the proposed application, the default discretisation of the boundary is "surface-to-surface". This was chosen as it is expected to yield the most accurate stress results [73].

The element size of the cohesive surface can be independent to the surrounding crystal plasticity model, so an appropriate element size can be selected to properly capture the interaction between two surfaces. It was reported by Selament et al [422] that C3D8 elements minimise convergence issues for a cohesive boundary, this agrees with my experience testing both linear and quadratic hexahedral elements. For this reason, I will use C3D8 elements as default unless otherwise stated. The mesh size along the boundary was investigated in Figure A.10. It shows that even a coarse boundary mesh can result in accurate simulations. The boundary mesh size was 100 nm, unless stated. This mesh is sufficiently fine so that many elements can fit inside the boundaries' cohesive zone. The edge seeds, as defined in section 17.4 of the Abaqus user manual [419], were applied such that the mesh on the slave and master surfaces was matched across the boundary.

The tension-separation law is made up of different regions, referring to the changing relationship between neighbouring nodes (Figure A.7). The initial section of the tension-separation law reflects linear elastic behaviour. This elastic

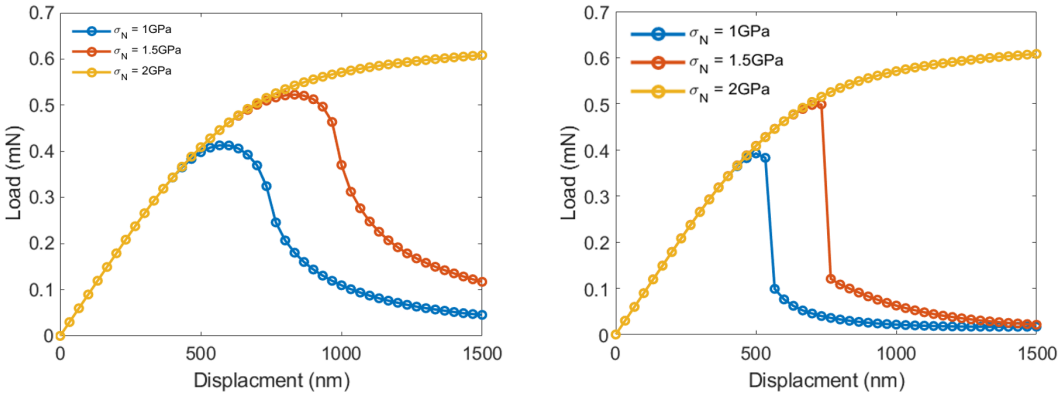


(a) (b)

Figure A.10: (a) The simulated load-displacement curves using models with varying mesh size using C3D8 elements. The hardening fitting parameter was held constant. (b) The Maximum simulated load is displayed against the mesh size. Little change is observed from mesh sizes of 1um to 0.2um.

behaviour has a fitted initial stiffness K, which was chosen to be 10-times greater than the modulus of the surrounding material. In the case of an interface between two different materials, this is 10-times the mean modulus. This principle follows a relationship established by Turon, where the magnitude needs to be sufficiently large enough to prevent artificial compliance or a significant initial opening of the boundary at $T = 0$ [423], but not too larger to cause instabilities [424]. The initial boundary stiffness has minimal effect on the simulated load-displacement due to the volume fraction of the boundary being very small.

The cohesive boundary behaves elastically, until the nodes on either side of the boundary experience a stress greater or equal to the boundary strength σ_{max}. In this instance, the transverse boundary strength (Mode II, III) σ_{tt} is set to 10-times the normal strength (Mode I) σ_{nn} to prevent shear failure. This means that we can consider σ_{max}=σ_{nn}. The displacement that corresponds to σ_{nn} is referred to as δ_0. Once the stress exceeds the boundary strength, damage is initiated and the interface stiffness starts to degrade with increased separation. The user defined boundary strength is an important parameter in simulating the failure observed experimentally. Figure A.11, shows that as the boundary strength increases, the failure load increases. Due to the plastic deformation and hardening of the can-



(a) (b)

Figure A.11: (a) The influence of the maximal nominal stress on the simulated load-displacement response for $\delta_{max} = 100nm$. (b) The influence of the maximal nominal stress on the simulated load-displacement response for $\delta_{max} = 50nm$.

tilever, this means that small changes in the boundary strength can result in large additional deflections before any failure occurs. This will be calibrated using the experimental data collected.

The degradation of the boundary will continue, until the separation between the surfaces reaches δ_{max}. After this point, the mechanical connection is completely broken. This is another fitting parameter that is influential on the simulated response. As summarised in Figure A.12, this term depicts how quickly the system fails once damage is initiated; a sort of quasi-brittleness value. To replicate the observed failure, the value of maximum allowed separation δ_{max} was decided to be either 20 or 50 nm. This comes with several problems. Firstly, the smaller this value the greater the computation cost. This results from a small step size being used to simulate the instantaneous fracture.

The stability limit of the simulation was determined to be 150nm. As the proposed values are well below this limit and it is expected that our choices we will cause instabilities to arise. Publications by Dohr et.al [73] and Dugdale et.al [384] have typically used smaller values, such as 5nm. This value was tested, but proved too unstable for application. This is likely caused by the coupling with crystal plasticity, which was absent in the cited publications. The best way to avoid instabilities is to introduce a viscosity term μ. Initially, this term was introduced

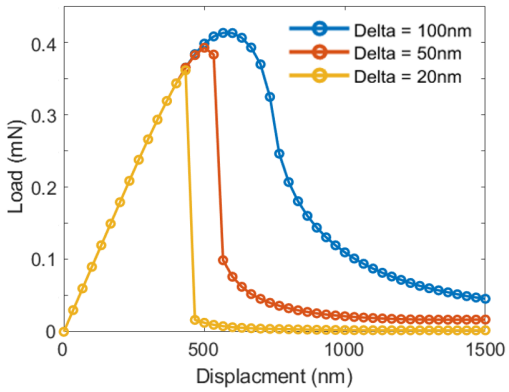


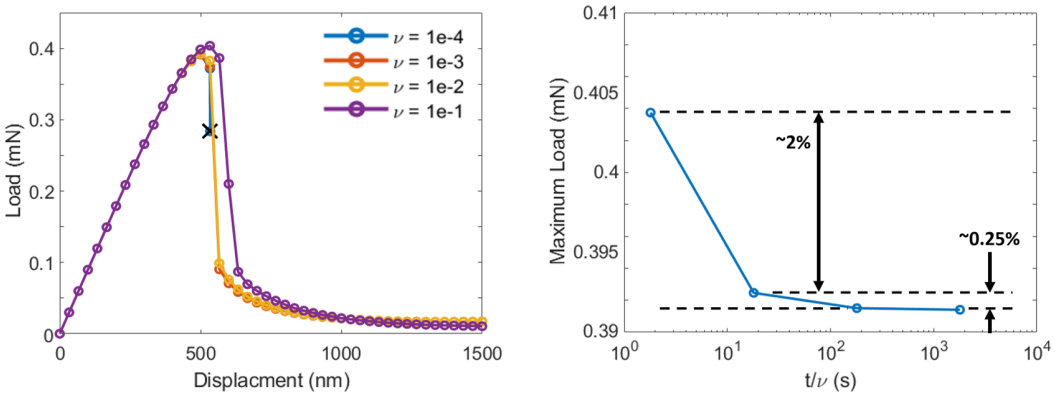
Figure A.12: The effect of the maximum separation on the mechanical behaviour of the cantilever systems. The smaller this value the less ductile the boundary model becomes.

avoid convergence difficulties when the stiffness changed suddenly as damage was initiated. But it was found to be a useful term for avoiding convergence problems when δ_{max} is below this energetic stability limit.

To prevent over-damping of the system, the viscous term had to be sufficiently small. To ensure this is the case, a study was completed on two different values of δ_{max} = 50 and 100 nm. The results from δ_{max}=100 nm are presented in Figure A.13, as no viscosity term was used for δ_{max}=50 nm. The viscosity term, when sufficiently small, should not influence the loading. There is a negligible change in load once the value of $\mu < 0.1$. This is reaffirmed in Figure A.13d, where when $t/\mu \rightarrow \infty$ we observed convergence in the applied load. It is determined that for unstable systems, any value of $\mu \leq 10^{-2}$ will return reliable results as the change in the applied load is a fraction of a percent.

A.3.2.3 Carbides and Cavities

As the grain boundary in the cantilever is decorated with intergranular cavities and carbides, these are included in the simulation. It is known that the intergranular carbides present are either Cr_7C_3 or $Cr_{23}C_6$ [303]. For the purposes of this work, it is assumed that the intergranular carbide inclusions are stiff elastic inclusions with a Young's modulus of E = 302 GPa, and a Poisson's ratio of $\nu = 0.336$ [425]. The carbides were assumed to be ellipsoids, this was chosen to be computationally



(a) (b)

Figure A.13: The viscosity term and its effects on the simulated load-displacement fro two different systems (a)$\delta_{max} = 100nm$ and (c) $\delta_{max} = 50nm$. To figure out if each term was sufficiently small figures (b) and (d) show the maximum load plotted for each of the plots listed above. If the plots show convergence, then the value is small enough.

efficient, simple and provide a good packing fraction to achieve a high boundary coverage. The coverage is defined as the area fraction of the boundary occupied by a precipitate along the 2D boundary plane, and was extrapolated from the linear coverage measured in SEM images. Shen et al [396] has classified three distinct arrangements of carbides and cavities in the sample. As summarised in Figure A.14, these are narrow connected carbides, carbides separated by cavities, and carbides surrounded by cavities.

To implement intergranular carbides into our model, we must alter the matrix-matrix (M-M) interface, and define a new carbide-matrix (C-M) interface. The carbide-matrix interface is defined as a new cohesive surface, using the same parameters as the M-M interface. This was chosen to limit the number of variables. As seen in Figure A.15a, the boundary was strengthened by the carbides. This is because the applied stress is along the C-M surface normal, and the resolved components of stress have to satisfy either $\sigma_{res} > \sigma_{nn}$ or $\sigma_{res} > \sigma_{tt} = 10\sigma_{nn}$ to initiate damage (illustrated in Figure A.15b). The ratio of σ_{tt} to σ_{nn} was varied from (1:1) through to (10:1). The results demonstrate that even at (1:1) ratio, there is an observed strengthening due to the carbides. There is no reliable way of

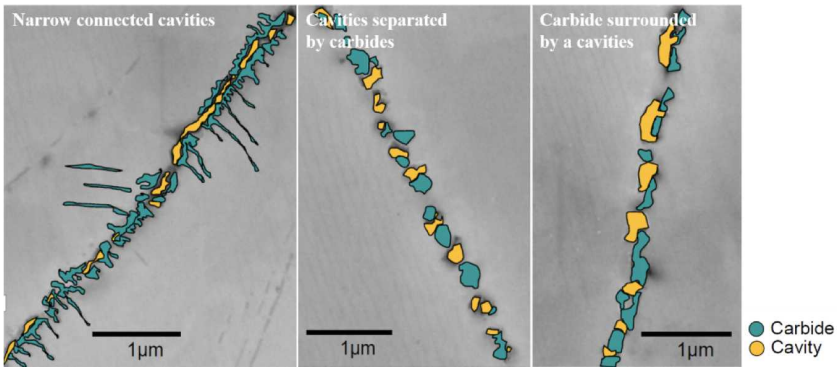
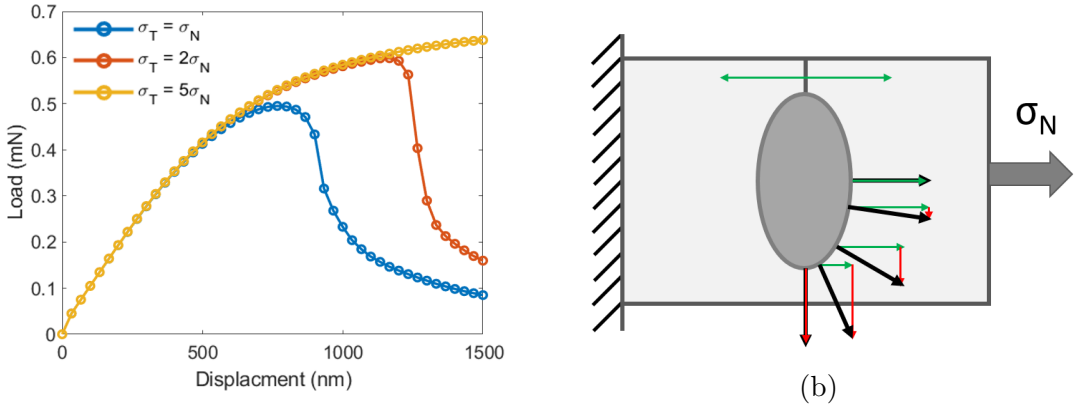


Figure A.14: SE2 images collected of the sample surface of the A690 sample. This demonstrates the three observable types of carbide and cavity combinations. Taken from [396].



(a) (b)

Figure A.15: (a) The effect of the ratio between the transverse and normal maximum boundary strengths has on the simulated mechanical behaviour. The boundary parameters used to collect this data is $\sigma_{nn} = 1$ GPa, $\delta_{max} = 100$ nm and $\nu = 10^{-5}$. (b) Illustration of why the transverse strength is important. If the normal is parallel to the boundary plane then it is the only possible mode of failure. If it is too strong it can cause convergence problems.

calibrating this parameter, so holding it at a fixed value is, at the very least, self-consistent throughout all the simulations detailed. For this reason, I have decided to set $\sigma_{nn} = \sigma_{tt}$ in all future simulations unless otherwise stated.

Cavities were modelled as absent material along the boundary, they are the same as the carbides in every other way.

A.3.2.4 *Case Study:* Carbides

A model system was created with a grain boundary that is populated with only carbide precipitates. The carbides are located equi-distant from its nearest neighbours, this arrangement was chosen to ensure the carbides are discrete, and simplified calculating the coverage in the models. This size range was selected to reflect the range of sizes carbides found on the macro-cantilevers. In this study, the boundary coverage and precipitate size was varied from 20 - 80 pct and 100 - 200 nm respectively in a systematic way. The maximum applied load, or the load required to fracture, was recorded.

The maximum applied load during the simulated deflection test where only carbides are present is shown in Figure A.16. There are two observable trends. As the carbide boundary coverage increases (holding the carbide size constant and moving vertically up the graph), the maximum load increases by up to 50%, and as the radius of the carbides is increased (holding coverage constant and moving horizontally across the graph), the maximum load undergoes up to a 18% increase. There is a clear correlation between the boundary strength and the carbide precipitation. Carbides have a strengthening effect on the boundary and the dominant strengthening effect comes from a higher carbide coverage. This replicates previous observations on A600 and A690 with low cold-work [426, 61]. Through conserving the total amount of Cr in the alloy, it is suggested that a fine semi-continuous distribution is the optimum configuration for strengthening the interface. Simulations (0.25μm,60%), (0.375μm,40%), (0.5μm,20%) have the same carbide volume, but the fine-continuous distribution has a maximum applied load 30% greater than that of the large-discrete carbides. As more carbides populate the boundary this effect diminishes as (0.25μm,80%), (0.375μm,60%), (0.5μm,40%) have similar recorded loads to failure.

There are several physical reasons why the observed trends occurred, it is likely that to it is a combination of the following reasons. First could be because adding a carbide replaces a flat region of the boundary with a curved surface. This essentially doubles the effective boundary area in the region occupied by the carbide. Secondly, as the carbides are defined as rigid stiff objects, they reinforce the boundary. This strengths the boundary by making it harder for the nodes to

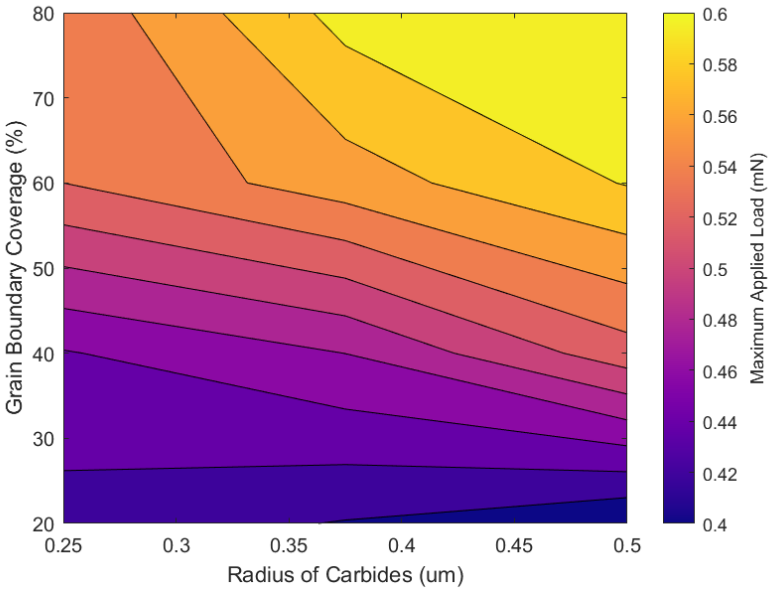


Figure A.16: The maximum applied load for a range of carbide sizes and carbide coverage. Achieved using the following parameters: $\sigma_n = 1$ GPa, $\delta_{max} = 100$ nm, $\nu = 10^{-3}$.

reach the δ^{max} threshold and loose mechanical coupling. Finally, with the addition of carbides, the boundary is no longer a straight plane; the boundary normal is diverted and constantly changing. To overcome this, a greater applied load is required to continue the crack propagation. It is thought that the observed size-effect is caused by a combination of these final two factors.

There are factors that are not tested here, namely the shape or crystallographic orientation of the carbides. The carbide shape was fixed due to complications of implementing faceted carbides in the finite element model. Similarly, implementing the crystallographic orientation of the carbides would be challenging, but possible in simplified cases. These recommendations are made based on the experimental work completed by Francisco et al. [427] who identified that boundaries with different carbide distributions, and shapes, resulted in differing cavity formations and cracking behaviours.

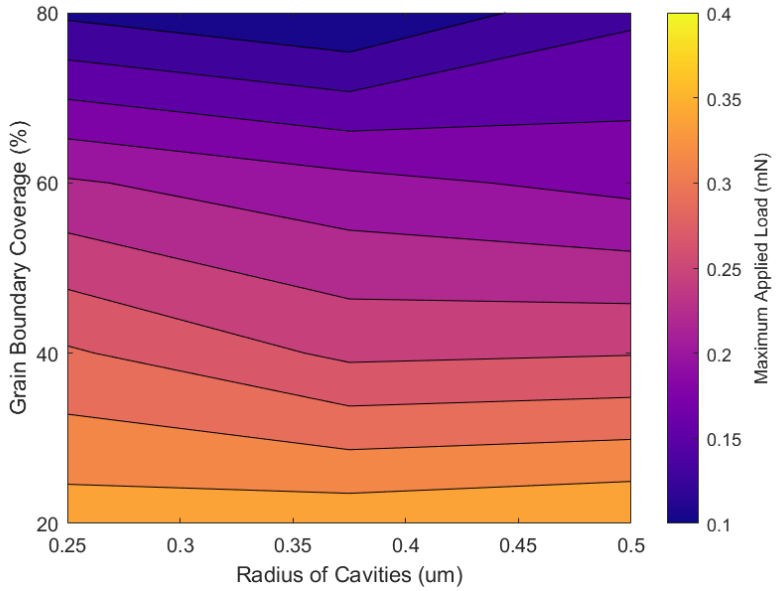


Figure A.17: The maximum applied load for a range of cavity sizes and cavity coverage. Achieved using the following parameters: $\sigma_n = 1$ GPa, $\delta_{max} = 100$ nm, $\nu = 10^{-3}$.

A.3.2.5 *Case Study:* Cavities

To model the affect of intergranular cavity coverage, the model system previously describe had all the carbides removed to replicate the absence of material in the FEA model. Nothing else was changed.

The maximum applied load when the simulated boundary is occupied by cavities is shown in Figure A.17. There is one observable trend - as the boundary coverage increases the maximum load decreases. The maximum load drops by approximately 70%. There is no noticeable effect of the size of the cavities on the boundary strength. We are able to determine that the only role of observed cavitation is to lower the load to failure of the boundary.

It is suggested that, contrary to carbides, which offer an increase in the boundary area, the role of the cavity is to only decrease the effective area of the boundary. This means that the stress per unit applied force is greater. This also explains why no size effect is observed. As the coverage is fixed, the area of the boundary occupied does not change and, therefore, neither does the maximum load required

to fracture the boundary. Here the cavities are the same shape as the carbides, but it was noted that several shapes of cavities exist. For the reasons stated above, it is thought that the shape of the cavity is irrelevant and formulations should yield the same results.

After exploring the components of crystal plasticity, cohesive surfaces, carbides and cavities that will make up these cantilver models. I am now in a position of understanding to re-produce the experimental observations, and extract useful physical properties for industry. Over the next two sections, I will document the simulation process of two cantilever beams, one with only intergranular carbide coverage and one with both intergranular carbide and cavity coverage. At the end, I will summarise and give my thoughts on the role of carbides and cavities on the bonding strength of boundaries in A690.

A.3.3 Results

It has been demonstrated that carbides strengthen the boundary, while cavities weaken it. Our motif now it to implement both intergranular carbides and cavities along a single boundary. If cavities are detrimental to the boundary strength, the observed experimental fracture should be linked to the introduction of an intergranular cavity coverage in the simulations.

Introducing both of these precipitates into a combined model, reveals that the effects of both the carbides and cavities becomes more subtle than that observed in sections A.3.2.4 and A.3.2.5. The outcome of simulations are sensitive on the positioning of the carbides and cavities, i.e. the effects of the carbides and cavities are weighted based on their proximity to the top of the cantilever, where the greatest tensile stress is applied. While a full study of this effect was not completed, emphasis should be placed on the importance of accurately positioning the carbides and cavities to ensure the reliability during the simulations. The carbides and cavities were place in accordance to the micro-graphs where possible.

A.3.3.1 *A690* with intergranular carbide coverage and no cavities

The CPFEM is calibrated against the boundary with only intergranular carbide coverage that did not fracture. This model simplifies the fitting process. The

stronger boundary has an increased plastic response, which makes it more suited to determining hardening constants C and D. This fitting procedure would not be as reliable on the fractured beam. The crystal plasticity parameters are material specific, and can be used to simulate the fractured boundary.

It was determined from the micro-graphs that the beam has the dimensions (H,W,L) of 2.75μm, 2.96μm and 11.95μm. The boundary was 2.16μm from the base. The intergranular carbides coverage was assessed using an in-lens detector to show channelling contrast. The intergranular carbide coverage was 68% and there was a mean radius of 0.34μm. The major and minor radii of the intergranular carbides were 0.35μm and 0.15μm respectively. The cantilever simulations presented provide a direct comparison to experimental observations.

We have demonstrated that it is possible to accurately replicate the fracture direction, or tilt, of the beam, as shown in Figure A.18, by using appropriate CPFEM parameters. The resulting tilt rises from an asymmetric stress states introduced by the CP along the boundary prior to failure. This can be attributed to the CP as when isotropic values are used, this tilted fracture is replaced by a pure normal fracture along the y-axis (as displayed). The crystal plasticity parameter used are $\tau_{CRSS} = 675MPa$, $C = 0.25$ and $D = 5 \times 10^3$.

The results of the simulated cantilever beam are displayed in (Fig A.19 - Yellow), where they are compared to the experimental results. This beam displays only plastic deformation during the simulation. We identified that a boundary strength of 3.1 GPa was sufficiently high to prevent fracture during the simulated experiment.

A.3.3.2 *A690* with intergranular carbide and cavity coverage

The second beam simulated contains the failed boundary and has intergranular carbides and cavities present. We again use the experimental coverage of 42 and 32 % respectively, with an average major radius of 100 nm. The model was simulated and the results compared to the experiment (Fig A.19 - orange). We calculate that the effective boundary strength is 1.7GPa, this accounts for the weakening due to the cavities. To demonstrate that cavities are greatly influencing this result, when removed from the simulation, and no other features or parameters are changed, no fracture is observed (Fig A.19 - blue).

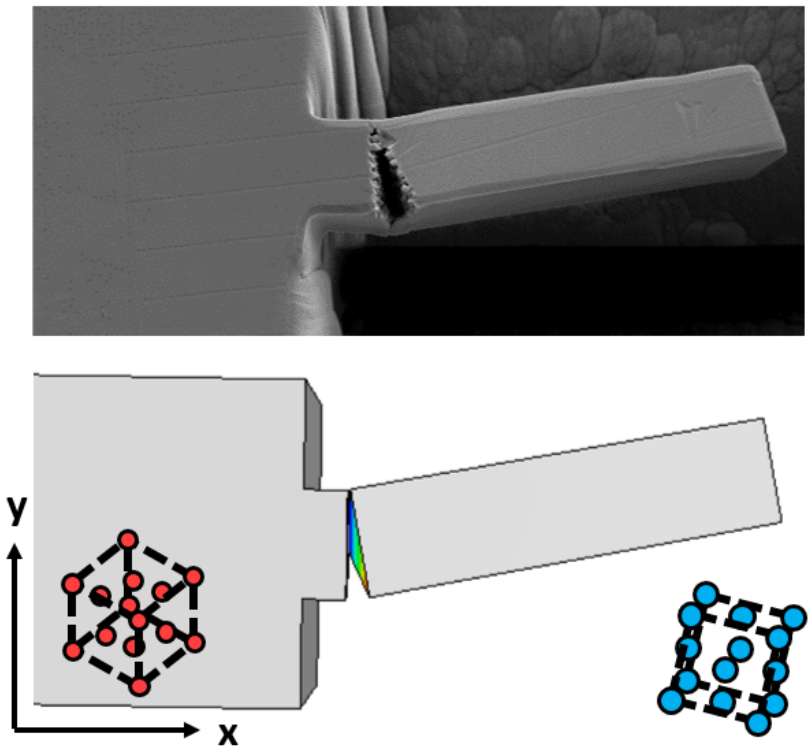


Figure A.18: A comparison of the boundary behaviour once failed. The crystal plasticity is able to re-create the shear direction due to as-symmetrical stress states introduced by the anisotropic modulii. The lattice orientation is shown for both the beam and base grains.

When cavities are present the model predicts failure similar to that experimentally observed. The greatest stresses along the beam are shown in Figure A.20. We determine that the stress in the fractured sample reached a high tensile value in regions surrounding the cavities, while the stress in the remaining beam is lower than that in the deformed beam. The highest stress is localised around the cavities suggests that the cavities localise stress and allow much higher values to be applied to the material.

A.3.4 Discussion

Others have used a similar CP formulation. Kareer et al used the formulation to conduct scratch tests on copper, and the hardening factor C and D are of a similar order of magnitude [418].

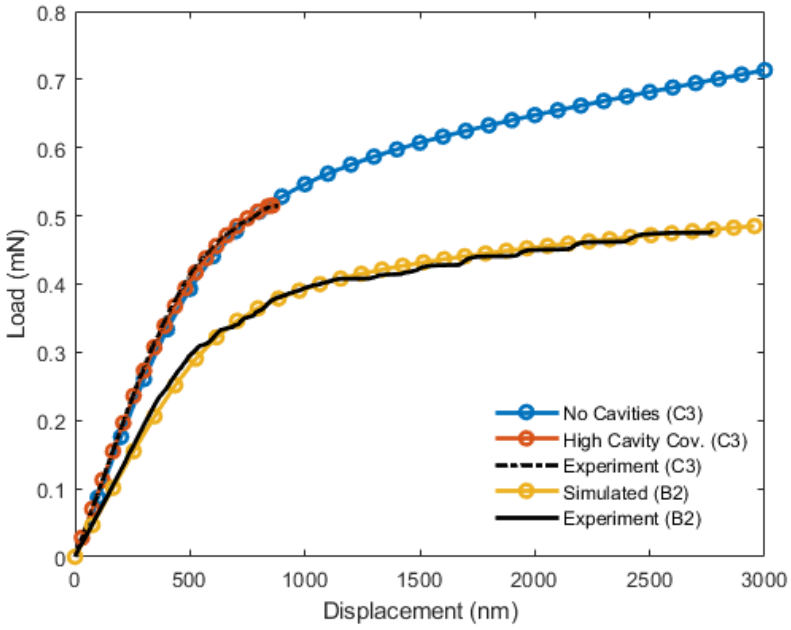


Figure A.19: The L-D for representative beams with simulated experiments overlaid.

The $\sigma_{nn} = 3.1$ GPa boundary strength is lower than the $\sigma_{nn} = 5$ GPa found by Dohr et al [73] in A600. Discrepancies in the chosen values can be partially attributed to the defined criterion for failure; there is no mitigation of shear so the boundary will need to be artificially stronger to prevent premature failure. A better comparison between models is achieved by examining the critical free energy of the boundary. For A690, this is calculated to be $G = 31$ Jm^{-2}, some 60% higher than a boundary in A600. This demonstrates that A690 boundaries are harder to fracture than A600 boundaries, as the crack is able to absorb a greater amount of energy before fracture. The results suggest that due to the strength and ductility of A690, the boundaries will need weakening to fracture. In the autoclaved A690 tested and modelled in this work, the predominant method of weakening is boundary cavitation. Cavitation reduces the free energy of the boundary to $G = 17$ Jm^{-2}, meaning that the beams require 45% less energy to fail, which is a significant reduction. Oxidation is another known type of boundary weakening. Using figures presented by Dohr et al [73], the potential link between

oxidation and cavitation has been explored in greater detail. While this concept is outside the remit of this chapter, we leave the interested reader to follow up with the following chapter by Shen et al [396].

A.4 Summary

A synergistic combination of micro-cantilevers and computational simulation have been used to explore the effects of intergranular carbide and cavity coverage on the bonding strength of grain boundaries in alloy 690.

Boundary fracture has been experimentally verified, and modelling has related this to the presence of intergranular cavity coverage. This confirms Arioka's hypothesis that cavities weaken the grain boundaries in cold-worked A690. A result that could not be achieved using traditional SCC corrosion testing.

It has been demonstrated that cavities are able to reduce the energy to fracture by up to 45%, and that the boundaries of A690 are stronger than A600. Using FEA, we have further isolated the effect of cavities. Demonstrating that cavities both increase and concentrate the applied stress along the boundary to cause premature failure. It was found that carbides have a strengthening effect on the boundary, with the optimum configuration of carbides been a fine semi-continuous distribution. This is inline with observations of A600. When a combination of cavities and carbides are present along a boundary, then a sufficiently high cavity coverage is needed to induce fracture.

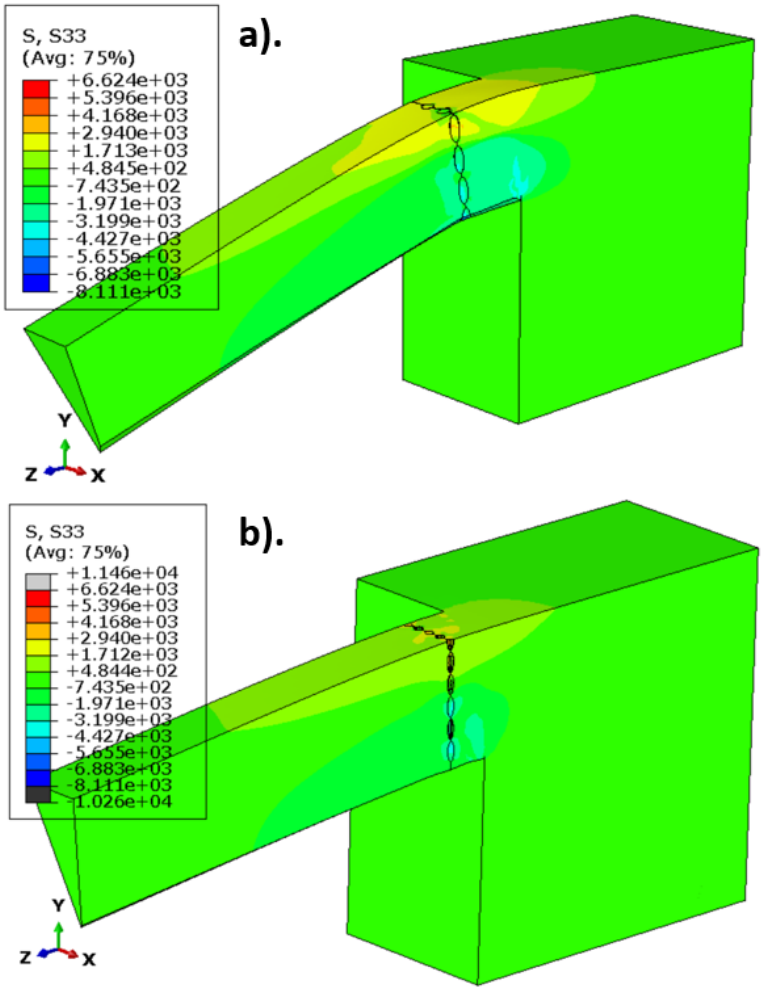


Figure A.20: A comparison of the highest stresses along the (a) beam that has only carbides and (b) the fractured beam with carbides and cavities.

References

[1] William H Johnson. On some remarkable changes produced in iron and steel by the action of hydrogen and acids. *Proceedings of the Royal Society of London*, 23(156-163):168–179, 1874.

[2] UNCCC. The Paris Agreement, 2021.

[3] World-Nuclear. Where does our electricity come from, 2021.

[4] H. Barth\'{e}l\'{e}my. Hydrogen storage - Industrial prospectives. *International Journal of Hydrogen Energy*, 37:17364–17372, 2012.

[5] M. A Stopher and P Rivera-diaz-del castillo. Hydrogen embrittlement in bearing steels Hydrogen embrittlement in bearing steels. *Materials Science and Technology ISSN:*, 32(11):1184–1193, 2016.

[6] J. Chêne. *Stress corrosion cracking and hydrogen embrittlement*. European Federation of Corrosion, 2016.

[7] Marta Gospodarczyk and Marianne Nari Fisher. IAEA Releases 2019 Data on Nuclear Power Plants Operating Experience, 2020.

[8] R W Staehle. *1 - Historical views on stress corrosion cracking of nickel-based alloys: the Coriou effect*. European Federation of Corrosion, 2016.

[9] H. Coriou, L. Grall, Y. Le Gall, and S. Vettier. Corrosion Fissurante Sous Contrainte De L'Inconel Dans L'Eau A Haute Temperature. *North Holland*, page 161, 1959.

[10] H. R. Copson and S. W. Dean. Effect of Contaminants on Resistance To Stress Corrosion Cracking Of Ni-Cr Alloy 600 in Pressurized Water. *Corrosion*, 21(1):1–8, 1965.

[11] K. Arioka, T. Yamada, T. Terachi, and R. W. Staehle. Intergranular stress corrosion cracking behavior of austenitic stainless steels in hydrogenated high-temperature water. *Corrosion*, 62(1):74–83, 2006.

[12] Koji Arioka, Takuyo Yamada, Tomoki Miyamoto, and Masanori Aoki. Intergranular stress corrosion cracking growth behavior of Ni-Cr-Fe alloys in pressurized water reactor primary water. *Corrosion*, 70(7):695–707, 2014.

[13] Koji Arioka, Tomoki Miyamoto, Takuyo Yamada, and Masanori Aoki. Role of cavity formation in crack initiation of cold-worked carbon steel in high-temperature water. *Corrosion*, 69(5):487–496, 2013.

[14] Koji Arioka, Roger W. Staehle, T. Yamada, T. Miyamoto, and T. Terachi. Degradation of alloy 690 after relatively short times. *Corrosion*, 72(10):1252–1268, 2016.

[15] Sergio Lozano-Perez, Judith Dohr, Martina Meisnar, and Karen Kruska. SCC in PWRs: Learning from a Bottom-Up Approach. *Metallurgical and Materials Transactions E*, 1(2):194–210, 2014.

[16] Zhao Shen. *Understanding the mechanisms controlling stress corrosion cracking through high-resolution characterization.* PhD thesis, University of Oxford, 2018.

[17] Zhao Shen, Koji Arioka, and Sergio Lozano-Perez. A mechanistic study of SCC in Alloy 600 through high-resolution characterization. *Corrosion Science*, 132(September 2017):244–259, 2018.

[18] Zhao Shen, Martina Meisnar, Koji Arioka, and Sergio Lozano-Perez. Mechanistic understanding of the temperature dependence of crack growth rate in alloy 600 and 316 stainless steel through high-resolution characterization. *Acta Materialia*, 165(November):73–86, 2019.

[19] Zhao Shen, Judith Dohr, and Sergio Lozano-Perez. The effects of intergranular carbides on the grain boundary oxidation and cracking in a cold-worked Alloy 600. *Corrosion Science*, 155(January):209–216, 2019.

[20] Zhao Shen, Phani Karamched, Koji Arioka, and Sergio Lozano-perez. Observation and quantification of the diffusion-induced grain boundary migration ahead of SCC crack tips. *Corrosion Science*, 147:163–168, 2019.

[21] TJ Smith and RW Staehle. Role of slip step emergence in the early stages of stress corrosion cracking in face centered iron-nickel-chromium alloys. *Corrosion*, 23(5):117–129, 1967.

[22] Ziqing Zhai, Mychailo Toloczko, Karen Kruska, Daniel Schreiber, and Stephen Bruemmer. Grain boundary damage evolution and scc initiation of cold-worked alloy 690 in simulated PWR primary water. *Minerals, Metals and Materials Series*, (January):457–483, 2019.

[23] LL Shreir. *Corrosion control*. Butterworth-Heinemann, 1994.

[24] Fabien Leonard and Robert A Cottis. *Study of stress corrosion cracking of alloy 600 in high temperature high pressure water*. University of Manchester, 2010.

[25] JM Boursier, D Desjardins, and F Vaillant. The influence of the strain-rate on the stress corrosion cracking of alloy 600 in high temperature primary water. *Corrosion science*, 37(3):493–508, 1995.

[26] T Yonezawa and K Onimura. Effect of chemical compositions and microstructure on the stress corrosion cracking resistance of nickel base alloys in high temperature water. In *International Conference on Evaluation of Materials Performance in Severe Environments.*, volume 1, pages 235–242, 1989.

[27] F Delabrouille, L Legras, F Vaillant, P Scott, B Viguier, and E Andrieu. Effect of the Chromium Content and Strain on the Corrosion of Nickel Based Alloys in Primary Water of Pressurized Water Reactors. *12th International*

Conference on Environmental Degradation of Materials in Nuclear Power System, (February):903–911, 2005.

[28] GS Was, JK Sung, and TM Angeliu. Effects of grain boundary chemistry on the intergranular cracking behavior of ni-16cr-9fe in high-temperature water. *Metallurgical Transactions A*, 23(12):3343–3359, 1992.

[29] R B Rebak and F H Hua. The role of hydrogen and creep in intergranular stress corrosion cracking of alloy 600 and alloy 690 in pwr primary water environments. Technical report, Lawrence Livermore National Laboratory (LLNL), Livermore, CA, 2004.

[30] GS WAS. Micromechanical and microstructural effects on scc of nickel base alloys. In *PARKINS symposium on fundamental aspects of stress corrosion cracking*, 1991.

[31] François Vaillant, Jean-Denis Mithieux, Odile de Bouvier, Dominique Vançon, Guy Zacharie, Yves Brechet, and François Louchet. Influence of chromium content and microstructure on creep and pwscc resistance of nickel base alloys. In *Ninth International Symposium on Environmental Degradation of Materials in Nuclear Power Systems-Water Reactors*, pages 251–260. Wiley Online Library, 1999.

[32] S Lozano-Perez, T Yamada, T Terachi, M Schröder, CA English, GDW Smith, CRM Grovenor, and BL Eyre. Multi-scale characterization of stress corrosion cracking of cold-worked stainless steels and the influence of cr content. *Acta Materialia*, 57(18):5361–5381, 2009.

[33] Koji Arioka, Roger W Staehle, T Yamada, T Miyamoto, and T Terachi. Degradation of alloy 690 after relatively short times. *Corrosion*, 72(10):1252–1268, 2016.

[34] Karen Kruska, Ziqing Zhai, Daniel K Schreiber, and Stephen M Bruemmer. Characterization of stress corrosion cracking initiation precursors in cold-worked alloy 690 using advanced high-resolution microscopy. *Corrosion*, 75(7), 2019.

[35] S. Lozano-Perez, T. Yamada, T. Terachi, M. Schröder, C. A. English, G. D.W. Smith, C. R.M. Grovenor, and B. L. Eyre. Multi-scale characterization of stress corrosion cracking of cold-worked stainless steels and the influence of Cr content. *Acta Materialia*, 57(18):5361–5381, 2009.

[36] Judith Dohr. *Micromechanical Testing of Oxidized Grain Boundaries*. Doctor of philosophy, University of Oxford, 2016.

[37] Sergio Lozano-Perez, Judith Dohr, Martina Meisnar, and Karen Kruska. Scc in pwrs: learning from a bottom-up approach. *Metallurgical and Materials Transactions E*, 1(2):194–210, 2014.

[38] W. C. Moshier. Effect of cold work and processing orientation on stress corrosion cracking behavior of alloy 600. *Corrosion*, 56(3):307–320, 2000.

[39] SM Bruemmer, LA Charlot, and CH Henager Jr. Microstructure and microdeformation effects on igscc of alloy 600 steam generator tubing. *Corrosion*, 44(11):782–788, 1988.

[40] Elaine West, David Morton, Tyler Moss, John Dosch, Robert Morris, Caleb Hustedt, Paul Sander, and Bryan Miller. Fundemental Insights into Crack Retardation Behaviour through Advanced Characterisation. In *2021 Virtual MRS Spring Meeting*, Virtual, 2021.

[41] T. Terachi, T. Yamada, T. Miyamoto, and K. Arioka. SCC growth behaviors of austenitic stainless steels in simulated PWR primary water. *Journal of Nuclear Materials*, 426(1-3):59–70, 2012.

[42] JC Langevoort, I Sutherland, LJ Hanekamp, and PJ Gellings. On the oxide formation on stainless steels aisi 304 and incoloy 800h investigated with xps. *Applied surface science*, 28(2):167–179, 1987.

[43] JC Langevoort, T Fransen, and PJ Geilings. On the influence of cold work on the oxidation behavior of some austenitic stainless steels: High temperature oxidation. *Oxidation of metals*, 21(5):271–284, 1984.

[44] Tadao Watanabe. An approach to grain-boundary design for strong and ductile polycrystals. *Res Mechanica*, 11(1):47–84, 1984.

[45] ML Kronberg and u FH Wilson. Secondary recrystallization in copper. *JOM*, 1(8):501–514, 1949.

[46] VS Raja and Tetsuo Shoji. *Stress corrosion cracking: theory and practice*. Elsevier, 2011.

[47] D. N. Wasnik, V. Kain, I. Samajdar, B. Verlinden, and P. K. De. Resistance to sensitization and intergranular corrosion through extreme randomization of grain boundaries. *Acta Materialia*, 50(18):4587–4601, 2002.

[48] Bogdan Alexandreanu, Brent Capell, and Gary S Was. Combined effect of special grain boundaries and grain boundary carbides on igscc of ni–16cr–9fe–xc alloys. *Materials Science and Engineering: A*, 300(1):94–104, 2001.

[49] Stephen M Bruemmer and Gary S Was. Microstructural and microchemical mechanisms controlling intergranular stress corrosion cracking in light-water-reactor systems. *Journal of Nuclear Materials*, 216:348–363, 1994.

[50] Hiroyuki Kokawa, Masayuki Shimada, and Yutaka S Sato. Grain-boundary structure and precipitation in sensitized austenitic stainless steel. *JOM Journal of the Minerals, Metals and Materials Society*, 52(7):34–37, 2000.

[51] EA Trillo and LE Murr. Effects of carbon content, deformation, and interfacial energetics on carbide precipitation and corrosion sensitization in 304 stainless steel. *Acta materialia*, 47(1):235–245, 1998.

[52] A Kavner and TM Devine. Effect of grain boundary orientation on the sensitization of austenitic stainless steel. *Journal of materials science*, 32(6):1555–1562, 1997.

[53] K Arioka, T Yamada, T Terachi, and G Chiba. Influence of carbide precipitation and rolling direction on intergranular stress corrosion cracking of austenitic stainless steels in hydrogenated high-temperature water. *Corrosion*, 62(7):568–575, 2006.

[54] Phuong H Hoang, Anand Gangadharan, and Suresh C Ramalingam. Primary water stress corrosion cracking inspection ranking scheme for alloy 600 components. *Nuclear engineering and design*, 181(1-3):209–219, 1998.

[55] K Arioka, T Yamada, T Terachi, and RW Staehle. Intergranular stress corrosion cracking behavior of austenitic stainless steels in hydrogenated high-temperature water. *Corrosion*, 62(1):74–83, 2006.

[56] GS Was and K Lian. Role of carbides in stress corrosion cracking resistance of alloy 600 and controlled-purity ni-16% cr-9% fe in primary water at 360 c. *Corrosion*, 54(9):675–688, 1998.

[57] Helen Dugdale, David EJ Armstrong, Edmund Tarleton, Steve G Roberts, and Sergio Lozano-Perez. How oxidized grain boundaries fail. *acta materialia*, 61(13):4707–4713, 2013.

[58] Zhao Shen, Junliang Liu, Koji Arioka, and Sergio Lozano-Perez. On the role of intergranular carbides on improving the stress corrosion cracking resistance in a cold-worked alloy 600. *Journal of Nuclear Materials*, 514:50–55, 2019.

[59] JJ Kai, CH Tsai, and GP Yu. The igscc, sensitization, and microstructure study of alloys 600 and 690. *Nuclear engineering and design*, 144(3):449–457, 1993.

[60] T. B Casagne, P. Combrade, M. A Foucault, and A Gelpi. The influence of mechanical and environmental parameters on the crack growth behaviour of alloy 600 in PWR primary water. In *12th Scandinavian corrosion congress & Eurocorr'92*, pages 55–67, Espoo, Finland, 1992.

[61] K. Arioka, T. Yamada, T. Terachi, and G. Chiba. Influence of carbide precipitation and rolling direction on intergranular stress corrosion cracking of austenitic stainless steels in hydrogenated high-temperature water. *Corrosion*, 62(7):568–575, 2006.

[62] K. Arioka, T. Yamada, T. Miyamoto, and T. Terachi. Dependence of stress corrosion cracking of Alloy 690 on temperature, cold work, and carbide precipitation - Role of diffusion of vacancies at crack tips. *Corrosion*, 67(3):1–18, 2011.

[63] Peter L Andresen, Paul W Emigh, Martin M Morra, et al. Effects of pwr primary water chemistry and deaerated water on scc. In *CORROSION 2005*. NACE International, 2005.

[64] J Lepinoux and T. Magnin. Stress corrosion microcleavage in a ductile f.c.c. alloy. *Materials Science and Engineering, A*, 164:266–269, 1993.

[65] K Sieradzki and R C Newman. Brittle behavior of ductile metals during stress- corrosion cracking. 8610, 2006.

[66] J. R. Galvele. A stress corrosion cracking mechanism based on surface mobility. *Corrosion Science*, 27(1):1–33, 1987.

[67] R Mears, R Brown, and E Dix. A generalized theory of stress corrosion of alloys. In *Symposium on Stress-Corrosion Cracking of Metals*. ASTM International, 1945.

[68] Hugh L Logan. Film-rupture mechanism of stress corrosion. *Journal of Research of the National Bureau of Standards*, 48(2):99–105, 1952.

[69] RN Parkins. Predictive approaches to stress corrosion cracking failure. *Corrosion Science*, 20(2):147–166, 1980.

[70] Peter L Andresen and F Peter Ford. Life prediction by mechanistic modeling and system monitoring of environmental cracking of iron and nickel alloys in aqueous systems. *Materials Science and Engineering: A*, 103(1):167–184, 1988.

[71] Roger C Newman and Christopher Healey. Stability, validity, and sensitivity to input parameters of the slip-dissolution model for stress-corrosion cracking. *Corrosion Science*, 49(10):4040–4050, 2007.

[72] David A Vermilyea, J Electrochem Soc, and David A Vermilyea. A Theory for the Propagation of Stress Corrosion Cracks in Metals. *J. Electrochem. Soc*, 119:405–407, 1972.

[73] Judith Dohr, David E.J. Armstrong, Edmund Tarleton, Thierry Couvant, and Sergio Lozano-Perez. The influence of surface oxides on the mechanical response of oxidized grain boundaries. *Thin Solid Films*, 632:17–22, 2017.

[74] Denny A Jones. A unified mechanism of stress corrosion and corrosion fatigue cracking. *Metallurgical transactions A*, 16(6):1133–1141, 1985.

[75] PM Scott and M Le Calver. Some possible mechanisms of intergranular stress corrosion cracking of alloy 600 in pwr primary water. In *Proceedings of the sixth international symposium on environmental degradation of materials in nuclear power systems-water reactors*, 1993.

[76] Brent M Capell and Gary S Was. Selective internal oxidation as a mechanism for intergranular stress corrosion cracking of ni-cr-fe alloys. *Metallurgical and Materials Transactions A*, 38(6):1244–1259, 2007.

[77] Sergio Lozano-Perez, Martina Meisnar, Judith Dohr, and Karen Kruska. Reviewing the internal oxidation mechanism as a plausible explanation for scc in pwr primary water. In *Proc. 16th Int. Conf. on Environmental Degradation of Materials in Nuclear Power Systems–Water Reactors, eds. GO Ilevbare, PL Andresen, MD Wright, held August*, pages 11–15, 2013.

[78] Alisa Stratulat, David EJ Armstrong, and Steve G Roberts. Micromechanical measurement of fracture behaviour of individual grain boundaries in ni alloy 600 exposed to a pressurized water reactor environment. *Corrosion Science*, 104:9–16, 2016.

[79] Karen Kruska, Sergio Lozano-Perez, David W. Saxey, Takumi Terachi, Takuyo Yamada, and George D.W. Smith. Nanoscale characterisation of grain boundary oxidation in cold-worked stainless steels. *Corrosion Science*, 63:225–233, 2012.

[80] R. B. Rebak and Z. Szklarska-Smialowska. The mechanism of stress corrosion cracking of alloy 600 in high temperature water. *Corrosion Science*, 38(6):971–988, 1996.

[81] Julia R. Greer and Jeff Th M. De Hosson. Plasticity in small-sized metallic systems: Intrinsic versus extrinsic size effect. *Progress in Materials Science*, 56(6):654–724, 2011.

[82] Sergio Lozano-Perez, Karen Kruska, Ilya Iyengar, Takumi Terachi, and Takuyo Yamada. The role of cold work and applied stress on surface oxidation of 304 stainless steel. *Corrosion Science*, 56:78–85, 2012.

[83] Liberato Volpe, M Grace Burke, and Fabio Scenini. Understanding the role of diffusion induced grain boundary migration on the preferential intergranular oxidation behaviour of alloy 600 via advanced microstructural characterization. *Acta Materialia*, 175:238–249, 2019.

[84] Leif Viskari, Magnus Hörnqvist, KL Moore, Yu Cao, and Krystyna Stiller. Intergranular crack tip oxidation in a ni-base superalloy. *Acta Materialia*, 61(10):3630–3639, 2013.

[85] M. G. Burke, G. Bertali, E. Prestat, F. Scenini, and S. J. Haigh. The application of in situ analytical transmission electron microscopy to the study of preferential intergranular oxidation in Alloy 600. *Ultramicroscopy*, 176(September 2016):46–51, 2017.

[86] O Barrera, D Bombac, Y Chen, TD Daff, E Galindo-Nava, P Gong, D Haley, R Horton, I Katzarov, JR Kermode, et al. Understanding and mitigating hydrogen embrittlement of steels: a review of experimental, modelling and design progress from atomistic to continuum. *Journal of Materials Science*, pages 1–40, 2018.

[87] LL Shreir. Übersicht der elektkrochemischen methoden zur untersuchung von wasserstoffversprödung und spannungrsrißkorrosion. *Materials and Corrosion*, 21(8):613–629, 1970.

[88] SP Lynch. Environmentally assisted cracking: overview of evidence for an adsorption-induced localised-slip process. *Acta Metallurgica*, 36(10):2639–2661, 1988.

[89] HW Liu. A unified model of environment-assisted cracking. *Acta Materialia*, 56(16):4339–4348, 2008.

[90] S. P. Lynch. Hydrogen embrittlement (HE) phenomena and mechanisms. In *Stress Corrosion Cracking*, number 1st, pages 90–130. Woodhead Publishing Series in Metals and Surface Engineering, 2011.

[91] Alexander R Troiano. The role of hydrogen and other interstitials in the mechanical behavior of metals. *trans. ASM*, 52:54–80, 1960.

[92] RA Oriani. Whitney award lecture—1987: hydrogen—the versatile embrittler. *Corrosion*, 43(7):390–397, 1987.

[93] R. M. Latanision and Russell H. Jones. *Chemistry and physics of fracture*. M. Nijhoff, 1987.

[94] H Vehoff and W Rothe. Gaseous hydrogen embrittlement in fesi-and ni-single crystals. *Acta Metallurgica*, 31(11):1781–1793, 1983.

[95] CD Beachem. A new model for hydrogen-assisted cracking (hydrogen "embrittlement"). *Metallurgical and Materials Transactions B*, 3(2):441–455, 1972.

[96] IM Robertson and HK Birnbaum. An hvem study of hydrogen effects on the deformation and fracture of nickel. *Acta Metallurgica*, 34(3):353–366, 1986.

[97] Howard K Birnbaum and Petros Sofronis. Hydrogen-enhanced localized plasticity—a mechanism for hydrogen-related fracture. *Materials Science and Engineering: A*, 176(1-2):191–202, 1994.

[98] P Rozenak, IM Robertson, and HK Birnbaum. Hvem studies of the effects of hydrogen on the deformation and fracture of aisi type 316 austenitic stainless steel. *Acta metallurgica et materialia*, 38(11):2031–2040, 1990.

[99] DS Shih, IM Robertson, and HK Birnbaum. Hydrogen embrittlement of α titanium: in situ tem studies. *Acta Metallurgica*, 36(1):111–124, 1988.

[100] PJ Ferreira, IM Robertson, and HK Birnbaum. Hydrogen effects on the interaction between dislocations. *Acta materialia*, 46(5):1749–1757, 1998.

[101] Yu Jagodzinski, H Hänninen, O Tarasenko, and S Smuk. Interaction of hydrogen with dislocation pile-ups and hydrogen induced softening of pure iron. *Scripta materialia*, 43(3):245–251, 2000.

[102] Yiliang You, Quanquan Teng, Zheng Zhang, and Qunpeng Zhong. The effect of hydrogen on the deformation mechanisms of 2.25 cr–1mo low alloy steel revealed by acoustic emission. *Materials Science and Engineering: A*, 655:277–282, 2016.

[103] Jeongho Han, Jae-Hoon Nam, and Young-Kook Lee. The mechanism of hydrogen embrittlement in intercritically annealed medium mn trip steel. *Acta Materialia*, 113:1–10, 2016.

[104] Hannu Hänninen and Tero Hakkarainen. Fractographic characteristics of a hydrogen-charged aisi 316 type austenitic stainless steel. *Metallurgical Transactions A*, 10(8):1196–1199, 1979.

[105] Aurélie Laureys, Tom Depover, Roumen Petrov, and Kim Verbeken. Microstructural characterization of hydrogen induced cracking in trip-assisted steel by ebsd. *Materials Characterization*, 112:169–179, 2016.

[106] Motomichi Koyama, Cemal Cem Tasan, Eiji Akiyama, Kaneaki Tsuzaki, and Dierk Raabe. Hydrogen-assisted decohesion and localized plasticity in dual-phase steel. *Acta Materialia*, 70:174–187, 2014.

[107] SP Lynch. Mechanisms and kinetics of environmentally assisted cracking: current status, issues, and suggestions for further work. *Metallurgical and Materials Transactions A*, 44(3):1209–1229, 2013.

[108] John P Hirth. Effects of hydrogen on the properties of iron and steel. *Metallurgical Transactions A*, 11(6):861–890, 1980.

[109] C. D. Hardie, J. Xu, E. A. Charles, and Y. Wei. Hydrogen embrittlement of stainless steel overlay materials for hydrogenators. *Corrosion Science*, 46(12):3089–3100, 2004.

[110] E. Herms, J. M. Olive, and M. Puiggali. Hydrogen embrittlement of 316L type stainless steel. *Materials Science and Engineering A*, 272(2):279–283, 1999.

[111] Afrooz Barnoush. *Hydrogen embrittlement, revisited by in situ electrochemical nanoindentation*. PhD thesis, Saarland University, 2007.

[112] J Chêne, A-M Brass, P Trabuc, and O Gastaldi. Role of microstructure and heat treatments on the desorption kinetics of tritium from austenitic stainless steels. *Journal of nuclear materials*, 360(2):177–185, 2007.

[113] F. Jambon, L. Marchetti, F. Jomard, and J. Chêne. Mechanism of hydrogen absorption during the exposure of alloy 600-like single-crystals to PWR primary simulated media. *Journal of Nuclear Materials*, 414(3):386–392, 2011.

[114] Fanny Jambon, Loïc Marchetti, François Jomard, and Jacques Chêne. Characterisation of oxygen and hydrogen migration through oxide scales formed on nickel-base alloys in PWR primary medium conditions. *Solid State Ionics*, 231:69–73, 2013.

[115] Marie Dumerval, Stéphane Perrin, Loïc Marchetti, Michel Tabarant, François Jomard, and Yves Wouters. Hydrogen absorption associated with the corrosion mechanism of 316L stainless steels in primary medium of Pressurized Water Reactor (PWR). *Corrosion Science*, 85:251–257, 2014.

[116] Yi-Sheng Chen. *Characterisation of hydrogen trapping in steel by atom probe tomography*. PhD thesis, University of Oxford, 2017.

[117] R Rios. *Study of alloy 600 (NC15Fe) stress corrosion cracking mechanisms in high temperature water*. PhD thesis, Univ. Sciences et Technologie de Lille, 1993.

[118] J. Chêne, A. M. Brass, P. Trabuc, and O. Gastaldi. Role of microstructure and heat treatments on the desorption kinetics of tritium from austenitic stainless steels. *Journal of Nuclear Materials*, 360(2):177–185, 2007.

[119] V. Olden, C. Thaulow, and R. Johnsen. Modelling of hydrogen diffusion and hydrogen induced cracking in supermartensitic and duplex stainless steels. *Materials and Design*, 29(10):1934–1948, 2008.

[120] A. M. Brass and J. Chêne. Hydrogen uptake in 316L stainless steel: Consequences on the tensile properties. *Corrosion Science*, 48(10):3222–3242, 2006.

[121] Dong Wang, Xu Lu, Yun Deng, Xiaofei Guo, and Afrooz Barnoush. Effect of hydrogen on nanomechanical properties in Fe-22Mn-0.6C TWIP steel revealed by in-situ electrochemical nanoindentation. *Acta Materialia*, 166:618–629, 2019.

[122] Bachir Osman Hoch. *Modelling of hydrogen diffusion in heterogeneous materials : implications of the grain boundary connectivity*. PhD thesis, Universite de La Rochelle, 2016.

[123] Hamed Haftbaradaran, Jun Song, W. A. Curtin, and Huajian Gao. Continuum and atomistic models of strongly coupled diffusion, stress, and solute concentration. *Journal of Power Sources*, 196(1):361–370, 2011.

[124] I. M.A. Ghermaoui, A. Oudriss, A. Metsue, R. Milet, K. Madani, and X. Feaugas. Multiscale analysis of hydrogen-induced softening in f.c.c. nickel single crystals oriented for multiple-slips: elastic screening effect. *Scientific Reports*, 9(1):1–10, 2019.

[125] J. Li, A. Oudriss, A. Metsue, J. Bouhattate, and X. Feaugas. Anisotropy of hydrogen diffusion in nickel single crystals: The effects of self-stress and hydrogen concentration on diffusion. *Scientific Reports*, 7(October 2016):1–9, 2017.

[126] G. Hachet, J. Li, A. M. Hallil, A. Metsue, A. Oudriss, J. Bouhattate, and X. Feaugas. A multi-scale analysis of the different interactions between defects and hydrogen: A review on the contribution of the elastic fields. *Engineering Fracture Mechanics*, 218(March):1–10, 2019.

[127] E Zuzek, JP Abriata, A San-Martin, and FD Manchester. The h-zr (hydrogen-zirconium) system. *Journal of Phase Equilibria*, 11(4):385–395, 1990.

[128] Lawrence S Darken and Rodney P Smith. Behavior of hydrogen in steel during and after immersion in acid. *Corrosion*, 5(1):1–16, 1949.

[129] F. G. Wei, T. Hara, and K. Tsuzaki. Precise determination of the activation energy for desorption of hydrogen in two Ti-added steels by a single thermal-desorption spectrum. *Metallurgical and Materials Transactions B*, 35(3):587–597, 2004.

[130] Homer E Kissinger. Reaction kinetics in differential thermal analysis. *Analytical chemistry*, 29(11):1702–1706, 1957.

[131] WY Choo and Jai Young Lee. Thermal analysis of trapped hydrogen in pure iron. *Metallurgical and Materials Transactions A*, 13(1):135–140, 1982.

[132] Eun Ju Song, Dong-Woo Suh, and HKDH Bhadeshia. Theory for hydrogen desorption in ferritic steel. *Computational Materials Science*, 79:36–44, 2013.

[133] OD Gonzalez. The measurement of hydrogen permeation in alpha iron-an analysis of the experiments. *Trans Met Soc AIME*, 245(4):607–612, 1969.

[134] G. M. Pressouyre. A classification of hydrogen traps in steel. *Metallurgical Transactions A*, 10(10):1571–1573, 1979.

[135] K. Ono and M. Meshii. Hydrogen detrapping from grain boundaries and dislocations in high purity iron. *Acta Metallurgica Et Materialia*, 40(6):1357–1364, 1992.

[136] W Y Choo and Jai Young Lee. Thermal analysis of trapped hydrogen in pure iron. *Metallurgical Transactions A*, 13:135–140, 1982.

[137] ML Hill and EW Johnson. Hydrogen in cold worked iron-carbon alloys and the mechanism of hydrogen embrittlement. *Transactions of the metallurgical society of AIME*, 215:717–725, 1959.

[138] J. L. Lee and Jai Young Lee. Hydrogen trapping in AISI 4340 steel. *Metal Science*, 17(9):426–432, 1983.

[139] K. Y. Lee, Jai Young Lee, and D. R. Kim. A study of hydrogen-trapping phenomena in AISI 5160 spring steel. *Materials Science and Engineering*, 67(2):213–220, 1984.

[140] G. M. Pressouyre and I. M. Bernstein. A quantitative analysis of hydrogen trapping. *Metallurgical Transactions A*, 9(11):1571–1580, 1978.

[141] Sung Man Lee and Jai Young Lee. Trapping and Transport Phenomena of Hydrogen in Nickel. *Metallurgical transactions. A, Physical metallurgy and materials science*, 17 A(2):181–187, 1986.

[142] D. M. Symons, G. A. Young, and J. R. Scully. The effect of strain on the trapping of hydrogen at grain-boundary carbides in Ni-Cr-Fe alloys. *Metallurgical and Materials Transactions A: Physical Metallurgy and Materials Science*, 32(2):369–377, 2001.

[143] F. Besenbacher, B. Bech Nielsen, and S. M. Myers. Defect trapping of ion-implanted deuterium in copper. *Journal of Applied Physics*, 56(12):3384–3393, 1984.

[144] Yuh Fukai. Superabundant Vacancies Formed in Metal – Hydrogen Alloys. *Physica Scripta.*, T103:11–14, 2003.

[145] Y Yagodzinskyy, T Saukkonen, and S Kilpela. Effect of hydrogen on plastic strain localization in single crystals of austenitic stainless steel. 62:155–158, 2010.

[146] G A Young and J R Scully. Evidence that carbide precipitation produced hydrogen traps in Ni-17Cr-8Fe alloys. *Saipta Materialia*, 36(6):713–719, 1997.

[147] Motomichi Koyama, Takuro Ogawa, and Dingshun Yan. Hydrogen desorption and cracking associated with martensitic transformation in Fe-Cr-Ni-Based austenitic steels with different carbon contents. *International Journal of Hydrogen Energy*, 42(42):26423–26435, 2017.

[148] H. G. Lee and Jai Young Lee. Hydrogen Trapping By TiC Particles In Iron. *Acta Materialia*, 32(1):421–426, 1984.

[149] Sung Man Lee and Jai Young Lee. Hydrogen trapping by voids in nickel. *Scripta Metallurgica*, 21(12):1655–1658, 1987.

[150] F G Wei and K Tsuzaki. Quantitative Analysis on Hydrogen Trapping of TiC Particles in Steel. 37(February):331–353, 2006.

[151] Hideyuki Koike, Yoshiyuki Shizuku, Yuh Fukai, Hidehiko Sugimoto, Wenjing Qin, and Feng Ren. Superabundant Vacancies Formed in Metal – Hydrogen Alloys Superabundant Vacancies Formed in Metal – Hydrogen Alloys. 2003.

[152] W Y Choo and J A I Young Lee. Hydrogen trapping phenomena in carbon steel. 17:1930–1938, 1982.

[153] Gye Won Hong and Jai Young Lee. The interaction of hydrogen and the cementite-ferrite interface in carbon steel. *Journal of Materials Science*, 18(1):271–277, 1983.

[154] A McNabb and PK Foster. A new analysis of the diffusion of hydrogen in iron and ferritic steels. *Trans. Metall. Soc. AIME*, 227(3):618–627, 1963.

[155] M Enomoto. Simulation of thermal desorption spectrum of hydrogen from austenite embedded in the martensite matrix. *International journal of hydrogen energy*, 42(15):10579–10590, 2017.

[156] AJ Kumnick and HH Johnson. Deep trapping states for hydrogen in deformed iron. *Acta Metallurgica*, 28(1):33–39, 1980.

[157] A Turnbull. Perspectives on hydrogen uptake, diffusion and trapping. *International Journal of Hydrogen Energy*, 40(47):16961–16970, 2015.

[158] Richard A Oriani. The diffusion and trapping of hydrogen in steel. *Acta metallurgica*, 18(1):147–157, 1970.

[159] R Kirchheim. Keynote lecture: diffusion controlled thermal desorption spectroscopy. In *2nd international conference on steel and hydrogen*, volume 1, pages 237–53. OCAS, 2014.

[160] Y. Yagodzinskyy, O. Todoshchenko, and S. Papula. Hydrogen solubility and diffusion in austenitic stainless steels studied with thermal desorption spectroscopy. *Steel Research International*, 82(1):20–25, 2011.

[161] Olga Todoshchenko, Yuriy Yagodzinskyy, and Hannu Hänninen. Thermal desorption of hydrogen from AISI 316L stainless steel and pure nickel. *Defect and Diffusion Forum*, 344(February 2015):71–77, 2013.

[162] Gang Lu and Efthimios Kaxiras. Hydrogen embrittlement of aluminum: The crucial role of vacancies. *Physical Review Letters*, 94(15):1–4, 2005.

[163] Y. Fukai, S. Yamatomo, S. Harada, and M. Kanazawa. The phase diagram of the Ni-H system revisited. *Journal of Alloys and Compounds*, 372(1-2):4–5, 2004.

[164] M. L. Fullarton, R. E. Voskoboinikov, and S. C. Middleburgh. Hydrogen accommodation in α-iron and nickel. *Journal of Alloys and Compounds*, 587:794–799, 2014.

[165] T. Hiroi, Y. Fukai, and K. Mori. The phase diagram and superabundant vacancy formation in Fe-H alloys revisited. *Journal of Alloys and Compounds*, 404-406(SPEC. ISS.):252–255, 2005.

[166] T. Tabata and H. K. Birnbaum. Direct observations of the effect of hydrogen on the behaviour of dislocations in iron. *Scripta METALLURGICA*, 17:947–950, 1983.

[167] P. Sofroni and I. M. Robertson. Transmission electron microscopy observations and micromechanical/continuum models for the effect of hydrogen on the mechanical behaviour of metals. *Philosophical Magazine A: Physics*

of Condensed Matter, Structure, Defects and Mechanical Properties, 82(17-18):3405–3413, 2002.

[168] E. Sirois and H. K. Birnbaum. Effects of hydrogen and carbon on thermally activated deformation in nickel. *Acta Metallurgica Et Materialia*, 40(6):1377–1385, 1992.

[169] Shuai Wang, Naoyuki Hashimoto, and Somei Ohnuki. Effects of hydrogen on activation volume and density of mobile dislocations in iron-based alloy. *Materials Science and Engineering A*, 562:101–108, 2013.

[170] Howard K Birnbaum. *Mechanisms of hydrogen related fracture of metals.* PhD thesis, University of Illinois, 1989.

[171] P. J. Ferreira, I. M. Robertson, and H. K. Birnbaum. Hydrogen effects on the interaction between dislocations. *Acta Materialia*, 46(5):1749–1757, 1998.

[172] P. Sofronis and H. K. Birnbaum. Mechanics of the hydrogendashdislocationdashimpurity interactions-I. Increasing shear modulus. *Journal of the Mechanics and Physics of Solids*, 43(1):49–90, 1995.

[173] M.B. Whiteman and A.R. Troiani. The Influence of Hydrogen on the Stacking Fault Energy of an Austenitic Stainless Steel. *Phys. Stat. Sol.*, 7:109–110, 1964.

[174] J. P. Chateau, D. Delafosse, and T. Magnin. Numerical simulations of hydrogen-dislocation interactions in fcc stainless steels. Part I: Hydrogen-dislocation interactions in bulk crystals. *Acta Materialia*, 50(6):1507–1522, 2002.

[175] J.P. Chateau, D. Delafosse, and T. Magnin. Numerical simulations of hydrogen–dislocation interactions in fcc stainless steels. *Acta Materialia*, 50(6):1523–1538, 2002.

[176] Yuriy Yagodzinskyy, Evgenii Malitckii, Tapio Saukkonen, and Hannu Hanninen. Hydrogen-induced strain localization in austenitic stainless steels and possible origins of their hydrogen embrittlement. *SteelyHydrogen2014 Conference Proceedings*, pages 203–213, 2014.

[177] Eiji Akiyama and Saburo Matsuoka. Hydrogen visualization in steels using Ag decoration method. *Materials Transactions*, 56(6):793–797, 2015.

[178] S. D. Pu and S. W. Ooi. Hydrogen transport by dislocation movement in austenitic steel. *Materials Science and Engineering A*, 761(May):0–3, 2019.

[179] M Ménard, JM Olive, A-M Brass, and I Aubert. Effects of hydrogen charging on surface slip band morphology of a type 316l stainless steel. In *Environment-Induced Cracking of Materials*, pages 179–188. Elsevier, 2008.

[180] A. Oudriss, J. Creus, J. Bouhattate, C. Savall, B. Peraudeau, and X. Feaugas. The diffusion and trapping of hydrogen along the grain boundaries in polycrystalline nickel. *Scripta Materialia*, 66(1):37–40, 2012.

[181] A. Oudriss, J. Creus, J. Bouhattate, E. Conforto, C. Berziou, C. Savall, and X. Feaugas. Grain size and grain-boundary effects on diffusion and trapping of hydrogen in pure nickel. *Acta Materialia*, 60(19):6814–6828, 2012.

[182] S. Frappart, A. Oudriss, X. Feaugas, J. Creus, J. Bouhattate, F. Thébault, L. Delattre, and H. Marchebois. Hydrogen trapping in martensitic steel investigated using electrochemical permeation and thermal desorption spectroscopy. *Scripta Materialia*, 65(10):859–862, 2011.

[183] A. M. Brass and A. Chanfreau. Accelerated diffusion of hydrogen along grain boundaries in nickel. *Acta Materialia*, 44(9):3823–3831, 1996.

[184] B. Ladna and H. K. Birnbaum. SIMS study of hydrogen at the surface and grain boundaries of nickel bicrystals. *Acta Metallurgica*, 35(10):2537–2542, 1987.

[185] T. Tsuru and R.M. Latanision. Grain boundary transport of hydrogen in nickel. *Scripta METALLURGICA*, 16(5):575–578, 1982.

[186] R.M Latanision. Hydrogen induced intergranular cracking of nickel-base alloys. *Final Technical Report to Office of Naval Research*, 1982.

[187] Hongtao Wang, Wei Yang, and A. H.W. Ngan. Enhanced diffusivity by triple junction networks. *Scripta Materialia*, 52(1):69–73, 2005.

[188] Hao Zhang, David J. Srolovitz, Jack F. Douglas, and James A. Warren. Grain boundaries exhibit the dynamics of glass-forming liquids. *Proceedings of the National Academy of Sciences of the United States of America*, 106(19):7735–7740, 2009.

[189] Shinya Taketomi, Ryosuke Matsumoto, and Noriyuki Miyazaki. Atomistic study of hydrogen distribution and diffusion around a {1 1 2}<1 1 1> edge dislocation in alpha iron. *Acta Materialia*, 56(15):3761–3769, 2008.

[190] Thomas F. Kelly and Michael K. Miller. Invited review article: Atom probe tomography. *Review of Scientific Instruments*, 78(3), 2007.

[191] Baptiste Gault and Simon P Moody, Michael P Cairney, Julie M Ringer. *Atom probe microscopy*. Springer Science \& Business Media, 2012.

[192] Y. S. Chen, D. Haley, S. S.A. Gerstl, A. J. London, F. Sweeney, R. A. Wepf, W. M. Rainforth, P. A.J. Bagot, and M. P. Moody. Direct observation of individual hydrogen atoms at trapping sites in a ferritic steel. *Science*, 355(6330):1196–1199, 2017.

[193] Yi Sheng Chen, Hongzhou Lu, Jiangtao Liang, Alexander Rosenthal, Hongwei Liu, Glenn Sneddon, Ingrid McCarroll, Zhengzhi Zhao, Wei Li, Aimin Guo, and Julie M. Cairney. Observation of hydrogen trapping at dislocations, grain boundaries, and precipitates. *Science*, 367(6474):171–175, 2020.

[194] Ryota Gemma, Talaat Al-Kassab, Reiner Kirchheim, and Astrid Pundt. Visualization of deuterium dead layer by atom probe tomography. *Scripta Materialia*, 67(11):903–906, 2012.

[195] Jun Takahashi, Kazuto Kawakami, Yukiko Kobayashi, and Toshimi Tarui. The first direct observation of hydrogen trapping sites in TiC precipitation-hardening steel through atom probe tomography. *Scripta Materialia*, 63(3):261–264, 2010.

[196] Andrew J Breen, Yujiao Li, Leigh Stephenson, Baptiste Gault, and Michael Herbig. Direct Observation of Hydrogen in Cold-Drawn Pearlitic Steel Wires

Using Cryogenic Atom Probe Tomography. *Microscopy and Microanalysis*, 25(S2):2522–2523, 2019.

[197] Daniel Haley, Ingrid McCarroll, Paul A.J. Bagot, Julie M. Cairney, and Michael P. Moody. A Gas-Phase Reaction Cell for Modern Atom Probe Systems. *Microscopy and Microanalysis*, 25(2):410–417, 2019.

[198] Yi Sheng Chen, Paul A.J. Bagot, Michael P. Moody, and Daniel Haley. Observing hydrogen in steel using cryogenic atom probe tomography: A simplified approach. *International Journal of Hydrogen Energy*, 44(60):32280–32291, 2019.

[199] Sergio Lozano-perez. A guide on FIB preparation of samples containing stress corrosion crack tips for TEM and atom-probe analysis. 39:320–328, 2008.

[200] S. Lozano-Perez and J. M. Titchmarsh. TEM investigations of intergranular stress corrosion cracking in austenitic alloys in PWR environmental conditions. *Materials at High Temperatures*, 20(4):573–579, 2003.

[201] I. M. Robertson and H. K. Birnbaum. An HVEM study of hydrogen effects on the deformation and fracture of nickel. *Acta Metallurgica*, 34(3):353–366, 1986.

[202] Yukitaka Murakami, Toshihiko Kanezaki, Yoji Mine, and S. Mastsuoka. Hydrogen Embrittlement Mechanism in Fatigue of Austenitic Stainless Steels. *Metallurgical and Materials Transactions A*, 39A:1327–1339, 2008.

[203] I. M. A N M Robertson, P. Sofronis, A. Nagao, M. L. Martin, S. Wang, D W Gross, K. E. Nygren, and I. M. A N M Robertson. Hydrogen Embrittlement Understood. *Metallurgical and materials transactions A*, 46A(June):2323–2341, 2015.

[204] P. Rozenak, I.M. Robertson, and H.K. Birnbaum. HVEM studies of the effects of hydrogen on the deformation and fracture of AISI type 316 austenitic stainless steel. *Acta Metallurgica et Materialia*, 38(11):2031–2040, 1990.

[205] Greg McMahon, Bryan D. Miller, and M. Grace Burke. High resolution NanoSIMS imaging of deuterium distributions in 316 stainless steel specimens after fatigue testing in high pressure deuterium environment. *npj Materials Degradation*, 2(1):1–6, 2018.

[206] Kexue Li, Junliang Liu, Chris R.M. Grovenor, and Katie L. Moore. NanoSIMS Imaging and Analysis in Materials Science. *Annual Review of Analytical Chemistry*, 13(1):1–20, 2020.

[207] Sean S. Yardley, Katie L. Moore, Na Ni, Jang Fei Wei, Stuart Lyon, Michael Preuss, Sergio Lozano-Perez, and Chris R M Grovenor. An investigation of the oxidation behaviour of zirconium alloys using isotopic tracers and high resolution SIMS. *Journal of Nuclear Materials*, 443(1-3):436–443, 2013.

[208] Kexue Li, Thomas Aarholt, Junliang Liu, Helen Hulme, Alistair Garner, Michael Preuss, Sergio Lozano-Perez, and Chris Grovenor. 3D-characterization of deuterium distributions in zirconium oxide scale using high-resolution SIMS. *Applied Surface Science*, 464(March 2018):311–320, 2019.

[209] Jing Hu, Thomas Aarholt, B. Setiadinata, K. Li, Alistair Garner, Sergio Lozano-Perez, Michael Moody, Philipp Frankel, Michael Preuss, and C. Grovenor. A multi-technique study of "barrier layer" nano-porosity in Zr oxides during corrosion and hydrogen pickup using (S)TEM, TKD, APT and NanoSIMS. *Corrosion Science*, 158(April):108109, 2019.

[210] Andreas Röhsler, Oded Sobol, Hannu Hänninen, and Thomas Böllinghaus. In-situ ToF-SIMS analyses of deuterium re-distribution in austenitic steel AISI 304L under mechanical load. *Nature Scientific Reports*, 10(3611):1–9, 2020.

[211] James Sayers, Susan Ortner, Kexue Li, and Sergio Lozano-Perez. Effect of ph on hydrogen pick-up and corrosion in zircaloy-4. *Minerals, Metals and Materials Series*, (November):1169–1180, 2019.

[212] Katie L Moore, Markus Schroder, and Chris RM Grovenor. *Imaging secondary ion mass spectroscopy*. Wiley-VCH, 2012.

[213] Zhengli Hua, Shengyi Zhu, Bai An, Takashi Iijima, Chaohua Gu, and Jinyang Zheng. The finding of hydrogen trapping at phase boundary in austenitic stainless steel by scanning Kelvin probe force microscopy. *Scripta Materialia*, 162:219–222, 2019.

[214] Cem Örnek, Christofer Leygraf, and Jinshan Pan. Passive film characterisation of duplex stainless steel using scanning Kelvin probe force microscopy in combination with electrochemical measurements. *Nature*, 3(1):1–8, 2019.

[215] Z. X. Ma, X. L. Xiong, L. N. Zhang, Z. H. Zhang, Y. Yan, and Y. J. Su. Experimental study on the diffusion of hydrogen along individual grain boundaries in nickel. *Electrochemistry Communications*, 92(February):24–28, 2018.

[216] M. Duportal, A. Oudriss, F. Xavier, and S. Catherine. On the estimation of the diffusion coefficient and distribution of hydrogen in stainless steel. *Scripta Materialia*, page Unpublished, 2020.

[217] Zhengli Hua, Bai An, Takashi Iijima, Chaohua Gu, and Jinyang Zheng. The finding of crystallographic orientation dependence of hydrogen diffusion in austenitic stainless steel by scanning Kelvin probe force microscopy. *Scripta Materialia*, 131:47–50, 2017.

[218] S. H. Williams, A. Hilger, N. Kardjilov, I. Manke, M. Strobl, P. A. Douissard, T. Martin, H. Riesemeier, and J. Banhart. Detection system for microimaging with neutrons. *Journal of Instrumentation*, 7(2), 2012.

[219] Varley F. Sears. Neutron scattering lengths and cross sections. *Neutron News*, 3(3):26–37, 1992.

[220] K. Beyer, T. Kannengiesser, A. Griesche, and B. Schillinger. Neutron radiography study of hydrogen desorption in technical iron. *Journal of Materials Science*, 46(15):5171–5175, 2011.

[221] Axel Griesche, Eitan Dabah, Thomas Kannengiesser, Nikolay Kardjilov, André Hilger, and Ingo Manke. Three-dimensional imaging of hydrogen blister in iron with neutron tomography. *Acta Materialia*, 78:14–22, 2014.

[222] Mykhaylo Lototskyy, Roman Denys, Serge Nyallang Nyamsi, Irina Bessarabskaia, and Volodymyr Yartys. Modelling of hydrogen thermal desorption spectra. *Materials Today: Proceedings*, 5(4):10440–10449, 2018.

[223] Caitlin Hurley, Frantz Martin, Loïc Marchetti, Jacques Chêne, Christine Blanc, and Eric Andrieu. Numerical modeling of thermal desorption mass spectroscopy (TDS) for the study of hydrogen diffusion and trapping interactions in metals. *International Journal of Hydrogen Energy*, 40(8):3402–3414, 2015.

[224] A. Raina, V. S. Deshpande, and N. A. Fleck. Analysis of thermal desorption of hydrogen in metallic alloys. *Acta Materialia*, 144(August):777–785, 2018.

[225] A.M Jong and J.W Niemantsverdriet. Thermal Desorption Analysis: Comparative Test of Ten Commonly Applied Procedures. *Surface Science*, 233:355–365, 1990.

[226] Caitlin Hurley. *ROLE OF HYDROGEN IN THE CORROSION OF NICKEL-BASED ALLOYS IN PRIMARY ENVIRONMENT OF PWRs: KINETIC STUDY OF ABSORPTION AND TRAPPING MECHANISMS*. PhD thesis, University of Toulouse, 2016.

[227] Caitlin Hurley, Frantz Martin, Loïc Marchetti, Jacques Chêne, Christine Blanc, and Eric Andrieu. Role of grain boundaries in the diffusion of hydrogen in nickel base alloy 600: Study coupling thermal desorption mass spectroscopy with numerical simulation. *International Journal of Hydrogen Energy*, 41(38):17145–17153, 2016.

[228] Samantha K. Lawrence, Yuriy Yagodzinskyy, Hannu Hänninen, Esa Korhonen, Filip Tuomisto, Zachary D. Harris, and Brian P. Somerday. Effects of grain size and deformation temperature on hydrogen-enhanced vacancy formation in Ni alloys. *Acta Materialia*, 128:218–226, 2017.

[229] Yu Yagodzinskyy, O. Tarasenko, S. Smuk, P. Aaltonen, and H. Hänninen. A new method for studying thermal desorption of hydrogen from metals based on internal friction technique. *Physica Scripta*, 94(April):111–120, 2001.

[230] Caitlin Huotilainen, Ulla Ehrnstén, Matias Ahonen, and Hannu Hänninen. The ect of thermal aging on microstructure and hardness of industrial heats of Alloy 690. *19th International Conference on Environmental Degradation of Materials in Nuclear Power Systems - Water Reactors*, pages 156–164, 2019.

[231] Y. Yagodzinskyy and H. Hänninen. Hydrogen-dislocation interactions and their role in HELP mechanism of hydrogen embrittlement. *11th International Conference on Fracture 2005, ICF11*, 5:3442–3446, 2005.

[232] D. Pérez Escobar, L. Duprez, A. Atrens, and K. Verbeken. Influence of experimental parameters on thermal desorption spectroscopy measurements during evaluation of hydrogen trapping. *Journal of Nuclear Materials*, 450(1-3):32–41, 2014.

[233] Reiner Kirchheim. Bulk Diffusion-Controlled Thermal Desorption Spectroscopy with Examples for Hydrogen in Iron. *Metallurgical and Materials Transactions A: Physical Metallurgy and Materials Science*, 47(2):672–696, 2016.

[234] Ekaterina L. Alekseeva, Alexander K. Belyaev, Anatoly M. Polyanskiy, Vladimir A. Polyanskiy, Evgeniy A. Varshavchik, and Yuri A. Yakovlev. Surface vs diffusion in TDS of hydrogen. *E3S Web of Conferences*, 121:1–5, 2019.

[235] James Sayers, Susan Ortner, Kexue Li, and Sergio Lozano-Perez. Effect of ph on hydrogen pick-up and corrosion in zircaloy-4. In *Environmental Degradation of Materials in Nuclear Power Systems*, pages 1169–1180. Springer, 2017.

[236] Shinya Iwata, Yoshinori Sato, Kouta Nakai, Shohei Ogura, Tatsuo Okano, Masaru Namura, Atsuo Kasuya, Kazuyuki Tohji, and Katsuyuki Fukutani. Novel method to evaluate the carbon network of single-walled carbon nanotubes by hydrogen physisorption. *Journal of Physical Chemistry C*, 111(41):14937–14941, 2007.

[237] Siddhartha Pathak and Surya R. Kalidindi. Spherical nanoindentation stress-strain curves. *Materials Science and Engineering*, 91:1–36, 2015.

[238] M. V. Swain and J. Menčík. Mechanical property characterization of thin films using spherical tipped indenters. *Thin Solid Films*, 253(1-2):204–211, 1994.

[239] Jingzhou Zhang, Glen L. Niebur, and Timothy C. Ovaert. Mechanical property determination of bone through nano- and micro-indentation testing and finite element simulation. *Journal of Biomechanics*, 41(2):267–275, 2008.

[240] U. Ramamurty, S. Sridhar, A. E. Giannakopoulos, and S. Suresh. Experimental study of spherical indentation on piezoelectric materials. *Acta Materialia*, 47(8):2417–2430, 1999.

[241] W. C. Oliver and G. M. Pharr. An improved technique for determining hardness and elastic modulus using load and displacement sensing indentation experiments. *Journal of Materials Research*, 7(6):1564 – 1583, 1992.

[242] I A N N Sneddon. The relation between load and pentration in the axisymmetric BOUSSINESQ problem for a pucnh of arbitary profile. *Int. J. Engng Sci.*, 3(638):47–57, 1965.

[243] D Tabor. A simple theory of static and dynamic hardness. *Proceedings of the Royal Society of London. Series A. Mathematical and Physical Sciences*, 192(1029):247–274, 1948.

[244] A. Leitner, V. Maier-Kiener, and D. Kiener. Essential refinements of spherical nanoindentation protocols for the reliable determination of mechanical flow curves. *Materials and Design*, 146:69–80, 2018.

[245] Siddhartha Pathak, Joshua Shaffer, and Surya R. Kalidindi. Determination of an effective zero-point and extraction of indentation stress-strain curves without the continuous stiffness measurement signal. *Scripta Materialia*, 60(6):439–442, 2009.

[246] Surya R. Kalidindi and Siddhartha Pathak. Determination of the effective zero-point and the extraction of spherical nanoindentation stress-strain curves. *Acta Materialia*, 56(14):3523–3532, 2008.

[247] J. S. Field and M. V. Swain. Determining the mechanical properties of small volumes of material from submicrometer spherical indentations. *Journal of Materials Research*, 10(1):101–112, 1995.

[248] J. S. Field and M. V. Swain. A simple predictivity model for spherical indentation. *Journal of Materials Research*, 8(2):297–306, 1993.

[249] J B Pethica and W. C. Oliver. Tip Surface Interactions in STM and AFM. *Physica Scripta Tip*, (61), 1987.

[250] Yong Huan, Dongxu Liu, Rong Yang, and Taihua Zhang. Analysis of the practical force accuracy of electromagnet-based nanoindenters. *Measurement: Journal of the International Measurement Confederation*, 43(9):1090–1093, 2010.

[251] D. K. Kim. Nanoindentation lecture 1 basic principle,kaist: Daejeon, korea.

[252] Kai Feng, Guosong Wu, Zhuguo Li, Xun Cai, and Paul K. Chu. Corrosion behavior of SS316L in simulated and accelerated PEMFC environments. *International Journal of Hydrogen Energy*, 36(20):13032–13042, 2011.

[253] Qian Liu, Aleks D Andrej Atrens, Zhiming Shi, Kim Verbeken, and Aleks D Andrej Atrens. Determination of the hydrogen fugacity during electrolytic charging of steel. *Corrosion Science*, 87:239–258, 2014.

[254] J M Wheeler, D E J Armstrong, W Heinz, and R Schwaiger. High temperature nanoindentation : The state of the art and future challenges. 19:354–366, 2015.

[255] M. Beghini, L. Bertini, and V. Fontanari. Evaluation of the stress-strain curve of metallic materials by spherical indentation. *International Journal of Solids and Structures*, 43(7-8):2441–2459, 2006.

[256] D. L. Krumwiede, T. Yamamoto, T. A. Saleh, S. A. Maloy, G. R. Odette, and P. Hosemann. Direct comparison of nanoindentation and tensile test results on reactor-irradiated materials. *Journal of Nuclear Materials*, 504:135–143, 2018.

[257] Andrew J Bushby and Nigel M Jennett. Determining the area function of spherical indenters for nanoindentation. *MRS Online Proceedings Library Archive*, 649, 2000.

[258] PM Nagy, I Istvan Kükemezey, Spyridon Kassavetis, Peter Berke, M-P Delplancke-Ogletree, and Stergios Logothetidis. The effect of roughness on nanoindentation results. *Nanoscience and Nanotechnology Letters*, 5(4):480–483, 2013.

[259] Ju Young Kim, Seung Kyun Kang, Jung Jun Lee, Jae il Jang, Yun Hee Lee, and Dongil Kwon. Influence of surface-roughness on indentation size effect. *Acta Materialia*, 55(10):3555–3562, 2007.

[260] M. S. Bobji, K. Venkatesh, and S. K. Biswas. Roughness generated in surface grinding of metals. *Journal of Tribology*, 121(4):746–752, 1999.

[261] William D. Nix and Huajian Gao. Indentation size effects in crystalline materials: A law for strain gradient plasticity. *Journal of the Mechanics and Physics of Solids*, 46(3):411–425, 1998.

[262] Karsten Durst, Björn Backes, and Mathias Göken. Indentation size effect in metallic materials: Correcting for the size of the plastic zone. *Scripta Materialia*, 52(11):1093–1097, 2005.

[263] K. Durst, O. Franke, A. Böhner, and M. Göken. Indentation size effect in Ni-Fe solid solutions. *Acta Materialia*, 55(20):6825–6833, 2007.

[264] S. Shim, H. Bei, E. P. George, and G. M. Pharr. A different type of indentation size effect. *Scripta Materialia*, 59(10):1095–1098, 2008.

[265] T. G. Nieh, C. Schuh, J. Wadsworth, and Yi Li. Strain rate-dependent deformation in bulk metallic glasses. *Intermetallics*, 10(11-12):1177–1182, 2002.

[266] C. A. Schuh, J. K. Mason, and A. C. Lund. Quantitative insight into dislocation nucleation from high-temperature nanoindentation experiments. *Nature Materials*, 4(8):617–621, 2005.

[267] Weilie Zhou, Robert Apkarian, Zhong Lin Wang, and David Joy. Fundamentals of scanning electron microscopy (sem). In *Scanning microscopy for nanotechnology*, pages 1–40. Springer, 2006.

[268] T. B. Britton and A. J. Wilkinson. High resolution electron backscatter diffraction measurements of elastic strain variations in the presence of larger lattice rotations. *Ultramicroscopy*, 114:82–95, 2012.

[269] T. B. Britton and A. J. Wilkinson. Measurement of residual elastic strain and lattice rotations with high resolution electron backscatter diffraction. *Ultramicroscopy*, 111(8):1395–1404, 2011.

[270] Hongbing Yu, Junliang Liu, Phani Karamched, Angus J. Wilkinson, and Felix Hofmann. Mapping the full lattice strain tensor of a single dislocation by high angular resolution transmission Kikuchi diffraction (HR-TKD). *Scripta Materialia*, 164:36–41, 2019.

[271] Phani S Karamched, Naganand Saravanan, Jack C Haley, Angus J Wilkinson, and Sergio Lozano-perez. Ultramicroscopy Effect of sample thinning on strains and lattice rotations measured from Transmission Kikuchi diffraction in the SEM. *Ultramicroscopy*, 225(December 2020):113267, 2021.

[272] Junliang Liu, Sergio Lozano-Perez, Phani Karamched, Jennifer Holter, Angus J. Wilkinson, and Chris R.M. Grovenor. Forescattered electron imaging of nanoparticles in scanning electron microscopy. *Materials Characterization*, 155:1–15, 2019.

[273] Junliang Liu, Sergio Lozano-Perez, Angus J. Wilkinson, and Chris R.M. Grovenor. On the depth resolution of transmission Kikuchi diffraction (TKD) analysis. *Ultramicroscopy*, 205:5–12, 2019.

[274] Joachim Mayer, Lucille A. Giannuzzi, Takeo Kamino, and Joseph Michael. TEM sample preparation and FIB-induced damage. *MRS Bulletin*, 32(5):400–407, 2007.

[275] Felix Hofmann, Edmund Tarleton, Ross J Harder, Nicholas W Phillips, Pui-wai Ma, Jesse N Clark, Ian K Robinson, Brian Abbey, Wenjun Liu, and Christian E Beck. 3D lattice distortions and defect structures in ion-implanted nano-crystals. *Nature Publishing Group*, (December 2016):1–10, 2017.

[276] David B Williams and C Barry Carter. The transmission electron microscope. In *Transmission electron microscopy*, pages 3–17. Springer, 1996.

[277] J. L. Hutchison and L. A. Bursill. Fresnel fringe contrast of faceted voids within gem-quality diamond. *Journal of Microscopy*, 131(1):63–66, 1983.

[278] Daisuke. Shindo and Tetsuo. Oikawa. *Analytical electron microscopy for materials science*. Springer Science \& Business Media, 2013.

[279] Alfred Benninghoven, FG Rudenauer, and Helmut W Werner. *Secondary ion mass spectrometry: basic concepts, instrumental aspects, applications and trends*. John Wiley and Sons,, New York, NY, 1987.

[280] A. Baron-wiechec, K.wid Heinola, J. Likonen, E. Alves, N. Catarino, J. P. Coad, V. Corregidor, I. Jepu, G. F. Matthews, A. Widdowson, and J E T Contributors. Thermal desorption spectrometry of beryllium plasma facing tiles exposed in the JET tokamak. *Fusion Engineering and Design*, 133(September 2017):135–141, 2018.

[281] F. P.E. Dunne, R. Kiwanuka, and A. J. Wilkinson. Crystal plasticity analysis of micro-deformation, lattice rotation and geometrically necessary dislocation density. *Proceedings of the Royal Society A: Mathematical, Physical and Engineering Sciences*, 468(2145):2509–2531, 2012.

[282] O. Barrera, E. Tarleton, H. W. Tang, and A. C.F. Cocks. Modelling the coupling between hydrogen diffusion and the mechanical behaviour of metals. *Computational Materials Science*, 122:219–228, 2016.

[283] A. Krom, R. Koers, and A. Bakker. Hydrogen transport near a blunting crack tip. *Journal of the Mechanics and Physics of Solids*, (47):971–992, 1998.

[284] R.A Oriani. The diffusion and trapping of hydrogen in steels. *Acta Metallurgica*, 18:147–157, 1970.

[285] Edmund Tarleton. Incorporating hydrogen in mesoscale models. *Computational Materials Science*, 163:282–289, 2019.

[286] Chang-sik Oh and Yun-jae Kim. Coupled Analysis of Hydrogen Transport Within ABAQUS. pages 600–606, 2009.

[287] F Carette. EDF R&D Material Composition Data Sheet. 2017.

[288] Kashif I Choudhry, Shooka Mahboubi, Gianluigi A Botton, Joseph R Kish, and Igor M Svishchev. Corrosion of engineering materials in a supercritical water cooled reactor : Characterization of oxide scales on Alloy 800H and stainless. *Corrosion Science*, 100:222–230, 2015.

[289] Koji Arioka. 2014 W.R. Whitney award lecture: Change in bonding strength at grain boundaries before long-term SCC initiation. *Corrosion*, 71(4):403–419, 2015.

[290] Tadao Watanabe. Grain boundary engineering: historical perspective and future prospects. *Journal of materials science*, 46(12):4095–4115, 2011.

[291] Ignacio Arganda-Carreras, Verena Kaynig, Curtis Rueden, Kevin W. Eliceiri, Johannes Schindelin, Albert Cardona, and H. Sebastian Seung. Trainable Weka Segmentation: A machine learning tool for microscopy pixel classification. *Bioinformatics*, 33(15):2424–2426, 2017.

[292] W. Pantleon. Resolving the geometrically necessary dislocation content by conventional electron backscattering diffraction. *Scripta Materialia*, 58(11):994–997, 2008.

[293] Junjie Chen, Qian Xiao, Zhanpeng Lu, Xiangkun Ru, Hao Peng, and Qi Xiong. Characterization of interfacial reactions and oxide films on 316L stainless steel in various simulated PWR primary water environments. *Journal of Nuclear Materials*, 489:137–149, 2017.

[294] Takumi Terachi, Katsuhiko Fujii, and Koji Arioka. Microstructural characterization of scc crack tip and oxide film for SUS 316 stainless steel in simulated PWR primary water at 320°C. *Journal of Nuclear Science and Technology*, 42(2):225–232, 2005.

[295] G Was and Z Jiao. Oxidation of a Proton-Irradiated 316 Stainless Steel in Simulated BWR NWC Environment. In *Proceedings of the 15th International Conference on Environmental Degradation of Materials in Nuclear Power Systems — Water Reactors*, pages 1329–1338, 2011.

[296] Guangdong Han, Zhanpeng Lu, Xiangkun Ru, Junjie Chen, and Qian Xiao. Improving the oxidation resistance of 316L stainless steel in simulated pressurized water reactor primary water by electropolishing treatment. *Journal of Nuclear Materials*, 467:194–204, 2015.

[297] Mohamed Sennour, Loïc Marchetti, Stéphane Perrin, Régine Molins, Michèle Pijolat, and Olivier Raquet. The characterization of the oxide films formed at the surface of Ni-base alloys in pressurized water reactors primary coolant by transmission electron microscopy. *Materials Science Forum*, 595-598 PA:539–547, 2008.

[298] Stéphane Perrin, Loic Marchetti, Cécilie Duhamel, Mohamed Sennour, and François Jomard. Influence of irradiation on the oxide film formed on 316 L stainless steel in PWR primary water. *Oxidation of Metals*, 80(5-6):623–633, 2013.

[299] H. Lefaix-Jeuland, L. Marchetti, S. Perrin, M. Pijolat, M. Sennour, and R. Molins. Oxidation kinetics and mechanisms of Ni-base alloys in pressurised water reactor primary conditions: Influence of subsurface defects. *Corrosion Science*, 53(12):3914–3922, 2011.

[300] Tyler Moss, Guoping Cao, and Gary S Was. Oxidation of Alloy 600 and Alloy 690 : Experimentally Accelerated Study in Hydrogenated Supercritical Water. *Metallurgical and Materials Transactions A*, 48(4):1596–1612.

[301] Junjie Chen, Zhanpeng Lu, Fanjiang Meng, Xuelian Xu, Qian Xiao, Ho Sub Kim, and Changheui Jang. The corrosion behaviour of alloy 690 tube in simulated PWR secondary water with the effect of solid diffusing hydrogen. *Journal of Nuclear Materials*, 517:179–191, 2019.

[302] J. M. Boursier, D. Desjardins, and F. Vaillant. The influence of the strain-rate on the stress corrosion cracking of alloy 600 in high temperature primary water. *Corrosion Science*, 37(3):493–508, 1995.

[303] S. M. Bruemmer, M. J. Olszta, N. R. Overman, and M. B. Toloczko. One Dimensional Cold Rolling Effects on Stress Corrosion Crack Growth in Alloy 690 Tubing and Plate Materials. *17th International Conference on Environmental Degradation of Materials in Nuclear Power Sytems - Water Reactors*, pages 91–106, 2015.

[304] Masahito Mochizuki, Ryohei Ihara, Jinya Katsuyama, and Makoto Udagawa. SCC assesment base on probability fracture mechanics considering SCC initiation and propagation under residual stress fields generated by machining and welding process of pipes. In *ASME 2013 Pressure Vessels and Piping Conference*, pages 1–8, Paris, France, 2013.

[305] Emilio Martínez-Pañeda, Andres Díaz, Louise Wright, and Alan Turnbull. Generalised boundary conditions for hydrogen transport at crack tips. *Corrosion Science*, 173, 2020.

[306] H. Coriou, L. Grall, C. Mahieu, and M. Pelas. Sensitivity to Stress Corrosion and Intergranular Attack of High-Nickel Austenitic Alloys, 1966.

[307] BL Hackett, Andrew A Wereszczak, and GM Pharr. Evaluation of new technique to estimate yield stress in brittle materials via spherical indentation testing. In *Proceeding of the 42nd International Conference on Advanced Ceramics and Composites: Ceramic Engineering and Science Proceedings Volume 39, Issue 2*, volume 39, pages 61–71. John Wiley & Sons, Inc. Hoboken, NJ, USA, 2019.

[308] Siddhartha Pathak and Surya R Kalidindi. Spherical nanoindentation stress–strain curves. *Materials science and engineering: R: Reports*, 91:1–36, 2015.

[309] Ralf Hielscher, Felix Bartel, and T. Ben Britton. Gazing at crystal balls: Electron backscatter diffraction pattern analysis and cross correlation on the sphere. *Ultramicroscopy*, 2019.

[310] Sandemeyer Steel Company. Specification Sheet : Alloy 316 / 316L. *Sandemeyer Steel Company*, (1):9–11, 2013.

[311] Y Nomura, R Suzuki, and M Saito. Strength of copper alloys in high temperature environment. 311:681–685, 2002.

[312] Feifei Nie. *Thermal Kinetics of Helium Irradiation Hardening in Selected Alloys for the Canadian Gen . IV Nuclear Reactor Concept.* PhD thesis, The University of Western Ontario, 2017.

[313] Jordan S Weaver, Siddhartha Pathak, Ashley Reichardt, Hi T Vo, Stuart A Maloy, Peter Hosemann, and Nathan A Mara. Spherical nanoindentation of proton irradiated 304 stainless steel : A comparison of small scale mechanical test techniques for measuring irradiation hardening. 493:368–379, 2017.

[314] Special Metals. Incolloy alloy 800. page 12, 2004.

[315] Special Metals Corporation. Inconel 600 Alloy. 600(2), 2008.

[316] M Kulka, N Makuch, P Dziarski, and A Piasecki. A study of nanoindentation for mechanical characterization of chromium and nickel borides ' mixtures formed by laser boriding. *Ceramics International*, 40(4):6083–6094, 2014.

[317] Zhonglin Li, Jichun Xiong, Qingyan Xu, Jiarong Li, and Baicheng Liu. Deformation and recrystallization of single crystal nickel-based superalloys during investment casting. *Journal of Materials Processing Technology*, 217:1–12, 2015.

[318] David E J Armstrong, Angus J. Wilkinson, and Steve G. Roberts. Measuring anisotropy in Young's modulus of copper using microcantilever testing. *Journal of Materials Research*, 24(11):3268–3276, 2009.

[319] G D Tolstolutskaya, S A Karpov, G Y Rostova, B S Sungurov, and G N Tolmachova. The effect of irradiation with inert gas and hydrogen ions on nanohardness of SS316 stainless steel. pages 66–70, 2015.

[320] Baptiste Girault, Andreas S. Schneider, Carl P. Prick, and Eduard Arzt. Strength effects in micropillars of a dispersion strengthened superalloy. *Advanced Engineering Materials*, 12(5):385–388, 2010.

[321] Peter L Andresen, Thomas M Angeliu, Ronald M Horn, William R Catlin, and Lisa M Young. Effect of deformation on SCC of unsensitized stainless steel. In *CORROSION 2000*, 2000.

[322] Tetsuo Shoji. Quantification of yield strength effects on IGSCC of austenitic stainless steels in high temperature water. In *Proceedings of 11th Int. Symposium on Environmental Degradation of Materials in Nuclear Power System-Water Reactors*, 2003.

[323] D Gomez-Briceño, M Sol Garcia, and J Lapeña. SCC behaviour of austenitic stainless steels in high temperature water: effect of cold work, water chemistry and type of materials. In *Proc. 14th Int. Con. Environmental Degradation of Materials in Nuclear Power Systems–Water Reactors*, Virginia Beach, 2009.

[324] T. Terachi, T. Yamada, K. Arioka, and S Lozano-Perez. Roll of corrosion in LPSCC of Fe-and Ni-based alloys. In *Proc. Int. Symp. on Research for Aging Management of Light Water Reactors*, pages 215—-226, Fukui City, JAPAN, 2007.

[325] Markus O Speidel and Ruth Magdowski. Stress corrosion cracking of stabilized austenitic stainless steels in various types of nuclear power plants. In *Ninth International Symposium on Environmental Degradation of Materials in Nuclear Power Systems—Water Reactors*, pages 325—-329, Newport, 1999. Wiley Online Library.

[326] Karin H Antonsson, Mikael Grehk, Jun Lu, Lars Hultman, and Erik Holmstr. Stacking fault energies in austenitic stainless steels. 111:39–46, 2016.

[327] T S Byun. On the stress dependence of partial dislocation separation and deformation microstructure in austenitic stainless steels. 51(2003):3063–3071, 2008.

[328] Dávid Molnár, Xun Sun, Song Lu, Wei Li, Göran Engberg, and Levente Vitos. Effect of temperature on the stacking fault energy and deformation behaviour in 316L austenitic stainless steel. *Materials Science and Engineering A*, 759(April):490–497, 2019.

[329] Arpan Das. Revisiting Stacking Fault Energy of Steels. *Metallurgical and Materials Transactions A: Physical Metallurgy and Materials Science*, 47(2):748–768, 2016.

[330] L E Murr. stacking fault anomalies and the measurement of dtacking-fault free energy in F.C.C thin films. *Thin Solid Films*, 4:389–412, 1969.

[331] Alexandra J. Cackett, Chris C. Hardie, Joven J.H. Lim, and Edmund Tarleton. Spherical indentation of copper: Crystal plasticity vs experiment. *Materialia*, 7(March), 2019.

[332] Afrooz Barnoush and Horst Vehoff. In situ electrochemical nanoindentation of a nickel (111) single crystal: hydrogen effect on pop-in behaviour. *Zeitschrift fuer Metallkunde/Materials Research and Advanced Techniques*, 97(9):1224–1229, 2006.

[333] Afrooz Barnoush, Peter Hosemann, Jon Molina-Aldareguia, and Jeffrey M. Wheeler. In situ small-scale mechanical testing under extreme environments. *MRS Bulletin*, 44(6):471–477, 2019.

[334] A B Mann and J B Pethica. Contributed papers. *Studies in Logic and the Foundations of Mathematics*, 134(C):961–976, 1995.

[335] Y. Yao, L. J. Qiao, and Alex A. Volinsky. Hydrogen effects on stainless steel passive film fracture studied by nanoindentation. *Corrosion Science*, 53(9):2679–2683, 2011.

[336] Jinwoo Kim and Cemal Cem Tasan. Microstructural and micro-mechanical characterization during hydrogen charging: An in situ scanning electron microscopy study. *International Journal of Hydrogen Energy*, 44(12):6333–6343, 2019.

[337] Afrooz Barnoush and Horst Vehoff. Recent developments in the study of hydrogen embrittlement: Hydrogen effect on dislocation nucleation. *Acta Materialia*, 58(16):5274–5285, 2010.

[338] M J Cordill, M S Lund, J Parker, C Leighton, A K Nair, D Farkas, N R Moody, and W W Gerberich. The Nano-Jackhammer effect in probing near-surface mechanical properties. *International Journal of Plasticity*, 25(11):2045–2058, 2009.

[339] P Sofronis, Y Liang, and N Aravas. Hydrogen induced shear localization of the plastic flow in metals and alloys. *Eur. J. Mech. A/Solids*, 20:857–872, 2001.

[340] Rakesh Kumar, Deepesh Meena, and Dhiraj K. Mahajan. Modelling of fatigue crack initiation in hydrogen charged polycrystalline nickel. *Procedia Structural Integrity*, 14(2018):668–675, 2019.

[341] Susana del Busto, Covadonga Betegón, and Emilio Martínez-pañeda. A cohesive zone framework for environmentally assisted fatigue. *Engineering Fracture Mechanics*, 185:210–226, 2017.

[342] Weijie Wu, Yanfei Wang, Ping Tao, Xinfeng Li, and Jianming Gong. Cohesive zone modeling of hydrogen-induced delayed intergranular fracture in high strength steels. *Results in Physics*, 11(October):591–598, 2018.

[343] Elsiddig Elmukashfi, Edmund Tarleton, and Alan C.F. Cocks. *A modelling framework for coupled hydrogen diffusion and mechanical behaviour of engineering components*, volume 66. Springer Berlin Heidelberg, 2020.

[344] Steven W. Moore, Majid T. Manzari, and Yin Lin Shen. Nanoindentation in elastoplastic materials: Insights from numerical simulations. *International Journal of Smart and Nano Materials*, 1(2):95–114, 2010.

[345] Jérôme Blaizot, Thibaut Chaise, Daniel Nélias, Michel Perez, Sophie Cazottes, and Philippe Chaudet. Constitutive model for nickel alloy 690 (Inconel 690) at various strain rates and temperatures. *International Journal of Plasticity*, 80:139–153, 2016.

[346] J M. Wheeler and J Michler. Indenter materials for high temperature nanoindentation. *Review of Scientific Instruments*, 90(October), 2013.

[347] Roman Mouginot, Philippe Spätig, and Hans-peter Seifert. Mechanics of Materials Dynamic study of contact damping in martensitic stainless steels using nano- indentation. *Mechanics of Materials*, 149(January):103541, 2020.

[348] SpecialMetals. INCONEL alloy 690: SMC-079. *Special Metals*, pages 1–8, 2002.

[349] H Torres, M Varga, and M Rodríguez Ripoll. Materials Science & Engineering A High temperature hardness of steels and iron-based alloys. *Materials Science & Engineering A*, 671:170–181, 2016.

[350] M Nani Babu and G Sasikala. Effect of temperature on the fatigue crack growth behaviour of SS316L (N). *International Journal of Fatigue*, 140(May):105815, 2020.

[351] C. Anand Badrish, Nitin Kotkunde, Omkar Salunke, and Swadesh Kumar Singh. Study of anisotropic material behavior for inconel 625 alloy at elevated temperatures. *Materials Today: Proceedings*, 18:2760–2766, 2019.

[352] Harold J Frost and Michael F Ashby. *Deformation mechanism maps: the plasticity and creep of metals and ceramics*. Pergamon press, 1982.

[353] X. Li, V. Van Renterghem, and A. Al Mazouzi. Influence of Stacking Fault Energy (SFE) on the Deformation Mode of Stainless Steels. In *Structureal Materials for Innovative Nuclear Systems*, number June, pages 193 – 201, Karlsruhe, Germany, 2007. NEA, AEN.

[354] E O. Hall. The Deformation and Ageing of Mild Steel: III Discussion of Results. *Proceedings of the Physical Society. Section B*, 64:747–753, 1951.

[355] NJ Petch. The cleavage strength of polycrystals. *Journal of the Iron and Steel Institute*, 174:25–28, 1953.

[356] Jeffrey M Wheeler, Christoph Kirchlechner, Jean-sébastien Micha, Daniel Kiener, Jeffrey M Wheeler, Christoph Kirchlechner, and Jean-sébastien Micha. The effect of size on the strength of FCC metals at elevated temperatures : annealed copper. *Philosophical Magazine*, 6435:1–17, 2016.

[357] CE Packard, J M. Wheeler, J C. Trenkle, and C A. Schuh. Nanoindentation: High Temperature. In *Reference module in materials science and materials engineering*, number May, pages 1–8, 2016.

[358] J M Wheeler, R A Oliver, and T W Clyne. Diamond & Related Materials AFM observation of diamond indenters after oxidation at elevated temperatures. *Diamond & Related Materials*, 19(11):1348–1353, 2010.

[359] Martina Meisnar. *High Resolution Characterisation Of Stress Corrosion Cracking*. Dphil, University of Oxford, 2015.

[360] X. Y. Wang, Z. H. Li, Y. K. Bai, X. Y. Cao, T. G. Liu, Y. H. Lu, and T. Shoji. Insights into the SCC crack tip of Alloy 690TT in caustic solution at high temperature. *Journal of Nuclear Materials*, 553, 2021.

[361] S. Y. Persaud, J. M. Smith, B. Langelier, B. Capell, and M. D. Wright. An atom probe tomography study of Pb-caustic SCC in alloy 800. *Corrosion Science*, 140(February):159–167, 2018.

[362] Martina Meisnar, Arantxa Vilalta-clemente, Michael Moody, Koji Arioka, and Sergio Lozano-perez. A mechanistic study of the temperature dependence of the stress corrosion crack growth rate in SUS316 stainless steels exposed to PWR primary water. *Acta Materialia*, 114:15–24, 2016.

[363] Richard P. Gangloff and Brian P. Somerday. Austenitic Stainless Steels. In *Gaseous Hydrogen Embrittlement of High Performance Metals in Energy Systems*, chapter Austenitic, page 46. 2011.

[364] N. R. Moody, M. I. Baskes, S. L. Robinson, and M. W. Perra. Temperature effects of hydrogen-induced crack growth susceptibility of iron-based superalloys. *Engineering Fracture Mechanics*, 68(6):731–750, 2001.

[365] P. Shewmon, Y. L. Shen, C. H. Shen, and M. Meshii. Analysis of diffusion controlled release of hydrogen from nickel and inconel 600. *Acta Metallurgica*, 37(7):1913–1921, 1989.

[366] J. Panter, B. Viguier, J. M. Cloué, M. Foucault, P. Combrade, and E. Andrieu. Influence of oxide films on primary water stress corrosion cracking initiation of alloy 600. *Journal of Nuclear Materials*, 348(1-2):213–221, 2006.

[367] O. Barrera, E. Tarleton, and A. C.F. Cocks. A micromechanical image-based model for the featureless zone of a Fe-Ni dissimilar weld. *Philosophical Magazine*, 94(12):1361–1377, 2014.

[368] T Yonezawa. *4 - Coriou cracking in Japanese pressurized water reactors and its mitigation*. European Federation of Corrosion. Published by Elsevier Ltd, 2016.

[369] C San Marchi, B P Somerday, and S L Robinson. Permeability , solubility and diffusivity of hydrogen isotopes in stainless steels at high gas pressures. 32:100–116, 2007.

[370] M Uhlmann and B.G Pound. DIFFUSIVITY, SOLUBILITY AND TRAPPING BEHAVIOR OF HYDROGEN IN ALLOYS 600, 690tt AND 800. *Corrosion Screnc,*, 40(4):645–662, 1998.

[371] Hiraku Tanimoto, Hiroyoshi Tanaka, and Joichi Sugimura. Observation of Hydrogen Permeation into Fresh Bearing Steel Surface by Thermal Desorption Spectroscopy. 7:291–296, 2011.

[372] K Arioka, T Miyamoto, T Yamada, and T Terachi. ROLE OF CAVITY FORMATION ON CRACK GROWTH OF COLD- WORKED CARBON STEEL , TT 690 AND MA 600 IN HIGH. pages 55–69, 2011.

[373] Sandra Simonetti. Effect of hydrogen pair in an iron-nickel alloy embrittlement. *Journal of Nanostructure in Chemistry*, 3(1):81–84, 2013.

[374] Masaki Mizouchi, Yoshihiro Yamazaki, Yoshiaki Iijima, and Koji Arioka. Low Temperature Grain Boundary Diffusion of Chromium in SUS316 and 316L Stainless Steels. *Materials Transactions*, 45(10):2945–2950, 2004.

[375] B. Malard, B. Remy, C. Scott, A. Deschamps, J. Chêne, T. Dieudonné, and M. H. Mathon. Hydrogen trapping by VC precipitates and structural defects in a high strength Fe-Mn-C steel studied by small-angle neutron scattering. *Materials Science and Engineering A*, 536:110–116, 2012.

[376] Masato Ohnuma, Jun ichi Suzuki, Fu Gao Wei, and Kaneaki Tsuzaki. Direct observation of hydrogen trapped by NbC in steel using small-angle neutron scattering. *Scripta Materialia*, 58(2):142–145, 2008.

[377] Kan Sakamoto and Masayasu Sugisaki. Diffusion coefficient of tritium in Ni-based alloy. *Fusion Science and Technology*, 41(3 II):912–914, 2002.

[378] A Turnbull, RG Ballinger, IS Hwang, MM Morra, M Psaila-Dombrowski, and RM Gates. Hydrogen transport in nickel-base alloys. *Metallurgical Transactions A*, 23(12):3231–3244, 1992.

[379] Zhenbo Zhang, Katie L. Moore, Greg McMahon, Roberto Morana, and Michael Preuss. On the role of precipitates in hydrogen trapping and hydrogen embrittlement of a nickel-based superalloy. *Corrosion Science*, 146(October 2018):58–69, 2019.

[380] Carmen Makepeace. *Fuel Retention in Plasma Facing Materials of the JET ITER-like wall*. PhD thesis, University of Oxford, 2019.

[381] Karen Kruska, Ziqing Zhai, Stephen M Bruemmer, et al. Characterization of scc initiation precursors in cold-worked alloy 690. In *CORROSION 2017*. NACE International, 2017.

[382] S. M. Bruemmer, M. J. Olszta, M. B. Toloczko, and L. E. Thomas. Linking grain boundary microstructure to stress corrosion cracking of cold-rolled alloy 690 in pressurized water reactor primary water. *Corrosion*, 69(10):953–963, 2013.

[383] Takumi Terachi, Makie Okamoto, Takuyo Yamada, and Koji Arioka. Morphology of cavities formed on grain boundary of cracked alloy TT690. In *19th International Conference on Environmental Degradation of Materials in Nuclear Power Systems - Water Reactors*, pages 146–155, 2019.

[384] Helen Dugdale, David E.J. Armstrong, Edmund Tarleton, Steve G. Roberts, and Sergio Lozano-Perez. How oxidized grain boundaries fail. *Acta Materialia*, 61(13):4707–4713, 2013.

[385] Alisa Stratulat, David E.J. Armstrong, and Steve G. Roberts. Micromechanical measurement of fracture behaviour of individual grain boundaries in Ni alloy 600 exposed to a pressurized water reactor environment. *Corrosion Science*, 104:9–16, 2016.

[386] James M Gere and Barry J Goodno. *Mechanics of Materials*. Brooks Cole, 5th edition, 2001.

[387] Rebecca Midori Toda. *Lattice strain development in inconel-690 under biaxial compression and tension*. PhD thesis, Queens University, 2010.

[388] Amanda R. Jenks, Glenn A. White, and Paul Crooker. Crack growth rates for evaluating PWSCC of thick-wall Alloy 690 material and Alloy 52, 152, and variant welds. *American Society of Mechanical Engineers, Pressure Vessels and Piping Division (Publication) PVP*, 6B-2017:1–11, 2017.

[389] C. M. Brown and W. J. Mills. Fracture toughness of alloy 690 and EN52 welds in air and water. *Metallurgical and Materials Transactions A: Physical Metallurgy and Materials Science*, 33(6):1725–1735, 2002.

[390] B Alexandreanu, O K Chopra, and W J Shack. The Stress Corrosion Cracking Behaviour Of Alloys 690 And 152 Weld In A PWR Environment. In *Proceedings of the 2008 ASME Pressure Vessel and Piping Division Conference*, pages 1–11, Chicago,Illinois, USA, 2008.

[391] Y. F. Gao and A. F. Bower. A simple technique for avoiding convergence problems in finite element simulations of crack nucleation and growth on cohesive interfaces. *Modelling and Simulation in Materials Science and Engineering*, 12(3):453–463, 2004.

[392] Jicheng Gong and Angus J. Wilkinson. Micro-cantilever testing of a prismatic slip in commercially pure Ti. *Philosophical Magazine*, 91(7-9):1137–1149, 2011.

[393] C. Motz, T. Schöberl, and R. Pippan. Mechanical properties of micro-sized copper bending beams machined by the focused ion beam technique. *Acta Materialia*, 53(15):4269–4279, 2005.

[394] C. Motz, D. Weygand, J. Senger, and P. Gumbsch. Micro-bending tests: A comparison between three-dimensional discrete dislocation dynamics simulations and experiments. *Acta Materialia*, 56(9):1942–1955, 2008.

[395] Ryo Ishibashi, Toshiaki Horiuchi, J. Kuniya, M. Yamamoto, Sadahiro Tsurekawa, Hiroyuki Kokawa, T. Watanabe, and Tetsuo Shoji. Effect of Grain Boundary Character Distribution on Stress Corrosion Cracking Behavior in Austenitic Stainless Steels. *Materials Science Forum*, 475-479:3863–3866, 2005.

[396] E. Saravanan N Karamched P. Terachi T. Yamada T. Wu S. Tarleton E. Armstrong D. Withers P. Arioka K. Lozano-Perez S. Shen, Z. Roberts. On the role of intergranular nanocavities in long-term stress corrosion cracking of alloy 690. *Acta Materialia*, Submitted 2021.

[397] Bo-shiuan Li. *Measuring Fracture Resistance Behaviour of Tungsten Using Chevron-Notched*. PhD thesis, University of Oxford, 2017.

[398] J Fish and T Belytschko. *A First Course in Finite Element Analysis*. 2007.

[399] Francesco Ferroni, Edmund Tarleton, and Steven Fitzgerald. GPU accelerated dislocation dynamics. *Journal of Computational Physics*, 272:619–628, 2014.

[400] T Couvant, D Haboussa, S Meunier, N Gerald, E Julan, K Sato, and F Delabrouille. A simulation of IGSCC of austenitic stainless steels exposed to primary water. In *17th international conference on environmental degradation of materials in nuclear power systems-water reactors*, Ottawa, Canada, 2015.

[401] T Couvant, M Wehbi, C Duhamel, J Crepin, and R Munier. Development of a "local" model to predict IGSCC: Preliminary Calibration of Parameters for Nickel Alloys exposed to Primary Water. In *17th international conference on environmental degradation of materials in nuclear power systems-water reactors*, Ottawa, Canada, 2015.

[402] F Roters, P Eisenlohr, L Hantcherli, D D Tjahjanto, T R Bieler, and D Raabe. Overview of constitutive laws , kinematics , homogenization and multiscale methods in crystal plasticity finite-element modeling : Theory , experiments , applications. 58(149):1152–1211, 2010.

[403] E. P. Busso, F. T. Meissonnier, and N. P. O'Dowd. Gradient-dependent deformation of two-phase single crystals. *Journal of the Mechanics and Physics of Solids*, 48(11):2333–2361, 2000.

[404] F. T. Meissonnier, E. P. Busso, and N. P. O'Dowd. Finite element implementation of a generalised non-local rate-dependent crystallographic formulation for finite strains. *International Journal of Plasticity*, 17(4):601–640, 2001.

[405] M. Sachtleber, Z. Zhao, and D. Raabe. Experimental investigation of plastic grain interaction. *Materials Science and Engineering A*, 336(1-2):81–87, 2002.

[406] Nicolò Grilli, Alan C F Cocks, and Edmund Tarleton. Crystal plasticity finite element modelling of coarse-grained -uranium. *Computational Materials Science*, 171(April 2019):109276, 2020.

[407] F. P.E. Dunne, D. Rugg, and A. Walker. Lengthscale-dependent, elastically anisotropic, physically-based hcp crystal plasticity: Application to cold-dwell fatigue in Ti alloys. *International Journal of Plasticity*, 23(6):1061–1083, 2007.

[408] F Dunne and N Petrinic. *Introduction to computational plasticity*. Oxford University Press, 2005.

[409] D. S. Dugdale. Yielding of steel sheets containing slits. *Journal of the Mechanics and Physics of Solids*, 8(2):100–104, 1960.

[410] G. I. Barenblatt. THE MATHEMATICAL THEORY OF EQUILIBRIUM CRACKS FORMED IN BRITTLE FRACTURE (Translated from Source). *Zhurnal Prikladnoy Mekhaniki i Tekhnicheskoy*, 4:3–56, 1962.

[411] G. I. Barenblatt. The formation of equilibrium cracks during brittle fracture. General ideas and hypotheses. Axially-symmetric cracks. *Journal of Applied Mathematics and Mechanics*, 23(3):622–636, 1959.

[412] A. Needleman. AN ANALYSIS OF TENSILE DECOHESION ALONG AN INTERFACE. *J. Mech. Phys. Solids*, 38(3):289–324, 1990.

[413] P. Camanho and C.G. Davila. Mixed-Mode Decohesion Finite Elements in for the Simulation Composite of Delamination Materials. *Nasa*, TM-2002-21(June):1–37, 2002.

[414] A. F. Bower. Constitutive Models Relations between Stress and Strain, 2008.

[415] R. Hielscher and H. Schaeben. A novel pole figure inversion method: Specification of the MTEX algorithm. *Journal of Applied Crystallography*, 41(6):1024–1037, 2008.

[416] Suchandrima Das. *Investigating Irradiation Damage in Tungsten for Fusion Power under the supervision of*. PhD thesis, University of Oxford, 2019.

[417] M. E. Kartal, R. Kiwanuka, and F. P.E. Dunne. Determination of subsurface stresses at inclusions in single crystal superalloy using HR-EBSD, crystal plasticity and inverse eigenstrain analysis. *International Journal of Solids and Structures*, 67-68:27–39, 2015.

[418] A. Kareer, E. Tarleton, C. Hardie, S.V. Hainsworth, and A.J. Wilkinson. Scratching the Surface: Elastic Rotations Beneath Nanoscratch and Nanoindentation Tests. *SSRN Electronic Journal*, 2020.

[419] Abaqus Documentation and User Manual. Version 6.10. *Dassault systemes*, 2010.

[420] Christopher David Hardie. *Micro-Mechanics of Irradiated Fe-Cr Alloys for Fusion Reactors*. Doctor of philsophy, University of Oxford, 2013.

[421] Igor Simonovski and Leon Cizelj. Cohesive element approach to grain level modelling of intergranular cracking. *Engineering Fracture Mechanics*, 110:364–377, 2013.

[422] S Selamet and M Garlock. Guidelines for Modeling Three Dimensional Structural. In *International Symposium "Steel Structures:Culture & Sustainability 2010"*, number September, pages 1–10, Istanbul, Turkey, 2010.

[423] A Turon Travesa. *Simulation of delamination in composites under quasi-static and fatigue loading using cohesive zone models*. PhD thesis, University of Girona, 2006.

[424] Kyongchan Song, Cg Davila, and Ca Rose. Guidelines and parameter selection for the simulation of progressive delamination. *2008 ABAQUS User's Conference*, pages 1–15, 2008.

[425] B. Xiao, J. Feng, C. T. Zhou, Y. H. Jiang, and R. Zhou. Mechanical properties and chemical bonding characteristics of Cr 7 C3 type multicomponent carbides. *Journal of Applied Physics*, 109(2), 2011.

[426] Thomas M. Angeliu and Gary S. Was. Behavior of grain boundary chemistry and precipitates upon thermal treatment of controlled purity alloy 690. *Metallurgical Transactions A*, 21(8):2097–2107, 1990.

[427] Matthew J Olszta, Ziqing Zhai, Mychailo Toloczko, and Steven M Bruemmer. Examination of Cavity Formation in Cold-Worked Alloy 690. *Journal of Chemical Information and Modeling*, 53(9):1689–1699, 2013.